

The Effect of Leading-edge Tubercles on Airfoil Aerodynamic Performance

by

Payam MEHREGAN

THESIS PRESENTED TO ÉCOLE DE TECHNOLOGIE SUPÉRIEURE
IN PARTIAL FULFILLMENT FOR THE DEGREE OF
DOCTOR OF PHILOSOPHY
PH. D.

MONTREAL, OCTOBER 20, 2022

ÉCOLE DE TECHNOLOGIE SUPÉRIEURE
UNIVERSITÉ DU QUÉBEC



PAYAM MEHREGAN, 2022



This Creative Commons licence allows readers to download this work and share it with others as long as the author is credited. The content of this work can't be modified in any way or used commercially.

BOARD OF EXAMINERS (THESIS PH.D.)

THIS THESIS HAS BEEN EVALUATED

BY THE FOLLOWING BOARD OF EXAMINERS

Mr. Louis Dufresne, Thesis Supervisor
Department of Mechanical Engineering, École de technologie supérieure

Mrs. Annie Poulin, President of the Board of Examiners
Department of Construction Engineering, École de technologie supérieure

Mr. François Garnier, Member of the jury
Department of Mechanical Engineering, École de technologie supérieure

Mr. Simon-Philippe Breton, External Evaluator
Physical Scientist, Environment Canada

THIS THESIS WAS PRESENTED AND DEFENDED

IN THE PRESENCE OF A BOARD OF EXAMINERS AND PUBLIC

ON SEPTEMBER 16, 2022

AT ÉCOLE DE TECHNOLOGIE SUPÉRIEURE

ACKNOWLEDGMENT

I would like to thank all of the people that have supported me during my Ph.D. candidature here at ÉTS University.

First of all, I would like to express my sincere appreciation to my supervisor Prof. Louis Dufresne, for giving me the opportunity to be part of his team and for his continual support and excellent guidance from the very early stages of this research. I thank him for his patients, motivation, and great comments that I learned a lot from them. Without his support and advice, this research work and this thesis would have never been accomplished.

Last but of course not least, I want to thank my parents for their sacrifice and unconditional love. My wonderful mother to whom I owe most of my life, and my loving father who has made numerous sacrifices for me. Words cannot express the appreciation I feel for them.

L'effet des tubercules du bord d'attaque sur les performances aérodynamiques des profils

Payam MEHREGAN

RESUME

Dans cette recherche, l'effet des tubercules, situés au niveau du bord d'attaque, sur les performances aérodynamiques des profils NACA 0010 symétrique et RAF-19 à forte cambrure (aile 2D) est analysé numériquement en utilisant le logiciel ANSYS/CFX et le modèle de turbulence $k-\varepsilon$, au nombre de Reynolds de 2.5×10^5 .

Sur le profil NACA 0010, ces ondulations tendent à réduire le coefficient de portance pré-décrochage tout en améliorant le coefficient de portance post-décrochage. De plus, en augmentant la longueur et l'amplitude d'onde des ondulations, le coefficient de portance s'améliore pour des angles d'attaque au-delà du décrochage. Cependant, sur les profils RAF-19 modifiés, les améliorations de performance concernant le coefficient de portance sont uniquement observées pour les profils dont la longueur et l'amplitude d'onde sont les plus courts, ce qui pourrait augmenter la C_{Lmax} , ainsi que le coefficient de portance avant et après décrochage. Pour chaque type de profils, les ondulations de bord d'attaque tendent à augmenter les coefficients de traînée de tous les profils modifiés.

Les résultats concernant les contraintes de cisaillement de la paroi et les tourbillons dans le sens du courant montrent que pour tous les profils modifiés, la couche limite est dynamisée par les tourbillons contrarotatifs générés par les ondulations. Dans cette recherche, l'effet de l'amplitude, de la longueur d'onde et du rapport amplitude/longueur d'onde des tubercules sur la force et l'interaction des tourbillons dans le sens du courant par conséquent, leurs effets sur les coefficients de portance et de traînée des profils modifiés sont discutés.

On en conclut qu'alors que l'augmentation de l'amplitude des tubercules entraîne une augmentation de la force des tourbillons dans le sens du courant, l'augmentation de la longueur d'onde des tubercules entraîne une réduction de l'intensité de l'interaction des tourbillons dans le sens du courant. Ainsi, entre les profils NACA 0010 modifiés avec des rapports d'amplitude et de longueur d'onde proches, des valeurs plus élevées du coefficient de portance sont observées aux angles d'attaque post-décrochage sur les profils dont la longueur et l'amplitude d'onde est plus grand.

Dans cette recherche, la relation entre les tourbillons dans le sens de l'écoulement et les régions d'écoulement séparées, générées derrière la section en auge des profils modifiés aux angles d'attaque avant décrochage, est également discutée. Ces régions d'écoulement séparées sont responsables de la réduction du coefficient de portance sur les profils modifiés aux angles d'attaque avant décrochage.

VIII

De plus, durant cette étude, l'effet des bosses générés le long de la corde des profils modifiés et leur influence sur l'interaction des tourbillons dans le sens du courant sont discutés. Ces bosses dans le sens de l'envergure sont générées en raison de préserver le rapport épaisseur/corde lors de la conception des profils modifiés.

Mots-clés : tubercules du bord d'attaque, aérodynamique, tourbillons dans le sens du courant, la force et l'interaction des tourbillons dans le sens du courant

The effect of leading-edge tubercles on airfoil aerodynamic performance

Payam MEHREGAN

ABSTRACT

In this research, the effect of leading-edge tubercles on the aerodynamic performance of symmetric NACA 0010 and high-cambered RAF-19 airfoils (2D wings) is numerically analyzed using the software ANSYS/CFX and the $k-\epsilon$ turbulence modeling at the Reynolds number of 2.5×10^5 .

On the NACA 0010 airfoil, these tubercles cause to reduce the pre-stall lift coefficient while improving the post-stall lift coefficient. Besides, the airfoils with the largest wavelength and amplitude sizes of tubercles are shown to have the highest value of lift coefficient at post-stall angles of attack. However, on the modified RAF-19 airfoils, the performance improvements in the case of lift coefficient are only observed in the shortest wavelength and amplitude airfoils which could increase the C_{Lmax} , as well as the pre-and post-stall lift coefficient. On both airfoil types, the leading-edge tubercles cause the increase in drag coefficients on all the modified airfoils.

The wall shear stresses and streamwise vortices results show that on all the modified airfoils, the boundary layer is energized by the counter-rotating streamwise vortices generated by the tubercles. In this research, the effect of amplitude, wavelength, and amplitude to wavelength ratio size of tubercles on the strength and interaction of the streamwise vortices and consequently their effect on the lift and drag coefficient of the modified airfoils are discussed. It is concluded that while increasing the amplitude of tubercles causes to increase the strength of the streamwise vortices, increasing the wavelength of tubercles causes to reduce the intensity of interaction of the streamwise vortices. Thus, between the modified NACA 0010 airfoils with close values of amplitude and wavelength ratio sizes, higher values of lift coefficient are observed at post-stall angles of attack on airfoils having larger-amplitude and wavelength of tubercles.

In this research, the relation between the streamwise vortices and the separated flow regions generated behind the trough section of the modified airfoils at pre-stall angles of attack are also discussed. These separated flow regions are responsible for the lift coefficient reduction on the modified airfoils at pre-stall angles of attack.

Moreover, in this study, the effect of spanwise bumps generated along the chord of the modified airfoils and their influence on the interaction of the streamwise vortices are discussed. These spanwise bumps are generated due to preserving the thickness to chord ratio while designing the modified airfoils.

X

Keyword: Leading-edge tubercles, aerodynamics, streamwise vortices, strength and interaction of streamwise vortices

TABLE OF CONTENTS

	Page
INTRODUCTION	1
0.1 Aerodynamic forces	1
0.1.1 Lift and drag forces	2
0.1.2 Boundary layer and flow separation	5
0.1.3 Components drag and end effects on 3D finite span wings	7
0.2 Flow control	10
0.2.1 Leading-edge tubercles	11
CHAPTER 1 LITERATURE REVIEW	17
1.1 The effect of leading-edge tubercles on the aerodynamic performance	17
1.1.1 Effect of leading-edge tubercles on Humpback whale flipper models	17
1.1.2 Comparing the effect of leading-edge tubercles on 2D infinite-span and 3D wings	19
1.1.3 Effect of amplitude and wavelength sizes of tubercles on the aerodynamic performance of the modified 2D wings	23
1.1.4 The effect of leading-edge tubercles on different type of airfoils	27
1.2 Research done on the flow mechanism on 2D wings with tubercles	30
1.2.1 Interaction of the streamwise vortices	32
1.3 Potential applications of leading-edge tubercles	36
1.4 Research objectives	38
CHAPTER 2 METHODOLOGY	41
2.1 Geometrical configurations	41
2.2 Equations and turbulence modeling	46
2.2.1 <i>The k-ε</i> turbulence modeling	47
2.2.2 Scalable wall function	49
2.2.3 Mesh convergence study on NACA 0010 airfoil	52
2.2.4 Baseline NACA 0010 airfoil validation	54
2.2.5 Mesh convergence study on RAF-19 airfoil	57
2.2.6 Baseline RAF-19 airfoil Validation	59
CHAPTER 3 EFFECT OF LEADING-EDGE TUBERCLES ON SYMMETRIC AIRFOIL	65
3.1 Integral quantities	65
3.1.1 The effect of the amplitude of tubercles on integral quantities	65
3.1.2 The effect of the wavelength of tubercles on integral quantities	66
3.1.3 The effect of the amplitude to wavelength ratio of tubercles on integral quantities	66
3.2 The streamwise vortices	71

3.2.1	The convergence and interaction of the stream-wise vortices	71
3.2.2	Circulation.....	75
3.3	The effect of streamwise vortices on integral quantities	82
3.3.1	The effect of the streamwise vortices at post-stall angles of attack of 16-degrees.....	84
3.3.2	Unsteady simulations.....	89
3.3.3	The effect of the streamwise vortices at pre-stall angles of attack	91
CHAPTER 4	EFFECT OF LEADING-EDGE TUBERCLES ON HIGH-CAMBERED AIRFOIL	95
4.1	Integral quantities.....	95
4.1.1	The effect of the amplitude of tubercles on integral quantities	95
4.1.2	The effect of the wavelength of tubercles on integral quantities	97
4.1.3	The effect of the amplitude to wavelength ratio of tubercles on integral quantities.....	97
4.2	The streamwise vortices.....	107
4.2.1	The convergence and interaction of the stream-wise vortices	107
4.2.2	Circulation.....	110
4.3	The effect of streamwise vortices on integral quantities of RAF-19 airfoil	116
4.4	Discussions	127
CHAPTER 5	THE EFFECT OF LEADING-EDGE TUBERCLES ON NACA 0010 AERODYNAMIC PERFORMANCE.....	129
5.1	Abstract.....	129
5.2	Introduction.....	130
5.3	Methodology.....	135
5.3.1	Geometrical configurations.....	135
5.3.2	Equations and turbulence modeling.....	138
5.3.2.1	$k-\epsilon$ turbulence modeling.....	139
5.3.2.2	Scalable wall function.....	141
5.3.3	Mesh convergence study.....	144
5.3.4	Baseline airfoil validation	146
5.4	Results.....	150
5.4.1	Integral quantities.....	150
5.4.1.1	The effect of the amplitude of tubercles on integral quantities.....	150
5.4.1.2	The effect of the wavelength of tubercles on integral quantities.....	151
5.4.1.3	The effect of the amplitude to wavelength ratio of tubercles on integral quantities	151
5.4.2	The streamwise vortices.....	156
5.4.2.1	Interaction of the streamwise vortices	156
5.4.2.2	Circulation.....	160
5.4.3	The effect of streamwise vortices on integral quantities	167

5.4.3.1	The effect of the streamwise vortices at post-stall angles of attack.....	169
5.4.3.2	Unsteady flow behavior	174
5.4.3.3	The effect of the streamwise vortices at pre-stall angles of attack.....	176
5.5	Conclusion	179
CHAPTER 6 CONCLUSIONS AND RECOMMENDATIONS		182
6.1	Conclusions.....	182
6.2	Recommendations.....	186
LIST OF REFERENCES.....		189

LIST OF TABLES

		Page
Table 2.1	NACA0010 airfoil geometrical characteristics.....	41
Table 2.2	RAF-19 airfoil geometrical characteristics	41
Table 2.3	Tubercles' amplitudes and wavelength sizes.....	42
Table 2.4	Model coefficients used in the $k-\varepsilon$ turbulence modeling.....	49
Table 2.5	Mesh convergence study of the NACA 0010 baseline airfoil.....	53
Table 2.6	Number of elements used in NACA 0010 modified airfoils.....	53
Table 2.7	SD 8020 airfoil characteristics (% C)	54
Table 2.8	Comparison of the lift and drag coefficient of the NACA 0010 baseline airfoil obtained by the XFOIL code and ANSYS/CFX at 0-degree angle of attack	56
Table 2.9	Mesh convergence study on RAF-19 baseline airfoil	57
Table 2.10	Number of elements used in RAF-19 modified airfoils.....	58
Table 3.1	Effective length of the streamwise vortices on NACA 0010 modified airfoils at a 16 degree AOA	87
Table 4.1	Effective length of the streamwise vortices on the RAF-19 modified airfoils at 16-degree AOA	121
Table 5.1	Tubercles' amplitudes and wavelength sizes.....	136
Table 5.2	Model coefficients used in the $k-\varepsilon$ turbulence modeling formulation.....	141
Table 5.3	Mesh convergence study	145
Table 5.4	Number of elements used in each airfoil with undulating leading edge	145
Table 5.5	NACA 0010 airfoil characteristics (% C).....	146

Table 5.6	SD 8020 airfoil characteristics (% C)147
Table 5.7	Comparison of the lift and drag coefficient obtained by the XFOIL code and ANSYS/CFX at a 0-degree angle of attack.....149
Table 5.8	Effective length of the streamwise vortices on NACA 0010 modified airfoils at a 16-degree AOA.....172

LIST OF FIGURES

	Page
Figure 0.1	The four forces acting on an airplane in steady flight.....2
Figure 0.2	Resultant aerodynamic force and moment on the body3
Figure 0.3	Resultant aerodynamic force, splits in to lift and drag forces.....3
Figure 0.4	Schematic of lift and drag coefficients versus angle of attack; illustration of maximum lift coefficient and minimum drag coefficient.....4
Figure 0.5	Illustration of the boundary layer in the Prandtl's boundary layer theory.....6
Figure 0.6	Boundary layer separation illustration based on Prandtl's boundary layer theory.....7
Figure 0.7	Illustration of wingtip vortices rotation and the associated downwash and upwash.....9
Figure 0.8	Illustration of lift-induced drag due to downwash9
Figure 0.9	Humpback whale (<i>Megaptera novaeangliae</i>) flipper with leading edge tubercles (left), breaching humpback whale showing relative size of the flipper (top right), and cross section of flipper (bottom right)13
Figure 0.10	Calculated and observed turning performance of the Humpback whale15
Figure 1.1	Smooth (left) and scalloped (right) idealized humpback whale flipper models.....18
Figure 1.2	a) Lift coefficient b) Drag coefficient c) Lift-to-drag ratio of the scalloped and smooth leading-edge flipper models19
Figure 1.3	Infinite-span wings and semi-span flipper models.....21

XVIII

Figure 1.4	Effect of leading-edge tubercles on lift coefficient (left) and lift to drag ratio (right) of 2D wing	21
Figure 1.5	Effect of leading-edge tubercles on lift coefficient (left) and lift to drag ratio (right) on finite span wings.....	22
Figure 1.6	a) Instantaneous vorticity magnitude slices in chord-wise direction and (b) Averaged shear-stress lines at $\alpha = 15$ degree and $Re = 500,000$	23
Figure 1.7	Baseline and modified airfoils with leading-edge protuberances	24
Figure 1.8	The effect of amplitude of the tubercles on lift (left) and drag (right) coefficients of the modified airfoils.....	25
Figure 1.9	The effect of wavelength of the tubercles on lift (left) and drag (right) coefficients of the modified airfoils (with small amplitude size)	25
Figure 1.10	The effect of wavelength of the tubercles on lift (left) and drag (right) coefficients of the modified airfoils (with medium amplitude size).....	26
Figure 1.11	Effect of wavelength of tubercles on the lift coefficient of NACA0021 airfoil.....	27
Figure 1.12	Effect of leading-edge tubercles on lift coefficient of S-1223 airfoil	29
Figure 1.13	Effect of leading-edge tubercles on drag coefficient of S-1223 airfoil	29
Figure 1.14	Photograph of flow visualization analysis using surface tufts on baseline (top) and modified NACA634 -021 airfoils (bottom) at 12, 18 and 24 degree angles of attack from left to right.....	31
Figure 1.15	Streamwise vorticity contours on a modified hydrofoil as a function of angle of attack at a chordwise spatial location of $0.12C$	33
Figure 1.16	Streamwise vorticity, contours on a modified hydrofoil as a function of angle of attack at a chordwise spatial location of $0.36C$	34
Figure 1.17	Counter-rotating vortices with image pairs.....	35

Figure 2.1	Modified NACA 0010 airfoil geometries with multiple tubercles a) baseline b) A3W11 C) A6W11 D) A6W21 E) A6W43 and F) A11W43	43
Figure 2.2	Modified RAF-19 airfoil geometries with multiple tubercles a) baseline b) A3W11 C) A6W11 D) A6W21 E) A6W43 and F) A11W43	44
Figure 2.3	Modified NACA 0010 airfoil geometries with single tubercle a) baseline b) A3W11 C) A6W11 D) A6W21 E) A6W43 and F) A11W43	45
Figure 2.4	Modified RAF-19 airfoil geometries with single tubercle a) baseline b) A3W11 C) A6W11 D) A6W21 E) A6W43 and F) A11W43	46
Figure 2.5	Computational domain with segmented mesh and the boundary conditions.....	52
Figure 2.6	Comparison of the lift coefficients of NACA 0010 and SD 8020 airfoils in the numerical simulation and experimental research of Selig (1995).....	55
Figure 2.7	Comparison of the drag coefficients of NACA 0010 and SD 8020 airfoils in the numerical simulation and experimental research of Selig (1995).....	56
Figure 2.8	Comparison of the pressure coefficients of the NACA 0010 baseline airfoil obtained by XFOIL code and ANSYS/CFX at a 0-degree angle of attack.....	57
Figure 2.9	Comparison of calculated lift (a) and drag (b) coefficients of RAF-19 baseline airfoil using SST turbulence modeling and XFOIL results.....	60
Figure 2.10	Comparison of calculated lift (a) and drag (b) coefficients of RAF-19 baseline airfoil using K- ϵ turbulence modeling and XFOIL results.....	61
Figure 2.11	Comparison of the CFX and XFOIL pressure coefficients on the suction side of the RAF-19 baseline airfoil at 4 (a) and 6 (b) degree angle of attack respectively.....	62
Figure 3.1	Analyzing the effect of the amplitude of tubercles on the lift (a) and drag (b) coefficients of the NACA 001 modified airfoils (first set).....	67

Figure 3.2	Analyzing the effect of the amplitude of tubercles on the lift (a) and drag (b) coefficients of the NACA 001 modified airfoils (second set).....	68
Figure 3.3	Analyzing the effect of the wavelength of tubercles on the lift (a) and drag (b) coefficients of the NACA 001 modified airfoils.....	69
Figure 3.4	Analyzing the effect of the amplitude to wavelength ratio of tubercles on the lift (a) and drag (b) coefficients of the NACA 001 modified airfoils.....	70
Figure 3.5	Streamwise vortices on NACA 0010_A11W43 airfoil at 0, 4, 8, 10, 12, 16, 20, and 24 degrees of angles of attack	73
Figure 3.6	Streamwise vortices on NACA 0010_A6W11 airfoil at 0, 4, 8, 10, 12, 16, 20, and 24 degrees of angles of attack	74
Figure 3.7	Positive (a) and negative (b) circulation values of all NACA0010 Modified airfoils.....	77
Figure 3.8	Effect of the amplitude of tubercles on positive (a) and negative (b) circulation values of NACA0010 Modified airfoils (first set)	78
Figure 3.9	Effect of the amplitude of tubercles on positive (a) and negative (b) circulation values of NACA0010 Modified airfoils (second set).....	79
Figure 3.10	Effect of the wavelength of tubercles on positive (a) and negative (b) circulation values of NACA0010 Modified airfoils	80
Figure 3.11	Effect of the amplitude to wavelength ratio of tubercles on positive (a) and negative (b) circulation values of NACA0010 Modified airfoils.....	81
Figure 3.12	Lift (a) and drag (b) coefficient results for all the NACA 0010 modified airfoils.....	83
Figure 3.13	Wall shear stresses from left to right on the baseline NACA 0010, A3W11, A6W11, A6W21, A6W43 and A11W43 airfoils at a 16 degree angle of attack.....	87
Figure 3.14	Streamwise vortices on the modified NACA 0010 airfoils at a 16-degree angle of attack	88
Figure 3.15	Wall shear stresses and streamwise vortices at time-steps of 140 (a and b) and 145 (c and d) on the NACA 0010_A6W21 airfoil at a 16 degree AOA.....	90

Figure 3.16	Wall shear stresses from left to right on baseline NACA 0010, A3W11, A6W11, A6W21, A6W43, and A11W43 airfoils at a 10 degree angle of attack.....	92
Figure 3.17	Streamwise vorticity (a) vs. tangential projection of the velocity field (b) on NACA0010_A11W43 airfoil at a slice at 0.2 C	93
Figure 4.1	Comparison of the effect of the amplitude of tubercles on the lift coefficients of RAF-19 (a) and NACA 0010 (b) airfoils (first set).....	99
Figure 4.2	Comparison of the effect of the amplitude of tubercles on the drag coefficients of RAF-19 (a) and NACA 0010 (b) airfoils (first set)	100
Figure 4.3	Comparison of the effect of the amplitude of tubercles on the lift coefficients of RAF-19 (a) and NACA 0010 (b) airfoils (second set).....	101
Figure 4.4	Comparison of the effect of the amplitude of tubercles on the drag coefficients of RAF-19 (a) and NACA 0010 (b) airfoils (second set).....	102
Figure 4.5	Comparison of the effect of the wavelength of tubercles on the lift coefficient of RAF-19 (a) and NACA 0010 (b) airfoils.....	103
Figure 4.6	Comparison of the effect of the wavelength of tubercles on the drag coefficient of RAF-19 (a) and NACA 0010 (b) airfoils.....	104
Figure 4.7	Comparison of the effect of the amplitude to wavelength ratio of tubercles on the lift coefficient of RAF-19 (a) and NACA 0010 (b) airfoils	105
Figure 4.8	Comparison of the effect of the amplitude to wavelength ratio of tubercles on the drag coefficient of RAF-19 (a) and NACA 0010 (b) airfoils	106
Figure 4.9	Streamwise vortices on RAF-19_A11W43 airfoil at a) 0, b) 4, c) 8, d) 10, e) 12, f) 16, g) 20, and h) 24- angles of attack.....	109
Figure 4.10	Positive (a) and negative (b) circulation values of all the modified RAF-19 airfoils.....	111
Figure 4.11	Effect of the amplitude of tubercles on positive (a) and negative (b) circulation values of the modified RAF-19 airfoils (first set).....	112

Figure 4.12	Effect of the amplitude of tubercles on positive (a) and negative (b) circulation values of the modified RAF-19 airfoils (second set).....	113
Figure 4.13	Effect of the wavelength of tubercles on positive (a) and negative (b) circulation values of the modified RAF-19 airfoils	114
Figure 4.14	Effect of the amplitude to wavelength of tubercles on positive (a) and negative (b) circulation values of the modified RAF-19 airfoils	115
Figure 4.15	All lift (a) and drag (b) coefficients of the modified RAF-19 airfoils	117
Figure 4.16	Streamwise wall shear stresses at 12-degree angle of attack on the RAF-19 baseline, A3W11, A6W11, A6W21, A6W43, and A11W43 from left to right	120
Figure 4.17	Streamwise wall shear stresses at 16-degree angle of attack on the RAF-19 baseline, A3W11, A6W11, A6W21, A6W43, and A11W43 from left to right	121
Figure 4.18	Streamwise vortices at 12-degree angle of attack on RAF-19_A3W11 (a), A6W11 (b), and A11W43 (c) airfoils	122
Figure 4.19	Streamwise vortices at 16-degree angle of attack on RAF-19_A3W11 (a), A6W11 (b), and A11W43 (c) airfoils	122
Figure 4.20	Top-front and Top-side views of streamwise vortices on A3W11 airfoil at 12-degree angle of attack on RAF-19 (a and b) and NACA 0010 (c and d) airfoils	123
Figure 4.21	Top-front and top-side view of streamwise vortices on A6W11 airfoil at 12-degree angle of attack on RAF-19 (a and b) and NACA 0010 (c and d) airfoils	124
Figure 4.22	Top-front and side view of streamwise vortices on A3W11 airfoil at 16-degree angle of attack on RAF-19 (a and b) and NACA 0010 (c and d) airfoils	125
Figure 4.23	Top-front and top-side view of streamwise vortices on A6W11 airfoil at 16-degree angle of attack on RAF-19 (a and b) and NACA 0010 (c and d) airfoils	126
Figure 4.24	Dorsal fin on Sail fish	128

Figure 5.1	Modified airfoil geometries with multiple tubercles a) baseline b) A3W11 C) A6W11 D) A6W21 E) A6W43 and F) A11W43.....	137
Figure 5.2	Modified airfoil geometries with single tubercles a) baseline b) A3W11 C) A6W11 D) A6W21 E) A6W43 and F) A11W43.....	138
Figure 5.3	Computational domain with segmented mesh and the boundary conditions.....	144
Figure 5.4	Comparison of the lift coefficients in the numerical simulation and experimental research of Selig et al. (1995).....	148
Figure 5.5	Comparison of the drag coefficients in the numerical simulation and experimental research of Selig et al. (1995).....	148
Figure 5.6	Comparison of the pressure coefficients obtained by XFOIL and ANSYS/CFX at a 0-degree angle of attack.....	149
Figure 5.7	Analyzing the effect of the amplitude of tubercles on the lift coefficient (a) and drag coefficient (b) of the modified airfoils.....	152
Figure 5.8	Analyzing the effect of the amplitude of tubercles on the lift coefficient (a) and drag coefficient (b) of the modified airfoils.....	153
Figure 5.9	Analyzing the effect of the wavelength of tubercles on the lift coefficient (a) and drag coefficient (b) of the NACA 0010 modified airfoils.....	154
Figure 5.10	Analyzing the effect of the amplitude to wavelength ratio of tubercles on the lift coefficient (a) and drag coefficient (b) of the NACA 0010 modified airfoils.....	155
Figure 5.11	Streamwise vortices on A11W43 airfoil at 0, 4, 8, 10, 12, 16, 20, and 24 degrees of angles of attack.....	158
Figure 5.12	Streamwise vortices on A6W11 airfoil at 0, 4, 8, 10, 12, 16, 20, and 24 degrees of angles of attack.....	159
Figure 5.13	Positive (a) and negative (b) circulation values on modified airfoils at 0.05C of the mean-chord length.....	162
Figure 5.14	Effect of the amplitude of tubercles on positive (a) and negative (b) circulation values.....	163
Figure 5.15	Effect of the amplitude of tubercles on positive (a) and negative (b) circulation values.....	164

Figure 5.16	Effect of the wavelength of tubercles on positive (a) and negative (b) circulation values165
Figure 5.17	Effect of the amplitude to wavelength ratio of tubercles on positive (a) and negative (b) circulation values166
Figure 5.18	Lift (a) and drag (b) coefficient results for all the modified airfoils168
Figure 5.19	Shear stresses from left to right on baseline NACA 0010, A3W11, A6W11, A6W21, A6W43 and A11W43 airfoils at a 16-degree angle of attack172
Figure 5.20	Streamwise vortices on the modified airfoils at a 16-degree angle of attack173
Figure 5.21	Wall shear stresses and streamwise vortices at time-steps of 140 (a and b) and 145 (c and d) on the A6W21 airfoil at a 16-degree AOA175
Figure 5.22	Wall Shear stresses from left to right on baseline, A3W11, A6W11, A6W21, A6W43 and A11W43 airfoils at a 10-degree angle of attack177
Figure 5.23	Streamwise vorticity (a) vs. tangential projection of the velocity field (b) on A11W43 airfoil at a slice at 0.2 C178
Figure 6.1	Wavy wing section showing peak-to-peak angular amplitude (θ) expressed in degrees and wavelength (w) in millimeters (a), and tubercled wing section showing the amplitude (A) and wavelength (W) expressed in millimeters (b)187

LIST OF SYMBOLS

A	Amplitude of the tubercles
W	Wavelength of the tubercles
\bar{C}	Mean chord length
C	Chord length
$C(z)$	Tubercles chord length in each span-wise direction
z	Spanwise orient
U	Inlet velocity
V_∞	Free-stream velocity
ρ	Density
k	Turbulence kinetic energy
ε	Turbulence eddy annihilation
μ	Dynamic viscosity
α	Angle of attack
u_τ	Friction velocity
U_t	Known velocity tangent to the wall at a distance of y from the wall
u^*	Alternative velocity scale used in scalable wall-function
y	Distance from the wall
τ_w	Wall shear stress
K	Von Karman constant
L	log-layer constant depending on wall roughness
P	Pressure
p'	Modified pressure
μ_f	The effective viscosity accounting for turbulence
μ_t	Turbulent viscosity
P_k	Turbulence production due to viscous forces
P_{kb}	Production terms for k due to Buoyancy
$P_{\varepsilon b}$	Production terms for ε due to Buoyancy

GCI_{fine}^{21}	Fine-grid convergence index
G	Number of elements
r	Mesh refinement factor
e_a^{21}	Approximate relative error
$\vec{\omega}$	Vorticity vector
\vec{n}	Vector normal to the surface s
s	Surface area
ds	Element of surface area
Γ	Circulation
h	Vertical distance of the vortex core from the flat surface
$U_{induced}$	Induced velocity on a vortex
ϕ	Bank angle
m_v	Whale's virtual mass
C_{Lmax}	Maximum lift coefficient
C_L	Lift coefficient
C_D	Drag coefficient
U_∞	Free stream velocity
Re	Reynolds number
A_f	Total planar area of the flippers

INTRODUCTION

In recent years, the increasing demand for devices such as micro-air vehicles, small unmanned aerial vehicles, and wind turbines, has attracted researchers to investigate the efficiency of wings at low Reynolds numbers. Small UAVs (Unmanned Aerial Vehicles) and Micro Aerial Vehicles (MAV), due to their low flying speed and small chord length are generally flying at low Reynolds numbers, and their wings mostly operate in the laminar and transitional flow regimes (Bolzon, Kelso, & Arjomandi, 2016b). At these Reynolds numbers, the possibility of flow separation and stall increases causing a reduction in the aerodynamic performance, as well as the possibility of reduction in fatigue life of the devices working in these flow regimes (Zhang, Wang, & Xu, 2013).

Finding a method for delaying stall and increasing the lift coefficient generated on wings can have many benefits from increasing the maneuverability and stability of the aircrafts and UAVs and reducing their take-off and landing distances, to increase the power generation on wind turbines, etc.

In the following sub-sections, first, an introduction to aerodynamic forces, stall, and 3D effect on wings will be presented. Accordingly, the concept of flow separation will be described to explain the stall phenomenon. Then, the concept of flow control and the newly discussed flow control device known as leading-edge tubercles/undulations will be presented.

0.1 Aerodynamic forces

In steady flight configurations where no side forces exist, the aerodynamic forces on aircraft can be expressed in 2D. Thus, it is expected to have four forces of lift (L), weight (W), thrust (T), and drag (D) acting on an aircraft as shown in Figure 0.1 Where thrust force (T) is the

forward force produced by the aircraft engine/propeller and V_∞ is the free-stream velocity (Anderson Jr, 2017). The lift and drag forces are discussed in the following section (0.1.1).

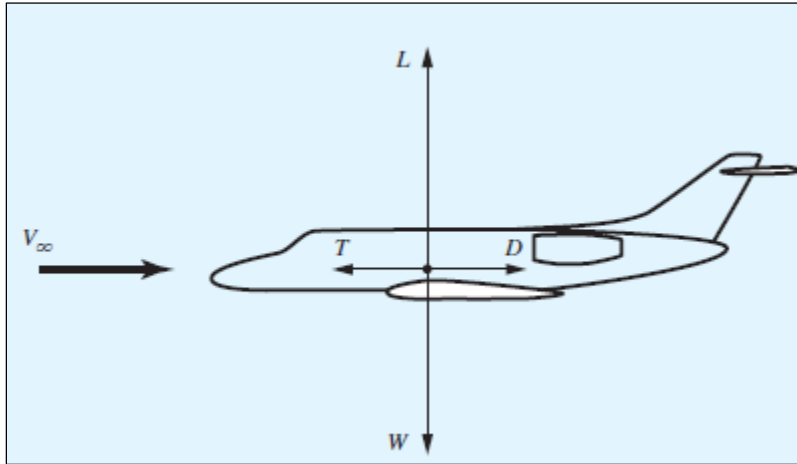


Figure 0.1 The four forces acting on an airplane in steady flight

Taken from Anderson (2017)

0.1.1 Lift and drag forces

A fluid flowing past an airplane, wing, airfoil, or any other body, causes to apply an aerodynamic force R and moment M on the body, as sketched in Figure 0.2.

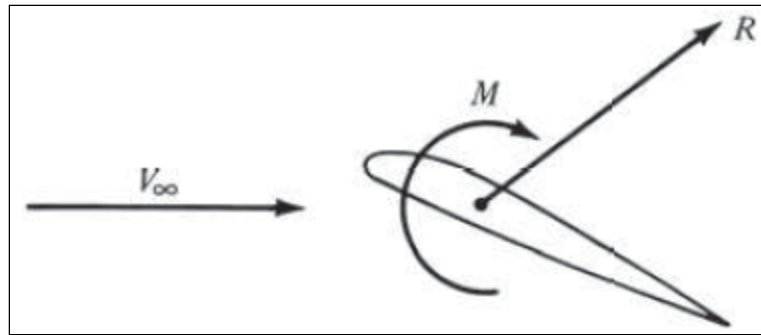


Figure 0.2 Resultant aerodynamic force and moment on the body

Taken from Anderson (2017)

The lift force (L) is the component of force (R) that is perpendicular to the oncoming flow direction and the drag force (D) is the component of force (R) parallel to the flow direction as shown in Figure 0.3 (Anderson Jr, 2017; Houghton & Carpenter, 2003; Kabir, Chowdhury, Islam, & Islam, 2019). There are different components of drag that exists on an aircraft wing. In section (0.1.3), a summary of them is described.

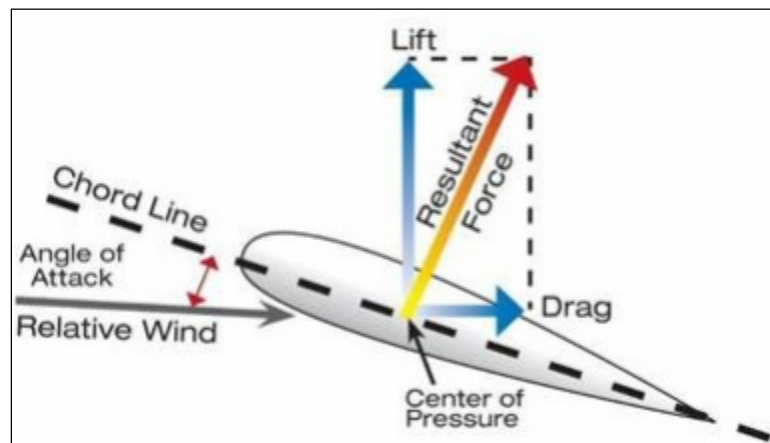


Figure 0.3 Resultant aerodynamic force, splits in to lift and drag forces

Taken from Kabir et al. (2019)

The coefficients of lift and drag can be obtained by equations (0.1) and (0.2) respectively, where S is the surface area and ρ is the density.

$$C_L = \frac{L}{\frac{1}{2}\rho V_\infty^2 S} \quad (0.1)$$

$$C_D = \frac{D}{\frac{1}{2}\rho V_\infty^2 S} \quad (0.2)$$

At a given Mach and Reynolds number, C_L and C_D are simply functions of the angle of attack (α) as shown in Figure 0.4. The C_L increases linearly with α until the lift coefficient reaches its peak value and the stall angle of attack is reached, then the C_L drops off as α is further increased. The maximum value of the lift coefficient is called C_{Lmax} as indicated in Figure 0.4 (Anderson Jr, 2017; Houghton & Carpenter, 2003; Kabir et al., 2019)

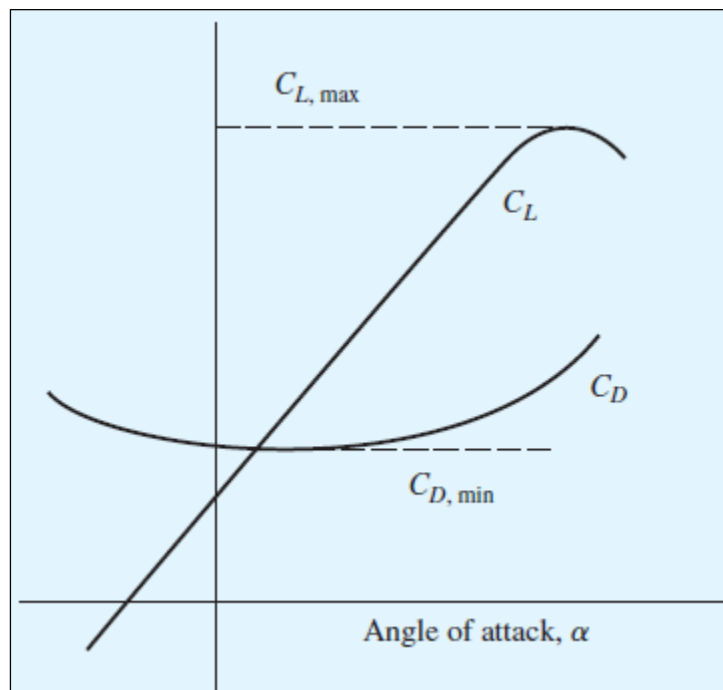


Figure 0.4 Schematic of lift and drag coefficients versus angle of attack; illustration of maximum lift coefficient and minimum drag coefficient

Taken from Anderson (2017)

Lift and drag coefficients play a strong role in the preliminary design and performance analysis of airplanes. Lift to drag ratio is the measurement of aerodynamic efficiency on the lifting bodies and hence it is desirable to augment this ratio by either reducing drag or increasing lift (Anderson Jr, 2017).

In order to understand more deeply the concept of aerodynamic performance and the stall, it is needed to understand the concept of boundary layer separation, which is described in the following section.

0.1.2 Boundary layer and flow separation

Ludwig Prandtl's seminal work on the boundary layer development which explained the flow behavior in the proximity of the wall revolutionized fluid dynamics in the early 20th century (Anderson, 2005). Based on his boundary layer theory, due to friction effects, the flow near the surface of the wall will stick to the surface and causes the generation of a tiny region near the wall called the "boundary layer". In the boundary layer, the velocity changes enormously in a very short distance normal to the wall as shown in Figure 0.5. Based on his theory, the friction effects were only experienced in the boundary layer region and the flow outside the boundary layer is considered inviscid (Anderson, 2005).

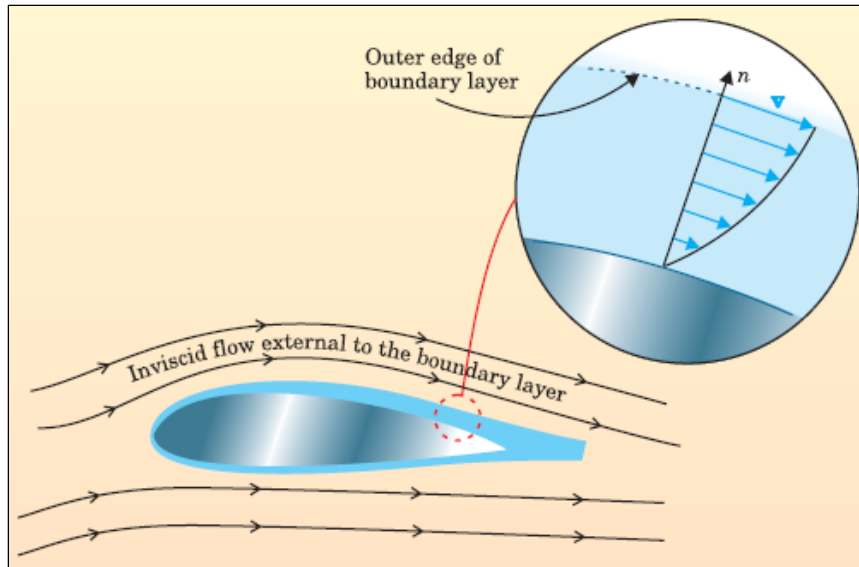


Figure 0.5 Illustration of the boundary layer in the Prandtl's boundary layer theory

Taken from Anderson (2005)

The boundary layer separation occurs when the flow encounters an adverse pressure gradient. The fluid elements deep inside the boundary layer, which had already lost a substantial portion of their kinetic energy dissipated by friction, cannot work their way uphill in the region where the pressure is increasing. Thus, the velocity profile is depleted near the surface and the separated flow with some low energy flow forms in the wake behind the body. Beyond the separation point, the boundary layer simply lift-off from the surface as shown in Figure 0.6 (Anderson, 2005).

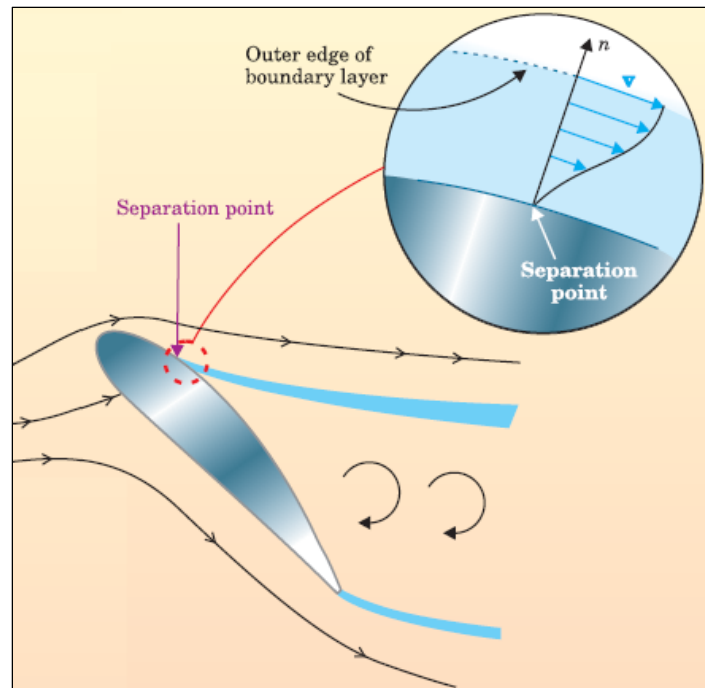


Figure 0.6 Boundary layer separation illustration based on Prandtl's boundary layer theory

Taken from Anderson (2005)

The boundary layer flow separation on wings causes an increase in drag and reduction in lift generation and hence reducing their aerodynamic efficiency. This phenomenon is known as stall (Anderson Jr, 2017).

0.1.3 Components drag and end effects on 3D finite span wings

The total drag on a body is the sum of the pressure and the skin friction drags. The skin friction drag is the drag due to the shear stress acting on the surface of the wing and pressure drag is the integral of the pressure over the surface area of an object, acting in the streamwise direction. The pressure drag is composed of the induced, wave, and form drags (Bolzon, 2017; Houghton & Carpenter, 2003).

Form drag: is the drag caused by the separation of the boundary layer from a surface and the wake created by that separation (as discussed in the previous section (1.1.2)), and it primarily depends upon the shape of the object.

Wave drag: is the drag associated with the formation of shock waves in high-speed flights (Houghton & Carpenter, 2003).

Induced drag: or lift-induced drag is the drag generated due to the generation of lift on wings. Lift on wings is generated by the pressure imbalance between the lower surface (with higher pressure) and the upper surface (with lower pressure) of the wing. Because of this pressure imbalance, the air on the lower surface of the wing flows around the wingtip and tries to displace the lower pressure air on the top surface which results in the formation of the wingtip vortices as illustrated in Figure 0.7 (Guerrero, Sanguineti, & Wittkowski, 2020). These vortices produce a swirling flow of air behind the wing which is very strong near the wing tips and its strength decreases toward the wing root, producing a downward flow in the neighborhood of the wing, called "downwash". This downwash also varies from wing tip to wing root, causing to decrease in the effective angle of attack at each cross-section of the wing, and tilting the lift vector rearward as indicated in Figure 0.8. This rearward tilt of the lift vector results in the creation of a component of drag called lift-induced drag. This drag component is an unavoidable consequence of lift generation in finite span wings (Bolzon, 2017; Guerrero et al., 2020).

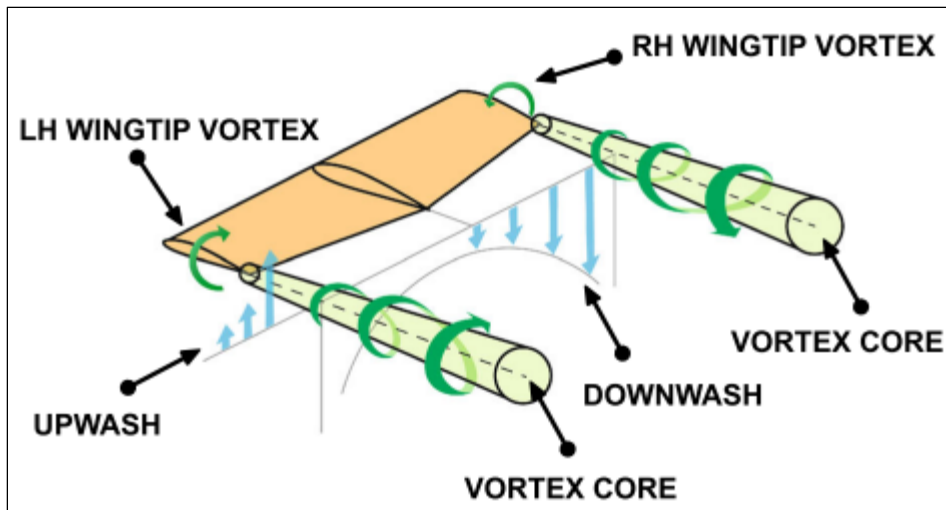


Figure 0.7 Illustration of wingtip vortices rotation and the associated downwash and upwash

Taken from Guerrero et al. (2020)

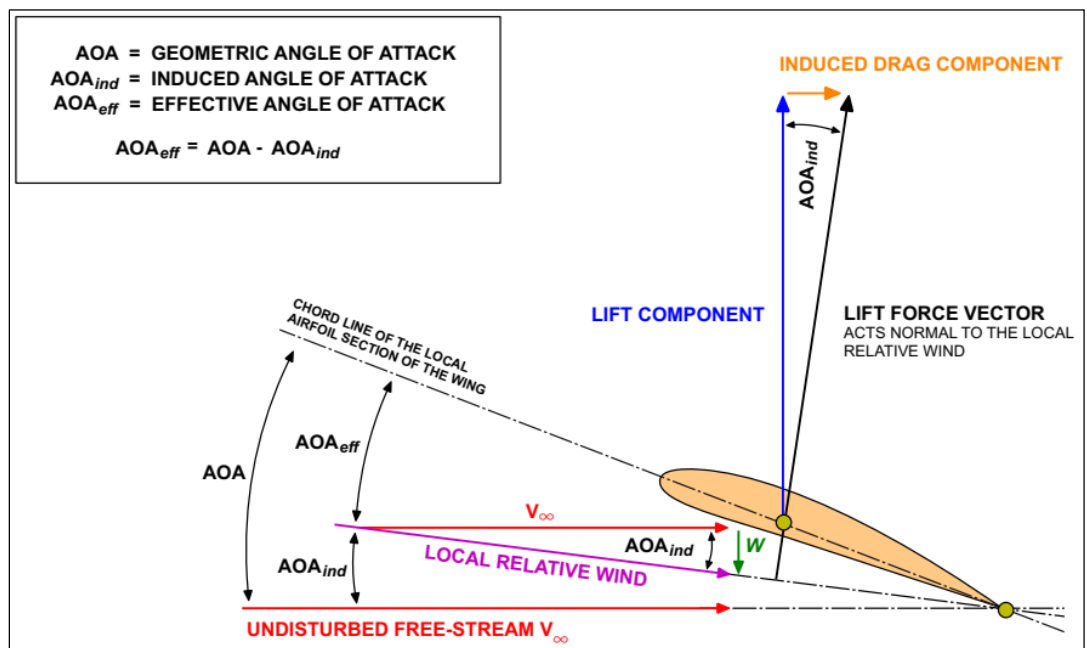


Figure 0.8 Illustration of lift-induced drag due to downwash

Taken from Guerrero et al. (2020)

As mentioned in this section, wing-tip vortices are generated on finite-span wings which affects the lift and drag coefficients of 3D wings in comparison with the 2D wings

detrimentally (Anderson Jr, 2017). In this research, in order to simplify the analysis on the effect of amplitude and wavelength sizes of the tubercles, the analysis is done on 2D wings and end effects are not considered which will be explained more in the methodology section.

In this section, the concepts of lift, drag, and aerodynamic efficiency of wings are discussed. In the following section the concept of "flow control" which is used to improve the aerodynamic efficiency of wings' is presented.

0.2 Flow control

To improve the aerodynamic performance of the lifting bodies, flow control devices may be used. Flow control is manipulating the flow field around the airfoil or wing to achieve a certain design objective such as increasing lift and reducing drag. Flow control devices are generally divided into passive and active. If the device requires no additional power input and only changes the flow physics by virtue of its geometry, it is classified as passive. Whereas active flow control devices use additional energy sources to operate devices such as actuators (Bolzon, 2017; Forster & White, 2014; Zhang et al., 2013). Synthetic jets, plasma actuators, leading-edge slats, trailing-edge flaps, gurney flaps, micro tabs, internal acoustic excitations, etc. are some examples of Active flow control devices. Active flow control devices can operate over a great range of conditions and generate less drag in comparison with passive flow control devices. In addition, they can be simply switched off if they are detrimental to wing performance under certain conditions. However, they are complicated to design, more costly, and require a greater level of maintenance to continue performing effectively. Besides that, they can increase the weight of the vehicles which is not desired especially in the industries like aerospace and Unmanned Aerial Vehicles that reducing the weight of the vehicles is always one of the main concerns. In contrast, passive flow control methods are simpler, more practical, and cheaper (Bolzon, 2017; Forster & White, 2014; Zhang et al., 2013).

Flow control devices are also classified according to their design goals to "lift enhancement" and "drag reduction". Airfoils' shape optimization (e.g., by increasing the camber), and

delaying the boundary layer separation by methods such as increasing the momentum exchange within the boundary layer (e.g., vortex generators) and restriction of the spanwise flow (e.g., wing fences), are some examples of passive lift enhancement flow control methods. Laminar-to-turbulent boundary layer transition delay (e.g., compliant coatings), and reduction of the turbulent fluctuations (e.g., riblets) are some examples of passive drag reduction flow control methods (Hansen, 2012).

One of the main mechanisms that can improve the aerodynamic performance of wings is a procedure to prevent or delay the boundary layer separation which increases the lift generation and delays stall on wings at high angles of attack. Delaying the boundary layer separation is especially more desirable at low Reynolds numbers where the laminar and transitional boundary layers exist, and the boundary layer has lower energy and hence is more susceptible of being separated. One way of delaying the boundary layer separation is to increase the momentum exchange within the boundary layer. Vortex generators, leading-edge serrations, and leading-edge extensions are some examples of passive flow control devices that are designed to delay the boundary layer separation by increasing the momentum exchange within the boundary layer (Rostamzadeh Torghabeh, 2016).

Now that a summary of different types of flow control devices is presented, a new type of passive flow control device, known as leading-edge tubercles, can be discussed.

0.2.1 Leading-edge tubercles

Recently, researchers have attempted to enhance the aerodynamic performance of wings with a new type of passive flow control method called "leading-edge undulations/protuberances". These undulations can be found in nature, for example, on the leading-edge part of the humpback whale's pectoral flippers. Humpback whales are mammals capable of impressive maneuverability. Despite their large size of about 12-18m and a massive weight of about 30-40 tons, they can execute complex underwater rolls and rapid pursuit of prey (Taheri, 2018) and they are even able to perform somersaults (Bolzon, Kelso, & Arjomandi, 2014).

The agility of these mammals has been attributed to their pectoral flippers which are the largest among all the cetaceans with 30.8% of their total body length size (Fish, 1999; Woodward, Winn, & Fish, 2006). These flippers have a high aspect ratio and backswept elliptical planform shape with protuberances called tubercles on their leading-edge part that gives the flipper a scalloped appearance which is unique among the baleen whales. Around 10 to 11 tubercles can be found on the leading edge of the whales' flipper which is mostly confined to the middle and tip sections of the flipper. The most proximal tubercle is located at 30% of the flipper span and the smallest tubercle can be found near the flipper tip. The Humpback whale flipper closely resembles the 21% thick, low drag NACA 634-021 wing in cross-section (Fish & Battle, 1995). The humpback whale, its pectoral flipper with tubercles, and its flipper's cross-sectional profile are demonstrated in Figure 0.9 (Fish & Lauder, 2006).

These whales normally swim at the speed of 3-9 mph (1.3-4 m/s) but can go up to 15-16.5 mph (6.7 -7.35 m/s) in bursts when in danger. Feeding speeds are slower, about 1.2-3.5 mph (0.53 – 1.56 m/s) (National Park & preserve). Thus, based on the flipper's mean-chord length of 0.51m (Fish & Battle, 1995), kinematic viscosity for the seawater at 15.6 degrees Celsius of $1.17 \times 10^{-6} \text{ m}^2/\text{s}$, and the seawater density of $1030 \text{ kg}/\text{m}^3$ (Gerhart, Gerhart, & Hochstein, 2016), the Reynolds number that the humpback whales flipper encounters during maneuvers can be estimated to be between 2.3×10^5 and 3.3×10^6 .

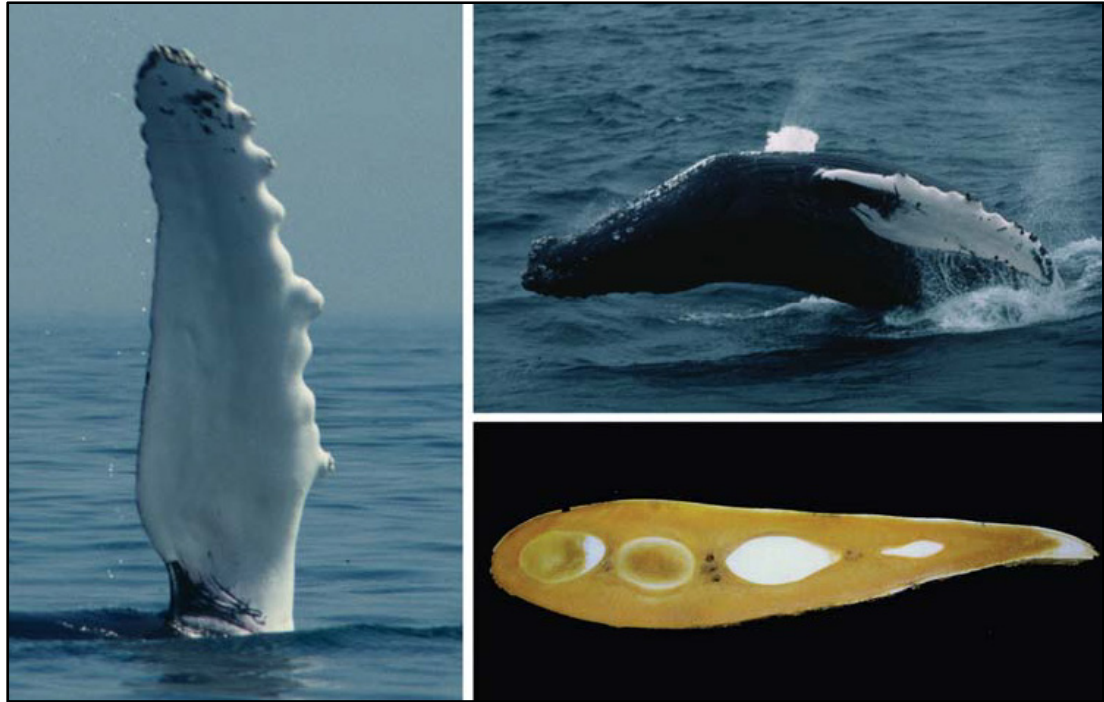


Figure 0.9 Humpback whale (*Megaptera novaeangliae*) flipper with leading edge tubercles (left), breaching humpback whale showing relative size of the flipper (top right), and cross section of flipper (bottom right)

Taken from Fish & Lauder (2006)

These whales are the only baleen whales that rely on maneuverability to capture prey. They use many techniques that require a high level of maneuverability to catch their prey such as lunge feeding, inside loop feeding, and bubble netting (Fish, Howle, & Murray, 2008).

In the "lunge feeding" technique, the whale lunges toward the prey at the speed of 2.6 m/s and an angle of attack of 30 to 90 degrees (Hain, Carter, Kraus, Mayo, & Winn, 1981).

In the "inside loop" feeding technique, the whale strikes the water's surface with its fluke and creates a turbulent area in the water and swims away from its prey, then rolls 180 degrees, making a sharp U-turn in 1.5–2 body lengths and then lunges toward the prey (Hain et al., 1981).

In the "bubble netting" technique, the whale swims upward from a depth of 3–5 m underwater toward the surface in a circular pattern while generating bubble clouds by exhaling air from its

blowhole. This way, the whale completely encircles and concentrates the prey. At the completion of the bubble net, the whale pivots with its flippers and banks to the inside as it turns sharply into the center of the net and feeds. The bubble net diameter can vary between 1.5m to a maximum of 50m (Hain et al., 1981).

Figure 0.10, shows the calculated and observed turning performance of these whales during bubble netting. The outer margin of the black circle shows the calculated minimum turning diameter for a 9m whale and the central circle and the outer circles show the minimum and maximum diameters of bubble nets respectively reported in the literature. The margins of the turn for various bank angles are also shown by curved lines (Fish et al., 2008). The turning diameter of the whale during bubble netting can be calculated by equating the lift force generated by the flippers to the centrifugal force acting on the whale, as depicted in equation (0.3) below.

$$D = \frac{4 m_v}{\rho A_f C_L \sin \phi} \quad (0.3)$$

Where:

ρ is the density of the fluid

m_v is the whale's virtual mass

A_f is the total planar area of the flippers

C_{Lmax} is the maximum lift coefficient

ϕ is the bank angle

It can be deduced from equation (0.3) that the smaller diameter turns can be achieved by increasing the bank angle, which increases the horizontal component of the lift vector and/or the angle of attack of the flipper. However, at too high angles of attack, the flipper stall can

occur. Thus, by delaying the stall and increasing lift, tubercles can help the Humpback whale to execute tighter turning maneuvers (Fish et al., 2008).

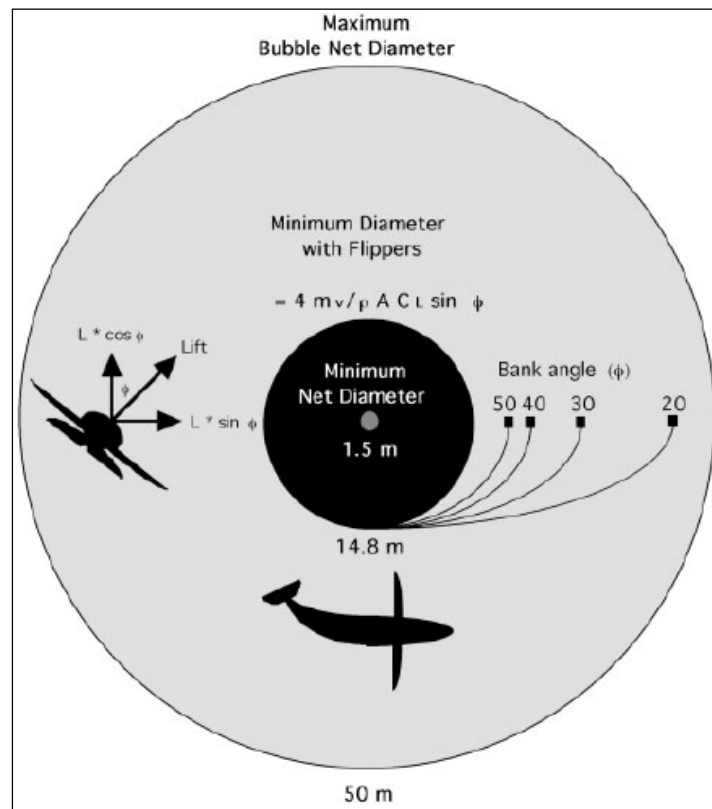


Figure 0.10 Calculated and observed turning performance of the Humpback whale

Taken from Fish et al. (2008)

While it was postulated that the agility and maneuverability of the humpback whales, can be attributed to the effect of the tubercles (Bushnell & Moore, 1991; Sudhakar, Venkatakrishnan, & Ramesh, 2020), some researchers suggested that these tubercles function as flow control devices that by generating vortices and, increasing the momentum exchange with the boundary layer, maintain lift and prevent stall at high angles of attack and hence increasing the whale's maneuverability (Fish & Battle, 1995). Consequently, the researchers were attracted to work

on a new kind of passive flow control method known as "leading edge protuberances" or "leading-edge undulations" or "leading-edge tubercles"(Fish & Battle, 1995).

CHAPTER 1

LITERATURE REVIEW

Several experimental and numerical studies were performed to analyze the effect of leading-edge undulations/tubercles on idealized humpback whale flipper models and 2D wings aerodynamic performance as well as to understand the underlying flow mechanism generated by the tubercles. In this section, the most important one of these researches is explained. The effect of leading-edge tubercles on the aerodynamic performance of 2D wings and idealized humpback whale flipper models are first explained in this chapter. After that, the studies that analyzed the flow behavior on wings with tubercles are presented.

1.1 The effect of leading-edge tubercles on the aerodynamic performance

1.1.1 Effect of leading-edge tubercles on Humpback whale flipper models

An experimental study on 3D idealized humpback whale flipper models, one with a smooth leading-edge and the other with scalloped one, at a Reynolds number of 5×10^5 (shown in Figure 1.1), showed that the scalloped model increases the stall angle by 40%, the maximum lift coefficient by 6%, reduces drag at post-stall angles of attack and increases the lift to drag ratio for all the angles of attack studied except for the angles of attack ranging between $10 < \alpha < 12$ degrees in comparison with the flipper model with a smooth leading-edge (as shown on Figure 1.2). It should be noted that in Figure 1.2, the aerodynamic coefficients at different angles of attack for the scalloped model is shown by dotted lines while the aerodynamic coefficients values for the smooth leading-edge model is shown by the solid line. The author postulated that there are analogies between the leading-edge tubercles and vortex generators, which by generating the streamwise vortices, cause a greater momentum exchange within the boundary layer and hence prevents the boundary layer flow separation (Miklosovic, Murray, Howle, & Fish, 2004).

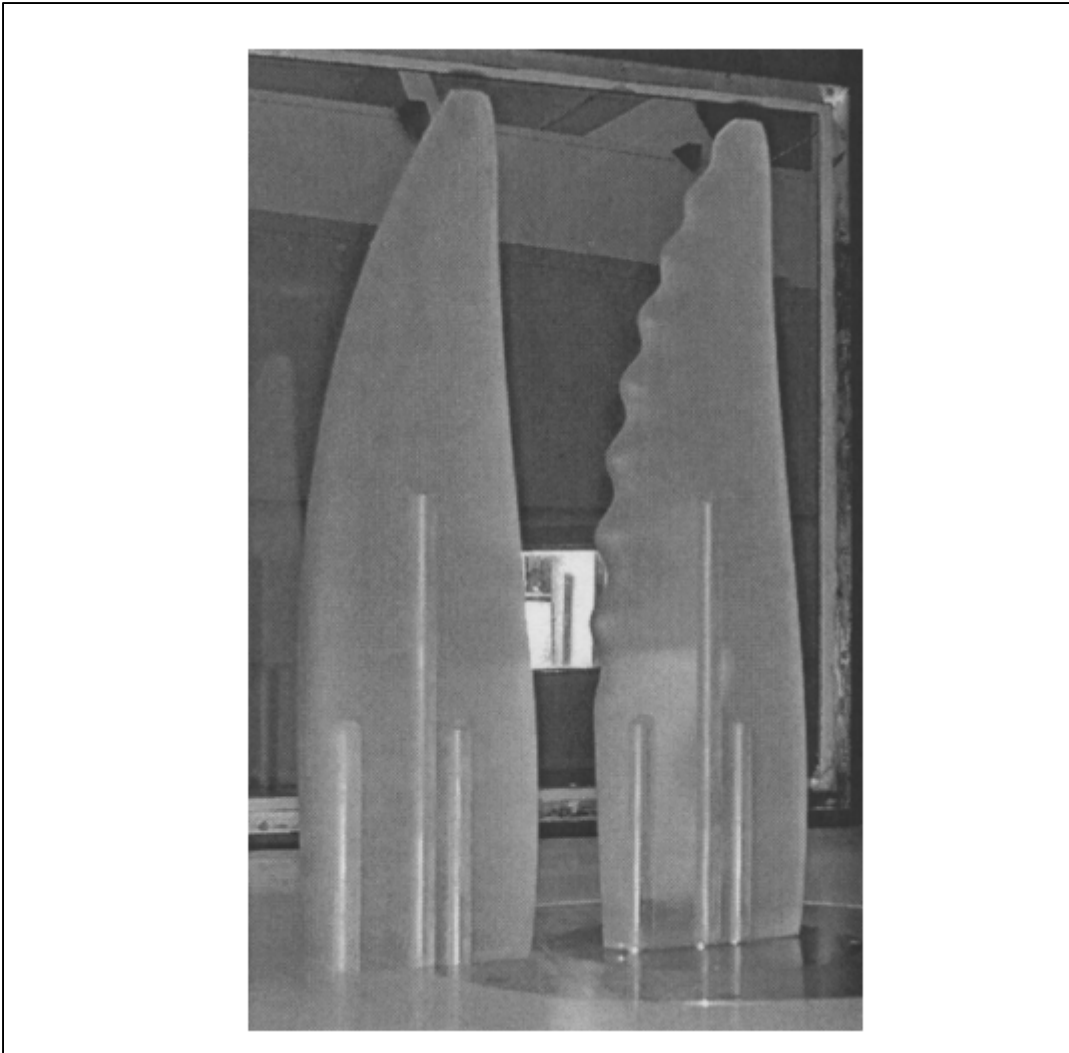


Figure 1.1 Smooth (left) and scalloped (right) idealized humpback whale flipper models

Taken from Miklosovic et al. (2004)

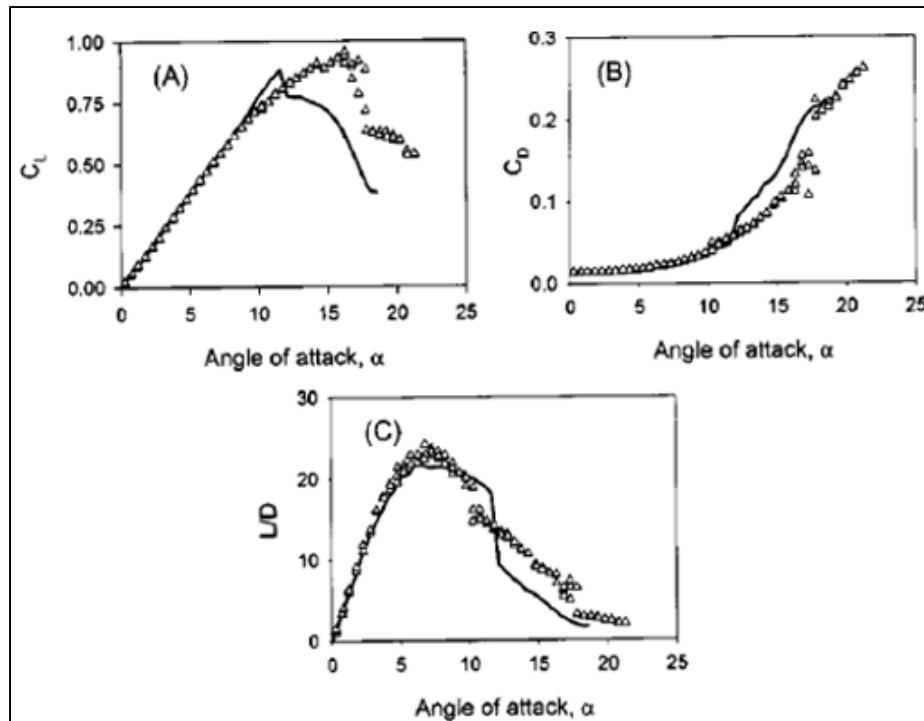


Figure 1.2 a) Lift coefficient b) Drag coefficient c) Lift-to-drag ratio of the scalloped and smooth leading-edge flipper models (see text for details)

Taken from Miklosovic et al. (2004)

1.1.2 Comparing the effect of leading-edge tubercles on 2D infinite-span and 3D wings

Although tubercles showed an increase in aerodynamic performance at both pre-and post-angles of attack on idealized flipper models (Carreira Pedro & Kobayashi, 2008; Miklosovic et al., 2004; Watts & Fish, 2001b), the effect of leading-tubercles on (2D) symmetric infinite-span wings was a reduction in the lift coefficient at pre-stall angles of attack and an improvement in the lift coefficient at post-stall angles of attack (Hansen, Kelso, & Dally, 2011; Johari, Henoch, Custodio, & Levshin, 2007; Miklosovic, Murray, & Howle, 2007; Yoon, Hung, Jung, & Kim, 2011). For example, Figure 1.3 shows the wind tunnel analysis done on the effect of tubercles on idealized flipper model (finite span wing) and full-span wings with NACA 0020 profile (Miklosovic et al., 2007).

The comparison of the results, showed that tubercles improve overall performance only when situated on a finite span wings (as shown in Figure 1.2 and Figure 1.5) rather than 2D wings (as illustrated in Figure 1.4). It was postulated that the vortices induced by the tubercles causes the early separation and considerable loss of lift and drag increase at pre-stall angles of attack for the full-span wing relative to the semi-span wing. The author also postulated that the more enhancements on the semi-span wing (idealized flipper model) aerodynamic performance is occurred by preventing the spanwise stall progression (Miklosovic et al., 2007).

In Figure 1.4, the experimental data (solid line) are compared with the analytic results for NACA 0020 airfoil produced by the XFOIL code (dotted line) at a Reynolds number of 270,000. The experimental runs of 101 and 103 were taken on scalloped leading-edge full-span wing several days apart to show repeatability. In Figure 1.5, the experimental data (solid line) are compared with the analytic results obtained by vortex lattice method (Lamar & Herbert, 1982)(dotted line) at Reynolds number of 534,000–631,000.

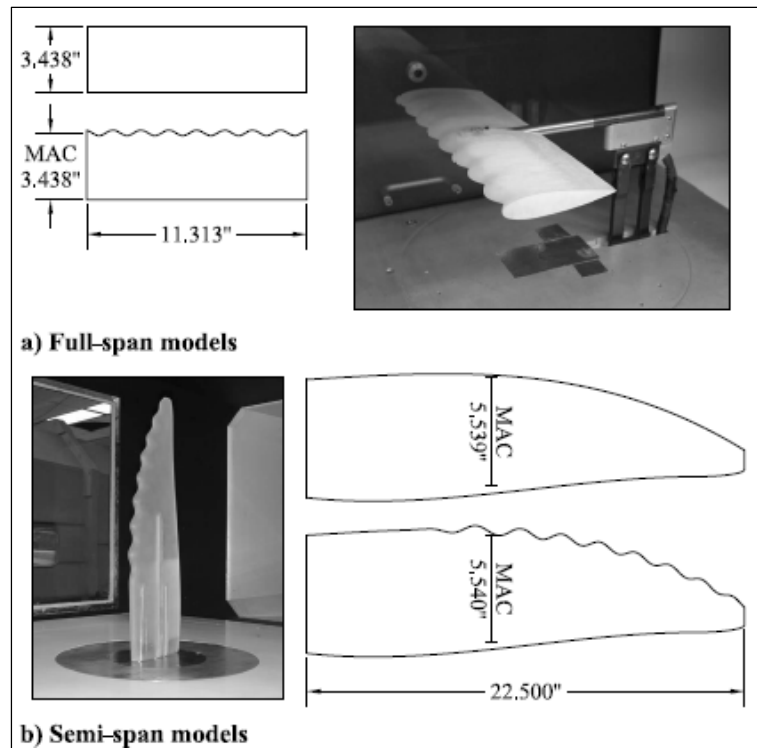


Figure 1.3 Infinite-span wings and semi-span flipper models

Taken from Miklosovic et al. (2007)

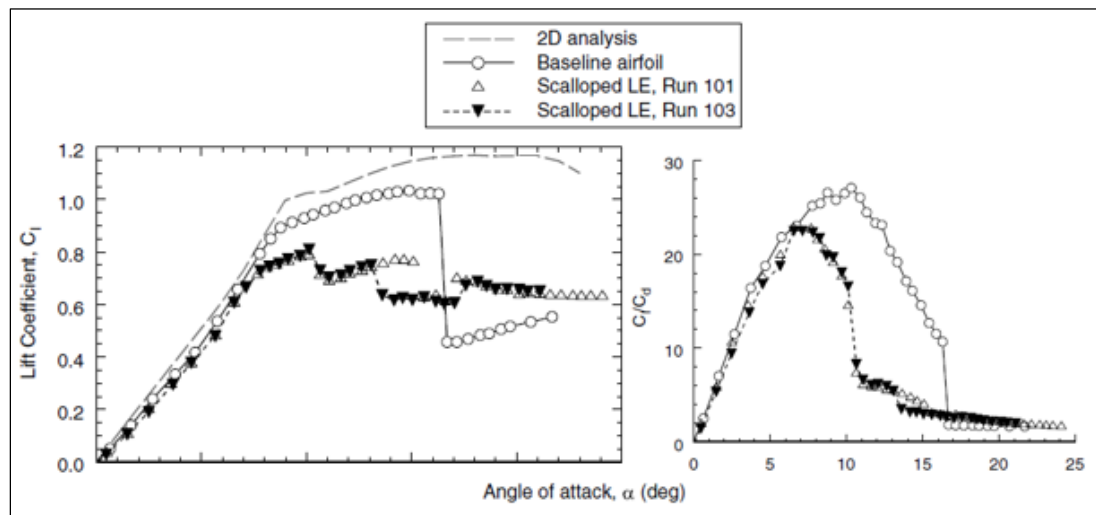


Figure 1.4 Effect of leading-edge tubercles on lift coefficient (left) and lift to drag ratio (right) of 2D wing (see text for details)

Taken from Miklosovic et al. (2007)

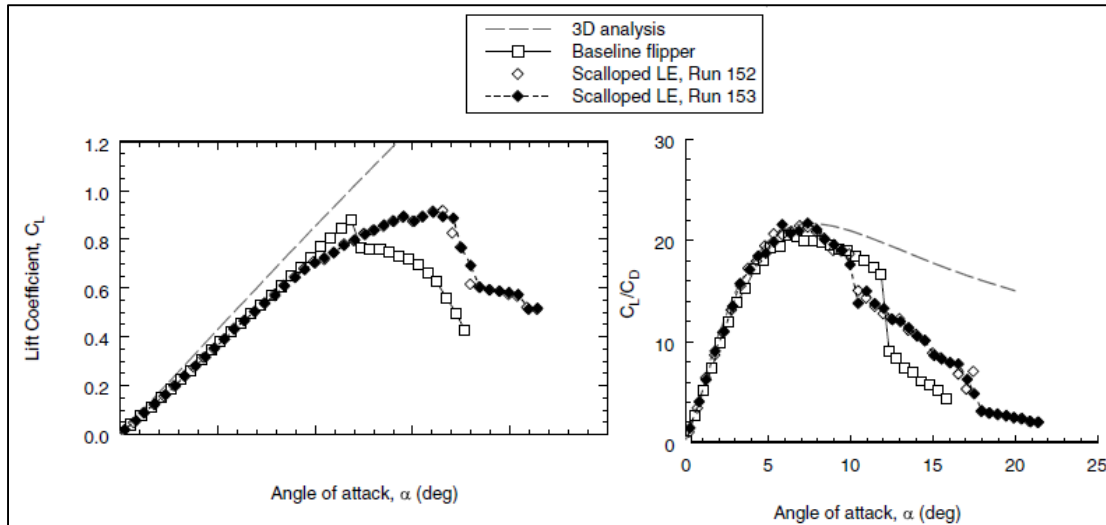


Figure 1.5 Effect of leading-edge tubercles on lift coefficient (left) and lift to drag ratio (right) on finite span wings (see text for details)

Taken from Miklosovic et al. (2007)

Numerical simulations (Carreira Pedro & Kobayashi, 2008) on the same smooth and scalloped flipper models and with the same settings of (Miklosovic et al., 2004) showed integral quantities with acceptable agreement with the experiment of (Miklosovic et al., 2004). It should be noted that, the flipper models tested were planar but tapered. Thus, the Reynolds number at the tip was lower than at the root; hence, the flow separates in the leading-edge at the tip, whereas near the root, trailing edge flow separation was observed (Carreira Pedro & Kobayashi, 2008). Based on the flow visualization results, the author concluded that the streamwise vortices generated by the tubercles energize the boundary layer and delay the trailing-edge flow separation as shown on Figure 1.6 (a). In addition, these vortices have effects similar to wing fences and confine the leading-edge flow separations to the wing-tip region (Carreira Pedro & Kobayashi, 2008) as shown on Figure 1.6 (b).

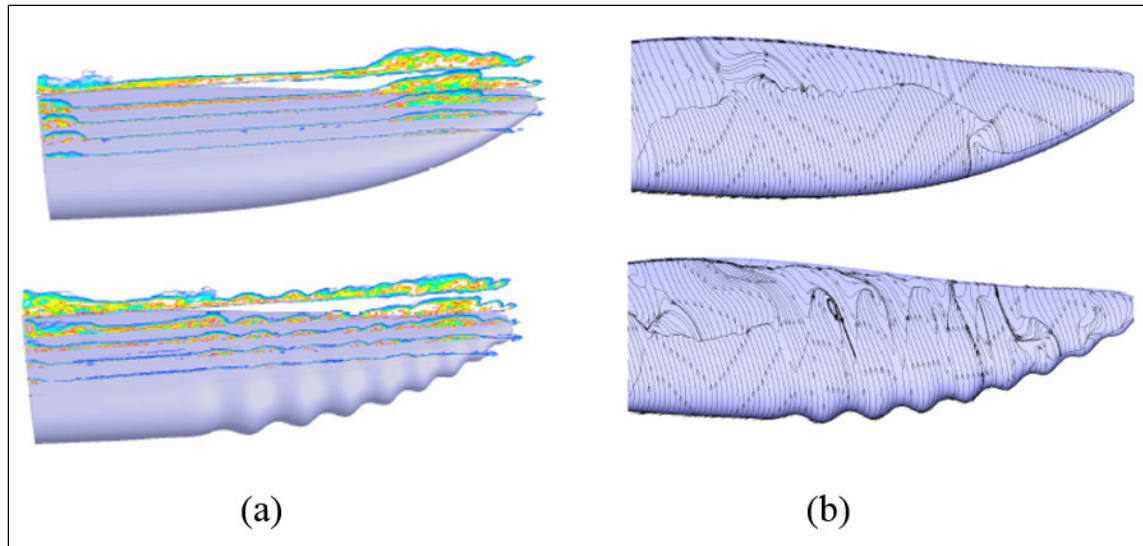


Figure 1.6 a) Instantaneous vorticity magnitude slices in chord-wise direction and (b) Averaged shear-stress lines at $\alpha = 15$ degree and $Re = 500,000$ (as provided by the authors)

Taken from Perdo & Kobayashi (2008)

In the meantime, keeping in mind that analyzing the effect of amplitude and wavelength sizes on finite span wings is more complex due to the 3D effects, some research was done on 2D wings to understand the aerodynamic effect of tubercles with different amplitude and wavelength sizes.

1.1.3 Effect of amplitude and wavelength sizes of tubercles on the aerodynamic performance of the modified 2D wings

By analyzing the effect of leading-edge undulations using 6 modified airfoils with different amplitude and wavelength sizes illustrated in Figure 1.7, at $Re = 183000$, It was found that although leading-edge tubercles reduce the airfoil's lift coefficient at the pre-stall angles of attack, they increase the lift coefficient up to 50% at post-stall angles of attack. Based on the results which part of it are illustrated on Figure 1.8 to Figure 1.10, it was concluded that the airfoils with smallest amplitude of tubercles had better performance in terms of stall angle and C_{Lmax} , while the airfoils with larger amplitude size had smoother stall characteristics. Meanwhile it was also mentioned that the effect of amplitude size on the modified airfoils

aerodynamic performance is significant while the effect of the wavelength size is negligible (Johari et al., 2007).

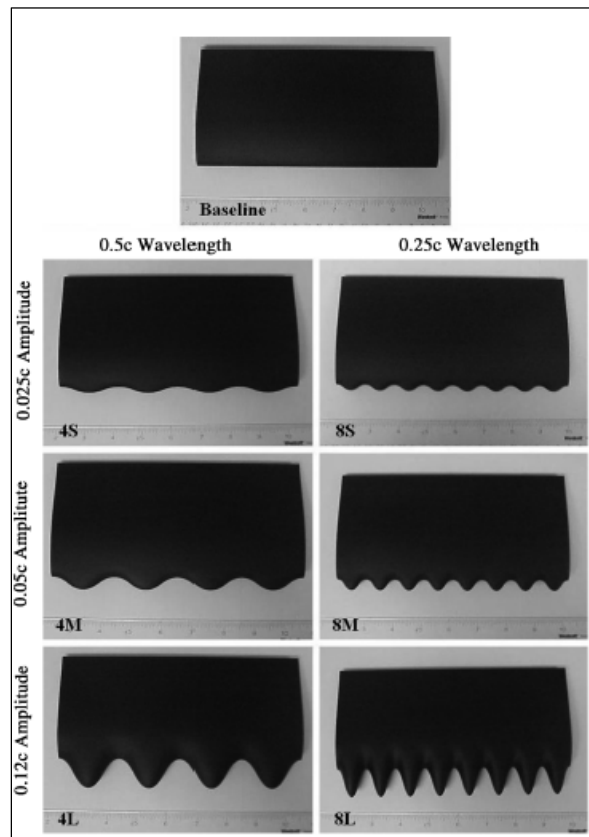


Figure 1.7 Baseline and modified airfoils with leading-edge protuberances

Taken from Johari et al. (2007)

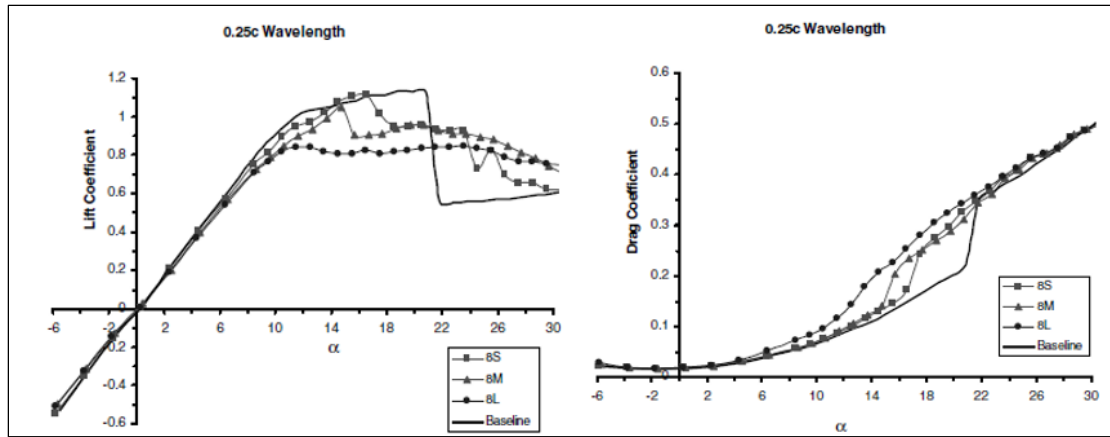


Figure 1.8 The effect of amplitude of the tubercles on lift (left) and drag (right) coefficients of the modified airfoils
 Taken from Johari et al. (2007)

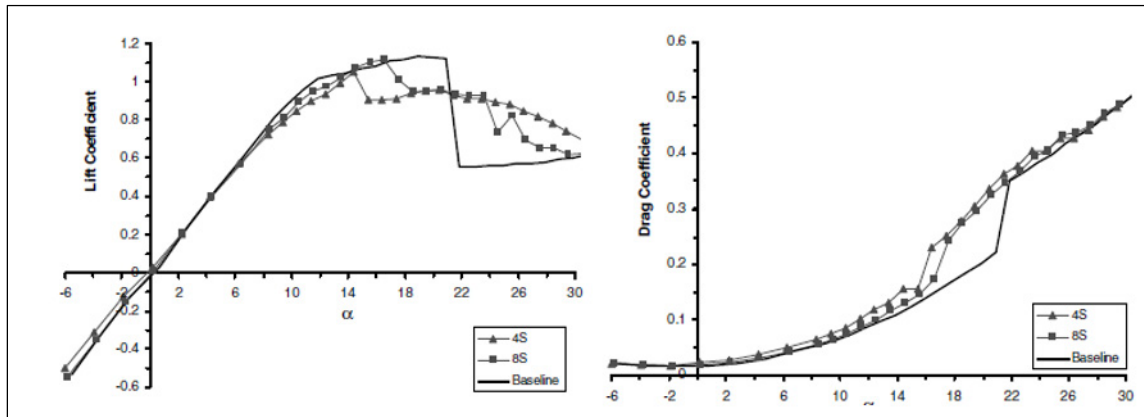


Figure 1.9 The effect of wavelength of the tubercles on lift (left) and drag (right) coefficients of the modified airfoils (with small amplitude size)
 Taken from Johari et al. (2007)

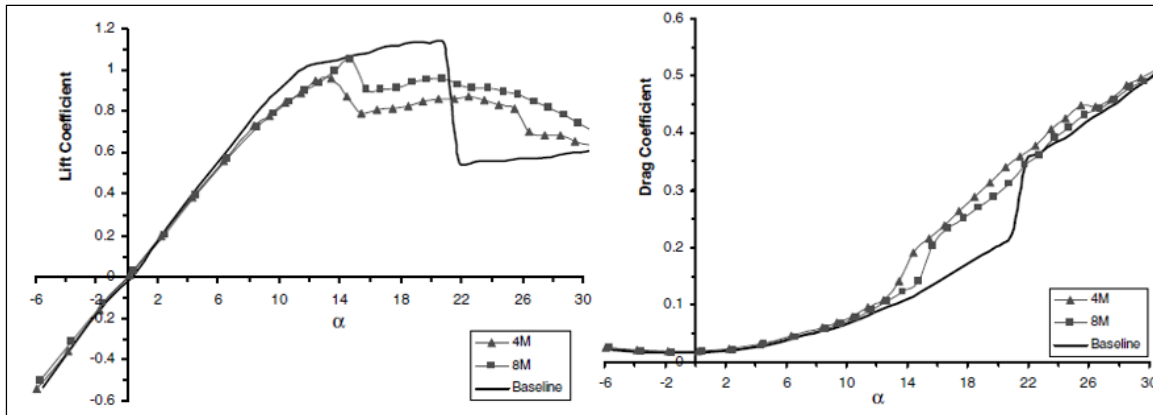


Figure 1.10 The effect of wavelength of the tubercles on lift (left) and drag (right) coefficients of the modified airfoils (with medium amplitude size)

Taken from Johari et al. (2007)

Although, it was postulated that the effect of wavelength size on aerodynamic characteristics of the modified airfoils are negligible (Johari et al., 2007), however, later other researcher Hansen (2012), by searching through the same results (Johari et al., 2007) which as an example shown in Figure 1.10 above, noticed that the tubercle configurations with smaller wavelength sizes achieved higher maximum lift coefficient and stall angle with generating less amount of drag coefficients while improving the post-stall aerodynamic performance. Meanwhile, in another research, it was observed that at higher Reynolds numbers, the aerodynamic performance (L/D) of a rudder with tubercles decreased by reducing the wavelength of the tubercles, which was attributed to the cavitation effects (Hansen, 2012; Weber, Howle, & Murray, January, 2010). Hence, Hansen (2012), questioned the idea of Johari et al. (2007) regarding the negligible effect of the wavelength size on aerodynamic performance of the modified airfoils.

Hansen et al. (2011) performed flow visualization and force measurement on two series of modified airfoils with NACA 65-021 and NACA 0021 profiles with different sizes of amplitudes and wavelengths of leading-edge protuberances. It was observed that by reducing the wavelength of the tubercles up to a certain limit while keeping the amplitude size constant, the lift coefficient increased by delaying the stall angle, in addition to achieving higher values

of the lift coefficient at post-stall angles of attack (see Figure 1.11). However, after that limit the lift coefficient reduced. For example, as shown in Figure 1.11 below, the $A4\lambda 7.5$ airfoil which has the smallest wavelength size generates less lift coefficients than the $A4\lambda 15$ airfoil with larger wavelength size from 10 to 18 degree angles of attack (where λ is the wavelength of the tubercles) (Hansen et al., 2011).

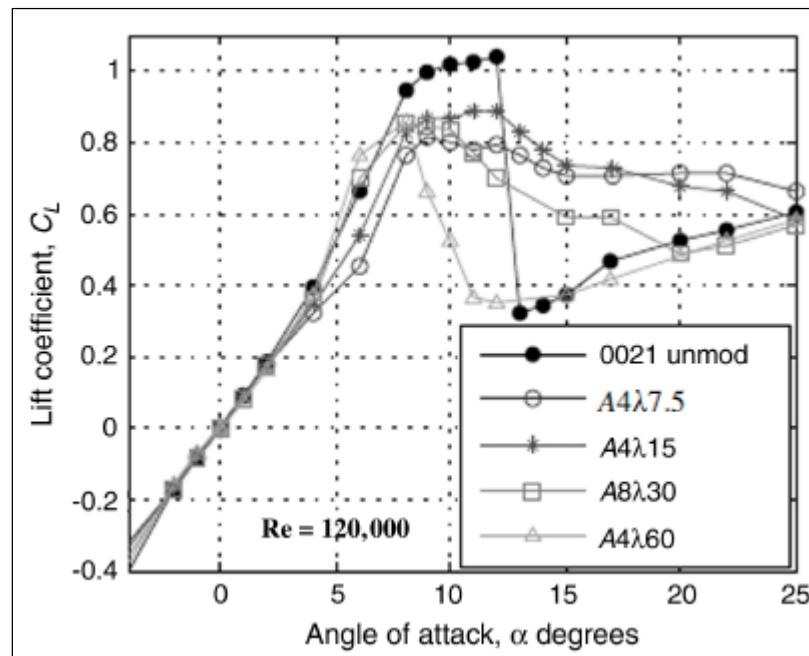


Figure 1.11 Effect of wavelength of tubercles on the lift coefficient of NACA0021 airfoil

Taken from Hansen et al. (2011)

1.1.4 The effect of leading-edge tubercles on different type of airfoils

It was also observed that the effect of leading-edge tubercles is different in different types of airfoils. For example, the results obtained in (Hansen et al., 2011) showed that the tubercles are more beneficial for the airfoils when their maximum thickness are located further aft which they had negligible effect in reducing the pre-stall lift coefficient while still beneficial on the post-stall lift coefficient. It was suggested that the reason for this difference in behavior is the

extension of the laminar boundary layer on the airfoils that their maximum thickness are located further aft which causes the tubercles to be more beneficial on them (Hansen et al., 2011).

While the effect of leading-edge tubercles on symmetric airfoils show the reduction in pre-stall and increase in post-stall lift coefficient (Hansen et al., 2011; Johari et al., 2007; Miklosovic et al., 2007; Yoon et al., 2011), the effect of these undulations on high cambered airfoils showed different trends (Sudhakar et al., 2020).

Leading-edge tubercles with the amplitude and wavelength of $0.025\% C$ and $0.25\% C$ respectively on high cambered S1223 airfoil (Sudhakar et al., 2020), exhibits the increased in lift, delayed stall, and lower drag coefficient values at the Reynolds numbers of 10^5 and 1.5×10^5 , but showed no improvements at Reynolds number of 2×10^5 as illustrated in Figure 1.12. The S-1223 airfoil has a maximum thickness of $12.1\% C$ located at $18.8\% C$ and a maximum camber of $8.1\% C$ located at $49\% C$, where C is the chord length. It was concluded that since the airfoil curvature on the upper surface of the high-cambered airfoils are greater than the lower cambered airfoils, the flow encounters a greater adverse pressure gradient downstream of their maximum suction for a given angle of attack. As a result, the laminar separated shear layer generated on the high-cambered airfoils at lower Reynolds numbers fails to reattach on their upper surface after transition which results in massive flow separation. Thus, the incorporation of leading-edge tubercles on the S-1223 airfoil helps the boundary layer to transfer momentum from the mean flow and modify the laminar separation bubble. The aerodynamic performance (lift, stall angle) for the Reynolds numbers of 10^5 and 1.5×10^5 is there by improved. As the Reynolds number is increased to 2×10^5 the laminar separated shear layer on the baseline S-1223 attains sufficient momentum during its transition process and reattaches on the airfoil's upper surface even at higher angle of attack. Hence, the incorporation of tubercles does not result in a significant performance improvement at $Re = 2 \times 10^5$. It should be noted that, in the experimental research of Sudhakar et al. (2020), no analysis was done on the shape and structure of the streamwise vortices generated by the tubercles (Sudhakar et al., 2020). It should be also noted that the variations of lift coefficients on the baseline S1223

airfoil at Reynolds numbers of 1.5×10^5 and 2×10^5 are due to hysteresis loop observed in the lift and drag characteristics.

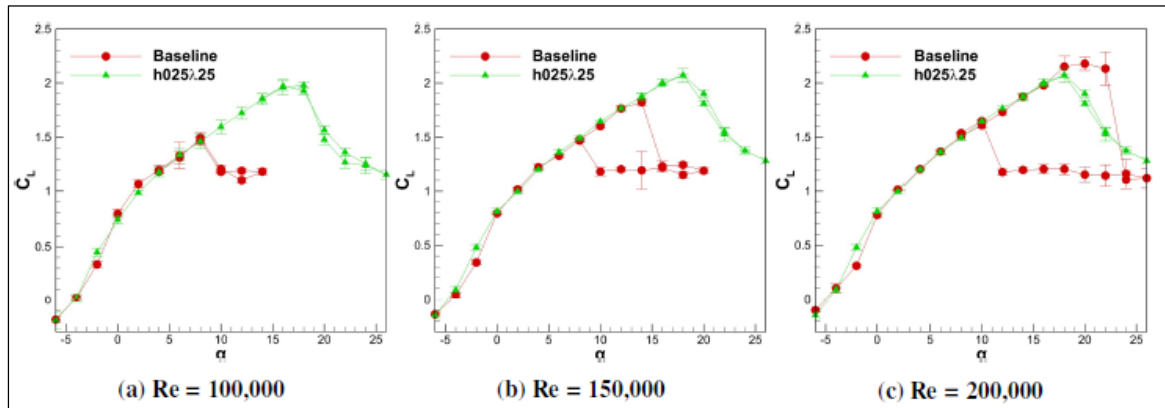


Figure 1.12 Effect of leading-edge tubercles on lift coefficient of S-1223 airfoil
Taken from Sudhakar et al. (2020) (see text for details)

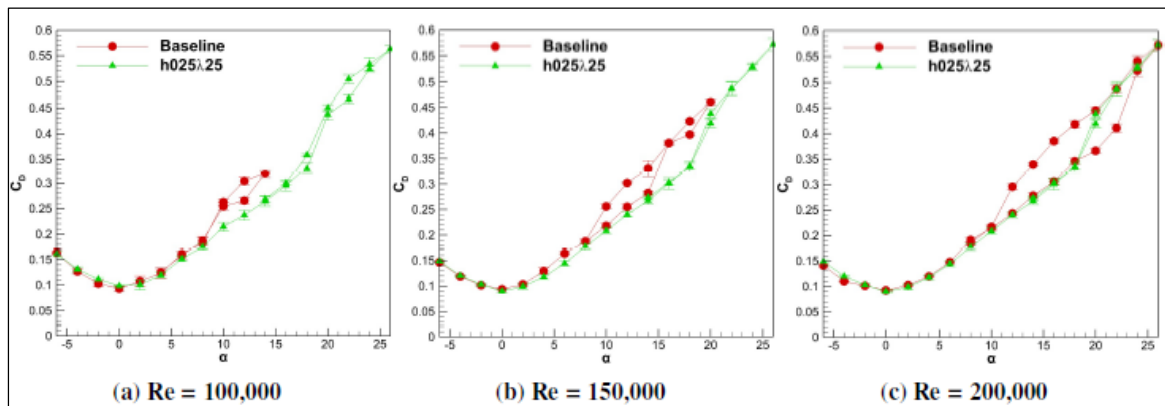


Figure 1.13 Effect of leading-edge tubercles on drag coefficient of S-1223 airfoil
Taken from Sudhakar et al. (2020) (see text for details)

Other than analyzing the effect of tubercles on airfoils with different geometrical characteristics, it was suggested to add the spanwise ridges and valleys generated along the chord of the modified wings as another key parameter other than the amplitude, wavelength, and amplitude to wavelength ratio sizes in the characterization of the airfoils with leading-edge undulations (Bolzon et al., 2016b). If the thickness to chord ratio is preserved during the design

of the modified airfoils, such as what is done in (Hansen et al., 2011), the foil shape will totally change, and spanwise ridges and valleys form along the entire chord of the modified airfoils. However, if the modified airfoils are designed by merely adding tubercles to the leading edge part of the airfoils such as what is done in (Johari et al., 2007), the foil has a constantly changing thickness-to-chord ratio which results in the foil geometry after the leading edge part remaining mostly unchanged (Bolzon et al., 2016b). The effect of these spanwise bumps is discussed in our research in chapter 4.

Besides the works, done to analyze the aerodynamic effect of the leading-edge undulations, many research were also performed to understand the flow behavior on the wings with leading-edge protuberances.

1.2 Research done on the flow mechanism on 2D wings with tubercles

The water tunnel flow visualization results using surface tufts in (Johari et al., 2007) shown in Figure 1.14, indicated that the separated flow regions originate from the troughs between tubercles at pre-stall angles of attack. As mentioned before (Miklosovic et al., 2007), these separated flow regions are responsible for the reduction of pre-stall lift coefficients on the modified airfoils. The numerical analysis on the same airfoil and at the same Reynolds number of 1.8×10^5 using the steady-state Reynolds Average Navier-Stokes (RANS) equations with one-equation Spalart-Allmaras turbulence modeling also confirms the origination of the separated flow behind the trough regions (Dropkin, Custodio, Henoch, & Johari, 2012). Moreover, it was observed in Figure 1.14 (Johari et al., 2007) that the flow stays attached more behind the tubercle peaks at higher angles of attack. Thus, the modified airfoils, do not stall in the traditional way with a sudden loss of lift, and their stall can be identified as the point which the amount of lift generated begins to decrease with angle of attack.

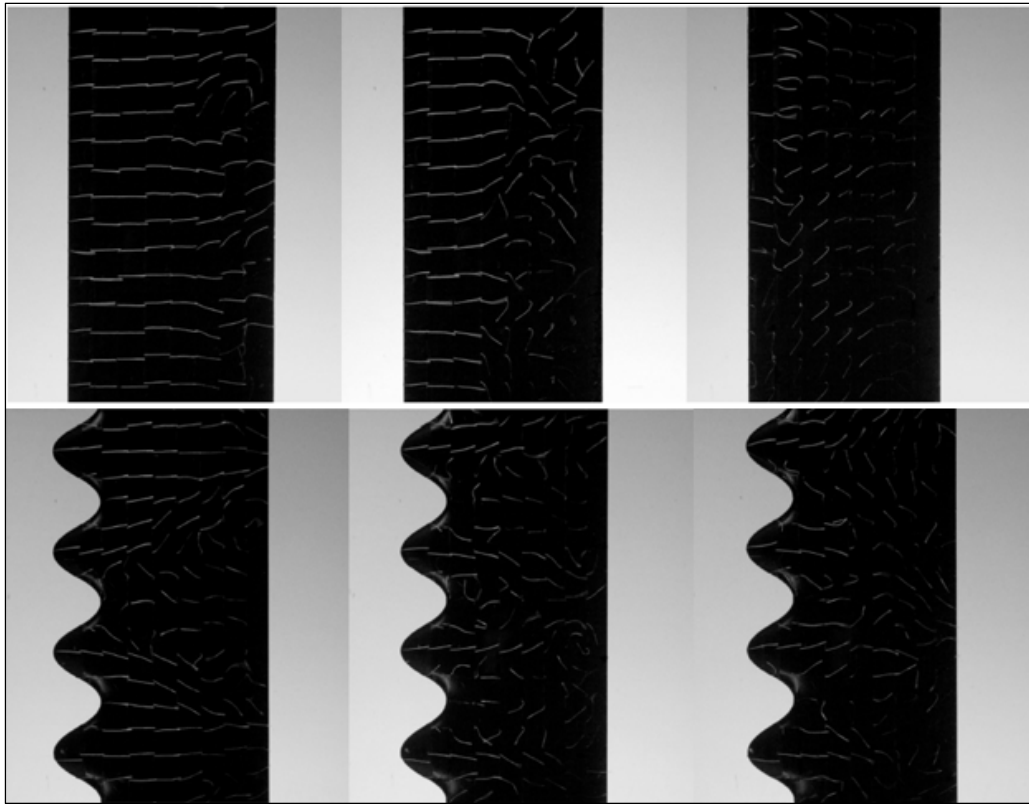


Figure 1.14 Photograph of flow visualization analysis using surface tufts on baseline (top) and modified NACA634 -021 airfoils (bottom) at 12, 18 and 24 degree angles of attack from left to right

Taken from Johari et al. (2007)

Based on the hydrogen bubble flow visualization analysis on 2D wings with different amplitude and wavelength sizes (Hansen et al., 2011), it was suggested that tubercles behave in the similar manner as counter rotating vortex generators and the optimum amplitude and wavelength of the tubercles have some analogies with optimum spacing and height of the vortex generators. It was also suggested that the airfoils with the same size of amplitude to wavelength ratio has equivalent maximum angle of leading-edge sweep and thus have the same vortex strength. It was also postulated that for the smaller wavelengths' airfoils, the vortices are spaced more closely together and are therefore more likely to interact with one another. This causes the onset of unsteadiness to occur further upstream, leading to increase in turbulence and increase of the momentum exchange within the boundary layer and thus more uniform attachment of the flow to the suction surface of the airfoil. In summary, Hansen *et al.*

(2011) suggested that, reducing the wavelength of the tubercles affects the level of mixing in the boundary layer while amplitude to wavelength ratio determines the vortex strength (Hansen et al., 2011).

While many researchers (Fish & Lauder, 2006; Hansen et al., 2011; Miklosovic et al., 2004; Watts & Fish, 2001a; Yoon et al., 2011; Zhang et al., 2013) suggested that there are similarities between leading-edge undulations and vortex generators or small delta wings (Custodio, 2012), some others questioned this idea (Stein & Murray, 2005; Van Nierop, Alben, & Brenner, 2008). Van Nierop et al. (2008) suggested that since the amplitude and wavelength of the undulations are much larger than the boundary layer thickness, the mechanism responsible for aerodynamic improvements must be different than the Vortex generators. The author developed an analytical model based on lifting line theory and conclude that regarding the non-uniform downwash that reduces the effective angle of attack behind the peaks, more delayed separation exists behind the chord peaks. Moreover, regarding the smaller chord length behind the troughs (chord minima), larger pressure gradients exist there, thus; troughs between tubercles, stall at a lower angle of attack in comparison with the peaks and thus the separation originates from the trough regions. The spanwise flow was not considered in that research.

1.2.1 Interaction of the streamwise vortices

One of the first works that show the interaction of the streamwise vortices on 2D wings with leading-edge tubercles (Custodio, 2012) was done at Reynolds numbers of 1.5×10^4 , 1.8×10^5 , and 4.5×10^5 . The analysis was done on the single NACA 634-021 modified airfoil with the amplitude and wavelength of $0.12C$ and $0.5C$ respectively, where C is the chord length. The author observed that at spatial locations ranging from $0C$ to $0.12C$, as the angle of attack is increased, the spanwise distribution of the neighboring counter-rotating streamwise vortices tends to remain symmetric as shown in Figure 1.15. However, at spatial locations greater than $0.12C$, this symmetry breaks down. By increasing the angle of attack, as the strength of the neighboring vortices increase, the interactions of the streamwise vortices generate asymmetry within the vorticity distribution, causing the neighboring vortices to change in size and shape

as shown in Figure 1.16. The author mentioned that the vortex interaction leads to the stretching and annihilation of the vortices, and as the counter-rotating vortices interact, vorticity is reduced, and stall characteristics become apparent. The height of the vortices also showed to change with the angle of attack, with vortices showing signs of lifting off from the surface at high angles of attack (Custodio, 2012).

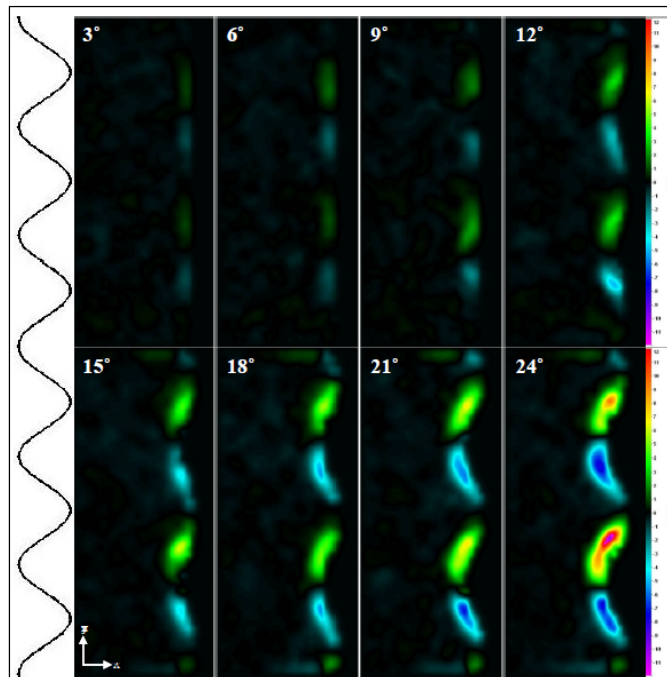


Figure 1.15 Streamwise vorticity contours on a modified hydrofoil as a function of angle of attack at a chordwise spatial location of $0.12C$

Taken from Custodio (2012)

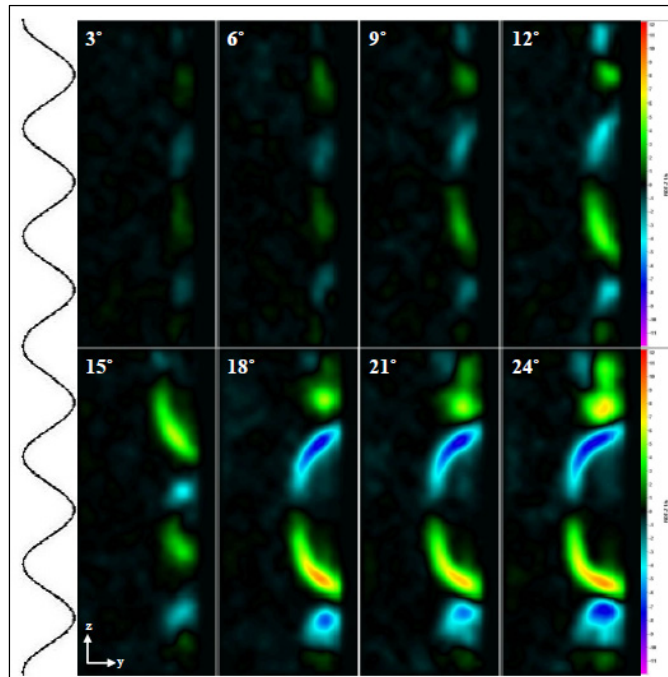


Figure 1.16 Streamwise vorticity, contours on a modified hydrofoil as a function of angle of attack at a chordwise spatial location of $0.36C$

Taken from Custodio (2012)

To prove the existence of the spanwise velocity on the streamwise vortices that results in vortex interaction, the method of vortex images commonly used in potential flow theory was used (Custodio, 2012). In this method, an infinite row of counter-rotating vortices of known vorticity was considered at a height h above a flat surface as shown in Figure 1.17, where λ is one modified airfoil protuberance wavelength and h is the vertical distance of the vortex core from the flat surface. Considering only the central vortex W , neighboring vortices above the surface will not influence on W due to symmetry, but W will have an induced velocity $U_{induced}$, in the z -direction generated by interactions with vortex images.

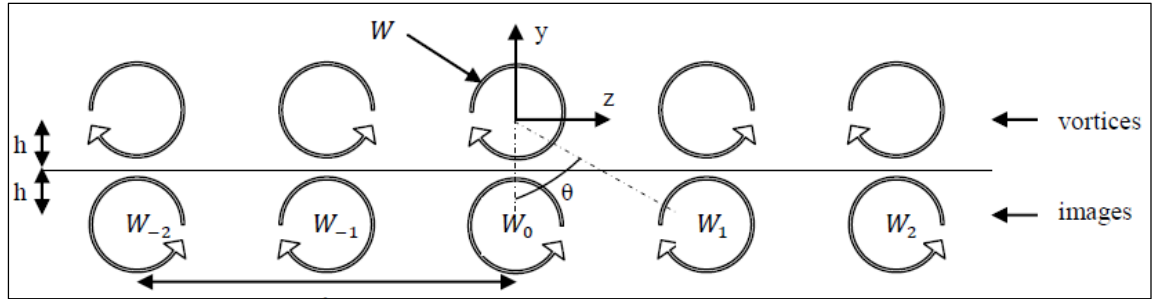


Figure 1.17 Counter-rotating vortices with image pairs

Taken from Custodio (2012)

Induced velocity due to any single vortex image on W can be calculated using equation (1.1).

$$u_{induced} = \frac{\Gamma}{2\pi\delta_j} \quad (1.1)$$

Where Γ is the circulation of W , $j = 1, 2, 3, \dots, n$, and δ_j is the distance from the core of W to the core of a given vortex image inducing a velocity on W . Considering the distance between neighboring counter-rotating vortices to be $\lambda/2$, set by the wavelength of the modified foil, δ_j can be written as equation (1.2).

$$\delta_j = \sqrt{(z - z_j)^2 + (y - y_j)^2} = \sqrt{j^2 \left(\frac{\lambda}{2}\right)^2 + (2h)^2} \quad (1.2)$$

Thus, the induced velocity of W in the spanwise direction can be calculated using equation (1.3).

$$U_{induced} = \sum_{j=1}^{\infty} \frac{\Gamma}{2\pi\delta_j} \cos \theta_j \quad (1.3)$$

Where

$$\cos \theta = \frac{2h}{\delta_j} \quad (1.4)$$

Thus, based on the above discussion, the existence of spanwise velocity that causes the interaction of the streamwise vortices is proved. This interaction of the streamwise vortices will also be discussed in our results presented in chapters 3, and 4.

1.3 Potential applications of leading-edge tubercles

The aerodynamic effects of leading-edge tubercles as a flow control device that helps the lifting bodies to maintain lift at high angles of attack can have many benefits for different applications. A summary of these benefits is discussed in this section.

Small UAVs (Unmanned Aerial Vehicles) and Micro Aerial Vehicles (MAV), due to their low flying speed and small chord length are generally flying at low Reynolds numbers, and their wings mostly operate in the laminar and transitional flow regimes. Thus, their wings are susceptible to boundary layer separation and severe stall, especially during take-off and landings, when slow flight speeds and high angles of attack are required. Implementing leading-edge tubercles on the MAV and UAV wings could make these aircraft to be more stable over a greater range of angles of attack by delaying and decreasing the severity of the stall (Bolzon et al., 2016b).

The runway length of an aircraft is a function of the square of the minimum stall speed. Leading-edge undulations, reduce the minimum stall speed by enabling the wing to reach larger angles of attack before stall. Thus these undulations enable the aircraft to reduce the take-off and landing distance without adding significantly to the drag or weight of the vehicle by implementing the devices such as flaps and slats (Hansen, 2012).

Besides, by delaying stall and increasing the lift coefficients on aircraft wings, tubercles can increase the maneuverability of the aircraft, in the same manner as they increase the maneuverability of the Humpback whales (Fish et al., 2008; Hain et al., 1981).

The other application of the leading-edge undulations can be on wind turbines. As mentioned by Miklosovic et al. (2004), leading-edge tubercles on the scaled whale flipper model cause to increase in the maximum lift coefficient by 6% and stall angle by 40% respectively. Wind turbines usually work in mild wind conditions and finding a method to increase their lift generation before stall can increase their capability in power generation. Besides that, by incorporating leading-edge tubercles, the stall angle of the wings increased, and hence the wind turbines can more efficiently operate in variable wind conditions (Hansen, 2012).

In addition to the increase in power generation, as tubercles have already shown their noise reduction capabilities (Bolzon et al., 2016b; Hansen, Kelso, & Doolan, 2010), they can also be used to reduce the wind turbine noise, which is a significant problem in wind farming as it can lead to health problems (Bolzon et al., 2016b).

Helicopter blades operate at high angles of attack when high forward speeds and large loads exist. As a consequence, dynamic stall can occur especially on the retreating blades if the blades exceed the stall angle for the given velocity, which results in blade torsions and vibrations. Thus, increasing the stall angle and reducing the severity of the stall by incorporating the leading-edge tubercles, can possibly reduce the fatigue, and improve the service life of the helicopter blades (Hansen, 2012).

The other application of leading-edge undulations is on ceiling fans. leading-edge tubercles have already shown their capability in increasing the efficiency and reducing the operational noise of the ceiling fans (Bolzon et al., 2016b).

Leading-edge tubercles have also shown their effect on increasing the efficiency as well as the tonal noise elimination on aircraft propellers (Asghar, Perez, Jansen, & Allan, 2020).

As the hydrodynamic noise level of underwater vehicles, such as submarines, torpedoes, and underwater unmanned vehicles (UUVs) is significantly related to their detection opportunities (Liu, Li, & Shang, 2019), the leading-edge undulations can also be implemented in these vehicles for stealth purposes.

1.4 Research objectives

As discussed in the literature review section, the effect of leading-edge tubercles' amplitude and wavelength sizes, on the aerodynamic performance of the 2D wings was discussed in different research studies. However, to the best of this author's knowledge, there was no research focused on the effect of the amplitude and wavelength sizes of the leading-edge tubercles on the circulation and interaction of the streamwise vortices. Hence, no research could make a formal quantitative observation, to justify the aerodynamic performance changes observed by changing the wavelength, amplitude, and amplitude to wavelength ratio sizes of the tubercles. The main objective of this research is thus, to analyze the effect of tubercles' amplitude, wavelength, and amplitude to wavelength ratio sizes on the circulation and interaction of the streamwise vortices and as a result, their effect on the aerodynamic performance of the airfoils with leading-edge tubercles using numerical simulations.

The second objective of this research is to do more analysis and discussions regarding the reason for the generation of separated flow regions on the modified airfoils at pre-stall angles of attack. As mentioned, these flow separations, cause the reduction of lift coefficients at pre-stall angles of attack on the modified airfoils, compared to the baseline airfoil. Although many articles, discussed the reason for the generation of these separated flow regions, the reason for their generation is still not fully determined.

Meanwhile, as mentioned in the literature review section, the effect of leading-edge tubercles/undulations can be different on the aerodynamic performance of different types of airfoils. For example, their effect can be different on symmetric or high-cambered airfoils. Besides, the effect of keeping the thickness to chord ratio while designing the modified airfoils

which results in the generation of spanwise ridges and valleys along the chord on the modified airfoils has not been discussed yet in the literature. The third objective of this thesis is to analyze the effect of leading-edge undulations on a high-cambered airfoil and discuss more the effect of these generated spanwise bumps along the chord on the modified airfoils.

In the next chapter (chapter 2), the methodology of the thesis is presented. In chapters 3 the first two objectives are discussed, and the third objective is discussed in chapter 4. In chapter 5, the article submitted to the "Journal of aircraft" is presented which explained the first two objectives of this thesis. The discussion will end in chapter 6 with some concluding remarks and some recommendations for future works.

CHAPTER 2

METHODOLOGY

The methodology is first discussed by presenting the geometrical configurations of the two airfoils studied in this research. After that, the numerical equations used in this research are explained. At the end, the mesh convergence study and the validation of each airfoil is presented.

2.1 Geometrical configurations

In this research, the analysis is performed on two different airfoils of NACA0010 and Raf-19 with almost the same thickness but with different levels of camber. The characteristics of these two airfoils are illustrated in Table 2.1 and Table 2.2 respectively.

Table 2.1 NACA0010 airfoil geometrical characteristics

Maximum thickness (%C)	10
Maximum thickness position (%C)	30
Maximum Camber (%C)	0
Maximum Camber position (%C)	0

Table 2.2 RAF-19 airfoil geometrical characteristics

Maximum thickness (%C)	10.5
Maximum thickness position (%C)	15
Maximum Camber (%C)	10.1
Maximum Camber position (%C)	40

On each airfoil, the baseline airfoil and five modified airfoils with varying wavelength and amplitude sizes are compared in this research. The amplitude (A) and wavelength (W) of the modified airfoils are selected based on the same percentage as the research of Hansen *et al.* (2011), shown in Table 2.3. These values fall in the same range of estimated values for the humpback whale flipper tubercles (Fish & Battle, 1995).

Table 2.3 Tubercles' amplitudes and wavelength sizes

Configurations	Label	A/W ratio
A=0	Baseline	0
A=30 (0.03C), W=110 (0.11C)	A3W11	0.27
A=60 (0.06C), W=110 (0.11C)	A6W11	0.54
A=60 (0.06C), W= 210 (0.21C)	A6W21	0.28
A=60 (0.06C), W= 430 (0.43C)	A6W43	0.14
A=110 (0.11C), W= 430 (0.43C)	A11W43	0.26

To design the modified airfoils, on both type of airfoils studied, the chord length of the undulating cases varies according to Eq. (2.1) used in (Skillen, Revell, Pinelli, Piomelli, & Favier, 2015). Where in Eq. (2.1), Z is the spanwise orient and \bar{C} is the mean chord length.

In order to reduce the computational cost in this study, only one tubercle is studied as shown in Figure 2.3 and Figure 2.4 rather than using multiple tubercles, such as what is shown in Figure 2.1 and Figure 2.2. This work also helps us to better analyze the effect of streamwise vortices, which will be discussed in next sections. In addition, to understand the effect of streamwise vortices on airfoils with multiple tubercles, it is required to first know the effect and behavior of the streamwise vortices on only one tubercle. Afterward, their effect on airfoils with multiple tubercles could be better understood. All the modified airfoils are designed to have the same mean chord length. Thus, all the airfoils have an average chord length of 1 and a span length equal to their wavelength sizes, as shown in Figure 2.3 and Figure 2.4.

$$C(z) = A \cos\left(\frac{2\pi z}{W}\right) + \bar{C} \quad (2.1)$$

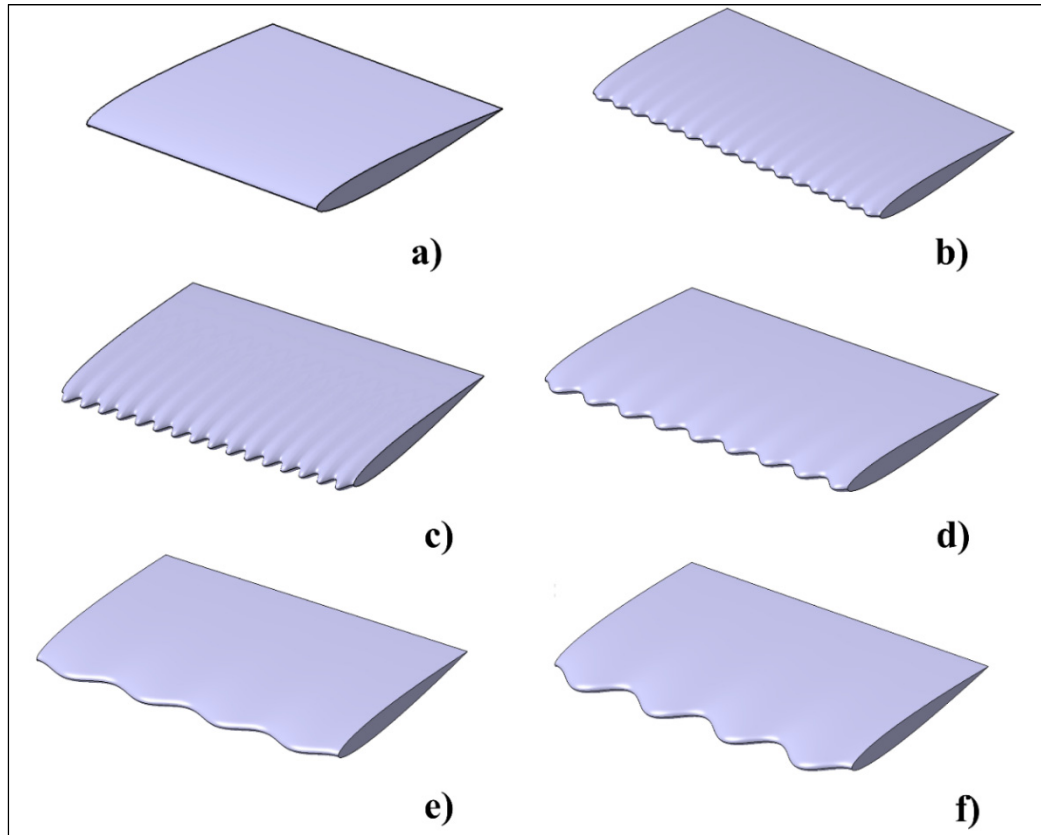


Figure 2.1 Modified NACA 0010 airfoil geometries with multiple tubercles
a) baseline b) A3W11 c) A6W11 d) A6W21 e) A6W43 and f) A11W43

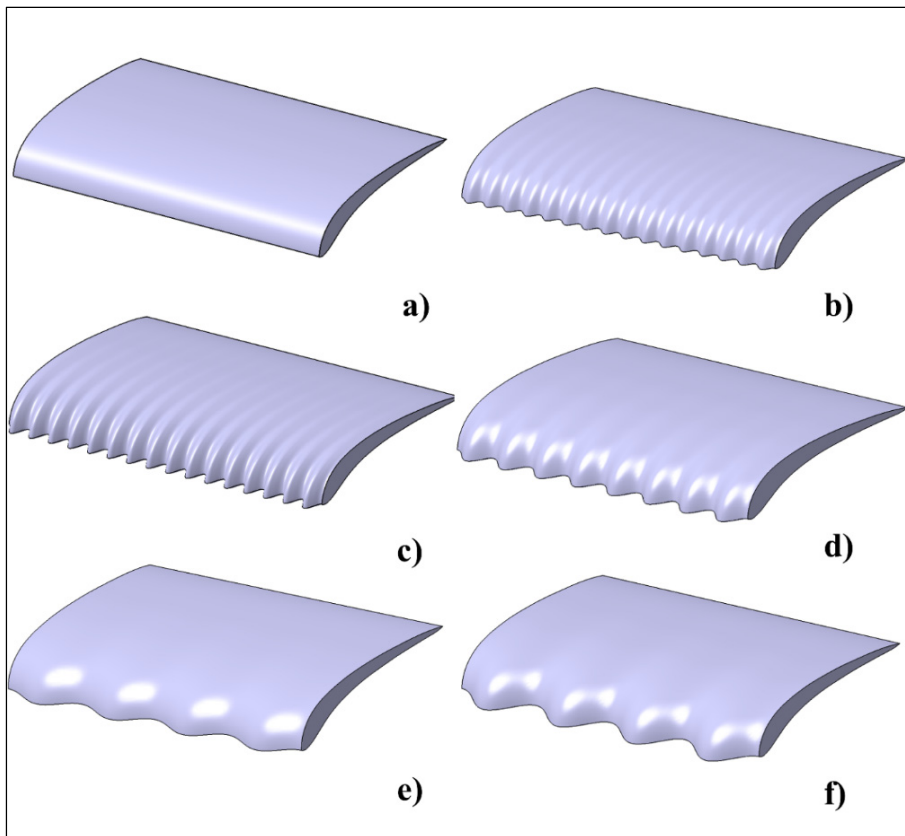


Figure 2.2 Modified RAF-19 airfoil geometries with multiple tubercles a) baseline b) A3W11 C) A6W11 D) A6W21 E) A6W43 and F) A11W43

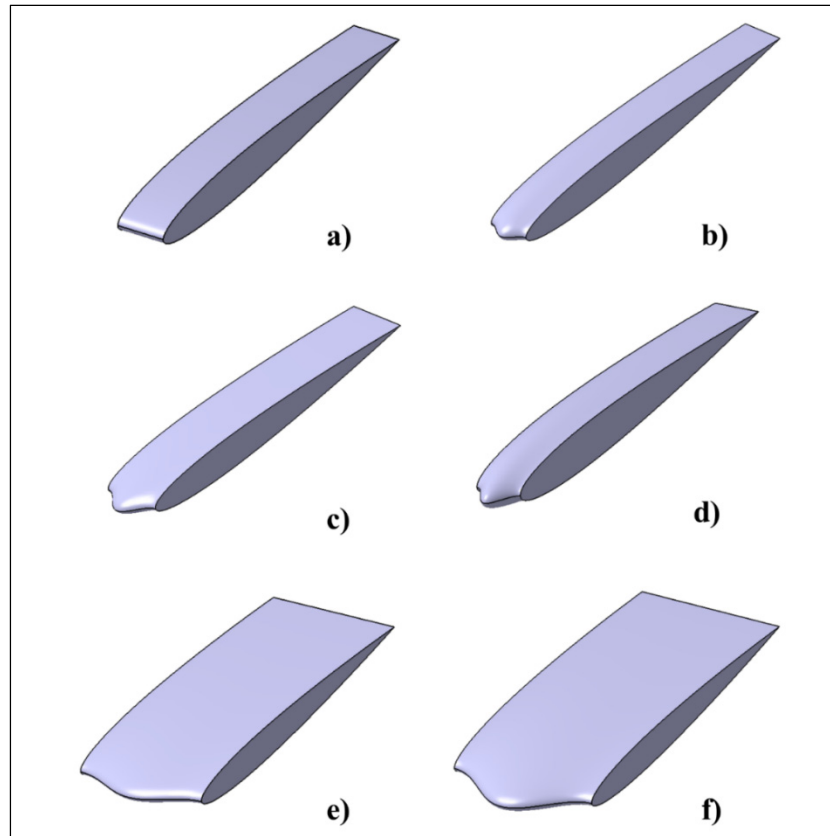


Figure 2.3 Modified NACA 0010 airfoil geometries with single tubercle a) baseline b) A3W11 C) A6W11 D) A6W21 E) A6W43 and F) A11W43

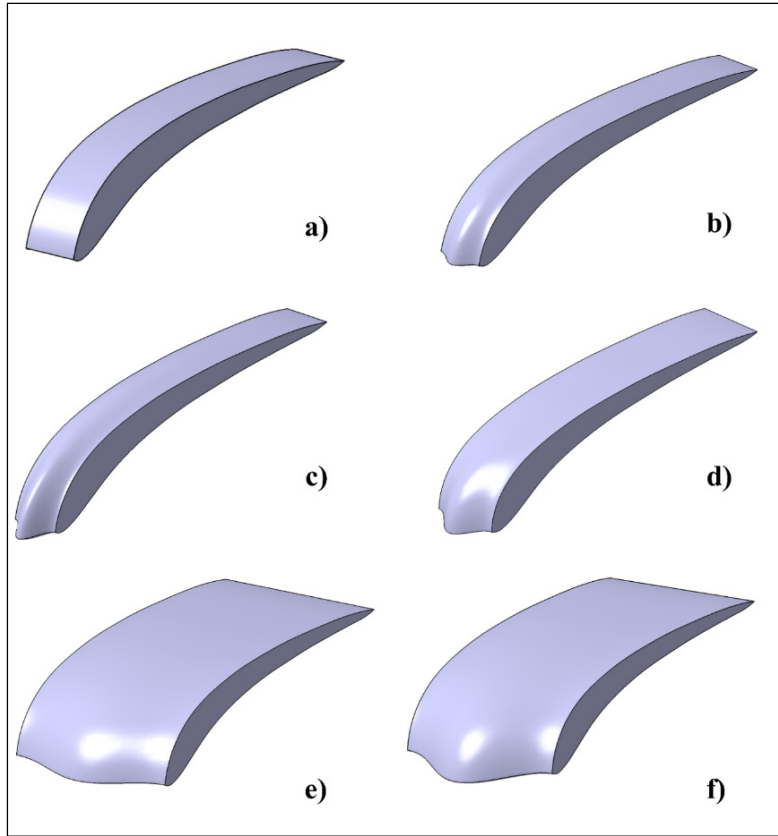


Figure 2.4 Modified RAF-19 airfoil geometries with single tubercle a) baseline b) A3W11 C) A6W11 D) A6W21 E) A6W43 and F) A11W43

2.2 Equations and turbulence modeling

In this research, the $k-\varepsilon$ turbulence model (Spalding, 1974; Wilcox, 1998) is used to analyze the baseline and modified airfoils. Working with limited computational resources, the mesh refinement is set to a first node at $y^+ > 30$. The value of $y^+ > 30$ is chosen based on the recommendations mentioned in (Spalding, 1974; Wilcox, 1998). Besides that, in other numerical researches done on the effect of leading-edge tubercle on flipper models such as the research of Pedro & Kobayashi (2008), the chosen value of $y^+ > 30$ has proved to provide good agreement of the results in comparison with the experimental data.

The results show good agreement with the experimental and numerical data available for the validation of the results on the baseline NACA 0010 and RAF-19 airfoils, which will be discussed in the next sections. The detailed formulation of the turbulence model used in this research is as follows:

2.2.1 The k - ε turbulence modeling

The continuity and momentum equations used in the k - ε turbulence modeling (Spalding, 1974; Wilcox, 1998) are shown in Eq. (2.2) and (2.3), respectively:

$$\frac{\partial \rho}{\partial t} + \frac{\partial}{\partial x_j} (\rho U_j) = 0 \quad (2.2)$$

$$\frac{\partial \rho U_i}{\partial t} + \frac{\partial}{\partial x_j} (\rho U_i U_j) = -\frac{\partial p'}{\partial x_i} + \frac{\partial}{\partial x_j} \left[\mu_f \left(\frac{\partial U_i}{\partial x_j} + \frac{\partial U_j}{\partial x_i} \right) \right] \quad (2.3)$$

In the above equations, U_i and U_j are the i and j components of velocity respectively, ρ is the density considered constant (due to incompressible flow simulations), μ_f is the effective viscosity accounting for turbulence shown in Eq. (2.4), and p' is the modified pressure as shown in Eq. (2.5).

$$\mu_f = \mu + \mu_t \quad (2.4)$$

$$p' = P + \frac{2}{3} \rho K + \frac{2}{3} \mu_f \frac{\partial U_j}{\partial x_j} \quad (2.5)$$

The k - ε model is based on the eddy viscosity concept shown in Eq. (2.4), and assumes that the turbulence viscosity μ_t is linked to the turbulence kinetic energy and dissipation via Eq. (2.6), where C_μ is a constant, and its value is illustrated in Table 2.4.

$$\mu_t = C_\mu \rho \frac{k^2}{\varepsilon} \quad (2.6)$$

In the k - ε turbulence modeling, k is the turbulence kinetic energy and ε is the turbulence dissipation. The values of k and ε will be obtained using their transport equations shown in Eq. (2.7) and (2.8), respectively.

$$\frac{\partial(\rho k)}{\partial t} + \frac{\partial}{\partial x_j} (\rho U_j k) = \frac{\partial}{\partial x_j} \left[\left(\mu + \frac{\mu_t}{\sigma_K} \right) \frac{\partial k}{\partial x_j} \right] + P_k - \rho \varepsilon + P_{kb} \quad (2.7)$$

$$\frac{\partial(\rho \varepsilon)}{\partial t} + \frac{\partial}{\partial x_j} (\rho U_j \varepsilon) = \frac{\partial}{\partial x_j} \left[\left(\mu + \frac{\mu_t}{\sigma_\varepsilon} \right) \frac{\partial \varepsilon}{\partial x_j} \right] + \frac{\varepsilon}{k} (C_{\varepsilon 1} P_k - C_{\varepsilon 2} \rho \varepsilon + C_{\varepsilon 1} P_{\varepsilon b}) \quad (2.8)$$

The $C_{\varepsilon 1}$, $C_{\varepsilon 2}$, σ_K , and σ_ε in Eq. (2.7) and (2.8) are constants and their values are shown in Table 2.4. P_k is the turbulence production due to viscous forces shown in Eq. (2.9), and P_{kb} and $P_{\varepsilon b}$ are the production terms due to buoyancy (Spalding, 1974; Wilcox, 1998).

$$P_k = \mu_t \left(\frac{\partial U_i}{\partial x_j} + \frac{\partial U_j}{\partial x_i} \right) \frac{\partial U_i}{\partial x_j} - \frac{2}{3} \frac{\partial U_j}{\partial x_j} \left(3\mu_t \frac{\partial U_j}{\partial x_j} + \rho k \right) \quad (2.9)$$

Table 2.4 Model coefficients used in the k - ε turbulence modeling

Model coefficient	Value
$C_{\varepsilon 1}$	1.44
$C_{\varepsilon 2}$	1.92
σ_K	1
σ_ε	1.3
C_μ	0.09

2.2.2 Scalable wall function

To calculate the wall-shear stresses, the scalable wall function is used (ANSYS, 2016; Menter & Esch, 2001). In a scalable wall function, an alternative velocity scale of u^* is used (Eq. (2.10)), which remains finite as U_t goes to zero. Then the y^* can be defined as Eq. (2.11) and u_τ can be obtained by Eq. (2.12).

$$u^* = C_\mu^{1/4} k^{1/2} \quad (2.10)$$

$$y^* = (\rho u^* y) / \mu \quad (2.11)$$

$$u_\tau = \frac{U_t}{\frac{1}{\kappa} \ln(y^*) + L} \quad (2.12)$$

In the above equations, u_τ is the friction velocity, y is the distance from the wall, y^* is the dimensionless distance from the wall in scalable wall-function, U_t is the known velocity tangent to the wall at a distance of y from the wall, κ is the von Karman constant and its value is 0.4, and L is a log-layer constant depending on wall roughness.

The absolute value of the wall shear stress is then obtained from Eq. (2.13).

$$\tau_w = \rho u^* u_\tau \quad (2.13)$$

The scalable wall function limits the y^* value used in the logarithmic formulation by a lower value of:

$$\tilde{y}^* = \max(y^*, 11.06) \quad (2.14)$$

Where 11.06 is the value of y^* at the intersection between the logarithmic and the linear near wall profile. The computed \tilde{y}^* is therefore not allowed to fall below this limit.

At high angles of attack, on the modified airfoils of both NACA 0010 and RAF-19 airfoils, the U-RANS simulation is performed due to the observed unsteadiness which will be explained in the next sections, when the unsteady flow behavior is discussed. To perform the U-RANS simulation, first a steady-state analysis is done to understand after how many iterations the steady-state solution for the aerodynamic coefficients become stable (have a uniform cyclic stability). It is observed that the steady-state solution for the modified NACA 0010 and RAF-19 airfoils become stable after 45 and 70 iterations respectively. Thus, in U-RANS analysis, 45 and 70 iterations per time-step is used for the modified NACA 0010 and RAF-19 airfoils respectively. A time-step study is also carried out, and it is observed that on both airfoils, for shorter time-step sizes below 0.25-time units, the lift and drag coefficient values remain constant. Thus, all the calculations are performed with the time-step size of 0.25-time units. The final solution of the U-RANS simulation for all the modified airfoils become steady-state and as a result the U-RANS analysis is performed until the steady-state solution is achieved.

The governing equations for the $k-\varepsilon$ turbulence model are discretized via the Finite Volume-based Finite Element approach developed by ANSYS/CFX. On both steady-RANS and U-RANS simulations, a high resolution (bounded second-order upwind biased discretization) is chosen for advection scheme and for turbulence numerics, the high-resolution option is

selected. The second-order backward Euler scheme is also chosen for transient scheme for U-RANS simulations.

On all the analysis done in this research, a non-dimensional form is used. Thus, the Chord-length (C) and inlet velocity (U) are chosen as reference scales and the Reynolds number is chosen as 2.5×10^5 . To perform the numerical analysis, a rectangular domain with a width of $X/C = 25$, a height of $Y/C = 20$ and a depth equal to the span length or wavelength of each airfoil is created. For example, the domain's depth for the A6W11 airfoil is 0.11, while the domain's depth for the A6W43 airfoil is 0.43. The airfoils had a horizontal distance of 10 from the wind tunnel inlet, 15 from the outlet and a vertical distance of 10 from the upper and lower wind tunnel's upper and lower walls. The angle of attack is changed by rotating the airfoil around ($-Z$) axis. Free slip wall is chosen for upper and lower wall boundaries. A no-slip boundary condition is chosen for the airfoil wall. The uniform Cartesian velocity of 1 in the X direction is considered for the inlet. The pressure outlet is chosen as zero and the periodic boundary condition is applied in the lateral boundaries. The domain is divided into smaller segments to create smaller elements around the airfoil. The boundary condition and the computational model used in this study are shown in Figure 2.5.

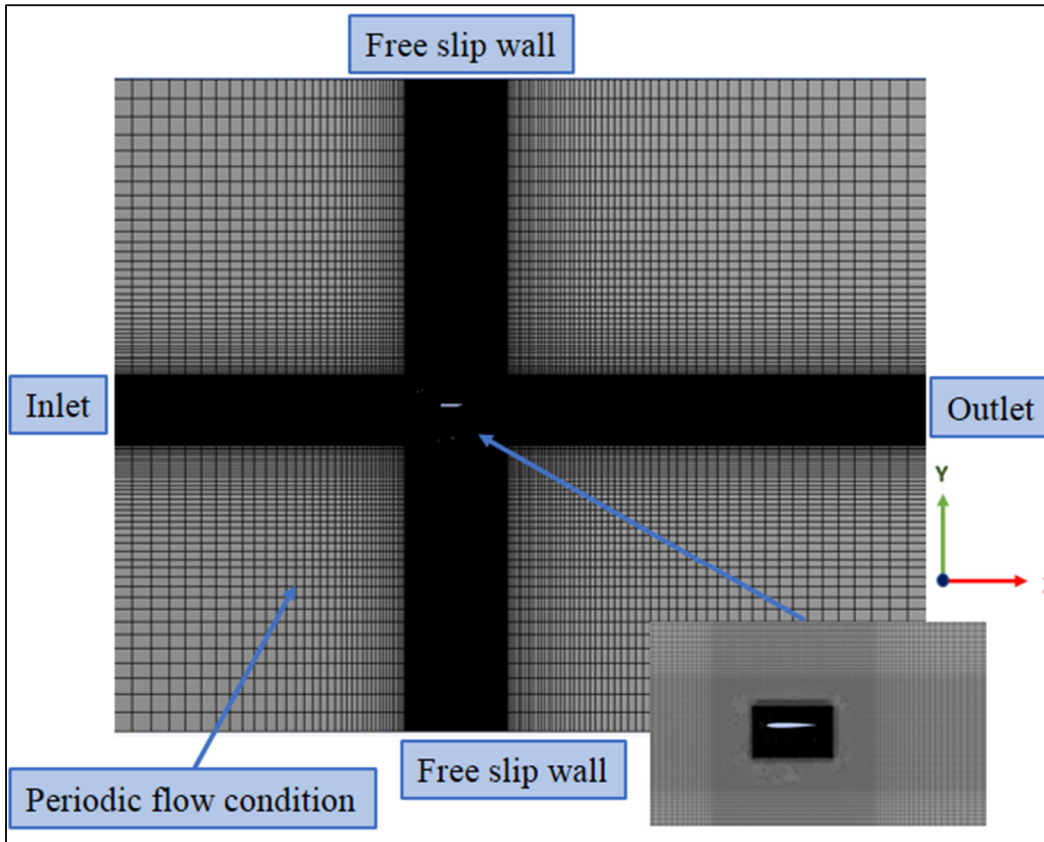


Figure 2.5 Computational domain with segmented mesh and the boundary conditions

2.2.3 Mesh convergence study on NACA 0010 airfoil

The mesh convergence study is carried out by increasing the number of elements in the inner most rectangular segment around the airfoil shown in Figure 2.5 at angle of attack of 6 degrees. The 6-degree angle of attack is chosen based on other literatures (e.g. the research of Dropkin et al. (2012)) and the inner rectangle is chosen to better analyze the effect of mesh resolution around the airfoil.

The results show that increasing the number of elements from 1.4×10^6 to 2.2×10^6 , does not yield significant changes in the generated values of lift and drag the drag coefficient as shown in Table 2.5.

Table 2.5 Mesh convergence study of the
NACA 0010 baseline airfoil

	Number of elements	C_D	C_L
G₃	886336	0.027477	0.57985
G₂	1377552	0.025242	0.58822
G₁	2217621	0.025915	0.58904

The mesh with 1.4×10^6 elements is therefore considered adequate for this study. The same mesh setting is used for all the modified airfoils and their number of elements are increased based on their shape and wavelength sizes. The number of elements used to analyze the modified airfoils are illustrated in Table 2.6.

Table 2.6 Number of elements used in
NACA 0010 modified airfoils

Airfoil	Number of elements
A3W11	1639054
A6W11	2240888
A6W21	3118716
A6W43	5508992
A11W43	5710483

The uncertainty resulting from the discretization in the computations were estimated using the procedure introduced by (Celik, Ghia, Roache, & Freitas, 2008) which is based on Richardson extrapolation. The drag coefficient was chosen as the key parameter for this estimation. The grids, G3, G2 and G1 were used for the uncertainty calculation which corresponds to the mesh refinement factor (r) of 1.15 and 1.17 between the mesh pairs respectively. The apparent order P of the method was solved as $P = 8.401012$ using the fixed-point iteration. As a result, the approximated relative error, and fine-grid convergence index were calculated as follows and

the relative error of 2.5% and the fine- grid convergence index of 1.16 % are reported for the computations done on symmetric NACA0010 airfoil.

$$e_a^{21} = \left| \frac{Cd1 - Cd 2}{Cd1} \right| = 0.025969516 \quad (2.15)$$

$$GCI_{fine}^{21} = \frac{1.25 * e_a^{21}}{r_{21}^p - 1} = 0.011620102 \quad (2.16)$$

2.2.4 Baseline NACA 0010 airfoil validation

As shown in Table 2.1 and Table 2.7, the NACA 0010 and SD8020 airfoils have almost the same geometric characteristics. Since the aerodynamic data for the NACA 0010 airfoil in reference such as Abbott & Von Doenhoff (1959) are at higher Reynolds numbers (in the order of 3×10^6 - 6×10^6), consequently, to validate the numerical results on the NACA 0010 airfoil, the numerical results are compared with the experimental data available for the SD8020 airfoil in the research of Selig (1959), that performed at lower Reynolds numbers.

Table 2.7 SD 8020 airfoil characteristics (% C)

Max thickness	10.1
Max thickness position	27.5
Max camber	0
Max camber position	0

The experiment of Selig (1995) was carried out at the Reynolds number of 2.0×10^5 . The numerical results are validated using the model with 1.4×10^6 elements at steady state condition and using the same angles of attack and Reynolds numbers used in the research of

Selig (1995). Different turbulence modeling such as $k-\varepsilon$, Spalart-almaras, $k-\omega$, SST and etc. is tested in Ansys/CFX, and the results using the $k-\varepsilon$ turbulence modeling shows better agreement comparing with the experimental data. As shown in Figure 2.6 and Figure 2.7, good agreement of the results can be seen in both lift and drag coefficient values, respectively. The experimental drag coefficient values were only available up to 8.79 degrees. It should be noted that, the main notion of this research is to perform the parametric study. Thus, the goal was to have a “good enough” quantification of lift/drag coefficients to capture the trend which is sufficient to perform the parametric study. It should be also noted that the differences observed between the experimental and numerical lift coefficient values at higher angles of attack (around 16, and 18 degrees) are around 20%, which is considered acceptable.

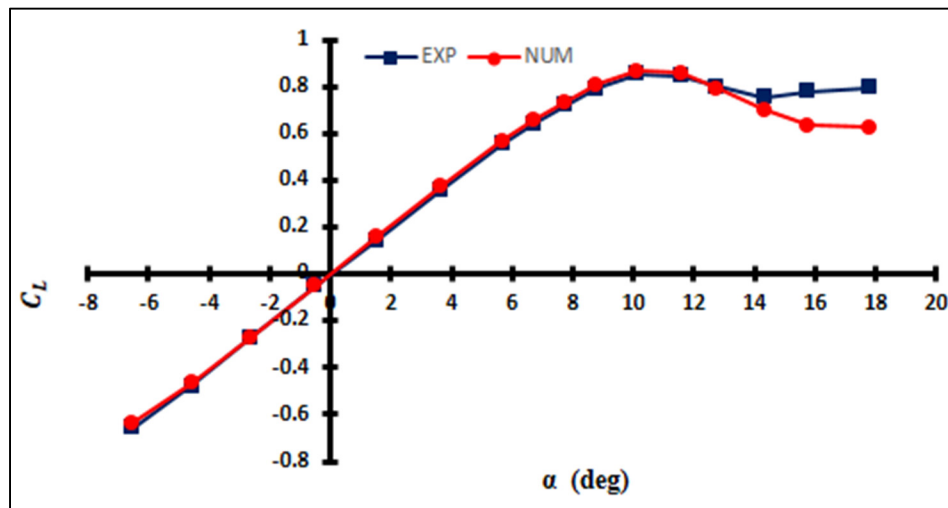


Figure 2.6 Comparison of the lift coefficients of NACA 0010 and SD 8020 airfoils in the numerical simulation and experimental research of Selig (1995)

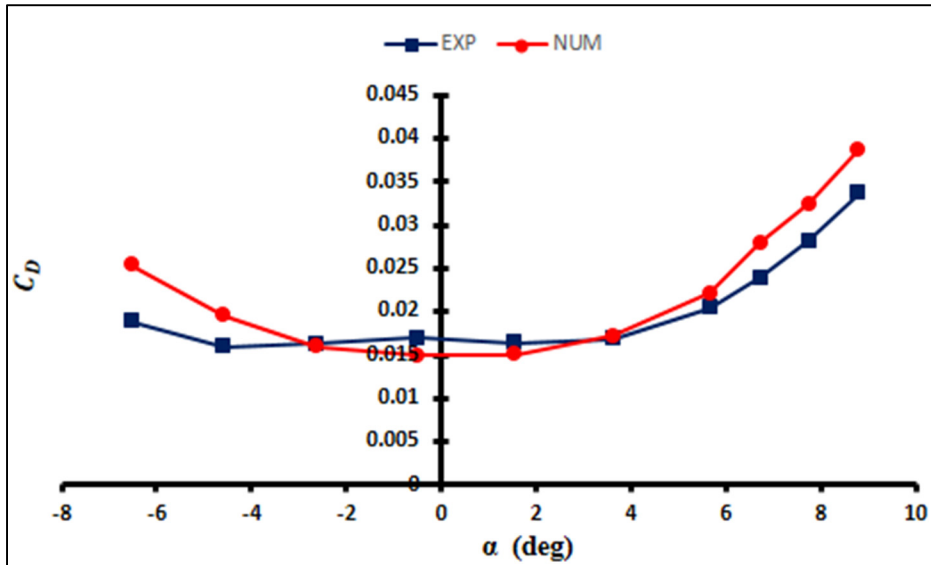


Figure 2.7 Comparison of the drag coefficients of NACA 0010 and SD 8020 airfoils in the numerical simulation and experimental research of Selig (1995)

To have a more "localized" validation of the results, the pressure coefficients are compared with the data obtained by the *XFLR5 (XFOIL)* code (Drela, 2000), and results with an acceptable level of agreement are obtained. For example, as shown in Figure 2.8, at a 0-degree angle of attack, the *XFLR5 (XFOIL)* and *ANSYS/CFX* pressure coefficients on the suction sides of the baseline airfoil at chord-wise locations between $0.1C$ to $0.8C$ with an increment of $0.1C$ are compared and the results demonstrate good agreement.

Table 2.8 Comparison of the lift and drag coefficient of the NACA 0010 baseline airfoil obtained by the XFOIL code and ANSYS/CFX at 0-degree angle of attack

	<i>XFOIL</i>	<i>CFX</i>
C_D	0.011	0.014
C_L	0.	0.0002

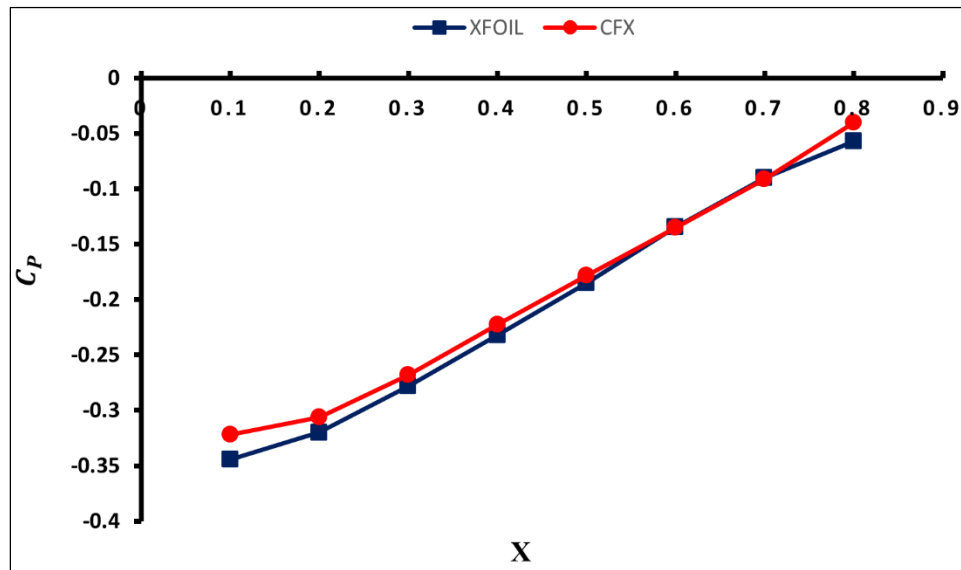


Figure 2.8 Comparison of the pressure coefficients of the NACA 0010 baseline airfoil obtained by XFOIL code and ANSYS/CFX at a 0-degree angle of attack

2.2.5 Mesh convergence study on RAF-19 airfoil

To do the mesh convergence study on the RAF-19 baseline airfoil, three models of (G_0 , G_1 and G_2) were used. Each model had 1.6 times the number of elements compare to the previous coarser mesh size and the results are compared at 6-degree angle of attack, shown in Table 2.9. The mesh convergence study was done by reducing the mesh size in the most inside rectangle around the airfoil shown on Figure 2.5. As shown in Table 2.9, by increasing the number of elements from $G_2 = 716296$ to $G_1 = 1146510$ less than 1% change are observed in C_L value and around 1.02% change are observed in C_D values.

Table 2.9 Mesh convergence study on RAF-19 baseline airfoil

	G_3	G_2	G_1
Number of elements	470591	716296	1146510
C_L	1.365	1.37009	1.36989
C_D	0.031099	0.030316	0.0300086

As a result, the G₂ model with 716296 elements were chosen as the mesh independent model for the baseline airfoil. The same mesh setting was used to analyze the other modified airfoils and the number of elements for the modified airfoils are hence increased based on their wavelength size and geometrical shape. For example, for A6W21 airfoil which had the double wavelength size of the baseline airfoil, the number of elements become almost double or 1581031. The number of elements used to analyze each airfoil model are shown on Table 2.10.

Table 2.10 Number of elements used in RAF-19 modified airfoils

Airfoil	Number of elements
A3W11	820304
A6W11	1073457
A6W21	1581031
A6W43	2839872
A6W86	5578947
A11W43	3155428

The uncertainty resulting from the discretization in the computations were estimated using the procedure introduced by (Celik et al., 2008) which is based on Richardson extrapolation. The drag coefficient was chosen as the key parameter for this estimation. The grids, G₃, G₂ and G₁ were used for the uncertainty calculation which corresponds to the mesh refinement factor (r) of 1.15 and 1.17 between the mesh pairs respectively. The apparent order P of the method were solved as $P= 7.131228802$ using the fixed-point iteration. As a result, the approximated relative error, and fine-grid convergence index were calculated as follows and the relative error of 1.02% and the fine- grid convergence index of 0.62% are reported for the computations done on high-cambered RAF-19 airfoil.

$$e_a^{21} = \left| \frac{Cd1 - Cd 2}{Cd1} \right| = 0.01024373 \quad (2.17)$$

$$GCI_{fine}^{21} = \frac{1.25 * e_a^{21}}{r_{21}^p - 1} = 0.0062184 \quad (2.18)$$

2.2.6 Baseline RAF-19 airfoil Validation

Since there is no recent experimental analysis on the RAF-19 airfoil, the validation of the results is done by comparing the computational results with the results obtained by the XFOIL (XFLR5) (Drela, 2000) code at $Re = 2.5 \times 10^5$. To run the XFOIL (XFLR5) code, between 250 to 300 panels were used, the analysis type was set to type 1 and NCrit was set to the default value of 9. Different turbulence modeling was tested in Ansys/CFX. For example Figure 2.9 and Figure 2.10 are showing the Ansys/CFX results obtained using Shear Stress Transport (SST) and $k-\varepsilon$ turbulence modeling and the comparison of their results with the data obtained by XFOIL code respectively. As can be seen, closer agreement of the results with the XFOIL code in both lift and drag coefficients is observed using the $k-\varepsilon$ turbulence modeling. As a result, this turbulence model is used for the continuation of this study.

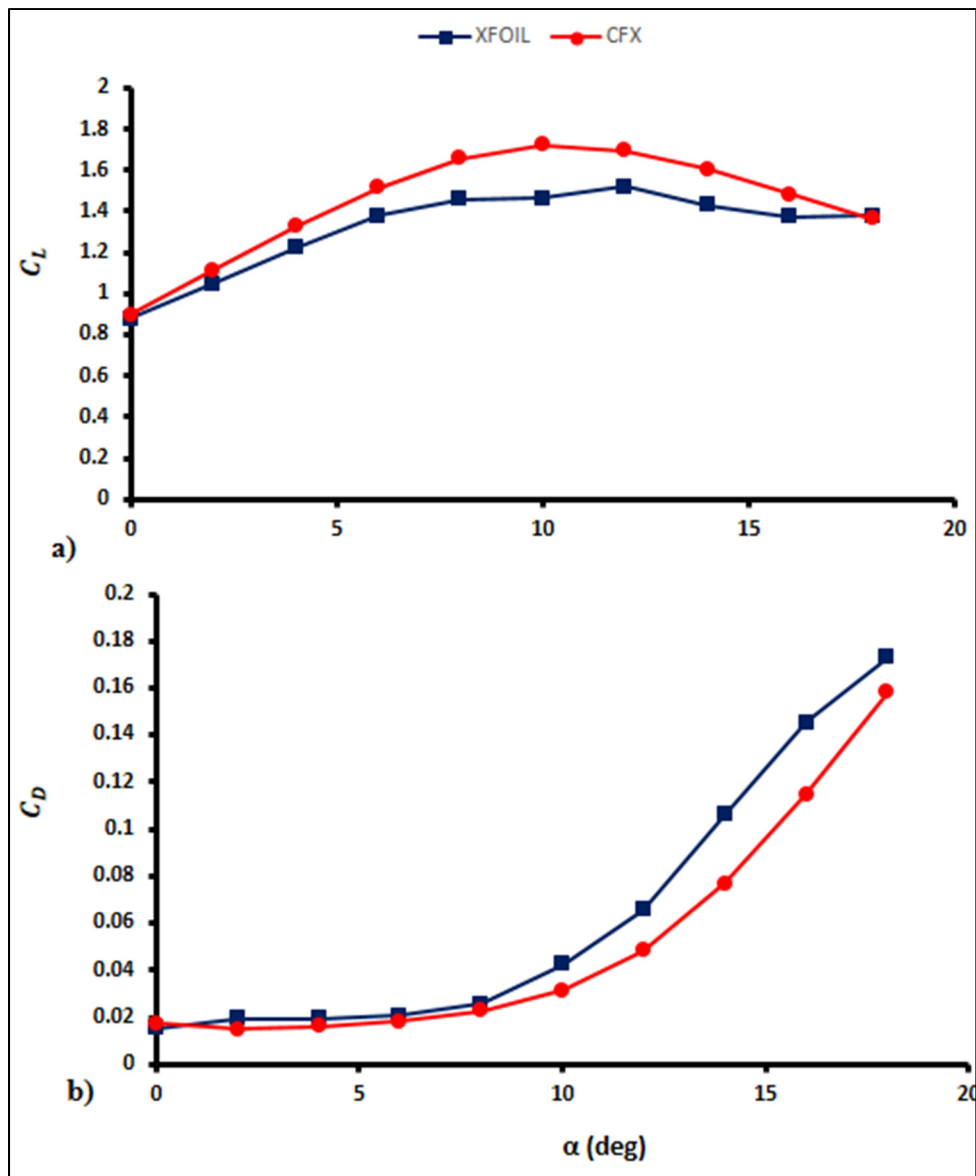


Figure 2.9 Comparison of calculated lift (a) and drag (b) coefficients of RAF-19 baseline airfoil using SST turbulence modeling and XFOIL results

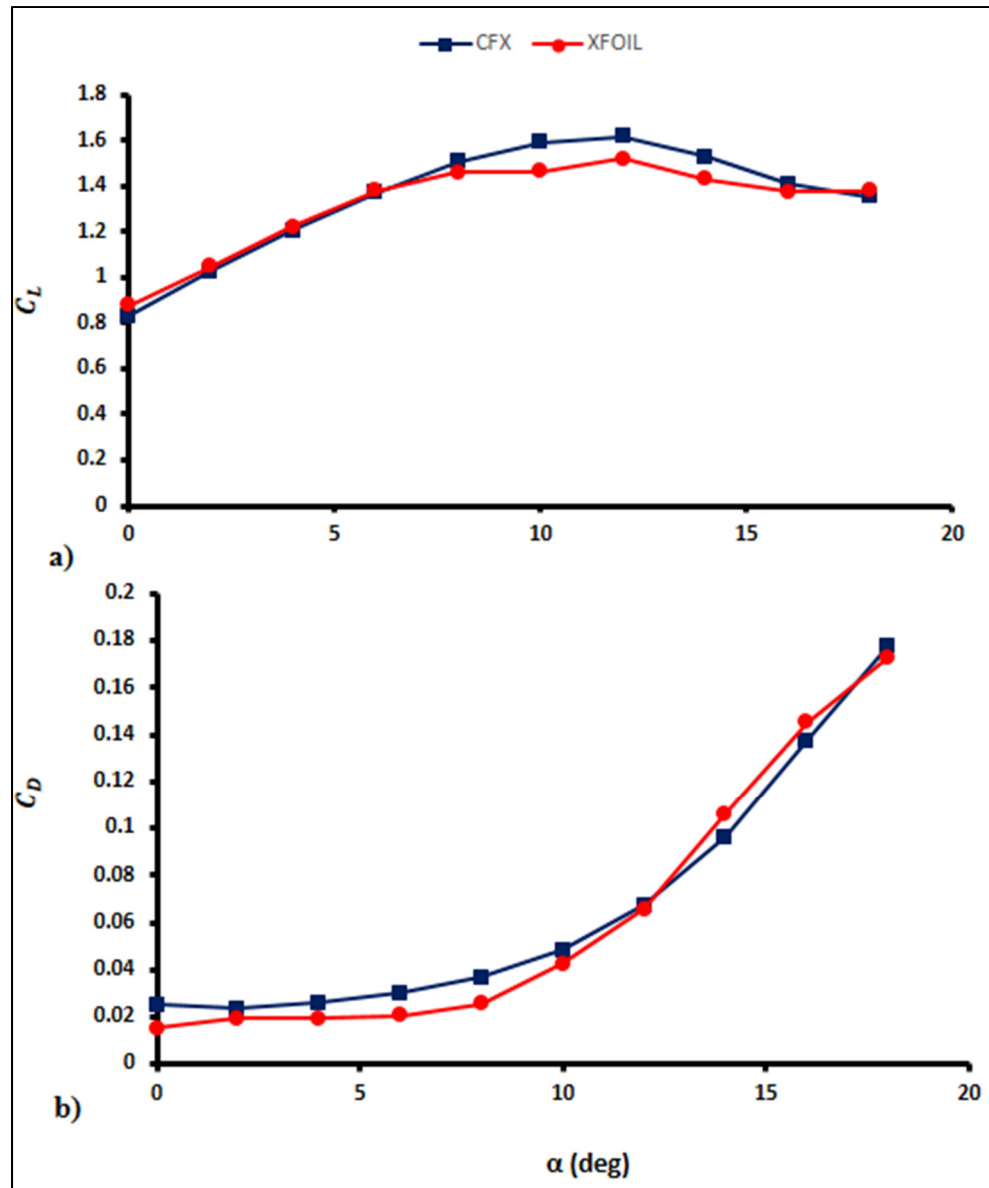


Figure 2.10 Comparison of calculated lift (a) and drag (b) coefficients of RAF-19 baseline airfoil using K- ϵ turbulence modeling and XFOIL results

To have a more localized validation of the results, the pressure coefficients on the suction side of the baseline RAF-19 airfoil at chordwise positions of 0.2, 0.4, 0.6, and 0.8, were derived by both the XFOIL code and the CFX software and the results were compared. For example, Figure 2.11 shows the comparison of pressure coefficients at 4- and 6-degree angles of attack respectively which indicates good agreement for the pressure coefficient results.

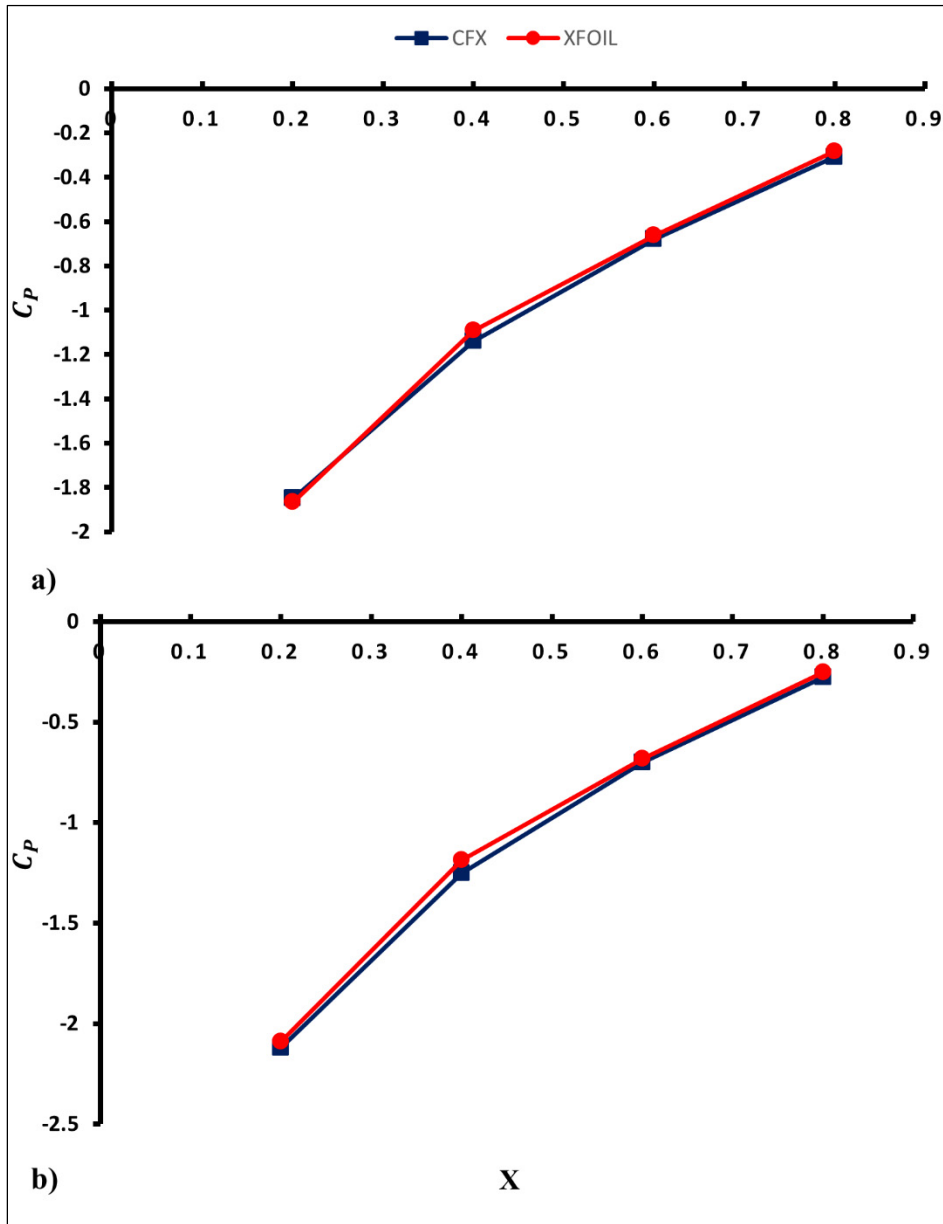


Figure 2.11 Comparison of the CFX and XFOIL pressure coefficients on the suction side of the RAF-19 baseline airfoil at 4 (a) and 6 (b) degree angle of attack respectively

Now that the mesh convergence study is done and the results on the baseline airfoils in case of lift, drag, and pressure coefficients are validated, the effect of leading-edge tubercles on both airfoils can be discussed.

The effect of leading-edge tubercles on symmetric NACA 0010 airfoil is first discussed in chapter 3. After that in chapter 4, the comparison between the effects of leading-edge tubercles on high cambered RAF-19 airfoil and symmetric NACA 0010 airfoil is presented.

The analysis on the modified NACA 0010 airfoils is done until 24 degrees. The steady-state analysis is done at 0, 2, 4, 6, and 8 degrees of angle of attack and the U-RANS analysis is performed at 12, 16, 20, and 24 degrees of angle of attack. The U-RANS analysis was performed at higher angles of attack due to the unsteadiness that occurs as a result of the interaction of the streamwise vortices (discussed in chapter 3).

On the modified RAF-19 airfoils, to reduce the computational cost, the analysis is performed until 16 degrees of angle of attack. Thus, the steady-state analysis is done at angles of attack of 0, 2, 4, 6, 8, 10, and 11 degrees and the U-RANS analysis is performed at 12, and 16 degrees of angle of attack.

CHAPTER 3

EFFECT OF LEADING-EDGE TUBERCLES ON SYMMETRIC AIRFOIL

In this chapter, the effect of amplitude, wavelength, and amplitude to wavelength ratio sizes of tubercles on the integral quantities of lift and drag coefficients of the NACA 0010 modified airfoils is first discussed. After that in the subsequent sections, the effect of streamwise vortices, their convergence, and the effect of amplitude and wavelength sizes of the tubercles on the circulation and interaction of the streamwise vortices will be explained to justify the differences observed in the integral quantities results of the modified airfoils.

3.1 Integral quantities

In this section, the effect of tubercles' geometrical parameters, such as the amplitude, wavelength, and amplitude to wavelength ratio, on the integral quantities of lift and drag coefficients generated by the modified airfoils is discussed.

3.1.1 The effect of the amplitude of tubercles on integral quantities

In general, tubercles cause a reduction in the pre-stall lift coefficient while increasing the post-stall lift coefficient of the modified NACA 0010 airfoils, which is a similar trend to other research done on symmetric airfoils, such as the research of Hansen *et al.* (2011) and Johari *et al.* (2007).

To analyze the effect of amplitude of the tubercles on lift and drag coefficients, two sets of results were compared, as shown in Figure 3.1 and Figure 3.2. In the first set of results shown in Figure 3.1, the lift coefficient results show that by reducing the amplitude of tubercles, the C_{L_max} and lift coefficient at pre-stall angles of attack increase, and by increasing the amplitude of the tubercles, the pre-stall lift coefficient is reduced while the post-stall lift coefficient

improves. Increasing the amplitude of the tubercles also results in smoother stall characteristics.

In the second set of results shown in Figure 3.2, decreasing the amplitude of the tubercles from A6W11 to A3W11 results in increasing lift coefficients at both pre-stall and post-stall angles of attack.

The drag coefficient results on both sets of results show that generally smaller amplitude airfoils generate a lower amount of drag coefficient.

3.1.2 The effect of the wavelength of tubercles on integral quantities

The effect of the wavelength of tubercles on lift and drag coefficients of the modified airfoils is illustrated in Figure 3.3. It can be seen from Figure 3.3, that by reducing the wavelength of the tubercles, the lift coefficient generally decreases at both pre-and post-stall angles of attack. The drag coefficient results show that the modified airfoils generate a higher amount of drag coefficients in comparison with the baseline airfoil except at 24 degrees. At 24 degrees, the modified airfoils generate a lower drag coefficient in comparison with the baseline airfoil. The results show that generally by increasing the wavelength of the tubercles, the drag coefficients increase.

3.1.3 The effect of the amplitude to wavelength ratio of tubercles on integral quantities

The modified airfoils with close values of amplitude to wavelength ratio are compared in Figure 3.4. It can be seen from the results illustrated in Figure 3.4, that the C_{L_max} is increased by reducing the amplitude and wavelength of the tubercles. For example, on the A11W43 airfoil with the largest amplitude and wavelength size of tubercles, C_{L_max} is the smallest. Meanwhile, it can be seen that the post-stall lift generation is increased by increasing the amplitude and wavelength of the tubercles and the A11W43 airfoil also acquires a higher post-stall lift coefficient and smoother stall characteristics in comparison with the other two

modified airfoils with smaller amplitude and wavelength of tubercles. Results shown in Figure 3.4, also illustrate that the drag coefficient is increased by increasing the amplitude and wavelength of the tubercles.

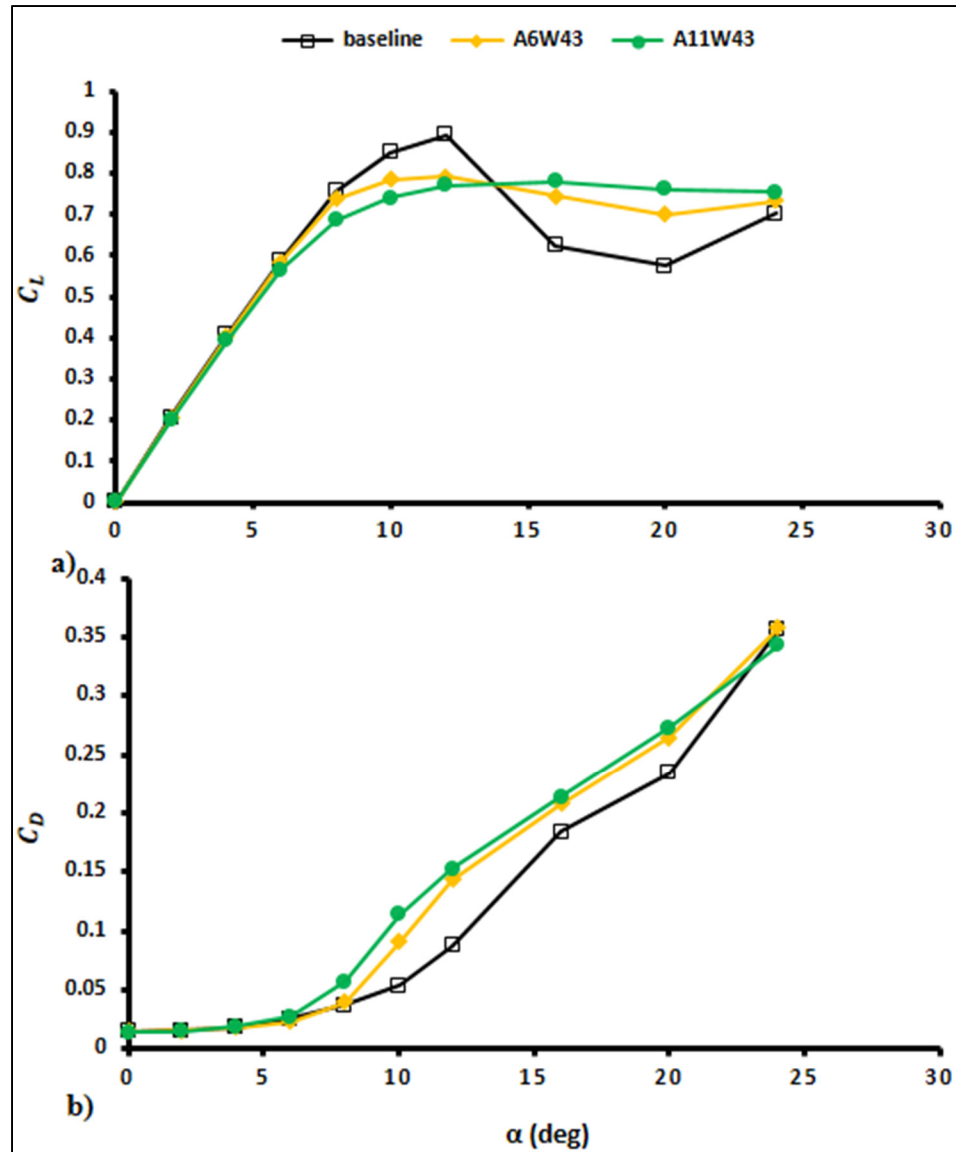


Figure 3.1 Analyzing the effect of the amplitude of tubercles on the lift (a) and drag (b) coefficients of the NACA 001 modified airfoils (first set)

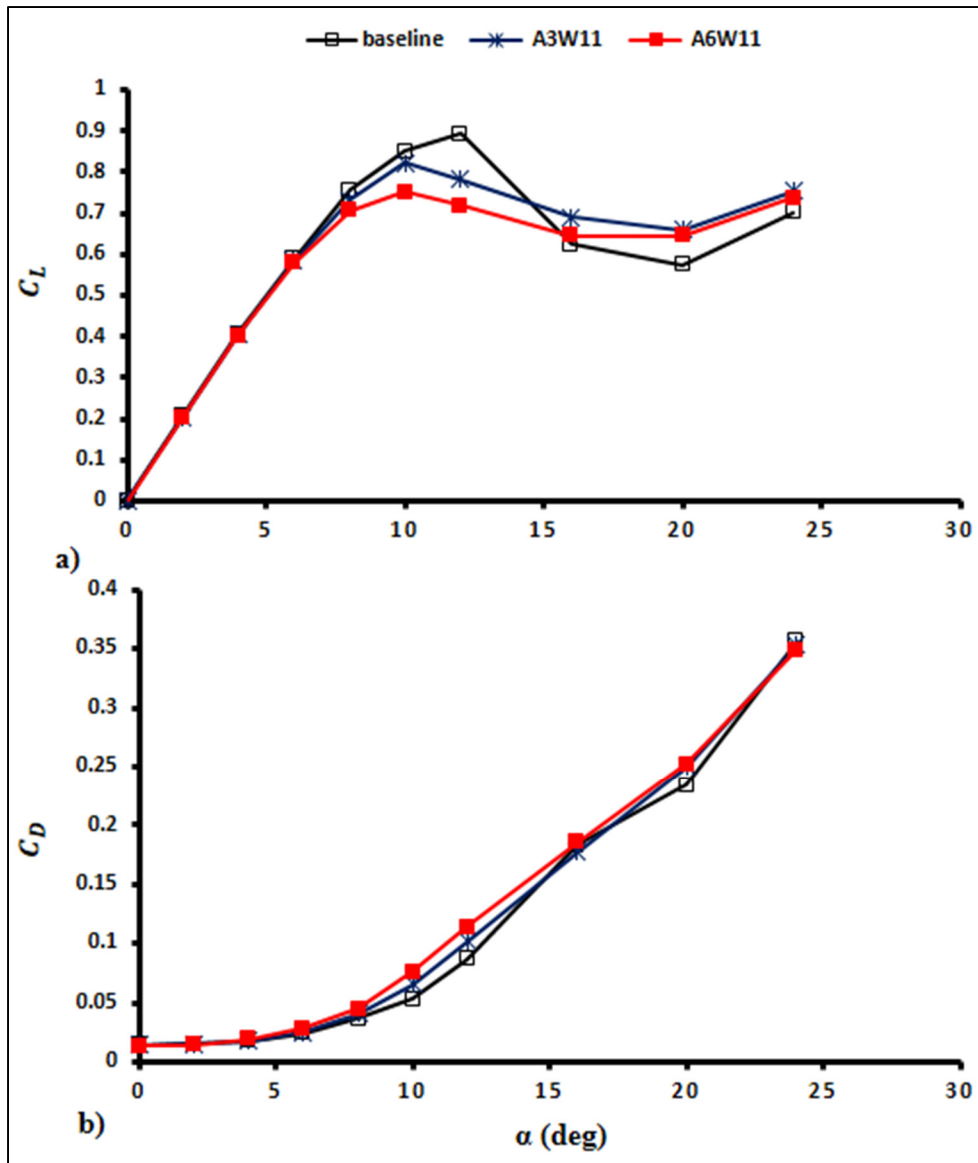


Figure 3.2 Analyzing the effect of the amplitude of tubercles on the lift (a) and drag (b) coefficients of the NACA 001 modified airfoils (second set)

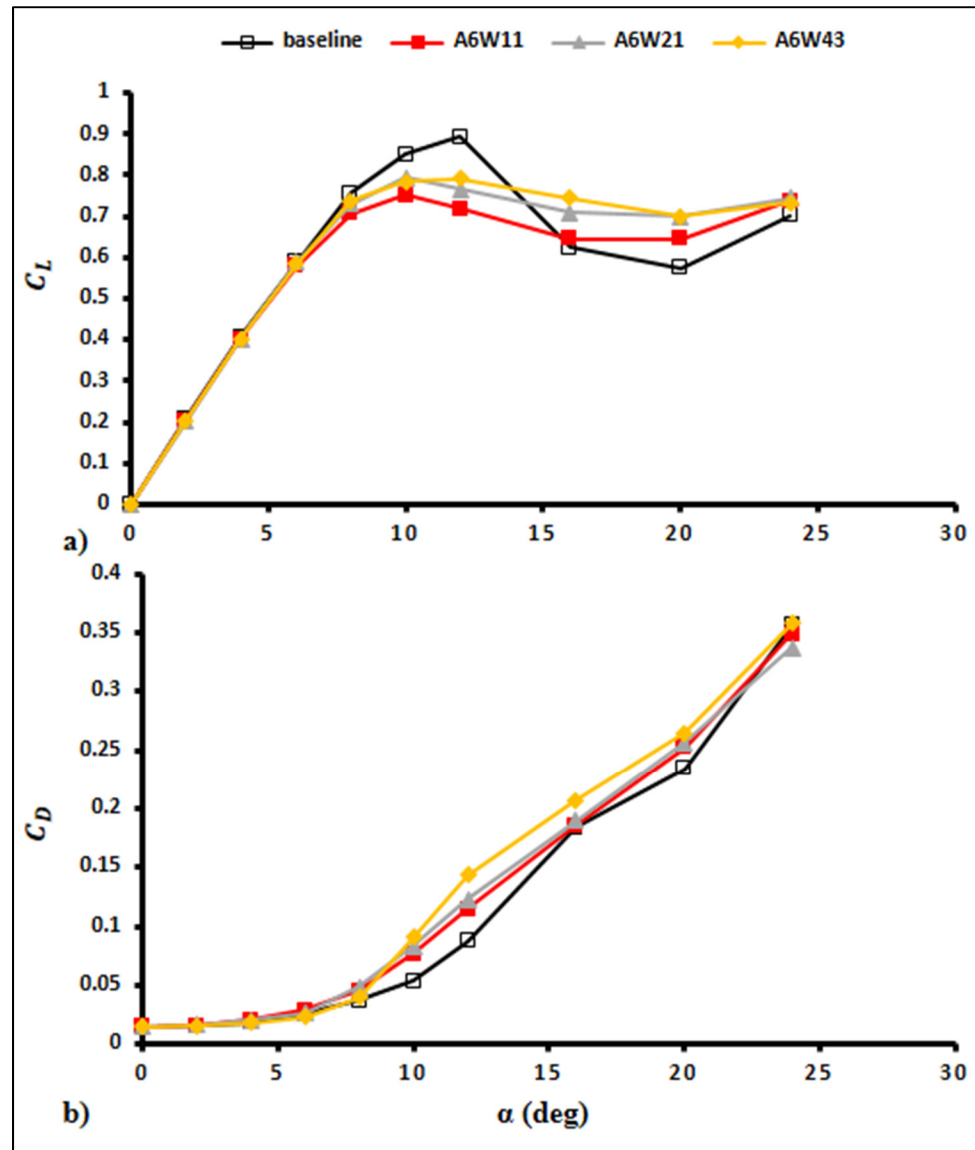


Figure 3.3 Analyzing the effect of the wavelength of tubercles on the lift (a) and drag (b) coefficients of the NACA 001 modified airfoils

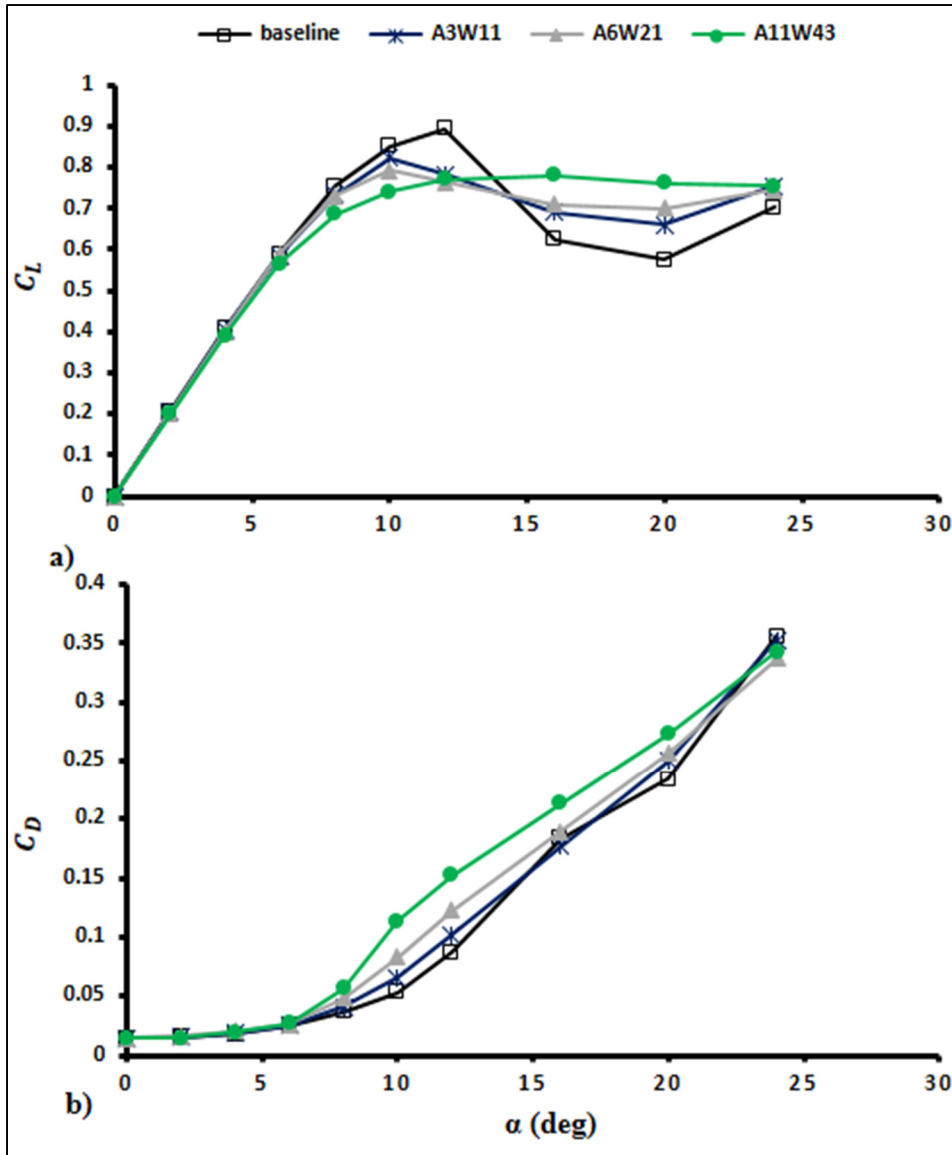


Figure 3.4 Analyzing the effect of the amplitude to wavelength ratio of tubercles on the lift (a) and drag (b) coefficients of the NACA 001 modified airfoils

In general, in this section, we noticed that tubercles reduce the pre-stall lift coefficient while increasing the post-stall lift coefficient, which is the same trend observed in previous research done on symmetric airfoils (Hansen et al., 2011; Johari et al., 2007). The results also show that by reducing the wavelength of the tubercles, the lift generated by the airfoils is reduced. Meanwhile, comparing the modified airfoils with close values of amplitude to wavelength ratio

has shown that by increasing the amplitude and wavelength of tubercles, the lift coefficient reduces at pre-stall angles of attack while at post-stall angles of attack the lift coefficient is increased by increasing the amplitude and wavelength of tubercles. Results also showed that the drag coefficient is increased by increasing the amplitude and wavelength, of tubercles.

3.2 The streamwise vortices

In the above section, the effect of amplitude, wavelength, and amplitude to wavelength ratio sizes of the leading-edge tubercles on the integral quantities of the lift and drag coefficient have been analyzed. To understand the effect of amplitude and wavelength sizes of tubercles on the lift and drag coefficient, the behavior and strength of the streamwise vortices on the modified airfoils should be discussed first.

3.2.1 The convergence and interaction of the stream-wise vortices

The streamwise vortices on the A11W43 airfoil at 0, 4, 8, 10, 12, 16, 20, and 24 degrees of angle of attack are illustrated in Figure 3.5. The solid arrow line shows the flow direction relative to the dashed line, which indicates the modified airfoils chord line. It can be seen from Figure 3.5 that the maximum value of the streamwise vortices is generally increased by increasing the angle of attack. This figure also indicates another important general trend of the streamwise vortices that by increasing the angle of attack, the two neighboring, counter-rotating streamwise vortices at each chordwise location are converging towards each other while moving along the chord, until they start to interact and annihilate each other. After the vortex annihilation, the flow completely separates from the surface of the airfoil. This separation point moves towards the leading-edge by increasing the angle of attack. This trend is observed on all the modified airfoils, such as on the A6W11 airfoil, where its relative figures are illustrated in Figure 3.6. It should be noted that to have a better comparison of the streamwise vorticity figures, the vortices values in some figures of this research work are standardized. This standardization is done, based on the minimum and maximum values of vorticity, found between all the modified airfoils in angles of attack ranges between $0 < \alpha < 16$

degrees. Thus, the streamwise vortices values are standardized based on the minimum and maximum vorticity values of -98 and 98 respectively.

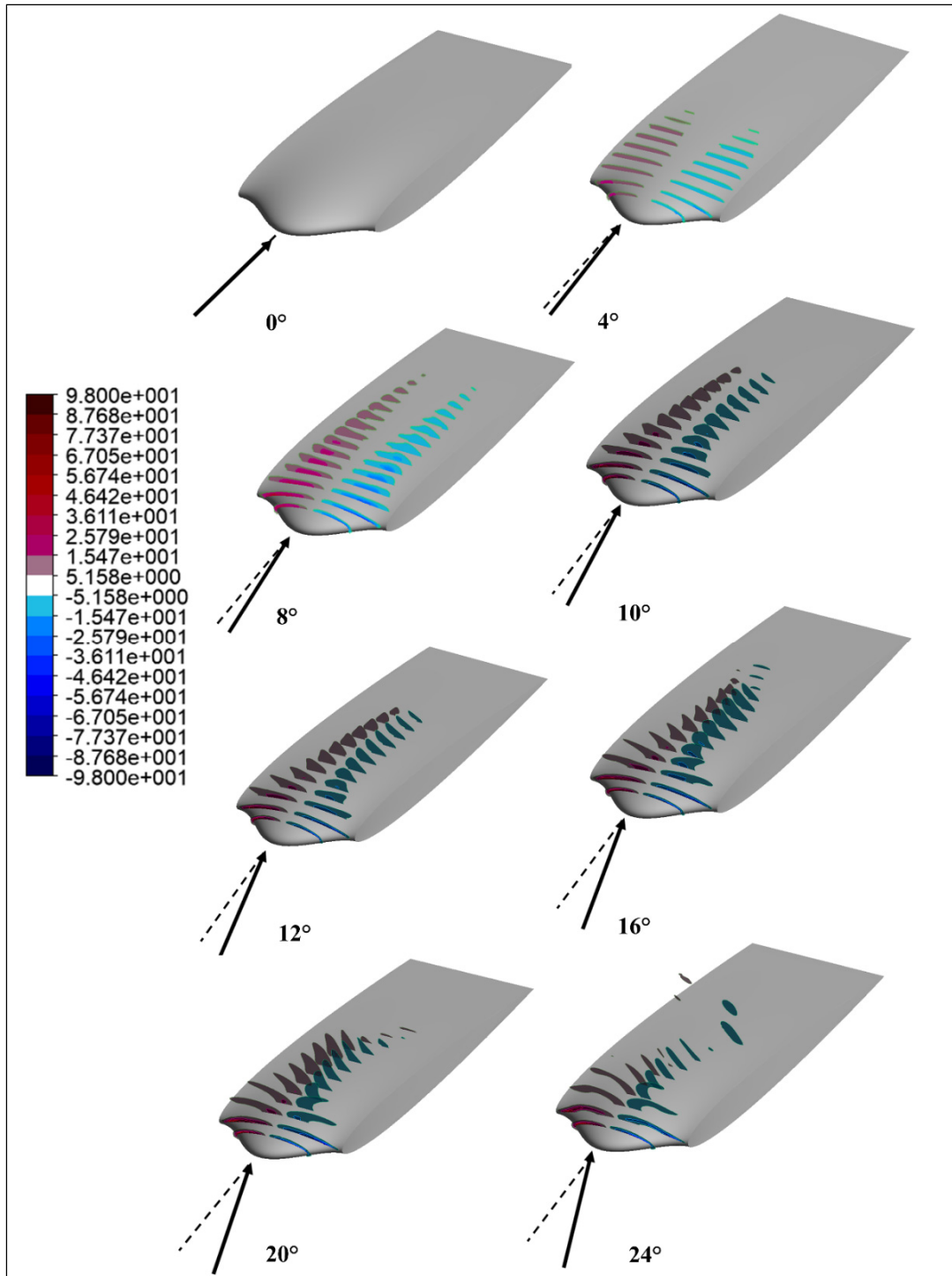


Figure 3.5 Streamwise vortices on NACA 0010_A11W43 airfoil at 0, 4, 8, 10, 12, 16, 20, and 24 degrees of angles of attack

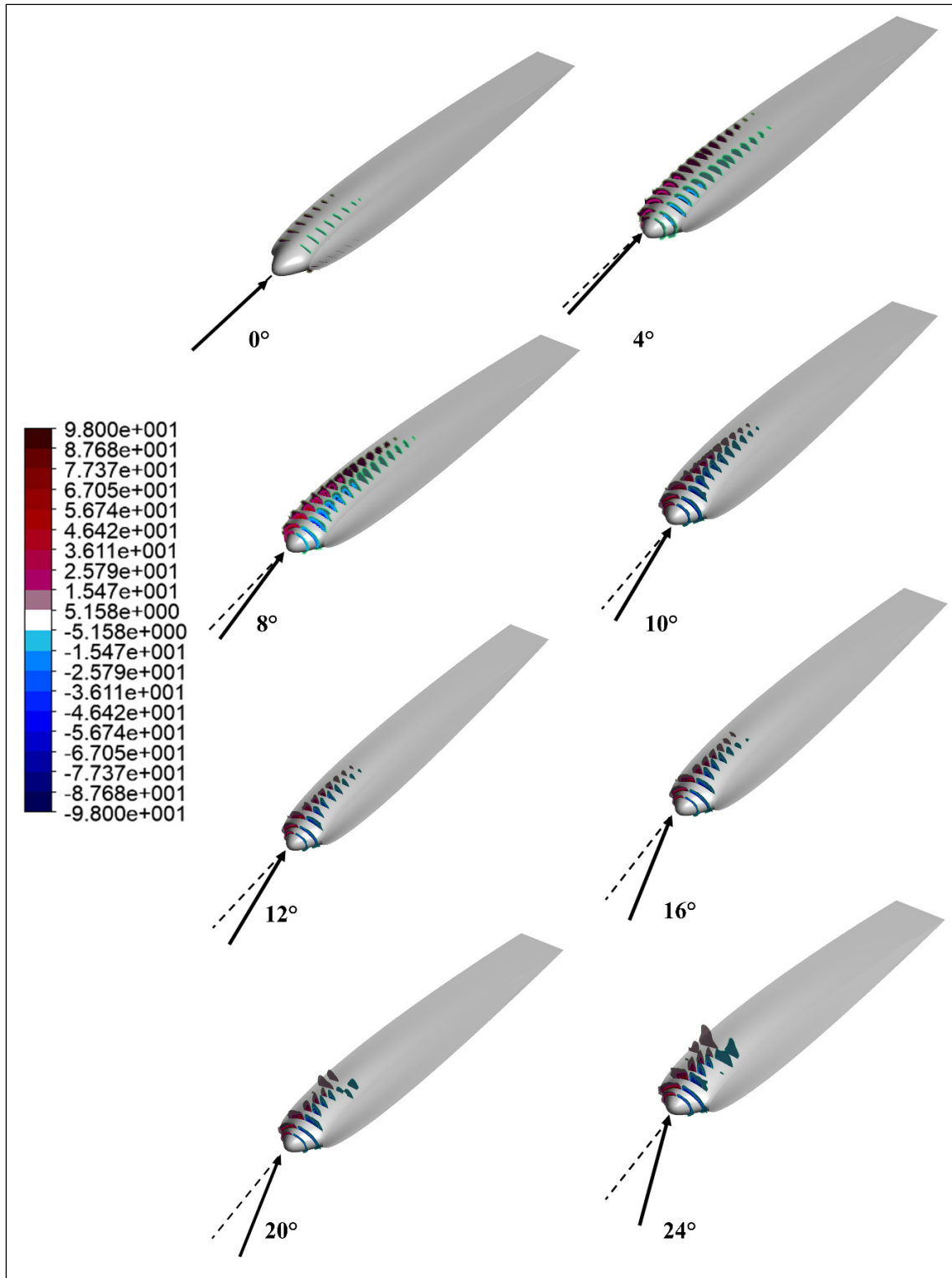


Figure 3.6 Streamwise vortices on NACA 0010_A6W11 airfoil at 0, 4, 8, 10, 12, 16, 20, and 24 degrees of angles of attack

In the next section, the effect of amplitude, wavelength, and the amplitude to wavelength ratio of tubercles on the circulation of the streamwise vortices is analyzed.

3.2.2 Circulation

In this subsection, the effect of amplitude, wavelength, and the amplitude to wavelength ratio of tubercles on the strength of the streamwise vortices is discussed. The strength of a vortex is quantified by its circulation value. To analyze the strength of streamwise vortices on modified airfoils, the circulation of these vortices is calculated using Eq. (3.1). In Eq. (3.1), $\vec{\omega}$ is the streamwise vorticity vector, \vec{n} is the vector normal to the surface s , ds is the element of surface area and Γ is the circulation. The calculations are done at a slice of $0.05C$ (5% of the mean chord length) at angles of attack of 0, 4, 8, 12, 16, 20 and 24 degrees from the upper surface of the modified airfoils to a distance of 0.5 above it. The calculation was done to a distance of 0.5 to make sure that all the streamwise vortices generated by the tubercles are included in the calculations.

$$\Gamma = \int_s \vec{\omega} \cdot \vec{n} ds \quad (3.1)$$

To be able to compare the circulation of streamwise vortices of modified airfoils, the circulation values are calculated per unit span of the airfoils. Thus, the circulations calculated on each airfoil are divided by its wavelength size. For example, the circulation of the A6W43 airfoil is divided by 0.43, and the circulation of the A3W11 airfoil is divided by 0.11.

The circulation values are all illustrated in Figure 3.7. Meanwhile Figure 3.8_Figure 3.11 illustrate the effect of amplitude, wavelength, and amplitude to wavelength ratio sizes of tubercles on the circulation values. The results of the effect of tubercles' amplitude sizes on the circulation values illustrated in Figure 3.8 and Figure 3.9 show that by increasing/reducing the amplitude of the tubercles, the circulation of the streamwise vortices is increased/decreased. Meanwhile, the results regarding the effect of tubercles' wavelength sizes illustrated in Figure 3.10, show that by reducing/increasing the wavelength of the tubercles, the circulation values are increased/decreased. Finally, by comparing the circulations results of the airfoils with close

values of tubercles' amplitude to wavelength ratio illustrated in Figure 3.11, it can be seen that by reducing the amplitude and wavelength of tubercles', the circulation of the streamwise vortices decreased. Although, up until the 12-degree angle of attack, the A3W11 and A6W21 airfoils show almost the same values of circulation, but it can be observed from the results that the airfoils with close values of amplitude to wavelength ratio do not generate exactly the same values of circulation.

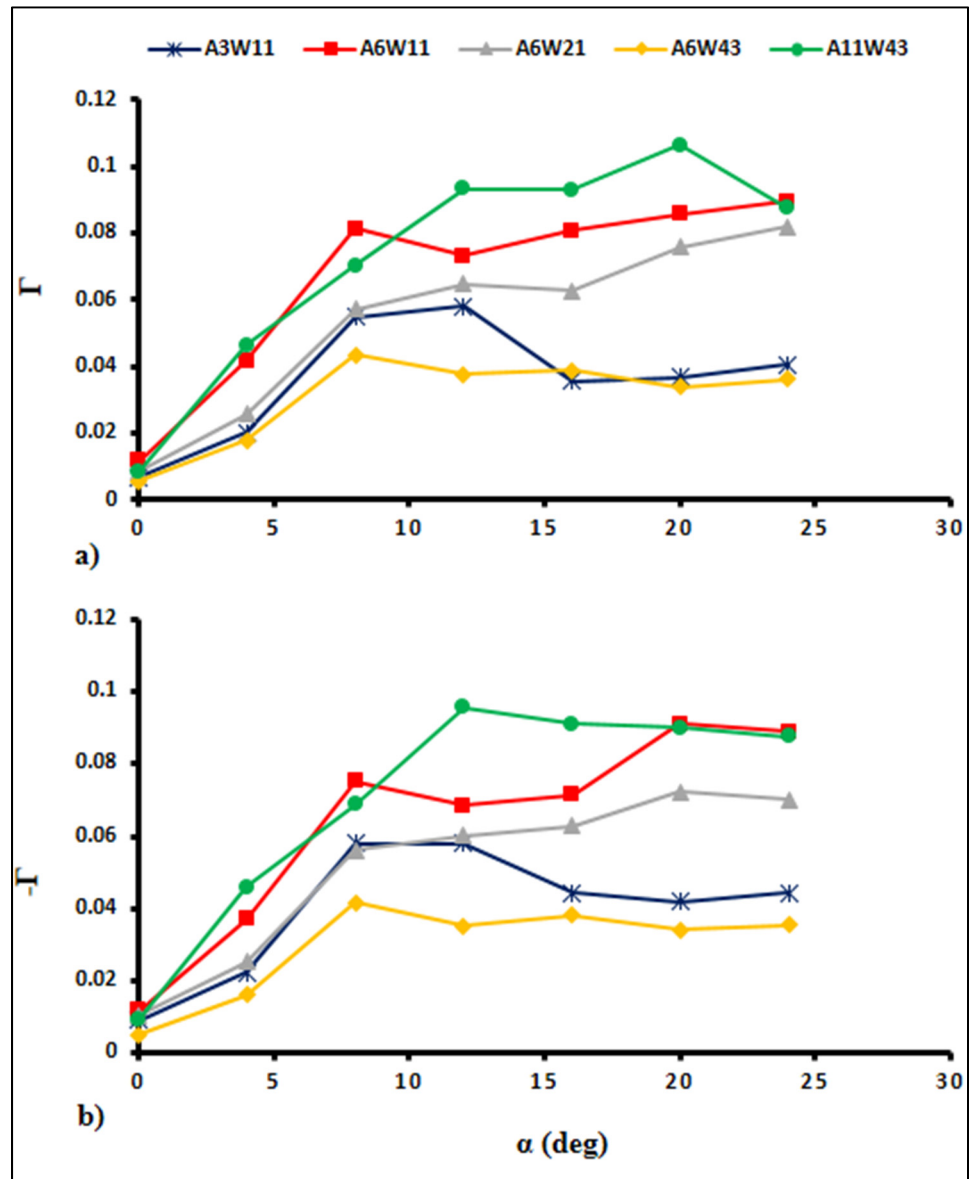


Figure 3.7 Positive (a) and negative (b) circulation values of all NACA0010 Modified airfoils

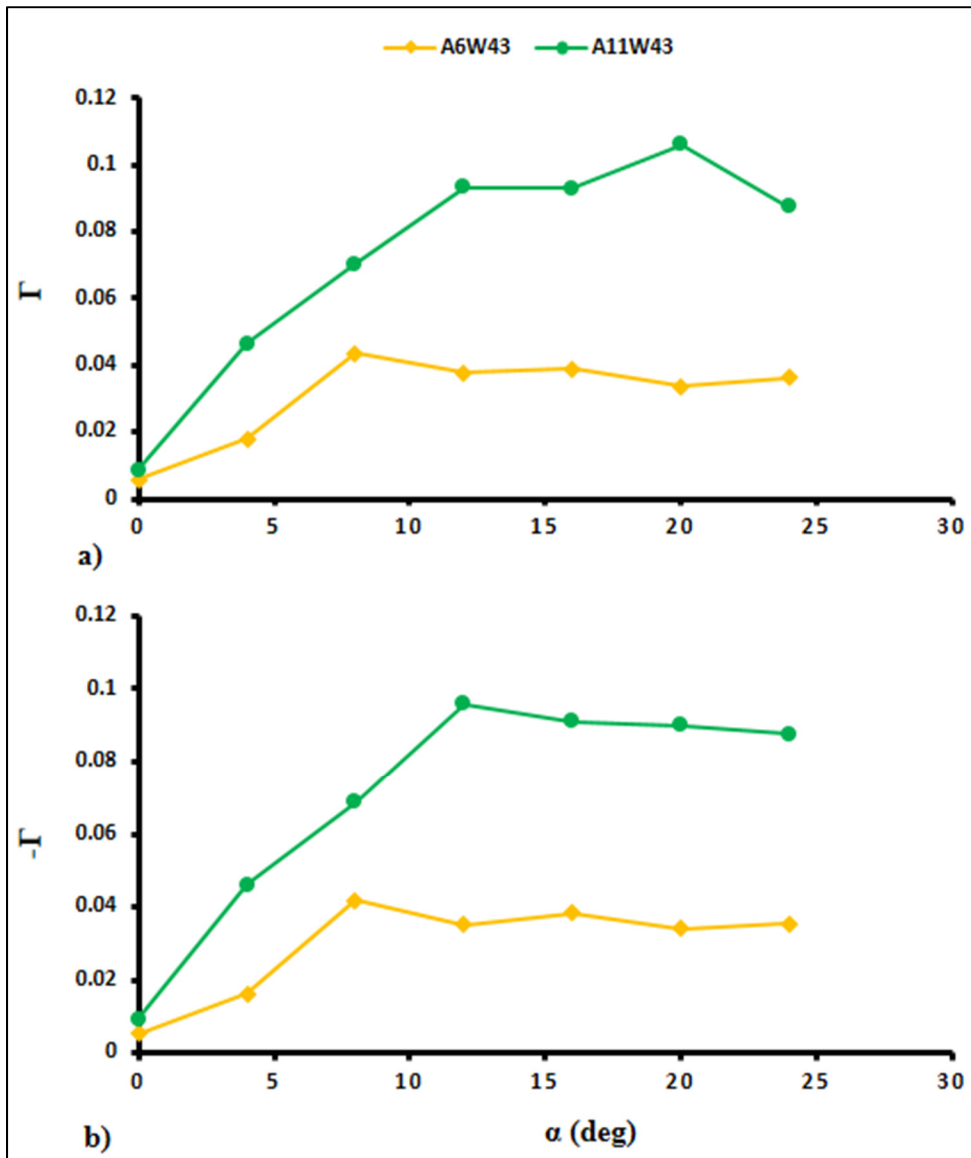


Figure 3.8 Effect of the amplitude of tubercles on positive (a) and negative (b) circulation values of NACA0010 Modified airfoils (first set)

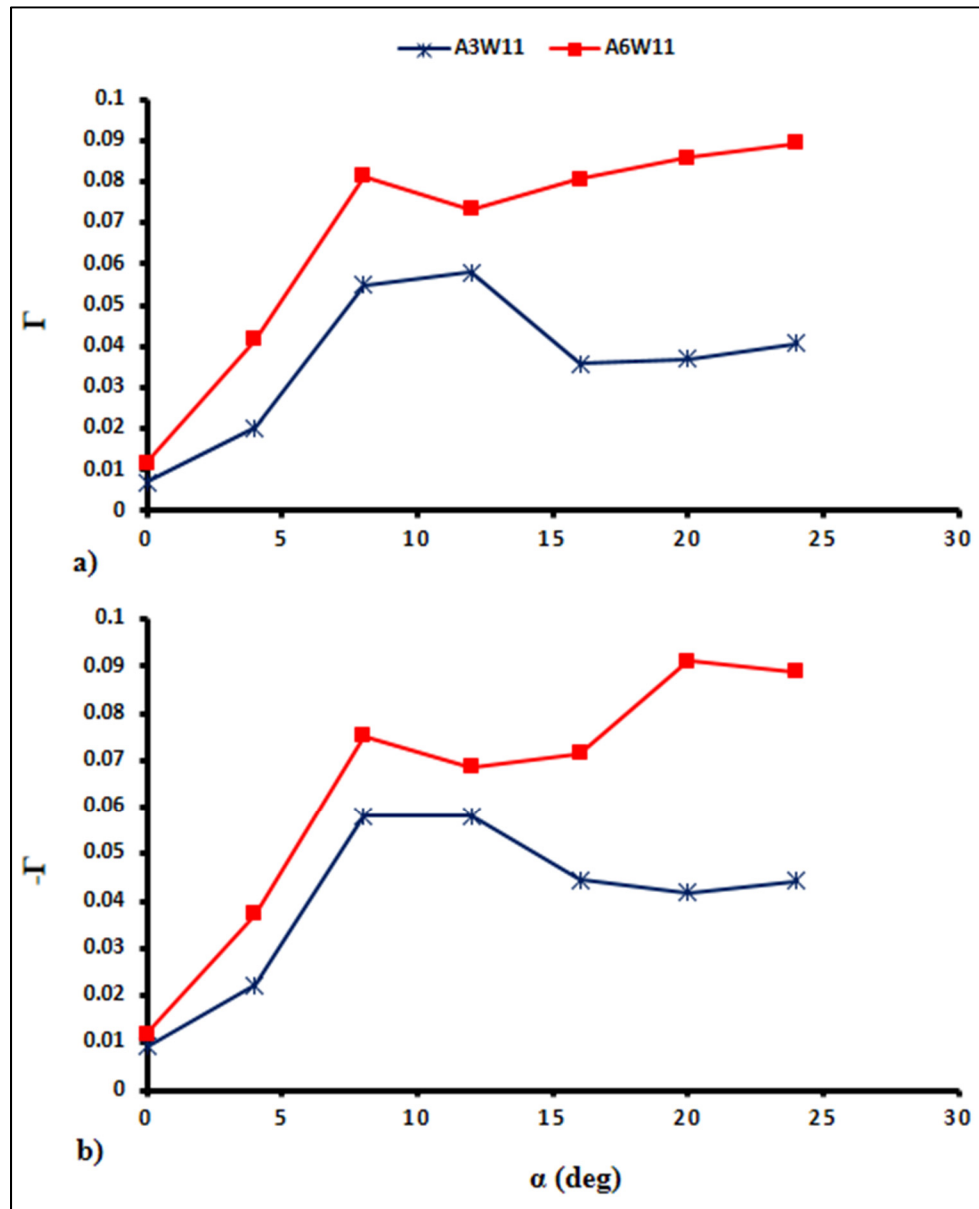


Figure 3.9 Effect of the amplitude of tubercles on positive (a) and negative (b) circulation values of NACA0010 Modified airfoils (second set)

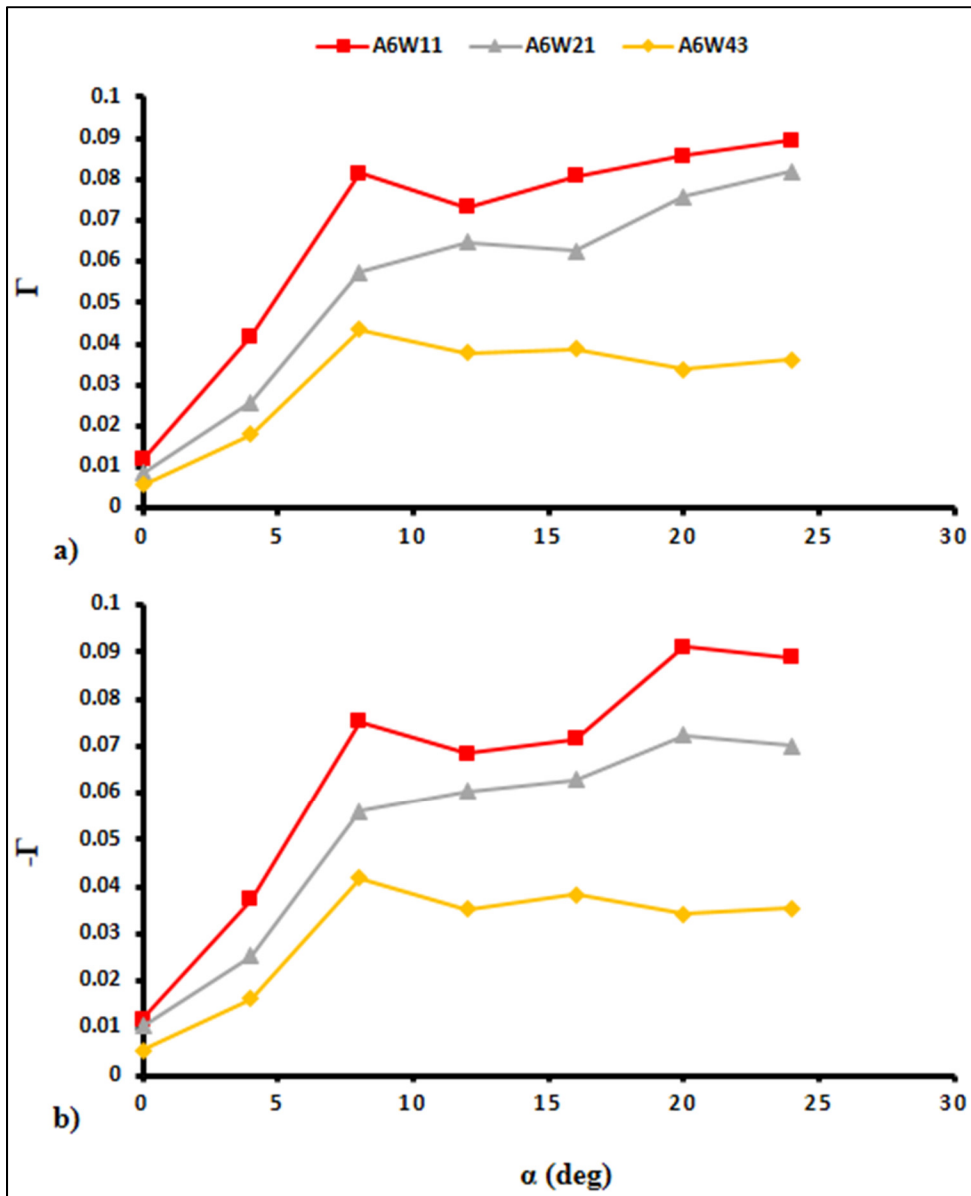


Figure 3.10 Effect of the wavelength of tubercles on positive (a) and negative (b) circulation values of NACA0010 Modified airfoils

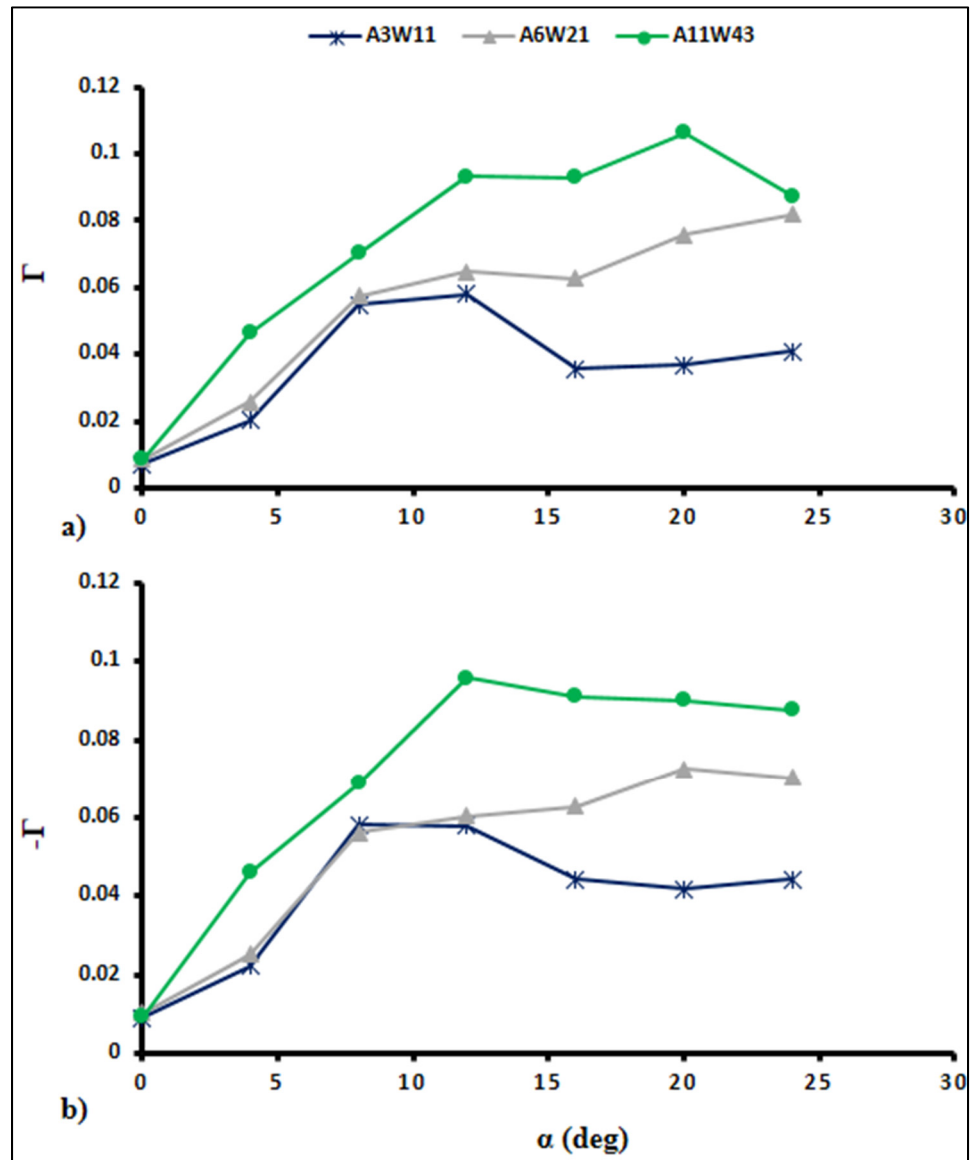


Figure 3.11 Effect of the amplitude to wavelength ratio of tubercles on positive (a) and negative (b) circulation values of NACA0010 Modified airfoils

In general, a comparison of the results shows that the circulation of the streamwise vortices on the airfoils with leading-edge tubercles is mostly the function of A/C and W/C, and the

circulation of the streamwise vortices is increased by reducing the wavelength and increasing the amplitude of the tubercles.

3.3 The effect of streamwise vortices on integral quantities

In the previous section, the effect of tubercles' geometrical parameters on the strength of the streamwise vortices was analyzed. Now the relation between the circulation and interaction of the streamwise vortices on the aerodynamic performance of the modified airfoils can be discussed more in detail. All the lift and drag coefficient results obtained in this research on the baseline and modified airfoils are compared in Figure 3.12. Thus, to understand the effect of leading-edge tubercles and the streamwise vortices on the aerodynamic performance of the modified airfoils at both pre-and post-stall angles of attack, two angles of attack of 10 and 16-degrees are chosen to do the comparison of the results, which will be discussed in the following sections.

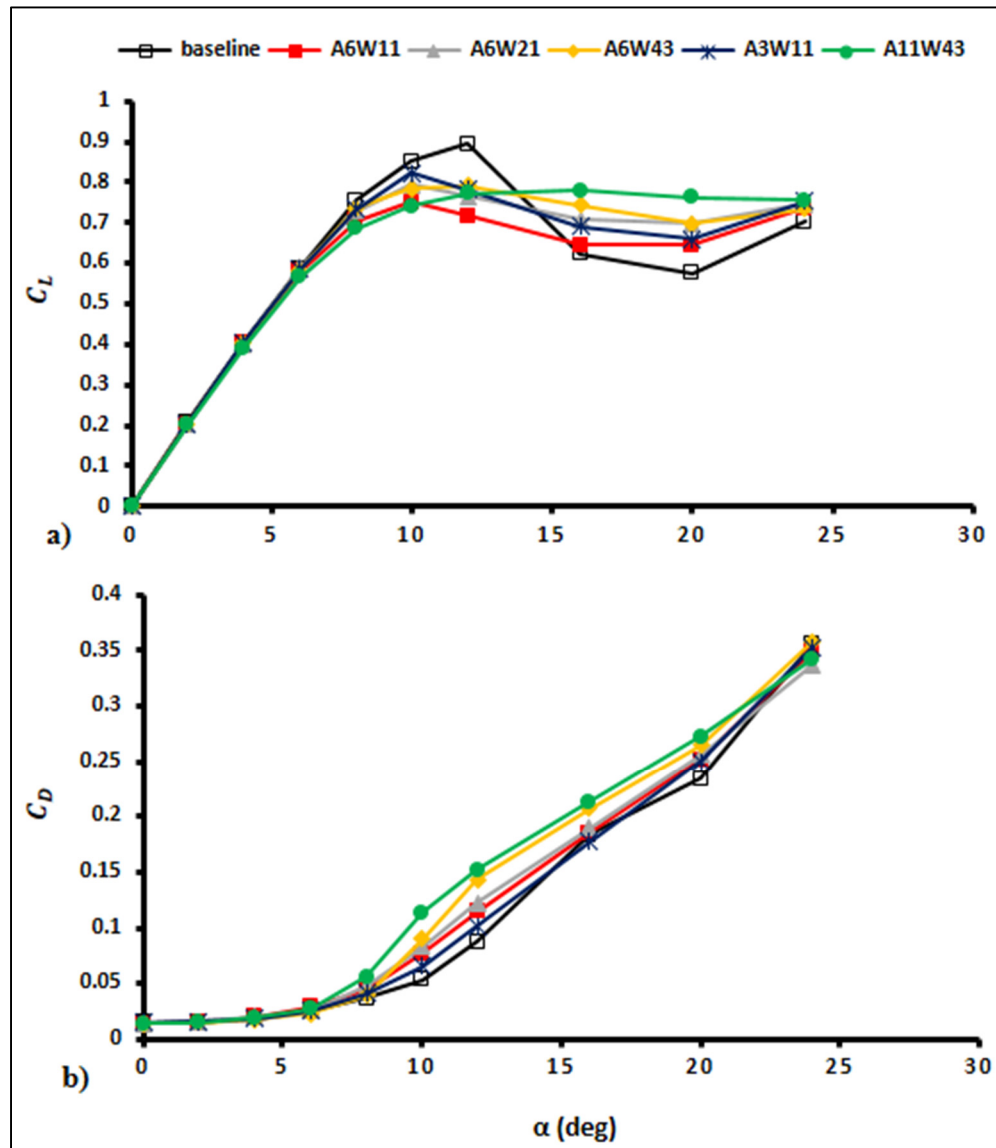


Figure 3.12 Lift (a) and drag (b) coefficient results for all the NACA 0010 modified airfoils

3.3.1 The effect of the streamwise vortices at post-stall angles of attack of 16-degrees

The lift coefficient results depicted in Figure 3.12 show that A11W43, A6W43, A6W21, A3W11, and A6W11 airfoils generate the highest lift coefficients at a 16-degree angle of attack in turn and the baseline airfoil generates the lowest generated lift coefficient.

To understand the effect of the streamwise vortices at post-stall angles of attack, the streamwise wall shear stresses on the modified airfoils at a 16-degree angle of attack are depicted in Figure 3.13. Meanwhile Figure 3.14 shows the streamwise vortices at a 16-degree angle of attack on all the modified airfoils.

As shown in Figure 3.13, most of the flow on the baseline airfoil upper surface is separated, while streamwise vortices prevent the separation of the flow on the modified airfoils. It is advantageous to define two new parameters of "effective length" and "effective mixing" to analyze the effectiveness of the streamwise vortices in energizing the boundary layer on the suction surface of the modified airfoils. Effective length is defined as the chordwise distance that the streamwise vortices can energize the boundary layer. Effective mixing is defined as the intensity or the extent that those vortices energize the boundary layer, which can be noted by higher values of positive streamwise wall-shear stresses.

The effective length of the streamwise vortices on the modified airfoils at a 16-degree angle of attack is measured and illustrated in Table 3.1. The values of effective length were calculated by dividing the mean chord length of the modified airfoils that are energized by the streamwise vortices (that has positive values of streamwise wall shear stresses) to the mean chord length of the modified airfoils.

As can be seen in Figure 3.13 and Table 3.1, the effective length of the streamwise vortices is decreased by reducing the wavelength, and amplitude of the tubercles. Meanwhile, the effective mixing of the streamwise vortices is increased by reducing the wavelength and increasing the amplitude of the tubercles. The degree of effective mixing can be seen by stronger colors, like darker yellow or orange in Figure 3.13.

The effective length of the streamwise vortices is the largest on the A11W43 and A6W43 airfoils, which show the most attached flow regions until 78% and 70% of the mean-chord-length, respectively. To understand the cause for a larger effective length of the streamwise vortices on larger wavelength airfoils, the behavior of the streamwise vortices formed on the modified airfoils must be analyzed. One important point that is observed in the general behavior of the streamwise vortices, is that by increasing the angle of attack, the two neighboring counter-rotating streamwise vortices converge towards each other while moving along the chord (as discussed in Figure 3.5 and Figure 3.6). After that, they start to interact and hence begin to annihilate each other. The annihilation of the streamwise vortices causes to stop the boundary layer energizing process, resulting in the flow separation afterward. This behavior is observed on all the modified airfoils. On larger wavelength airfoils, however the streamwise vortices are more distanced from each other. Thus, the interaction intensity of their streamwise vortices is less in comparison with the shorter wavelength airfoils. This issue causes the increase in the effective length of these streamwise vortices on larger wavelength airfoils of A6W43 and A11W43.

Circulation calculations, in the previous section, showed that the circulation of the streamwise vortices is enhanced by increasing the amplitude and reducing the wavelength of the tubercles. The augmentation in the strength of streamwise vortices by increasing the amplitude of tubercles, is noticeable by comparing the streamwise vortices on A11W43 with A6W43 airfoils, and A6W11 with A3W11 airfoils in Figure 3.14. Besides, the enhancement in the strength of vortices by reducing the wavelength of the tubercles is noticeable by comparing the vortices on A6W43, A6W21, and A6W11 airfoils in the same figure.

As discussed, the circulation of the counter-rotating streamwise vortices on the A11W43 airfoil, is higher than the A6W43 airfoil, due to its larger amplitude size. As a result, the effective mixing of the boundary layer, is also higher on the A11W43 airfoil, compared with the A6W43 airfoil. Thus, the A11W43 airfoil generates a higher amount of lift coefficient than the A6W43 airfoil.

The other observation in Figure 3.13, is that by decreasing the wavelength of the tubercles, the effective mixing of the boundary layer increase, while the effective length of the streamwise vortices decreases significantly. The increase in the effective mixing of the boundary layer is due to both, an increase in strength as well as, reducing the distancing between the streamwise vortices, by reducing the wavelength of the tubercles. However, reducing the distance between the streamwise vortices increases the intensity of interaction between them. As a result, they annihilate each other faster, and thus, their effective length is reduced significantly which compensates the increase in effective mixing by reducing the wavelength of the tubercles. Consequently, by reducing the wavelength of the tubercles, the lift coefficient values decrease.

Based on Figure 3.13, the increase in drag coefficient by increasing the amplitude, and wavelength of the tubercles can also be discussed. For example, at 16-degree angle of attack, the A6W11 airfoil generates higher drag coefficients than the A3W11 airfoil. This is because the A6W11 airfoil has stronger and larger separated and reversed flow regions behind its trough sections. Besides that, the drag coefficients are higher on larger wavelength airfoils of A6W43 and A11W43 airfoils, compared with the shorter wavelength airfoils. This is also due to their larger separated and reversed flow regions behind their trough sections. These separated and reverse flows, behind the trough regions of the modified airfoils, are possibly generated because of the effect of streamwise vortices, which will be discussed in the next subsection. In addition, because of a larger effective length of the streamwise vortices on larger wavelength airfoils and more flow attachments on their upper-surface, the skin friction drag is higher on these airfoils.

In conclusion, when analyzing the airfoils with leading-edge tubercles, the circulation, and intensity of interaction of the streamwise vortices appear to be the main parameters governing the flow phenomenon.

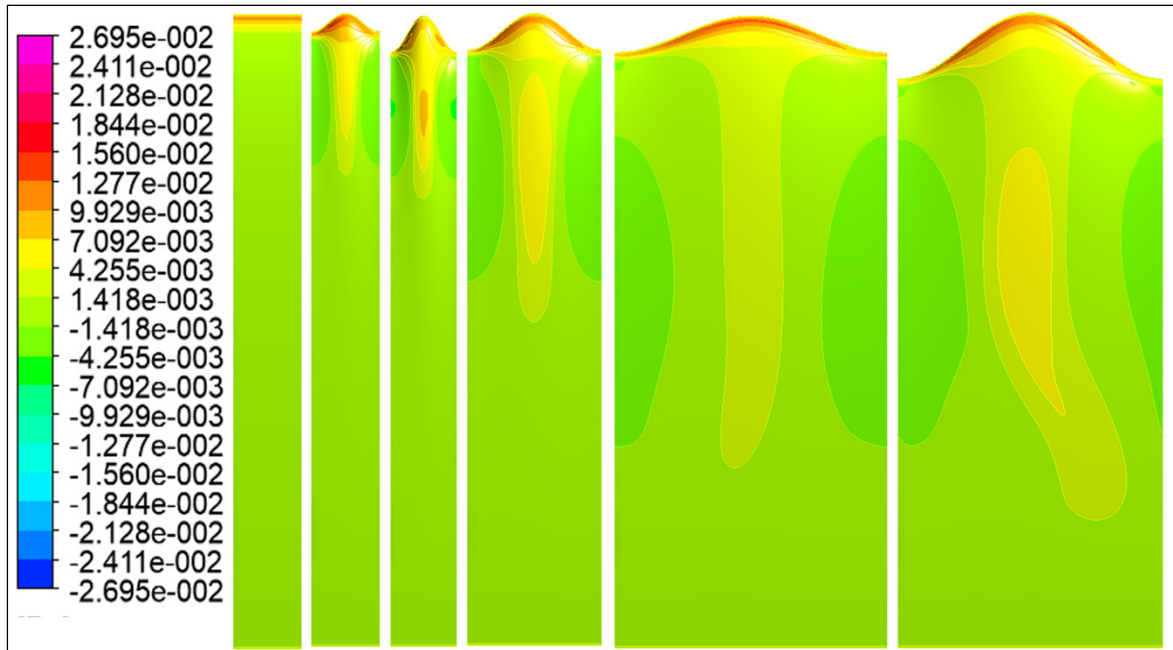


Figure 3.13 Wall shear stresses from left to right on the baseline NACA 0010, A3W11, A6W11, A6W21, A6W43 and A11W43 airfoils at a 16 degree angle of attack

Table 3.1 Effective length of the streamwise vortices on NACA 0010 modified airfoils at a 16 degree AOA

Airfoil Name	A3W11	A6W11	A6W21	A6W43	A11W43
Effective length (% C)	24	27	46	70	78

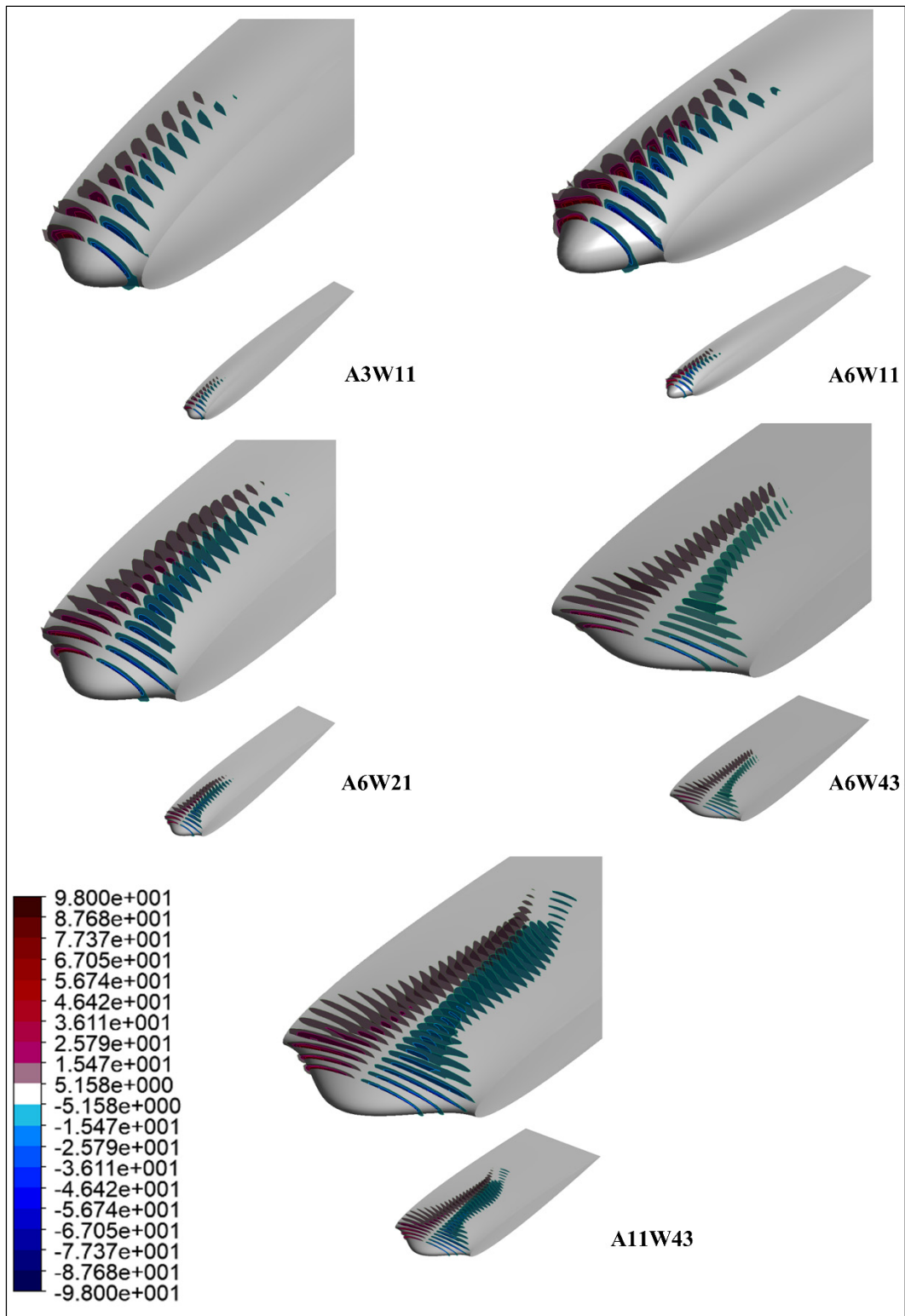


Figure 3.14 Streamwise vortices on the modified NACA 0010 airfoils at a 16-degree angle of attack

3.3.2 Unsteady simulations

As mentioned in the literature review, in the experimental research of Custodio (2012), by increasing the angle of attack, and hence increasing the circulation of the streamwise vortices, the streamwise vortices interaction was occurred which creates a low-frequency unsteadiness.

To assess the possibility of low-frequency unsteadiness at high angles of attack, the U-RANS simulations are carried out. Consequently, the low-frequency unsteadiness is observed at higher angles of attack on the modified airfoils, which occurs due to the interaction of the streamwise vortices. Thus, on the modified airfoils, the steady analysis is performed for the low angles of attack of 0, 2, 4, 6, and 8 degrees while for the angles of attack of 10, 12, 16, 20, and 24 degrees, the U-RANS simulations are performed.

To describe more in-depth the observed unsteadiness, the U-RANS simulation results of the A6W21 airfoil at a 16-degree angle of attack are illustrated in Figure 3.15. This figure shows how the streamwise vortices and streamwise wall-shear stresses are changing over time. As illustrated in Figure 3.15, this unsteadiness causes the counter-rotating streamwise vortices at the regions closer to the trailing edge to have a low-frequency spanwise motion and become small and large at different time steps (time steps of 140 and 145 in this case). This issue causes the low-frequency spanwise motion of the positive streamwise wall-shear stresses (attached flow regions) as a consequence. As can be seen, the attached flow region area is the same at different time-steps, but only the shape of the attached flow region is changing over time with low-frequency motion in the regions closer to the trailing edge. This indicates that the final solution for the aerodynamic coefficients (lift and drag coefficients) in this simulation is steady-state. It should be noted that the streamwise vortices in Figure 3.15 are not standardized to show the effect of the streamwise vortices better.

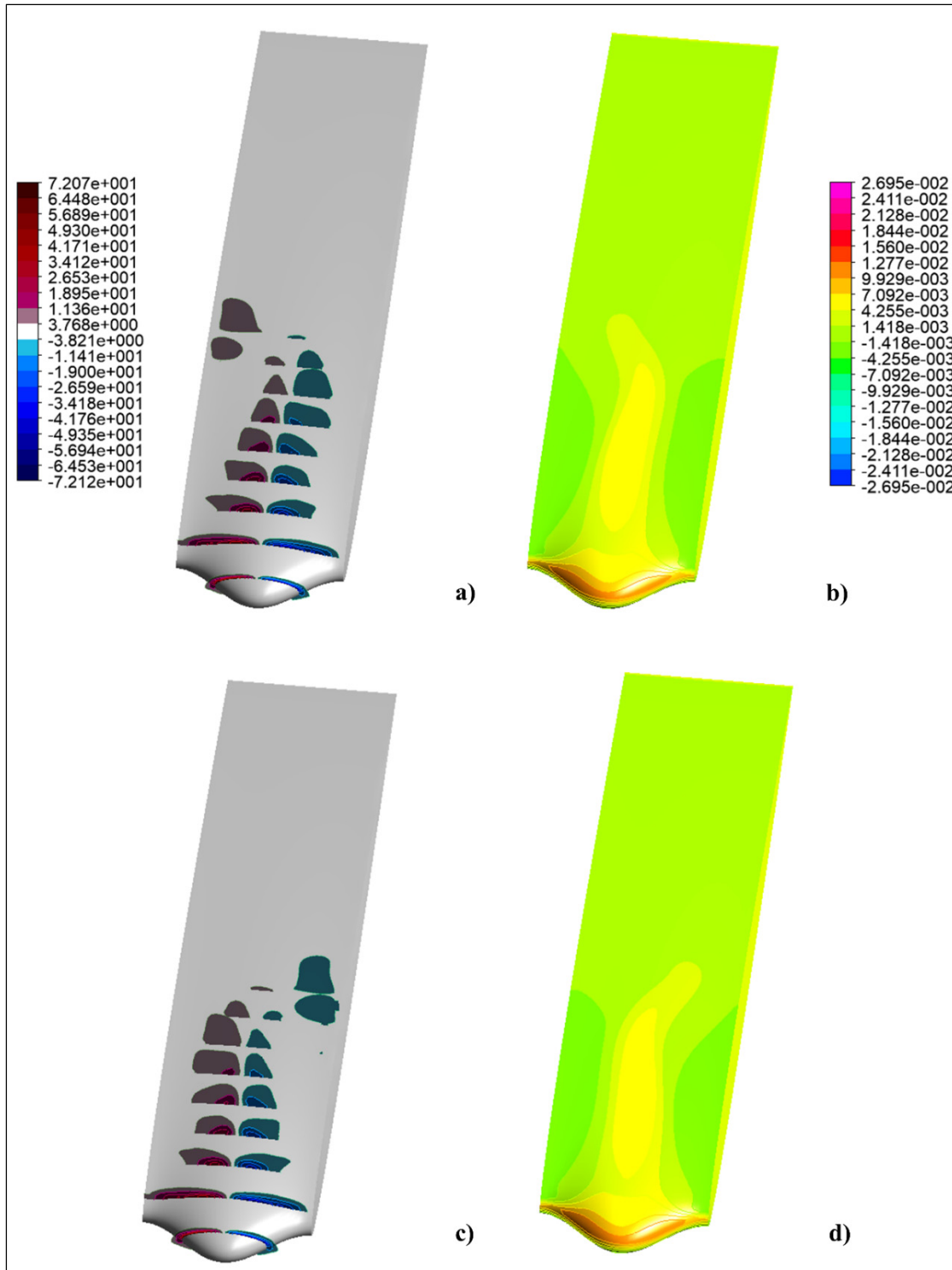


Figure 3.15 Wall shear stresses and streamwise vortices at time-steps of 140 (a and b) and 145 (c and d) on the NACA 0010_A6W21 airfoil at a 16 degree AOA

3.3.3 The effect of the streamwise vortices at pre-stall angles of attack

At 10-degree angle of attack, the flow behavior is observed to be steady, but the U-RANS mode is still used to confirm these observations. First, the wall shear stresses in the streamwise direction are compared in Figure 3.16, to understand the location of the most attached and separated flow regions. As can be seen in Figure 3.16, at a pre-stall angle of attack of 10-degrees, the flow is mostly attached on the baseline airfoil. This is the reason for a higher amount of lift coefficient on the baseline airfoil in comparison with the other modified airfoils at this angle of attack.

The separated flow regions can be seen behind the trough sections of all the modified airfoils. As discussed in the introduction section, these separated flow regions, originate from the troughs between tubercles (Johari et al., 2007). To understand better the reason for the generation of these separated flow regions, Figure 3.17 illustrates the streamwise vortices versus the tangential projection of the velocity at a slice at $0.2\bar{C}$ of the A11W43 airfoil, where \bar{C} is the mean chord length. As can be seen in Figure 3.17, the streamwise vortices generate upwash and downwash of the flow behind the troughs and peak sections of the modified airfoil, respectively. It should be noted that the streamwise vortices in Figure 3.17 are not standardized and are also illustrated with higher resolution to better illustrate the streamwise vortices. This upwash generates separated flow regions at pre-stall angles of attack, depending on the circulation of the streamwise vortices. For example, as can be seen on the A6W11 and A11W43 airfoils that generate the highest circulation streamwise vortices, the separated flow regions are the strongest (with darker blue color). This means that their streamwise vortices generate a stronger upwash in the regions behind the trough sections. Meanwhile, the separated flow region covers more chordwise positions behind the trough regions of the A11W43 and A6W43 airfoils, in comparison with other modified airfoils with a shorter wavelength. As discussed in the previous sub-section, this is because of less interaction intensity, and hence larger effective length of the streamwise vortices on larger wavelength modified airfoils. Thus, for the same reason that the A11W43 airfoil generates higher lift coefficients at a post-stall angle of attack of 16 degrees, (due to larger effective length and effective mixing of the

streamwise vortices), this airfoil due to its larger strength and effective length streamwise vortices which causes the generation of larger and stronger separated flow regions, generates the lowest lift coefficient at a pre-stall angle of attack of 10 degrees.

In addition, the separated flow regions on the A6W11 airfoil cover fewer chordwise locations in comparison with the other larger wavelength-modified airfoils with the same amplitude size. As discussed also in the previous sub-section, this issue is due to the more intense interaction of the streamwise vortices on shorter wavelength airfoils and, hence smaller effective length of streamwise vortices on them.

In a nutshell, it could be said that the same streamwise vortices that cause the creation of attached flow regions at post-stall angles of attack, cause the generation of separated flow regions at the pre-stall angles of attack.

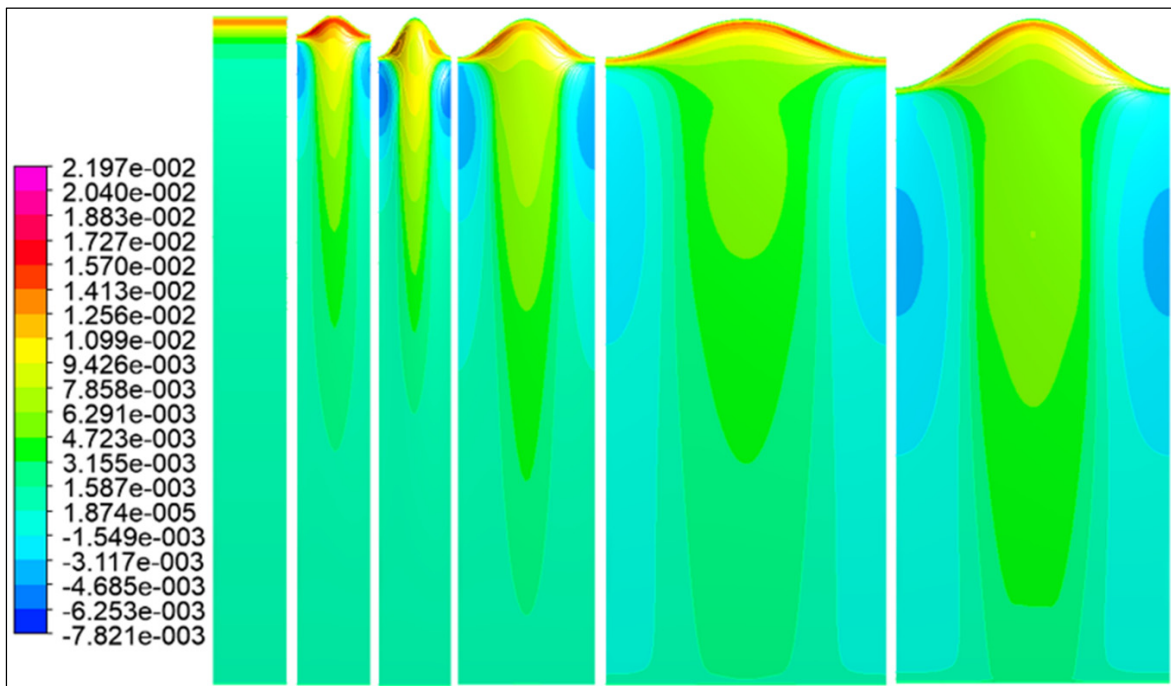


Figure 3.16 Wall shear stresses from left to right on baseline NACA 0010, A3W11, A6W11, A6W21, A6W43, and A11W43 airfoils at a 10 degree angle of attack

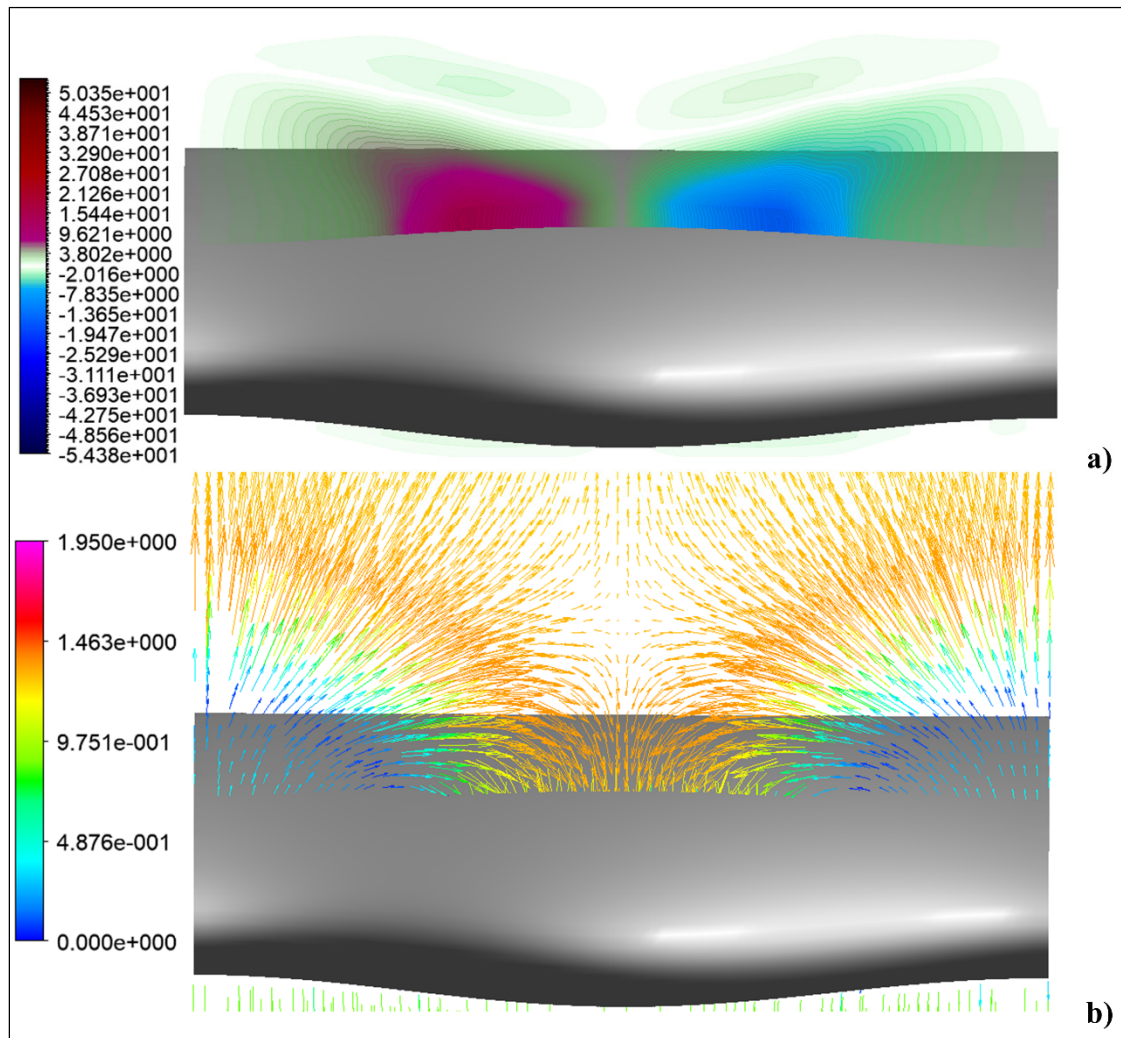


Figure 3.17 Streamwise vorticity (a) vs. tangential projection of the velocity field (b) on NACA0010_A11W43 airfoil at a slice at 0.2 C

In chapter 3, the effect of leading-edge tubercles on the symmetric NACA 0010 airfoil is discussed. Accordingly, the effect of amplitude, wavelength, and amplitude to wavelength ratio of tubercles in the strength and interaction of the streamwise vortices, and their effect on the lift and drag coefficients are analyzed. In addition, the reason for the generation of separated flow regions at pre-stall angles of attack and its relation with the streamwise vortices are explained. In the next chapter, the effect the tubercles and the streamwise vortices on the high-cambered RAF-19 airfoil will be analyzed.

CHAPTER 4

EFFECT OF LEADING-EDGE TUBERCLES ON HIGH-CAMBERED AIRFOIL

In this chapter, the effect of amplitude, wavelength, and amplitude to wavelength ratio sizes of tubercles on the integral quantities of lift and drag coefficients of the RAF-19 airfoil is first discussed and the results are compared with the results obtained on symmetric NACA 0010 airfoil. After that in the subsequent sections, the streamwise vortices, their convergence, and the effect of amplitude and wavelength sizes of the tubercles on the circulation of the streamwise vortices will be explained. The reason for the differences observed between the integral quantities results of the modified RAF-19 and NACA 0010 airfoils are then discussed. The effect of large spanwise bumps along the chord of the modified RAF-19 airfoils on the interaction of the streamwise vortices will also be explained in this chapter.

4.1 Integral quantities

In this section the effect of leading-edge tubercles amplitude, wavelength, and amplitude to wavelength ratio sizes on the RAF-19 airfoil integral quantities of lift and drag coefficients is analyzed and the results are compared with the effect of tubercles on the NACA 0010 airfoil, explained in the previous chapter.

4.1.1 The effect of the amplitude of tubercles on integral quantities

To analyze the effect of amplitude size of the tubercles, two sets of results were compared on both airfoils, shown in Figure 4.1_Figure 4.4. The first set of amplitude size analysis on the lift and drag coefficients results are illustrated in Figure 4.1, and Figure 4.2 respectively.

Lift coefficient results illustrated in Figure 4.1 show that, by reducing the amplitude of tubercles, the C_{Lmax} and lift coefficient at pre-stall angles of attack increase for both the NACA 0010 and RAF-19 modified airfoils. On NACA 0010 airfoil, tubercles cause the reduction in the pre-stall lift coefficient while increasing the post-stall lift coefficient which is a similar

trend that observed on the symmetric airfoils on other researches (Hansen et al., 2011; Johari et al., 2007). However, on the RAF-19 airfoil, this trend is not observed and no improvements on both pre-and post-stall angles of attack are observed for both the A6W43 and A11W43 airfoils in comparison with the baseline RAF-19 airfoil. This trend is very similar to the trend observed on high cambered S1223 airfoil, mentioned in the literature review section which showed that tubercles show no improvements at both the pre-and post-stall angles of attack at Reynolds number of 2×10^5 on high cambered S1223 airfoil (Sudhakar et al., 2020). On both NACA 0010 and RAF-19 airfoils, increasing the amplitude of the tubercles results in smoother stall characteristics. The drag coefficient results illustrated in Figure 4.2, show that increasing the amplitude of the tubercles on both airfoils, generally results in increasing the drag coefficient.

The second set of amplitude size analysis on the lift and drag coefficients results are illustrated in Figure 4.3 and Figure 4.4 respectively. As can be seen in Figure 4.3, reducing the amplitude of tubercles from A6W11 to A3W11, on NACA 0010 airfoil results in increasing lift coefficients at both pre-and post-stall angles of attack. On the RAF-19 airfoil, generally, the A3W11 and A6W11 generate the same amount of lift coefficient until 12 degrees of angle of attack, while at 16-degree angle of attack, the A3W11 airfoil generates a higher amount of lift coefficients than the A6W11 airfoil.

On the high-cambered RAF-19 modified airfoils, some unique features are also observed. In the A3W11 airfoil, which is the airfoil with the smallest amplitude, a higher lift coefficient in comparison with the baseline airfoil is observed from 10 to 16 degrees of angle of attack which covers the baseline airfoil pre-stall and post-stall angles of attack. This increase in lift coefficients on the A6W11 airfoil is between 10 to 12 degrees. Thus, the C_{Lmax} is increased in comparison with the baseline airfoil on both A6W11 and A3W11 airfoils.

Again, the trend of the results on the symmetric NACA 0010 airfoils are similar to the trends found in other research done on symmetric airfoils such as (Hansen et al., 2011; Johari et al., 2007) which showed that tubercles reduce the pre-stall and improving the post-stall

aerodynamic performance, and the trend of the results on the modified high cambered RAF-19 airfoils are similar to the trend found in (Sudhakar et al., 2020) on high cambered S1223 airfoil.

The drag coefficient results shown in Figure 4.4 show that on both types of airfoils, the smaller amplitude airfoils generally generate a lower amount of drag coefficient.

4.1.2 The effect of the wavelength of tubercles on integral quantities

On the high cambered RAF-19 airfoil, the trend of the results illustrated in Figure 4.5 shows that until 6 degrees of angle of attack the modified and baseline airfoils generate the same value of lift coefficient. Above 6 degrees of angle of attack by reducing the wavelength of the tubercles, the lift coefficient values increased. This trend was observed in the research of Hansen *et al.* (2011) who observed that the lift coefficient results increased by reducing the wavelength of the tubercles up to a certain limit and after that limit, the lift coefficient reduced by reducing the wavelength of the tubercles. On the other hand, on the NACA 0010 modified airfoils, the lift coefficient results show the same values for the modified and baseline airfoils until 8 degrees. However, at above 8 degrees, by reducing the wavelength of the tubercles, the lift coefficient values are generally decreased at both pre-stall and post-stall angles of attack. The reason for this difference between the RAF-19 and NACA 0010 modified airfoils will be discussed more in the next sections.

The drag coefficient results illustrated in Figure 4.6 on both airfoils showed that the modified airfoils generate higher drag coefficients than the baseline airfoil and drag coefficient values are higher for larger wavelength airfoils.

4.1.3 The effect of the amplitude to wavelength ratio of tubercles on integral quantities

The comparison of the lift and drag coefficients of the modified RAF-19 and NACA0010 airfoils with close values of amplitude to wavelength ratio of tubercles are illustrated in Figure

4.7 and Figure 4.8 respectively. It can be seen from the results illustrated in Figure 4.7 that on the modified NACA 0010 airfoils, the C_{Lmax} increased by reducing the amplitude and wavelength of the tubercles and the NACA 0010_A11W43 airfoil that has the largest amplitude and wavelength of tubercles, the C_{Lmax} is smaller than the other two airfoils with smaller amplitude and wavelength sizes. However, this airfoil acquires a higher post-stall lift coefficient as well as smoother stall characteristics in comparison with the other two airfoils with smaller amplitude and wavelength sizes of tubercles.

On the modified RAF-19 airfoils also, by reducing the amplitude and wavelength of the tubercles, the lift coefficient and C_{Lmax} improve. It can be seen that the RAF-19_A3W11 airfoil with the smallest amplitude and wavelength size can improve the lift coefficient at both pre- and post-stall angles of attack from 10 to 16 degrees. However, the airfoil with the largest amplitude and wavelength size (RAF-19_A11W43) does not improve the lift coefficient at all the angles of attack studied. It should be noted that the RAF-19 airfoil also does not have the sudden stall characteristics with a sudden loss of lift coefficient like the NACA 0010 airfoil. Results illustrated in Figure 4.8, show that on both NACA0010 and RAF-19 modified airfoils, the drag coefficient increased by increasing the amplitude and wavelength of tubercles.

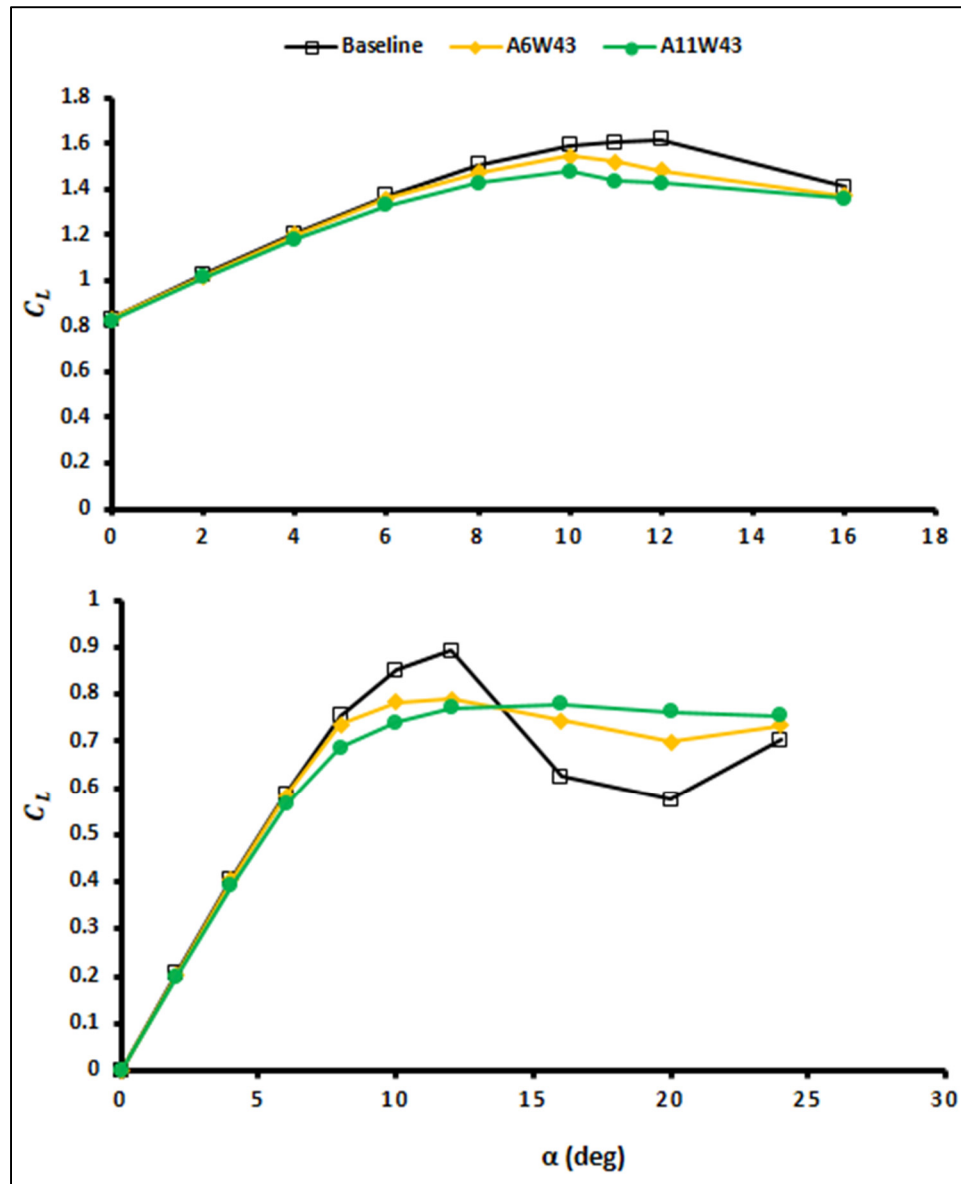


Figure 4.1 Comparison of the effect of the amplitude of tubercles on the lift coefficients of RAF-19 (a) and NACA 0010 (b) airfoils (first set)

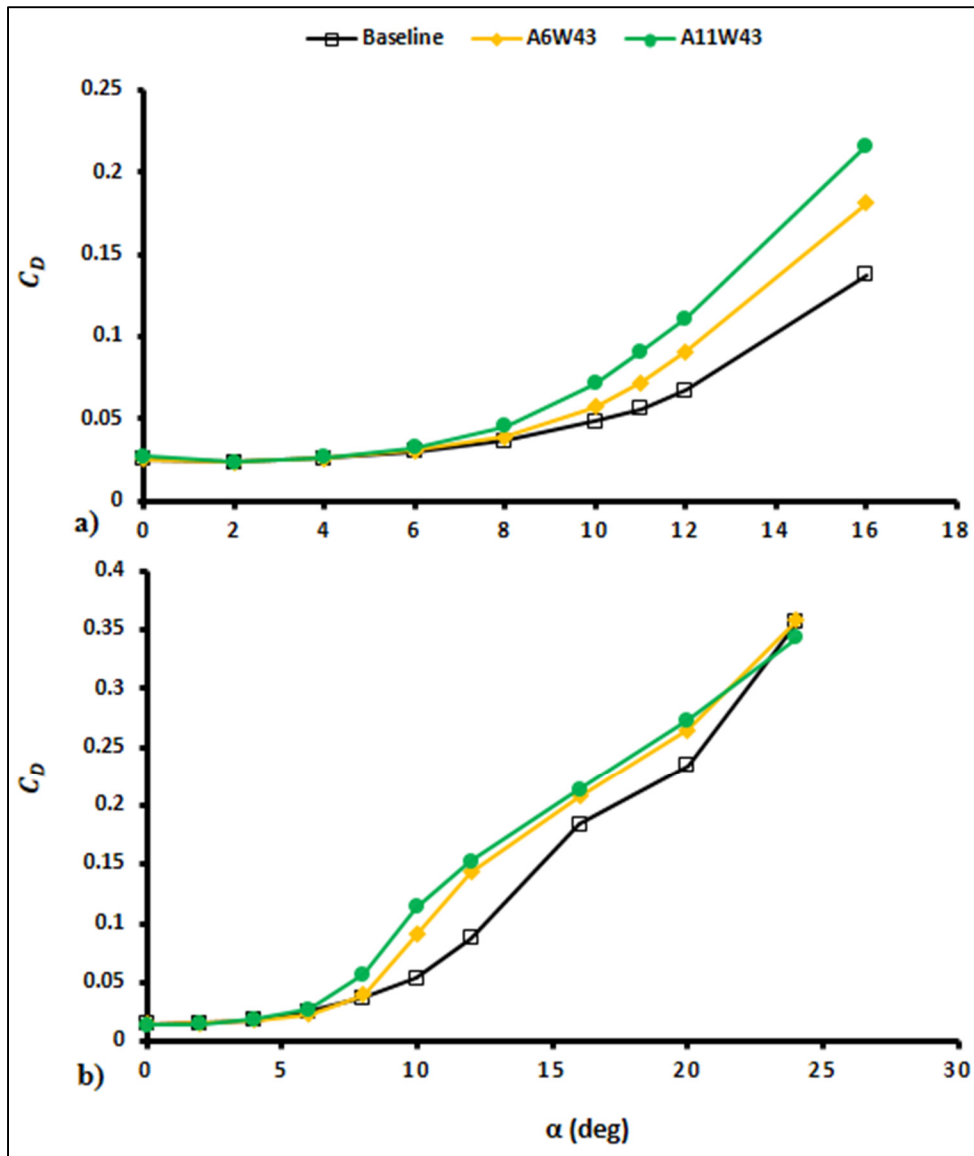


Figure 4.2 Comparison of the effect of the amplitude of tubercles on the drag coefficients of RAF-19 (a) and NACA 0010 (b) airfoils (first set)

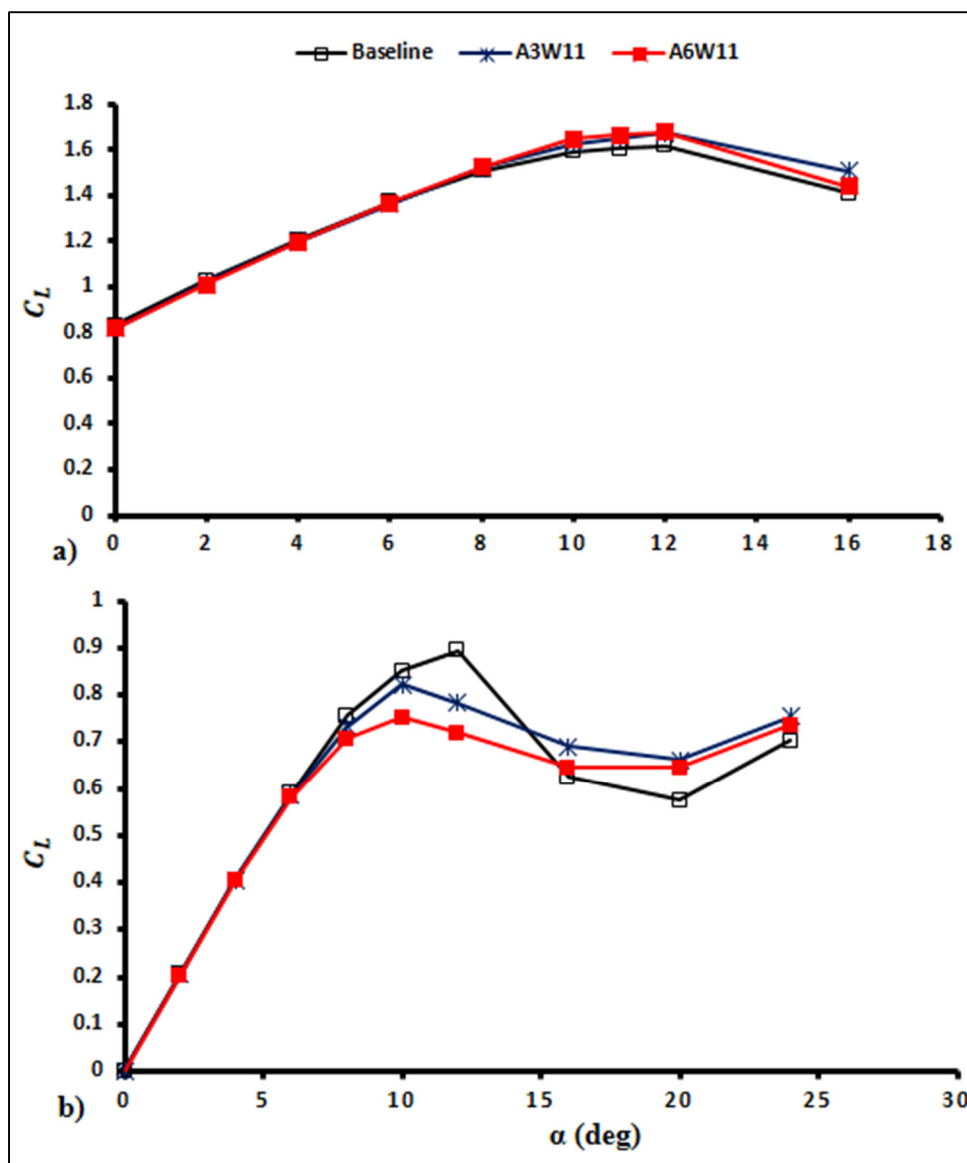


Figure 4.3 Comparison of the effect of the amplitude of tubercles on the lift coefficients of RAF-19 (a) and NACA 0010 (b) airfoils (second set)

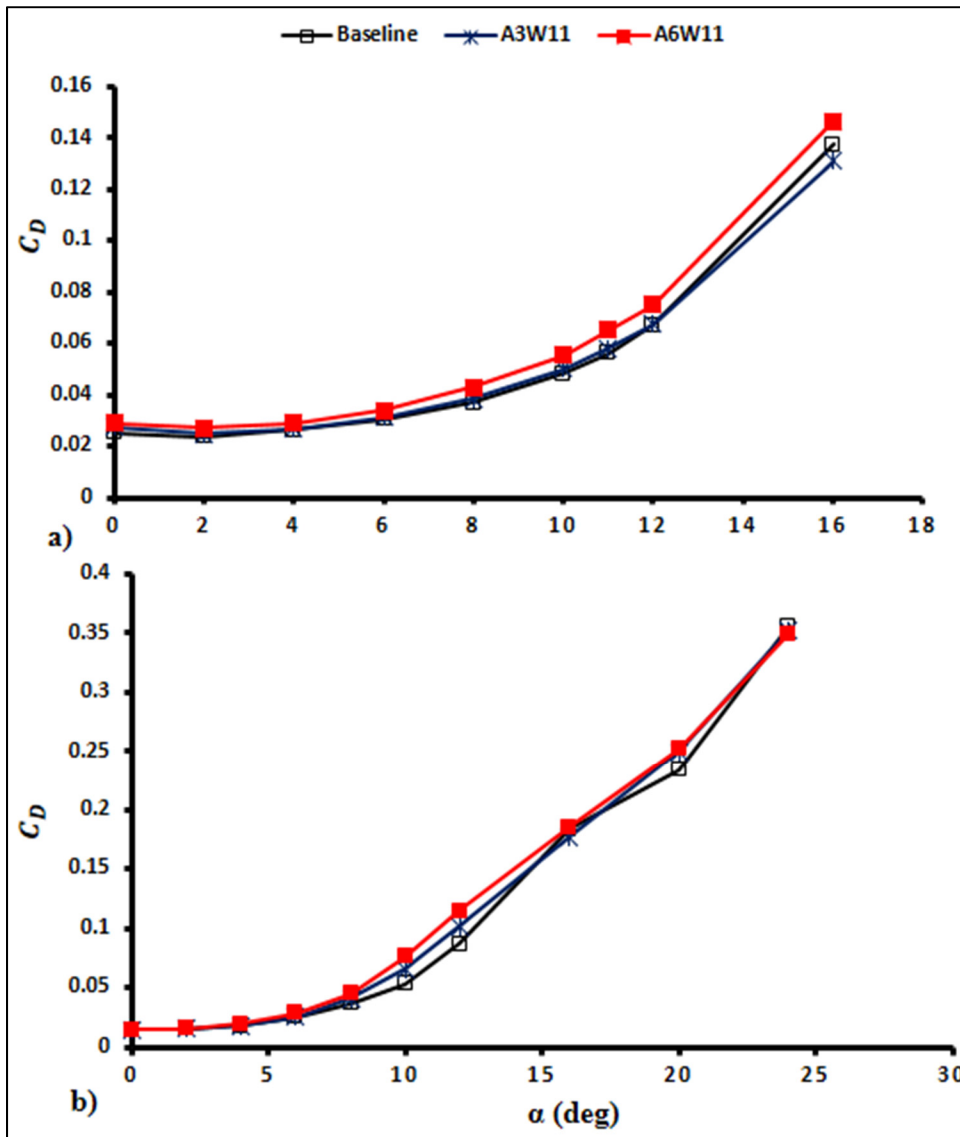


Figure 4.4 Comparison of the effect of the amplitude of tubercles on the drag coefficients of RAF-19 (a) and NACA 0010 (b) airfoils (second set)

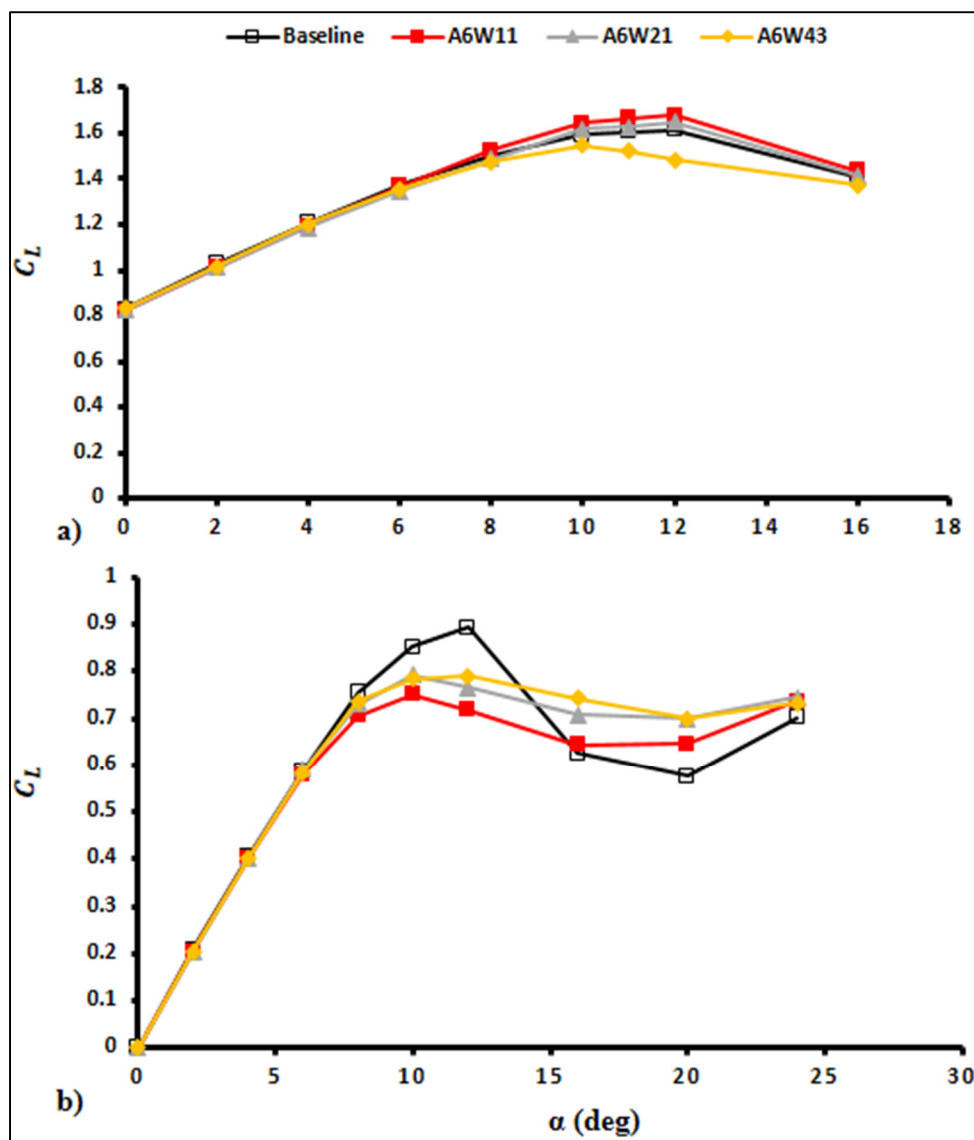


Figure 4.5 Comparison of the effect of the wavelength of tubercles on the lift coefficient of RAF-19 (a) and NACA 0010 (b) airfoils

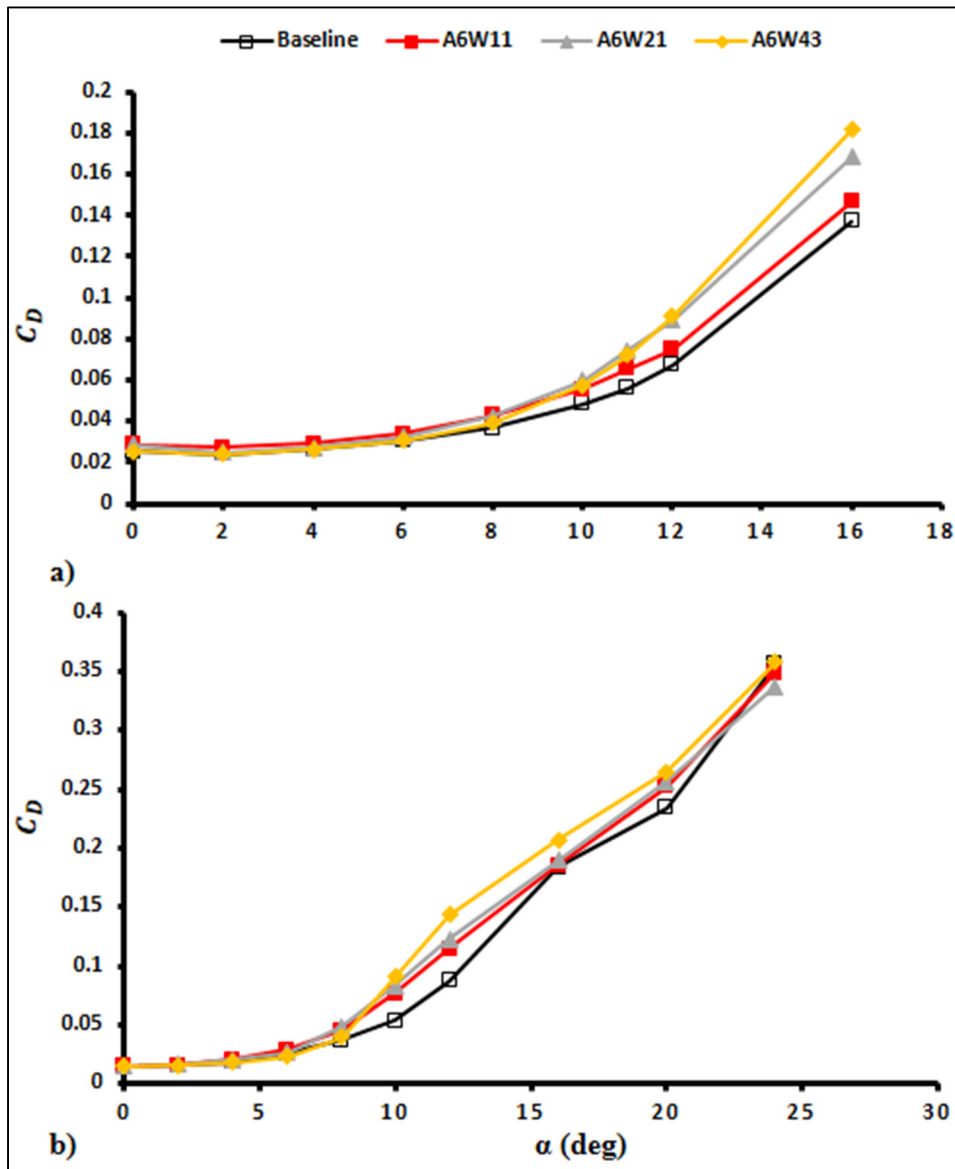


Figure 4.6 Comparison of the effect of the wavelength of tubercles on the drag coefficient of RAF-19 (a) and NACA 0010 (b) airfoils

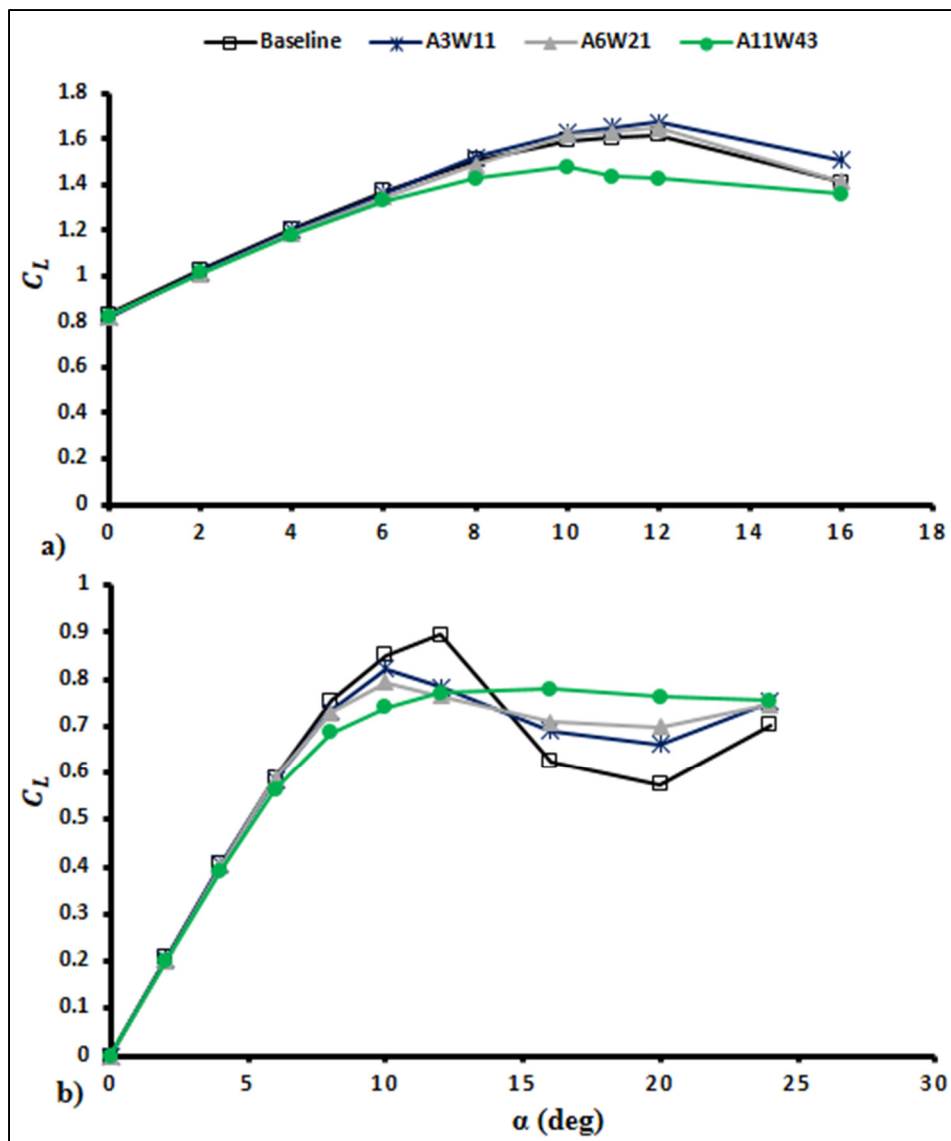


Figure 4.7 Comparison of the effect of the amplitude to wavelength ratio of tubercles on the lift coefficient of RAF-19 (a) and NACA 0010 (b) airfoils

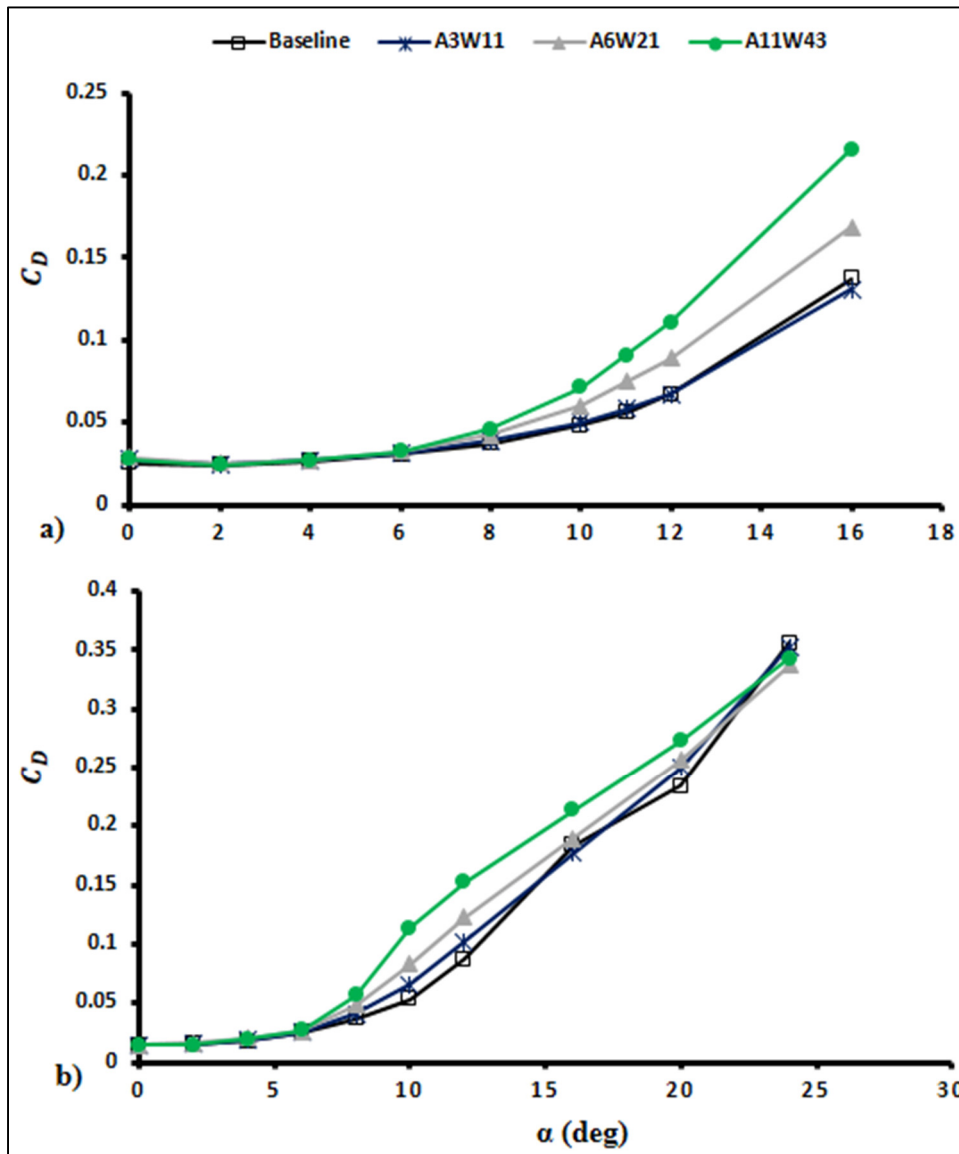


Figure 4.8 Comparison of the effect of the amplitude to wavelength ratio of tubercles on the drag coefficient of RAF-19 (a) and NACA 0010 (b) airfoils

In summary, the lift and drag coefficient results on the high camber RAF-19 modified airfoils show different trends than the symmetric airfoils. On symmetric airfoils, tubercles cause to reduce the pre-stall and increase the post-stall lift coefficient. However, improvements in the

case of lift coefficient on the modified RAF-19 airfoils were only observed in the shortest wavelength and amplitude airfoils of A6W11 and A3W11 respectively. The RAF-19_A3W11 airfoil could increase the C_{Lmax} , as well as the pre-and post-stall lift coefficient (from 10 to 16 degrees of angle of attack). The RAF-19_A6W11 airfoil only increases the lift coefficient from 10 to 12 degrees of angle of attack. Other modified_RAF-19 airfoils did not improve the lift coefficient for most of the angles of attack studied. Leading-edge tubercles cause the increase in drag coefficients on both RAF-19 and NACA 0010 airfoils. Besides, the drag coefficient values increased by increasing the amplitude and wavelength of the tubercles.

4.2 The streamwise vortices

In previous the effect of the amplitude, wavelength, and amplitude to wavelength ratio sizes of the leading-edge tubercles on the integral quantities of the lift and drag coefficient has been analyzed. To understand the reason for these differences, the behavior and strength of the streamwise vortices on the modified airfoils should be first discussed.

4.2.1 The convergence and interaction of the stream-wise vortices

The stream-wise vortices on RAF-19_A11W43 airfoil at 0, 4, 8-, 10-, 12, and -16 degrees of angle of attack are illustrated in Figure 4.9. The solid arrow-line shows the flow direction relative to the dashed line which indicates the modified airfoils chord line. As can be seen from Figure 4.9, the maximum value of the streamwise vortices is increased by increasing the angle of attack. This figure also shows that, by increasing the angle of attack, while the streamwise vortices move along the chord, they converge toward each other and hence interact and annihilate each other. Some signs of stretching and lifting-off of these streamwise vortices can also be observed at 16 degree angle of attack in the regions closer to the trailing edge.

Thus, the same as NACA 0010 modified airfoils (shown in Figure 3.5), the streamwise vortices on modified RAF-19 airfoils are also converging toward each other and interacting. One thing that can be noted by comparing Figure 4.9 and Figure 3.5 is that the interaction and annihilation of the streamwise vortices occur faster on NACA 0010_A11W43 airfoil. For example, at 12-

and 16-degree angles of attack, the streamwise vortices cover more chordwise regions on the RAF-19_A11W43 in comparison with the NACA 0010_A11W43. This is due to the larger spanwise bump generated on the modified RAF-19 airfoils which will be discussed more in the next sections. It should be noted that both the modified RAF-19 and NACA 0010 airfoils are designed by keeping the thickness to chord ratio constant which results in the generation of spanwise bump on the suction surface of the modified airfoils. Due to the higher camber of the RAF-19 airfoil, the generated spanwise bumps on its modified airfoils become larger than their counterparts on the modified NACA 0010 airfoil.

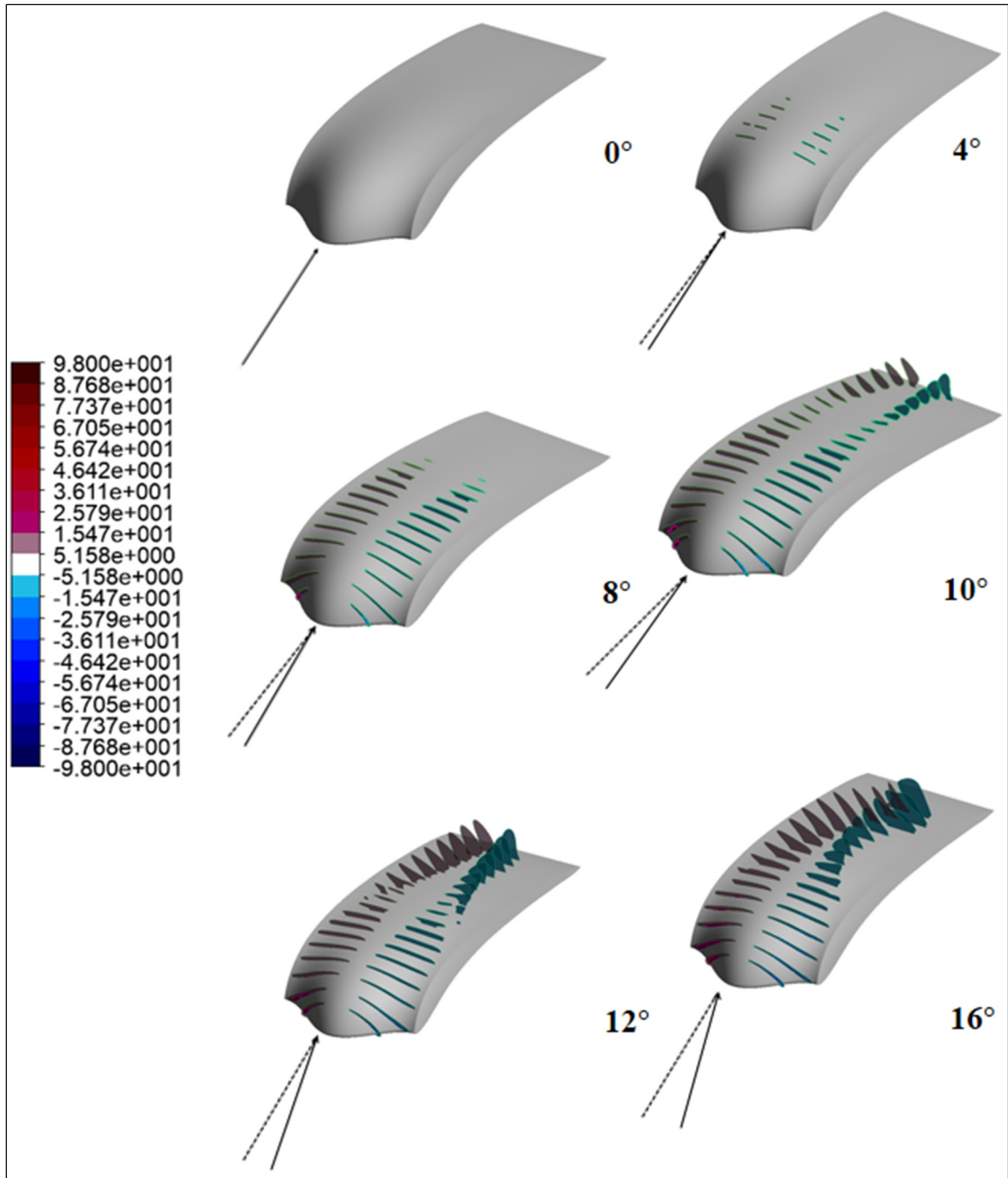


Figure 4.9 Streamwise vortices on RAF-19_A11W43 airfoil at a) 0, b) 4, c) 8, d) 10, e) 12, f) 16, g) 20, and h) 24- angles of attack

In summary, it can be concluded that the same as modified NACA 0010 airfoils, the convergence, and interaction of the streamwise vortices also occurs on RAF-19 modified

airfoils. However, the convergence of the streamwise vortices is more forwarded towards the trailing edge on the modified RAF-19 airfoil.

4.2.2 Circulation

In this section, the effect of amplitude, wavelength, and the amplitude to wavelength ratio of tubercles on the strength of the streamwise vortices generated on the modified RAF-19 airfoils are discussed.

The same as the calculation done on NACA 0010 modified airfoils, to analyze the strength of the streamwise vortices on the modified RAF-19 airfoils, the circulation of these vortices is calculated from the upper surface of the modified airfoils to the distance of 0.5 above them at a slice at $0.05C$ of the mean chord length using equation (3.1). The calculations are done at angles of attack of 0, 4, 8, 12, and 16- degrees. To be able to compare the strengths of vortices of the modified airfoils, the circulation values were calculated per unit span of the airfoils. Thus, the circulation calculated on each airfoil is divided by its wavelength. For example, the circulation value of the A6W43 airfoil was divided by 0.43, and the circulation of the A3W11 airfoil was divided by 0.11.

The calculated circulation values on all the modified RAF-19 airfoils are shown in Figure 4.10. Figure 4.11_Figure 4.14 show the effect of amplitude, wavelength, and amplitude to wavelength ratio of tubercles on the circulation values of modified RAF-19 airfoils discussed below.

As illustrated in Figure 4.11 and Figure 4.12, by increasing/reducing the amplitude of the tubercles, the strength of the stream-wise vortices increase/reduce. Besides, the results illustrated in Figure 4.13 shows that by reducing/increasing the wavelength of the tubercles, the circulation values increase/reduce.

The results depicted in Figure 4.14 show that by reducing the amplitude to wavelength ratio of tubercles, generally the strengths of the streamwise vortices are decreased. Meanwhile, it should be noted that until the 4-degree angle of attack, all the A3W11 and A6W21, and A11W43 airfoils show almost the same circulation values.

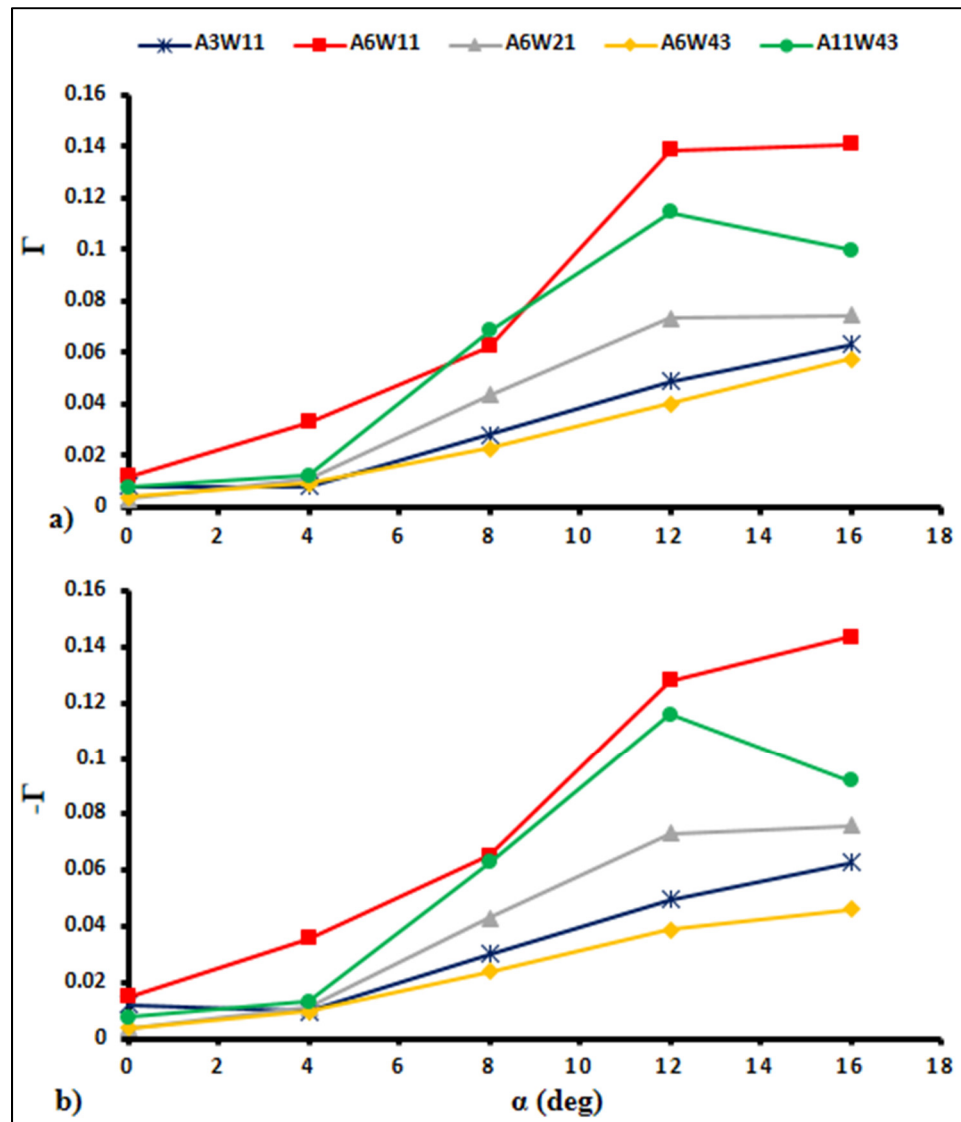


Figure 4.10 Positive (a) and negative (b) circulation values of all the modified RAF-19 airfoils

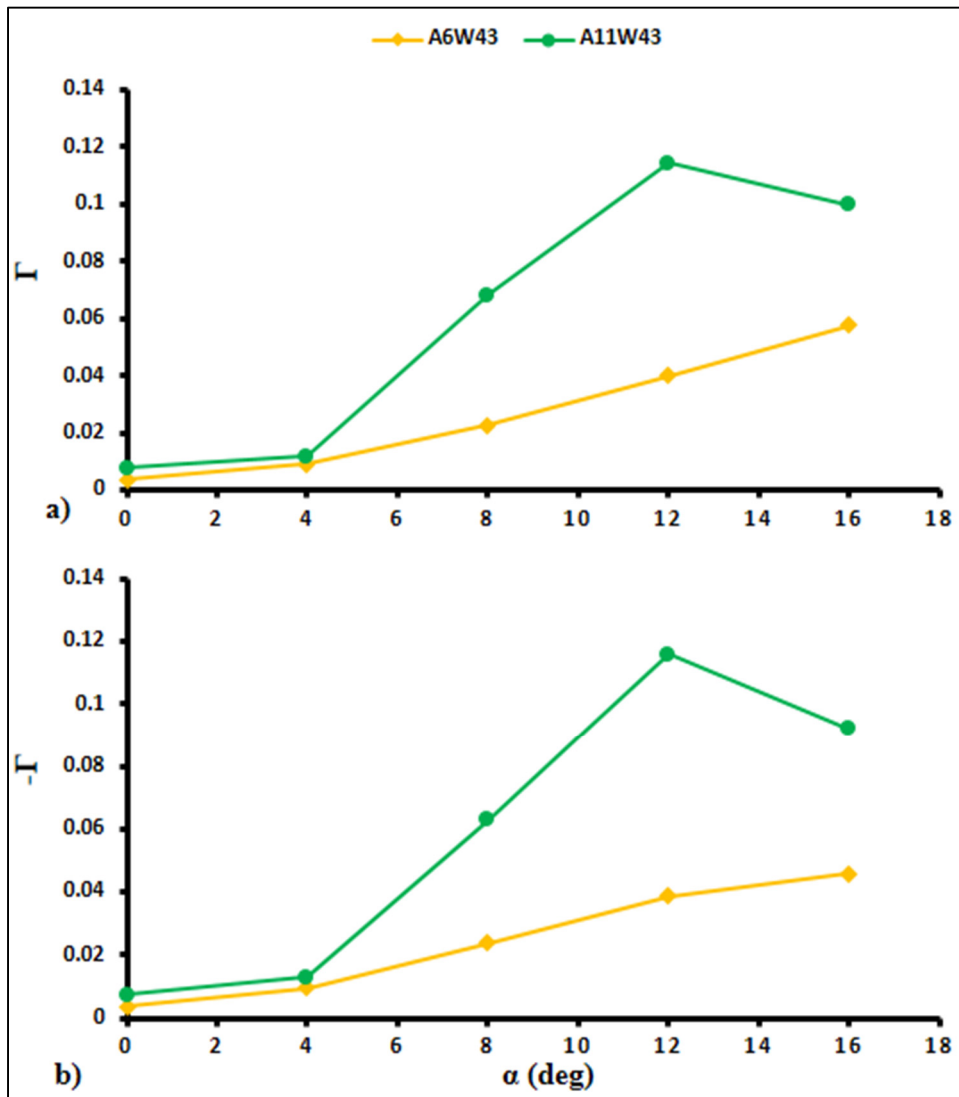


Figure 4.11 Effect of the amplitude of tubercles on positive (a) and negative (b) circulation values of the modified RAF-19 airfoils (first set)

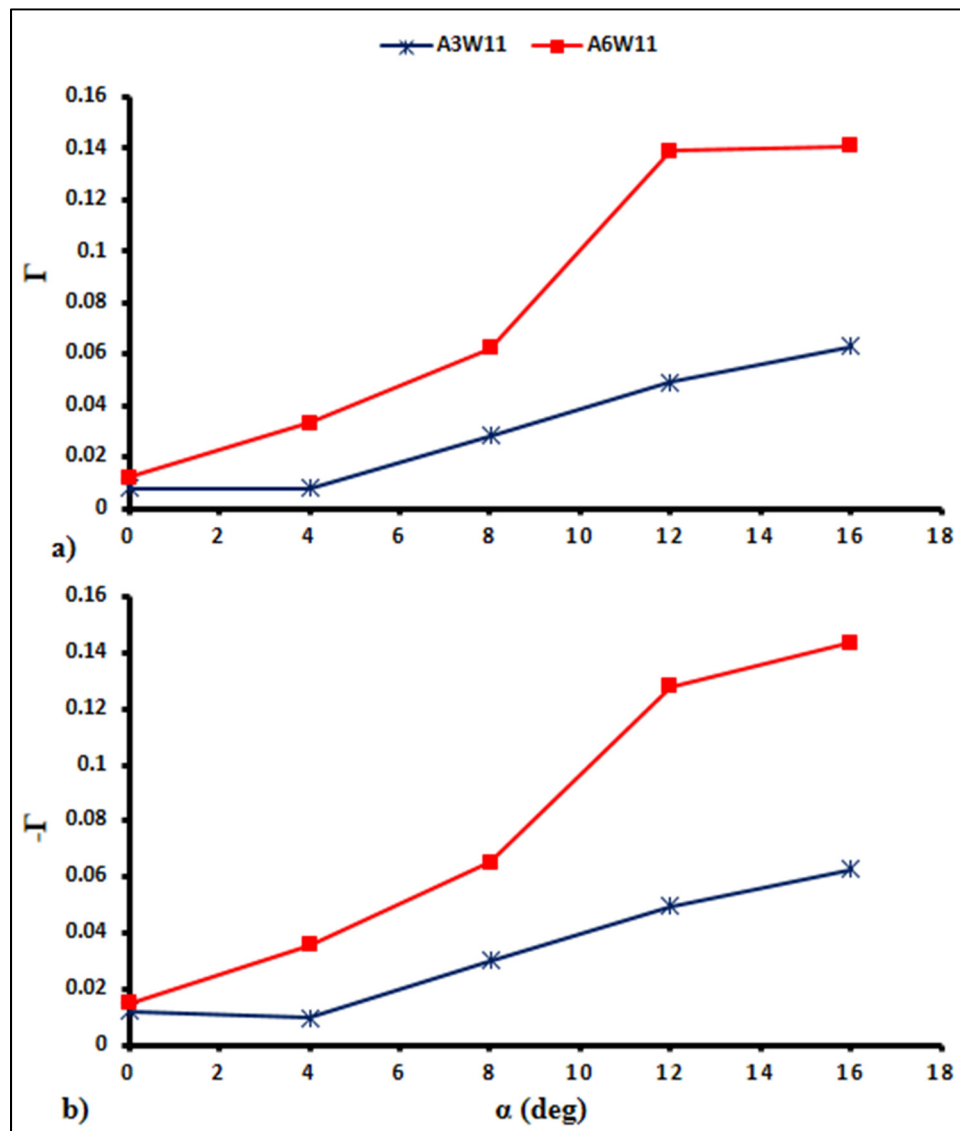


Figure 4.12 Effect of the amplitude of tubercles on positive (a) and negative (b) circulation values of the modified RAF-19 airfoils (second set)

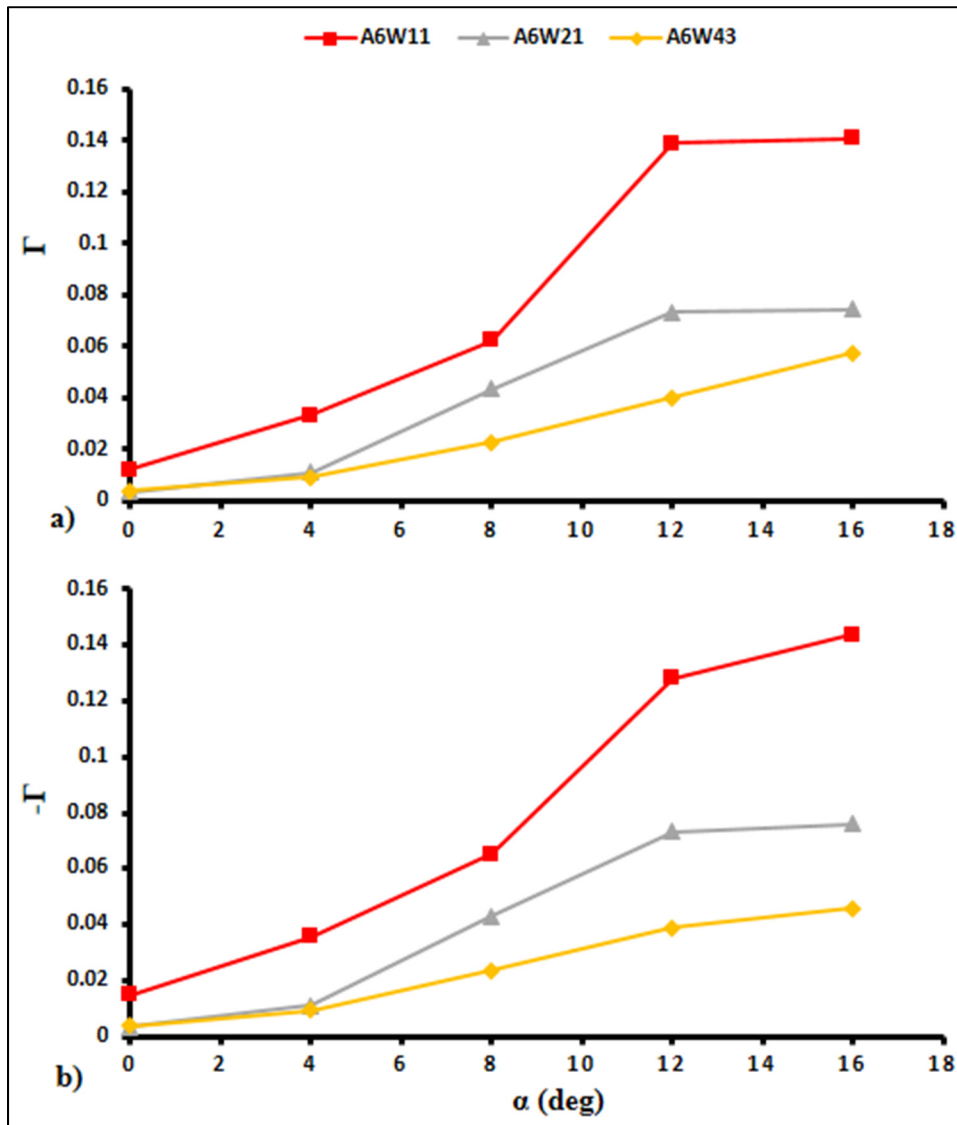


Figure 4.13 Effect of the wavelength of tubercles on positive (a) and negative (b) circulation values of the modified RAF-19 airfoils

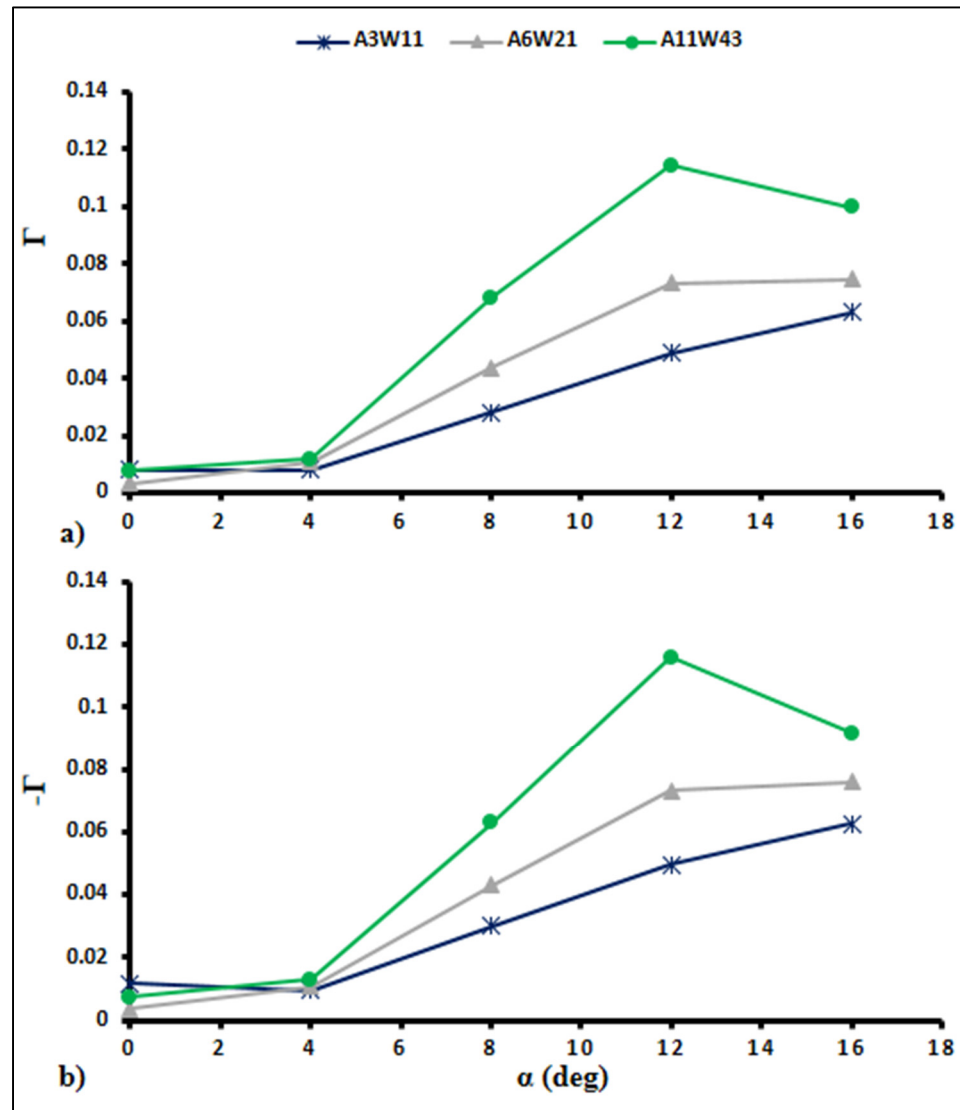


Figure 4.14 Effect of the amplitude to wavelength of tubercles on positive (a) and negative (b) circulation values of the modified RAF-19 airfoils

In summary, regarding the effect of amplitude and wavelength of tubercles on the strength of the streamwise vortices, the same conclusion as the modified NACA 0010 airfoil was obtained. It is concluded that the strength/circulation of the streamwise vortices on the modified RAF-

19 airfoils is mostly the function of A/C and W/C and the circulation of the streamwise vortices is increased by reducing the wavelength and increasing the amplitude of the tubercles.

4.3 The effect of streamwise vortices on integral quantities of RAF-19 airfoil

In the previous section, the effect of tubercles' geometrical parameters on the strength of the streamwise vortices was analyzed. Now the relation between the circulation and interaction of the streamwise vortices on the lift and drag coefficient of the modified airfoils can be discussed more in detail. All the lift and drag coefficient values are illustrated in Figure 4.15 and two angles of attack of 12 and 16 degrees are chosen for the analysis of the results.

As it is shown in Figure 4.15, the 12-degree angle of attack is the stall angle at which the A3W11 and A6W11 airfoils increase the C_{Lmax} , and the 16-degree angle of attack is the angle that the A3W11 airfoil shows higher values of lift coefficient compared with the baseline airfoil at post-stall region.

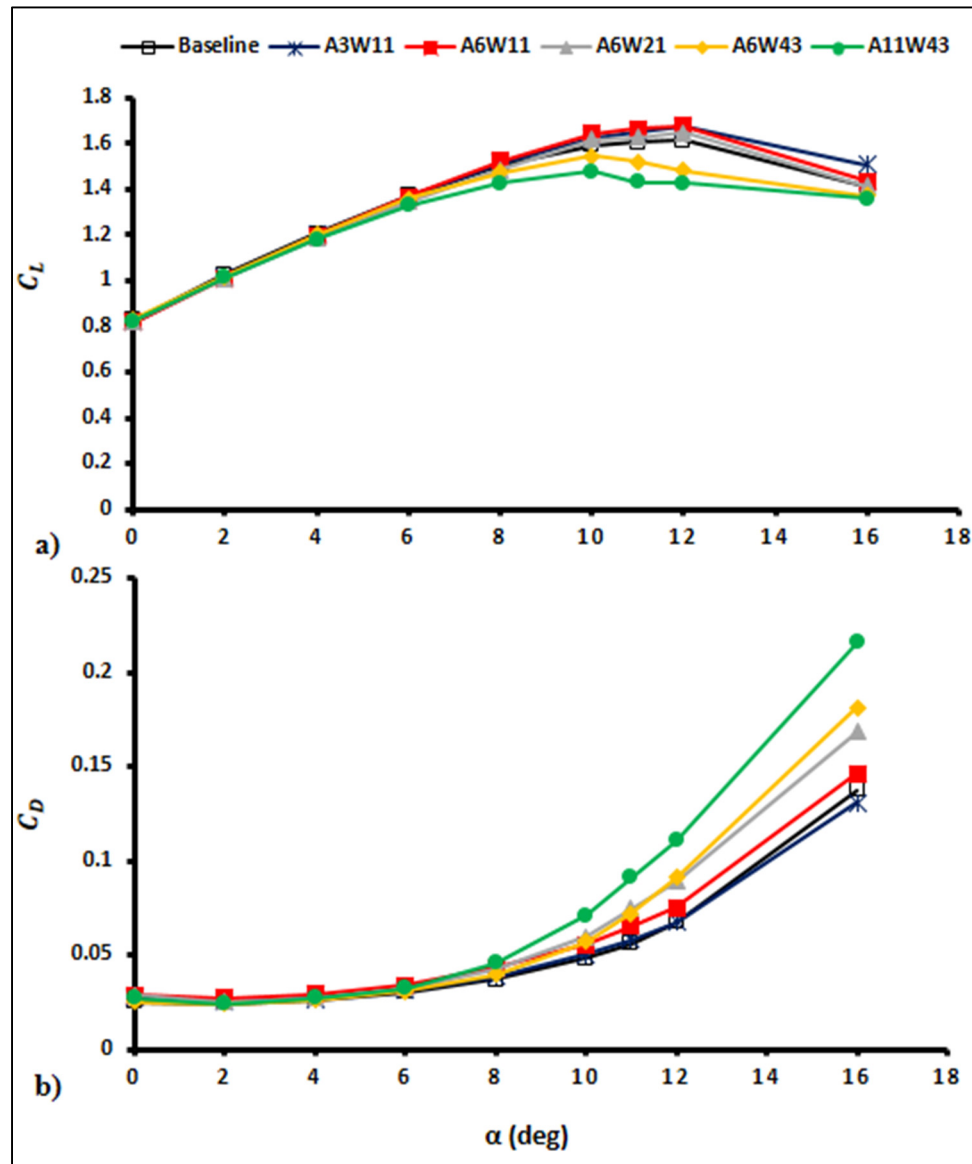


Figure 4.15 All lift (a) and drag (b) coefficients of the modified RAF-19 airfoils

To analyze the effect of streamwise vortices on the integral quantities of the modified RAF-19 airfoils, the streamwise wall shear stresses of the RAF-19 modified airfoils at 12- and 16-degree angles of attack are depicted in Figure 4.16 and Figure 4.17 respectively.

As mentioned, the RAF-19 airfoil has smoother stall characteristics in comparison with the NACA 0010 airfoil. These smoother stall characteristics can be observed by the attached flow regions on baseline RAF-19 airfoil at 12-and16-degree angles of attack as indicated in Figure 4.16 and Figure 4.17.

As mentioned in chapter 3, the leading-edge tubercles reduce the lift coefficient on symmetric airfoil at pre-stall angles of attack where the flow on the baseline airfoil is mostly attached. On high cambered RAF-19 airfoil, the separated and reversed flow regions generated behind the trough section of the modified RAF-19 airfoils neutralize the effect of attached flow regions generated behind the peak sections of the modified airfoils. Thus, no significant improvements in lift coefficients should be expected by implementing the leading-edge tubercles on the RAF-19 airfoil.

The same as modified NACA 0010 airfoils, it can be seen in Figure 4.16 and Figure 4.17 that the effective length of the streamwise vortices is increased by increasing the wavelength of the tubercles which is due to the less interaction intensity of streamwise vortices on larger wavelength airfoils.

It can be seen from Figure 4.16 and Figure 4.17 that the smaller wavelength airfoils of A6W11 and A3W11, have the highest values of streamwise wall shear stresses behind their leading-edge part in comparison with the other modified RAF-19 airfoils with larger wavelength sizes. This increase in effective mixing is due to both reducing the distancing between the vortices as well as increasing the strength of the streamwise vortices by reducing the wavelength of the tubercles. Thus, the same as the modified NACA 0010 airfoils, the effective mixing of the boundary layer is increased by reducing the wavelength of the tubercles.

The effective length of the streamwise vortices at 16-degree angle of attack on the modified RAF-19 and NACA 0010 airfoils are illustrated in Table 3.1 and Table 4.1 respectively. As can be seen from the Figure 4.17 and Table 3.1 and Table 4.1, the attached flow regions on the smaller wavelength airfoils like RAF-19_A3W11 and RAF-19_A6W11 are extended more

towards the trailing-edge in comparison with their counterparts on NACA 0010 airfoil. For example, at 16-degree angle of attack, the effective length of the streamwise vortices on the RAF-19_A3W11 and RAF-19_A6W11 airfoils are 62% and 66% of the mean chord length respectively. This value for the NACA 0010_A3W11 and NACA 001_A6W11 airfoils at 16-degree angle of attack is 24% and 27% of the mean chord respectively.

To understand more the reason for this difference, the streamwise vortices on the RAF-19_A3W11, A6W11, and A11W43 airfoils at 12 and 16-degree angles of attack are depicted on Figure 4.18 and Figure 4.19 respectively. Moreover, Figure 4.20_Figure 4.23 compares the top-front, and front-side views of the streamwise vortices on the RAF-19 and NACA 0010, A3W11 and A6W11 airfoils at 12, and 16-degree angles of attack respectively. It can be seen from the Figure 4.20_Figure 4.23 that in contrast with the NACA 0010_A3W11 and A6W11 airfoils that show the convergence and interaction of the two-neighboring counter-rotating streamwise vortices in the regions closer to the leading-edge, on the RAF-19_A3W11 and A6W11 airfoils, the streamwise vortices are effective for longer chordwise regions.

As mentioned before the generated spanwise bumps on the modified RAF-19 airfoils are greater than their counterparts on the modified NACA 0010 airfoils. It can be concluded from the Figure 4.20_Figure 4.23 that the reason for postponing the interaction of the streamwise vortices is because of the higher spanwise bump on the RAF-19 modified airfoils that creates an obstacle between the two-neighboring counter-rotating streamwise vortices. Besides that, as shown on Figure 4.20_Figure 4.23, because of the generated bumps, especially on the regions closer to the leading-edge, the two neighboring counter-rotating streamwise vortices and their cores are located and rotated more towards the spanwise sides. These two factors are the reason for the delay in convergence and interaction of the two-neighboring counter-rotating streamwise vortices and hence increase in the effective length of the streamwise vortices on the modified RAF-19 airfoils. Thus, on the modified RAF-19 airfoils, the effective mixing of the streamwise vortices is increased by reducing the wavelength of the tubercles, while the spanwise bump reduces the interaction intensity and hence increases the effective length of the

streamwise vortices. As a result, on the modified RAF-19 airfoils, the lift coefficient generally improves by reducing the wavelength of the tubercles.

Meanwhile, with smaller spanwise bump on the modified NACA 0010 airfoils, reducing the wavelength of the tubercles causes the increase in the interaction intensity of the streamwise vortices and hence their annihilation. As result, on the modified NACA 0010 airfoils, the lift coefficient of the modified airfoils is decreased by reducing the wavelength of the tubercles.

The same as the NACA 0010 modified airfoils, the drag coefficients on the modified RAF-19 airfoils are increased by increasing the wavelength and amplitude of tubercles. The reason is again the more effective length of the streamwise vortices on larger wavelength and amplitude airfoils and hence the generation of separated flow regions on larger chordwise ranges on these airfoils.

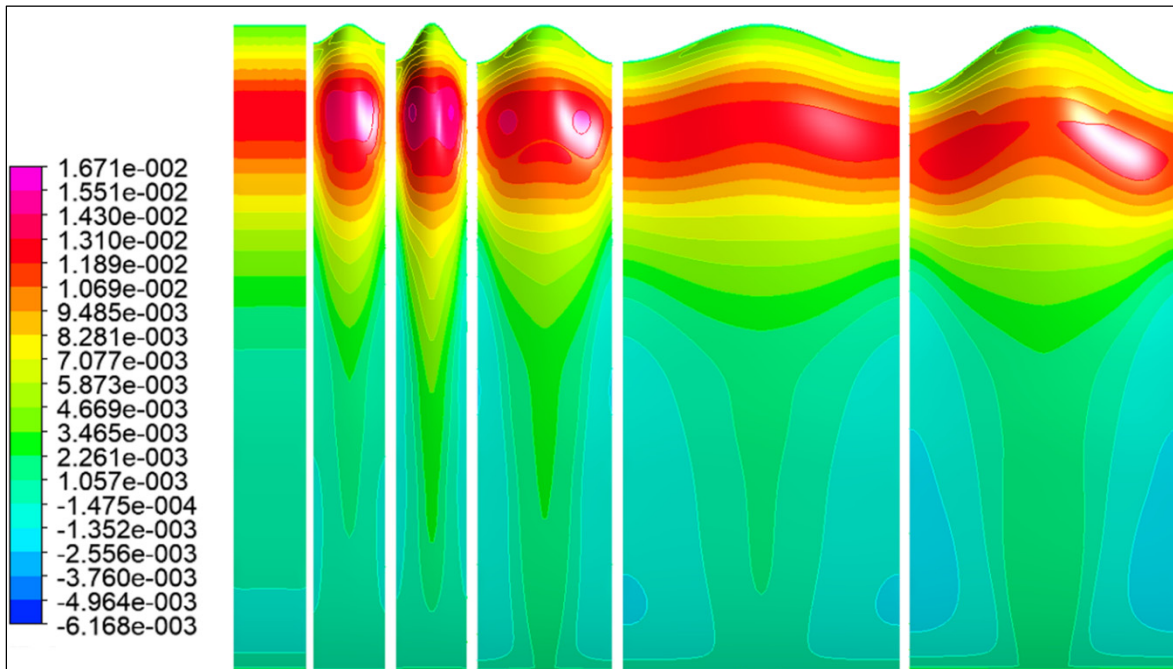


Figure 4.16 Streamwise wall shear stresses at 12-degree angle of attack on the RAF-19 baseline, A3W11, A6W11, A6W21, A6W43, and A11W43 from left to right

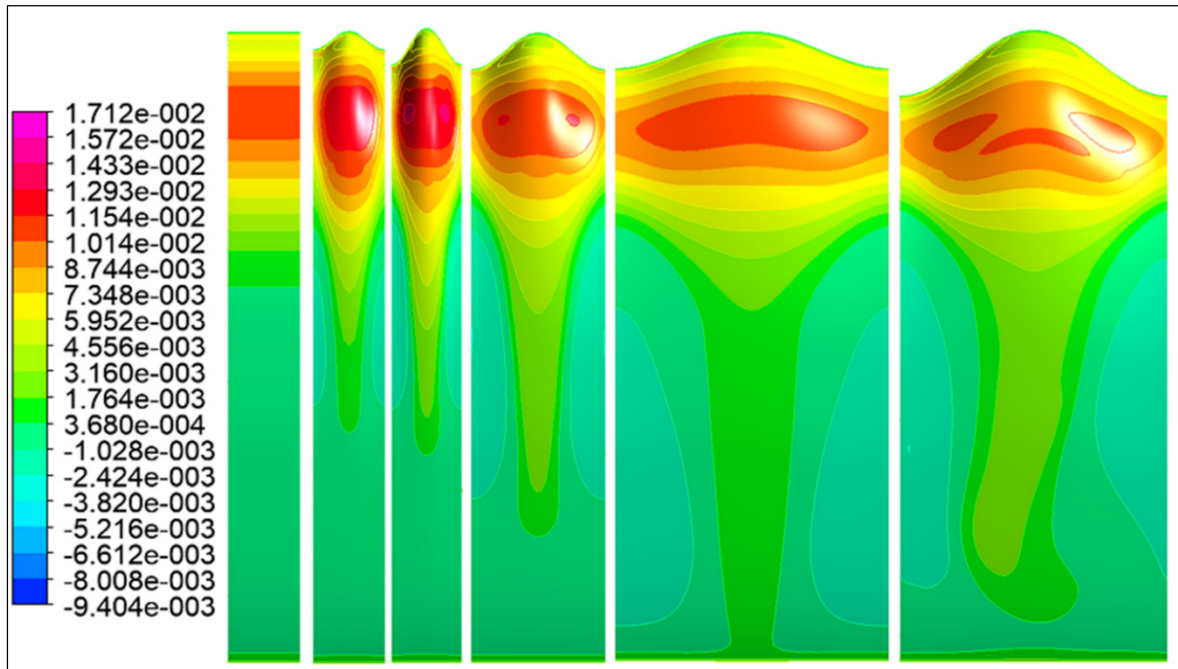


Figure 4.17 Streamwise wall shear stresses at 16-degree angle of attack on the RAF-19 baseline, A3W11, A6W11, A6W21, A6W43, and A11W43 from left to right

Table 4.1 Effective length of the streamwise vortices on the RAF-19 modified airfoils at 16-degree AOA

Airfoil name	A3W11	A6W11	A6W21	A6W43	A11W43
Effective length (%C)	62.28	66.07	79.27	100	93.11

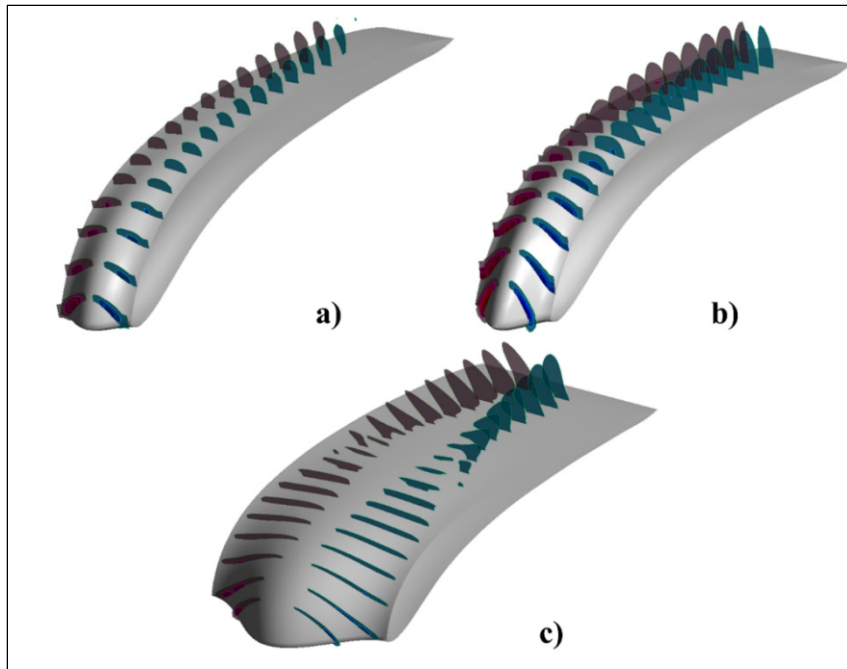


Figure 4.18 Streamwise vortices at 12-degree angle of attack on RAF-19_A3W11 (a), A6W11 (b), and A11W43 (c) airfoils

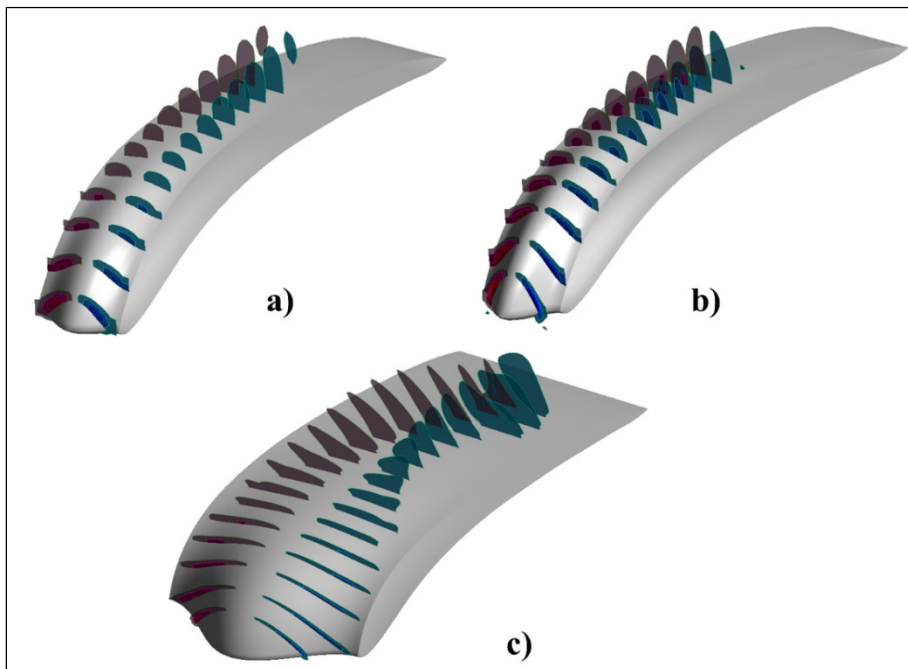


Figure 4.19 Streamwise vortices at 16-degree angle of attack on RAF-19_A3W11 (a), A6W11 (b), and A11W43 (c) airfoils

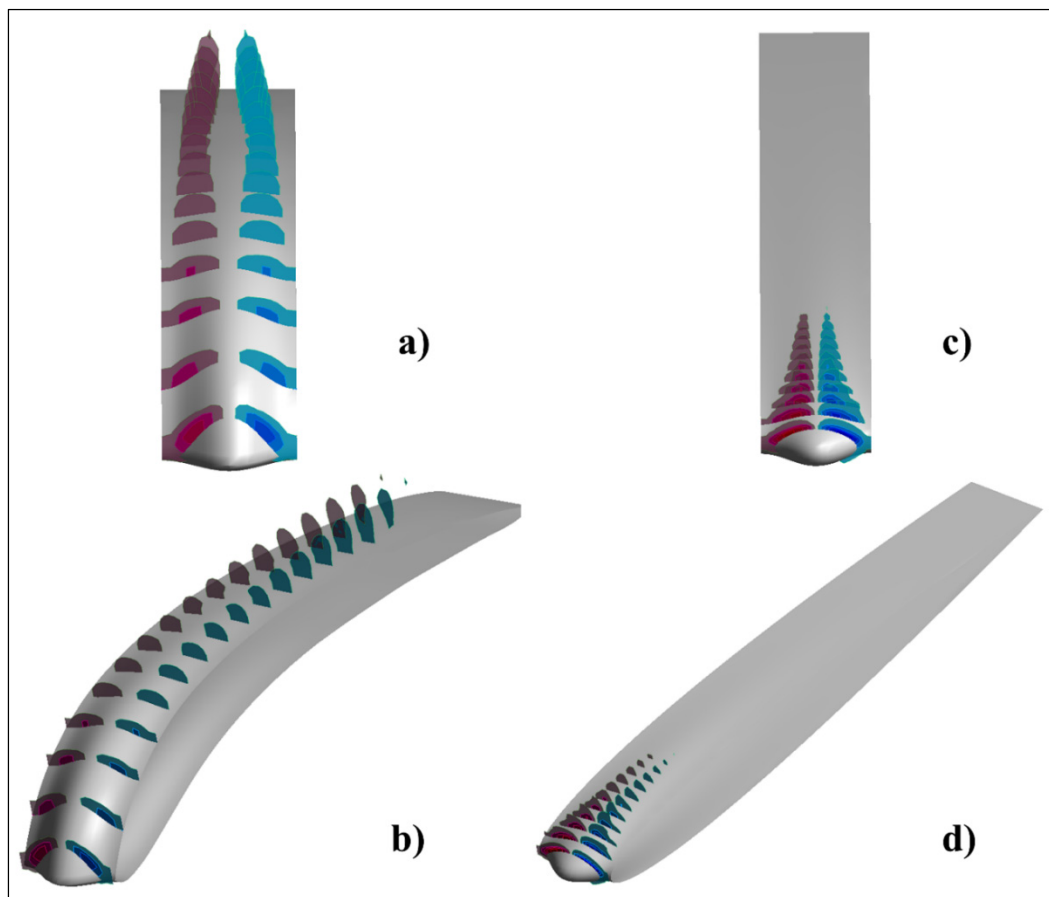


Figure 4.20 Top-front and Top-side views of streamwise vortices on A3W11 airfoil at 12-degree angle of attack on RAF-19 (a and b) and NACA 0010 (c and d) airfoils

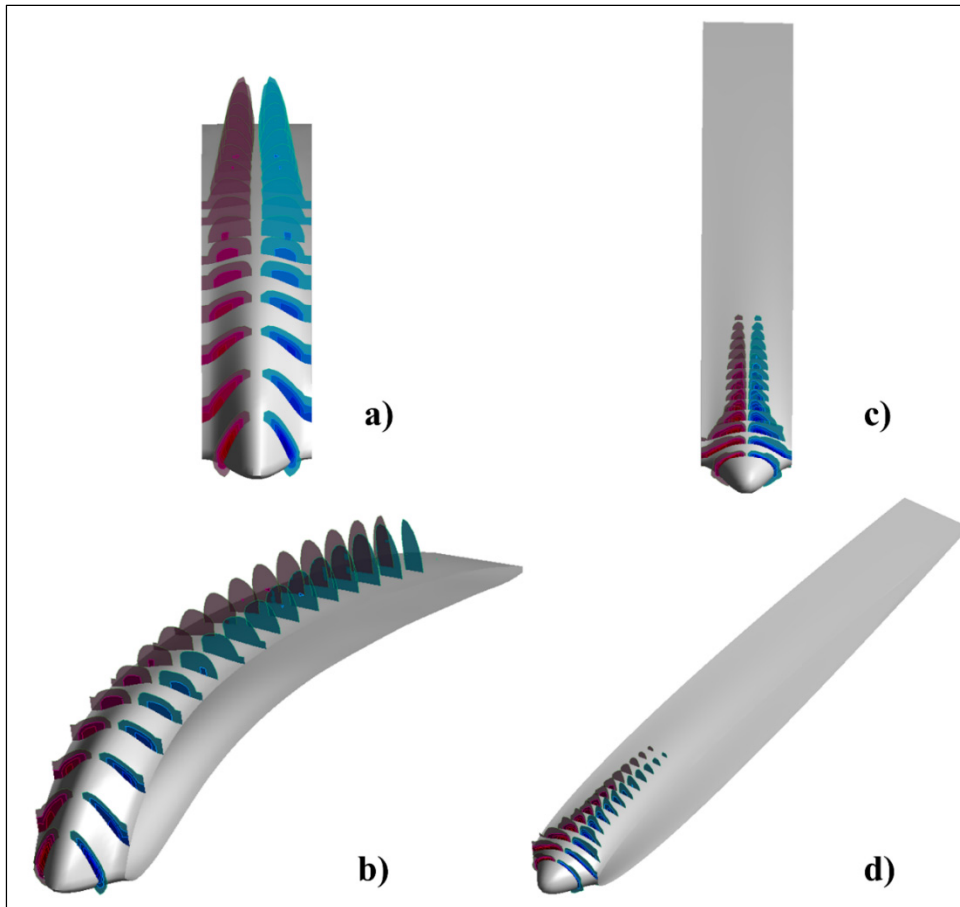


Figure 4.21 Top-front and top-side view of streamwise vortices on A6W11 airfoil at 12-degree angle of attack on RAF-19 (a and b) and NACA 0010 (c and d) airfoils

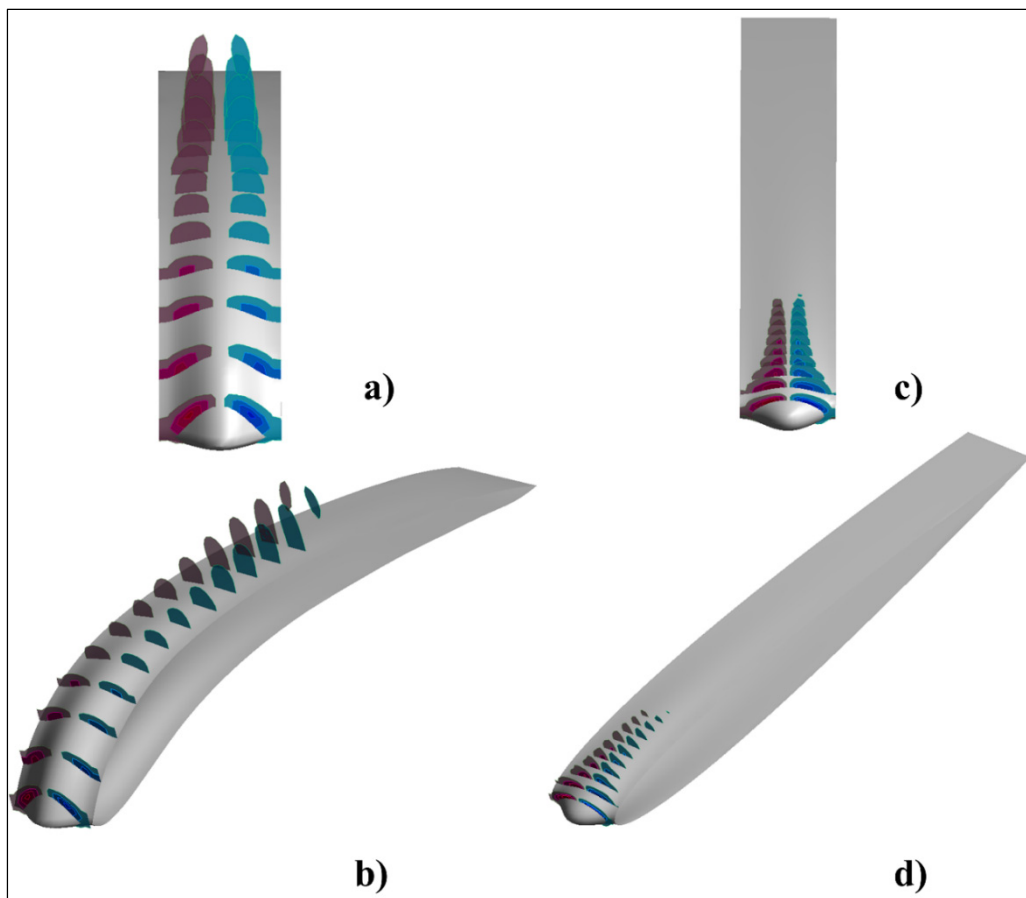


Figure 4.22 Top-front and side view of streamwise vortices on A3W11 airfoil at 16-degree angle of attack on RAF-19 (a and b) and NACA 0010 (c and d) airfoils

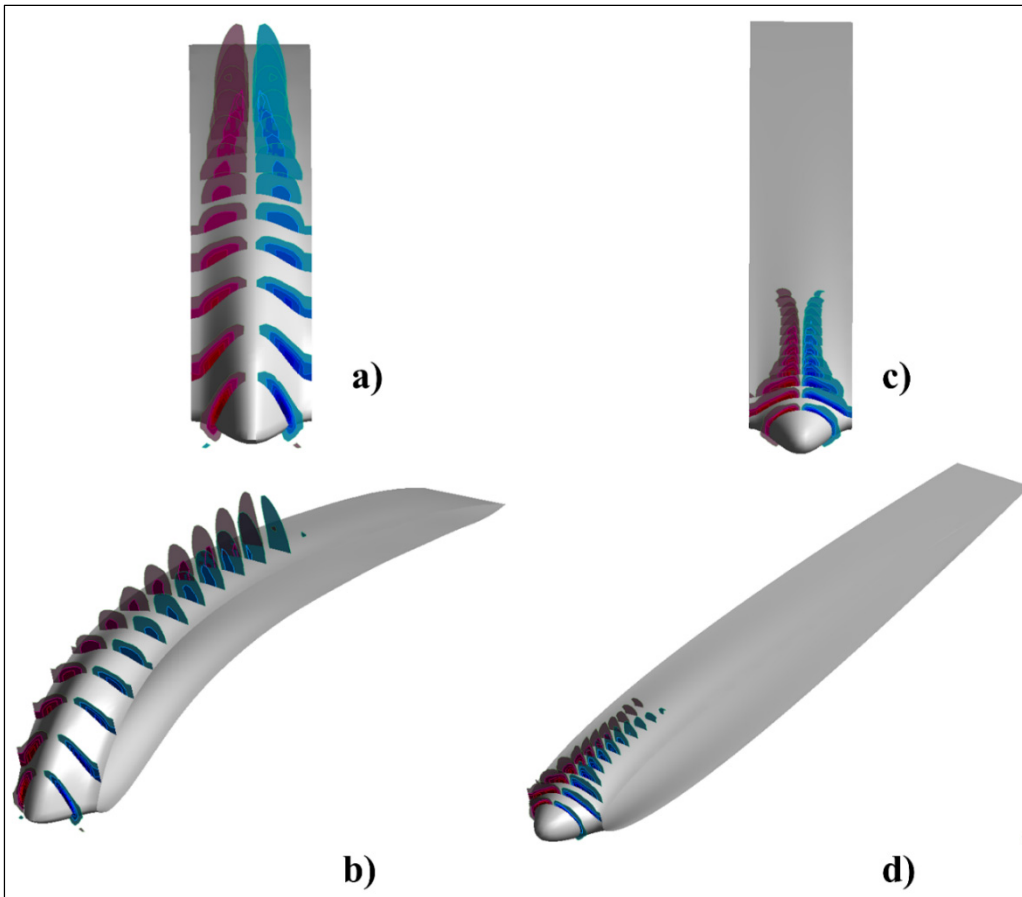


Figure 4.23 Top-front and top- side view of streamwise vortices on A6W11 airfoil at 16-degree angle of attack on RAF-19 (a and b) and NACA 0010 (c and d) airfoils

4.4 Discussions

- As mentioned in the literature section (Sudhakar et al., 2020), by implementing the leading-edge undulations on the high camber S1223 airfoil with the camber of 8% of the chord, the aerodynamic performance improvements were only observed at lower Reynolds numbers of 10^5 and 1.5×10^5 . Sudhakar et al. (2020) mentioned that since the airfoil curvature on the upper surface of the high-cambered airfoils is greater than the lower-cambered airfoils, the flow encounters a greater adverse pressure gradient downstream of their maximum suction for a given angle of attack. Thus, at a lower Reynolds numbers of 10^5 and 1.5×10^5 , the boundary layer is more susceptible to being separated and tubercles by increasing the momentum exchange on the boundary layer increase its aerodynamic performance. However, at Reynolds number of 2×10^5 , the laminar separated shear layer on the baseline S-1223 airfoil attains sufficient momentum during its transition process and reattaches to the airfoil upper surface even at higher angles of attack. Hence, the incorporation of tubercles did not result in a significant performance improvement at this Reynolds number. It should be noted that no analysis of the shape and structure of the counter-rotating streamwise vortices was performed in that research. In their research also the airfoil shape (thickness to chord ratio) was preserved during the generation of the modified airfoils and hence might result in the generation of spanwise bumps along the chord. Although in that research, no improvements were found at Reynolds number 2×10^5 on the S1223 airfoil (Sudhakar et al., 2020), in our research, on the high cambered RAF-19 airfoil with the higher camber of 10% of the mean-chord length, slightly higher C_{Lmax} and slightly higher lift coefficients at both pre-and post-stall angles of attack are observed on higher Reynolds number of 2.5×10^5 on smaller wavelength modified airfoils of RAF-19-A3W11 and RAF-19-A6W11. This slight increase in lift coefficient is due to the larger camber of RAF-19 airfoil in comparison with the S1223 airfoil which results in greater adverse pressure gradient on this airfoil in comparison with the S1223 airfoil. This greater adverse pressure gradient causes more flow separation on RAF-19 airfoil which as a result causes the tubercles to still be effective at higher Reynolds number of

2.5×10^5 . This research confirms the conclusion made in (Sudhakar et al., 2020) but besides, suggests that the effect of preserving the thickness to chord ratio while designing the modified airfoils and as a result, the generated spanwise bumps which delay the convergence and interaction of the two-neighboring counter-rotating streamwise vortices should also be taken into considerations.

- This postponing in the interaction of the streamwise vortices due to the generation of the spanwise bumps on the modified airfoils can give us some hints regarding the other hydrodynamic effect of spanwise bumps and dorsal fins on different fishes. Each fish body can be considered as a single lifting body with an undulation on its leading-edge part. As a postulation by this author, it seems, other than protecting the fish from rolling, these dorsal fins are also developed on different fishes like sail fish (Kurvers et al., 2017), based on their speed, length, and also their width to prevent the interaction of the streamwise vortices generated by the fish body. As a result, these spanwise bumps and dorsal fins increase the hydrodynamic performance of the fish at high angles of attack and hence increase their maneuverability.



Figure 4.24 Dorsal fin on Sail fish
Taken from Kurvers *et al.* (2017)

CHAPTER 5

THE EFFECT OF LEADING-EDGE TUBERCLES ON NACA 0010 AERODYNAMIC PERFORMANCE

Payam Mehregan^a and Louis Dufresne^b

^{a, b} Department of Mechanical Engineering, École de Technologie Supérieure,
1100 Notre-Dame West, Montreal, Quebec, Canada H3C 1K3

Paper submitted to the Journal of Aircraft, July 2022

5.1 Abstract

In this research, the effect of leading-edge tubercles on the aerodynamic performance of the NACA 0010 airfoil is numerically analyzed using the software ANSYS/CFX and the $k-\varepsilon$ turbulence modeling, at the Reynolds number of 2.5×10^5 . It is observed that on the modified airfoils, the boundary layer is energized by the counter-rotating streamwise vortices generated by the tubercles. The effect of amplitude and wavelength size of tubercles on the strength and interaction of the streamwise vortices and consequently their effect on the lift and drag coefficient of the modified airfoils are discussed. Results show that while increasing the amplitude of the tubercles increases the "effective mixing" of the streamwise vortices, increasing the wavelength of the tubercles increases the distancing between the vortices and hence increases their "effective length". Thus, comparing the airfoils with close values of amplitude to wavelength ratio sizes, higher lift coefficient values are observed at post-stall angles of attack, on airfoils with a larger amplitude and wavelength sizes of tubercles.

5.2 Introduction

In recent years, the increasing demand for devices, such as micro-air vehicles, small unmanned aerial vehicles, and wind turbines, has attracted researchers to investigate the aerodynamic efficiency of wings at low Reynolds number flow regimes, in which the flow behaves as an incompressible one. At these Reynolds numbers and laminar boundary layers the possibility of flow separation and stall increases causing a reduction in aerodynamic performance as well as the possibility of reduction in fatigue life of the devices working in these flow regimes (Zhang et al., 2013).

To improve the wings' aerodynamic performance, passive and active boundary layer flow control methods may be used. Considering that the passive flow control methods mainly rely on stationary components, they have higher manufacturing, maintenance, and economic viability in comparison with the active flow control methods. Vortex generators, roughness and riblets on the suction side of the airfoils are some examples of passive flow control devices (Forster & White, 2014; Zhang et al., 2013).

Flow control devices are also classified according to their design goals to "lift enhancement" and "drag reduction". Airfoil's shape optimization (e.g., by increasing the camber), and delaying the boundary layer separation by methods such as increasing the momentum exchange within the boundary layer (e.g., vortex generators) and restriction of the spanwise flow (e.g., wing fences), are some examples of passive lift enhancement flow control methods. Laminar-to-turbulent boundary layer transition delay (e.g., compliant coatings), and reduction of the turbulent fluctuations (e.g., riblets) are some examples of passive drag reduction flow control methods (Hansen, 2012).

Increasing lift generation, and postponing stall on wings can have many benefits, such as increasing the power generation on wind turbines and increasing the efficiency of ceiling fans. Moreover, it increases the maneuverability and stability of UAVs and also reduces their take-off and landing distances (Bolzon et al., 2016b; Hansen, 2012).

Recently, researchers have attempted to enhance the aerodynamic performance of wings with a new type of passive flow control method known as "leading-edge tubercles/protuberances". These tubercles can be found in nature, for example, on the leading-edge part of the humpback whale's pectoral flippers. Humpback whales are mammals capable of impressive maneuverability. Despite their large size of about 12-18m and a massive weight of about 30-40 tons, they can execute complex underwater rolls and rapid pursuit of their prey (Taheri, 2018) and they are even able to perform somersaults (Bolzon et al., 2014). These whales are the only baleen whales that rely on maneuverability to capture prey (Fish et al., 2008). Scientists have attributed this high level of maneuverability to their powerful flippers that have rounded tubercles on the leading-edge part (Bushnell & Moore, 1991; Fish & Battle, 1995; Sudhakar et al., 2020; Woodward et al., 2006). Besides, they postulated that these tubercles function as vortex generators, which postpone stall by generating streamwise vortices and increasing the momentum exchange within the boundary layer (Fish & Battle, 1995). Thus by increasing lift coefficients at high angles of attack and postponing stall, tubercles can increase the maneuverability of the whale and helps the whale in capturing its prey (Fish et al., 2008; Hain et al., 1981).

A significant amount of research has since been performed on idealized models of Humpback whale flippers, and 2D wings to understand the aerodynamic effect of leading-edge tubercles and their underlying flow mechanism. The most important one of them is summarized below.

An experimental study on 3D idealized humpback whale flipper models, one with a smooth leading-edge and the other with scalloped one, at a Reynolds number of 5×10^5 (Miklosovic et al., 2004), showed that the scalloped model increases the stall angle by 40%, the maximum lift coefficient by 6%, reduces drag at post-stall angles of attack and increases the lift to drag ratio for all the angles of attack studied except for the angles of attack ranging between $10 < \alpha < 12$ degrees. The author postulated that there are analogies between the leading-edge tubercles and vortex generators, which cause a greater momentum exchange within the boundary layer, preventing flow separation. Numerical simulation (Carreira Pedro & Kobayashi, 2008) on the

same smooth and scalloped flipper models using the same settings of (Miklosovic et al., 2004) showed lift and drag coefficients with an acceptable agreement with the experiment (Miklosovic et al., 2004). It should be noted that, the flipper models tested (Carreira Pedro & Kobayashi, 2008) were planar but tapered. Thus, the Reynolds number at the tip was lower than at the root; hence, the flow separates in the leading-edge at the tip, whereas near the root, trailing edge flow separation was observed. Based on the flow visualization results, the author concluded that the streamwise vortices generated by the tubercles, energize the boundary layer, and delay the trailing edge flow separation. In addition, these vortices have effects similar to wing fences, and confine the leading-edge flow separations to the tip region (Carreira Pedro & Kobayashi, 2008).

Furthermore, researchers analyzed the effect of tubercles on 2D wings. Although tubercles produced an increase in aerodynamic performance on idealized flipper models (Carreira Pedro & Kobayashi, 2008; Miklosovic et al., 2004), the effect of tubercles on (2D) symmetric wings (that have a uniform spanwise stall) was a reduction in the lift coefficient at pre-stall angles of attack and an improvement in lift coefficient at post-stall angles of attack (Hansen et al., 2011; Johari et al., 2007; Miklosovic et al., 2007). Meanwhile, experimental flow visualization results on these symmetric 2D-wings with leading-edge tubercles (Johari et al., 2007; Miklosovic et al., 2007) showed that the reduction in pre-stall lift coefficient is due to the flow separations that originate from the troughs between the tubercles (near the leading edge). Besides, the flow stays attached behind the tubercle peaks at post-stall angles of attack, while the flow over the baseline airfoil totally separates. Thus, it was concluded that the airfoils with leading-edge tubercles do not stall in the traditional way with a sudden loss of lift, and their stall can be identified as the point at which the amount of lift generated begins to decrease with the angle of attack (Johari et al., 2007). Steady-state numerical simulations using Spalart–Allmaras turbulence modeling (Dropkin et al., 2012) with the same settings as (Johari et al., 2007) also showed good agreement with the experimental data and confirmed that the flow separation originates from the troughs between the tubercles.

Some authors (Hansen et al., 2011; Miklosovic et al., 2004; Miklosovic et al., 2007; Zhang et al., 2013) suggested that there are similarities between the leading-edge tubercles and vortex generators or small delta wings (Custodio, 2012). The reductions in pre-stall aerodynamic performance would then be mostly related to the upwash (suction) of the vortical flow that causes the early separation of the flow behind the trough sections at pre-stall angles of attack (Miklosovic et al., 2007). However, Van Nierop *et al.* (2008) believe that since the amplitude and wavelength of the tubercles are much larger than the thickness of the boundary layer, the mechanism responsible for aerodynamic improvements on the lifting surfaces with tubercles must be different than the vortex generators. By developing an analytical model, Van Nierop *et al.* (2008) conclude that regarding the smaller chord length behind the troughs (chord minima), larger pressure gradients exist there. Therefore, the troughs between tubercles stall at lower angles of attack than the peaks and thus, the separation originates from there. Also, regarding the non-uniform downwash that reduces the effective angle of attack behind the peaks, more delayed separation exists there. The spanwise flow was not considered in that research (Van Nierop et al., 2008).

Keeping in mind that analyzing the effect of amplitude and wavelength sizes on finite span wings is more complex due to the 3D effects, some research was done on 2D wings to understand the aerodynamic effect of tubercles with different amplitude and wavelength sizes. Some research also mentioned that the amplitude size of the tubercles has more influence on the airfoil's aerodynamic performance than their wavelength sizes (Johari et al., 2007; Malipeddi, Mahmoudnejad, & Hoffmann, 2012). However, other research questioned this idea (Hansen et al., 2011). Some researchers observed a decrease in the lift-to-drag ratio of a rudder by reducing the wavelength of the tubercles at Reynolds numbers between 7×10^5 to 9×10^5 (Hansen, 2012; Weber et al., January, 2010). Some, however, observed improvements in lift coefficient by reducing the wavelength of the tubercles up to a certain limit of wavelength sizes. After that limit, reducing the wavelength of the tubercles resulted in a decrease in the lift coefficient of the modified airfoils (Hansen et al., 2011).

Tubercles have been shown to behave in a similar manner to counter-rotating vortex generators (Hansen et al., 2011). It was then suggested (Hansen et al., 2011) that the optimum amplitude and wavelength of the tubercles have some analogies with the optimum spacing and height of vortex generators. It was postulated that the airfoils with the same size of amplitude to wavelength ratio, have the equivalent maximum angle of leading-edge sweep angle relative to free-stream flow and thus have the same vortex strength. It was also postulated that on the smaller wavelength airfoils, the vortices are spaced more closely together and therefore more likely to interact with one another. This, causes the onset of unsteadiness to occur further upstream, leading to an increase in turbulence and the momentum exchange within the boundary layer and, thus, a more uniform attachment of the flow to the upper surface of the airfoil (Hansen et al., 2011).

One of the first works that show the interaction of the streamwise vortices on 2D wings with leading-edge tubercles (Custodio, 2012) was done at Reynolds numbers of 1.5×10^4 , 1.8×10^5 , and 4.5×10^5 . The analysis was done on the single NACA 634-021 modified airfoil with the amplitude and wavelength of $0.12C$ and $0.5C$ respectively, where C is the chord length. The author observed that at spatial locations ranging from $0C$ to $0.12C$, as the angle of attack is increased, the spanwise distribution of the neighboring counter-rotating streamwise vortices tends to remain symmetric. However, at spatial locations greater than $0.12C$, this symmetry breaks down. By increasing the angle of attack, as the strength of the neighboring vortices increase, the interactions of the streamwise vortices generate asymmetry within the vorticity distribution. This causes the neighboring vortices to change in size and shape. The author mentioned that the vortex interaction leads to the stretching and annihilation of the vortices, and as the counter-rotating vortices interact, vorticity is reduced, and stall characteristics become apparent. The height of the vortices changed with the angle of attack as well, with vortices showing signs of lifting off from the surface at high angles of attack (Custodio, 2012).

As discussed, the effect of leading-edge tubercles' amplitude and wavelength sizes, on the aerodynamic performance of the 2D wings was discussed in different research studies. However, to the best of our knowledge, there was no research focused on the effect of the

amplitude and wavelength sizes of the leading-edge tubercles on the circulation and interaction of the streamwise vortices. Hence, no research could make a formal quantitative observation, to justify the aerodynamic performance changes observed by changing the wavelength, amplitude, and amplitude to wavelength ratio sizes of the tubercles. The main objective of this research is thus, to analyze the effect of tubercles' amplitude, wavelength, and amplitude to wavelength ratio sizes on the circulation and interaction of the streamwise vortices and as a result, their effect on the aerodynamic performance of a symmetric airfoil with leading-edge tubercles using numerical simulations. The second objective of this research is do more analysis and discussions on the separated flow regions that are generated on the modified airfoils at pre-stall angles of attack.

In the following sections, the geometrical configuration and the numerical simulation setting of the parametric study that is performed on one baseline and five modified airfoils are first discussed. Subsequently, in the result section, the effect of amplitude, wavelength, and amplitude to wavelength ratio sizes on the integral quantities of lift and drag coefficients are explained. After that, the integral quantities results are analyzed by discussing the effect of amplitude, wavelength, and amplitude to wavelength ratio sizes on the circulation and interaction of the streamwise vortices generated by the tubercles, and the discussion will end with some concluding remarks.

5.3 Methodology

The methodology is first discussed by presenting the geometrical configurations in section 5.3.1. After that, the numerical equations, and mesh convergence study are discussed in sections 5.3.2, and 5.3.3 respectively. The validation of the baseline airfoil is then discussed in section 5.3.4.

5.3.1 Geometrical configurations

The Symmetric NACA 0010 airfoil with a maximum thickness of 10% of the chord is used as the cross-sectional profile of the baseline and modified airfoils. Thus, the baseline airfoil and

five modified airfoils with a NACA 0010 airfoil cross-sectional profile with varying wavelength and amplitude sizes are compared in this research. The amplitude (A) and wavelength (W) of the modified airfoils are selected based on the same percentage as the research of Hansen et al. (Hansen et al., 2011), shown in Table 5.1. These values fall in the same range of estimated values for the humpback whale flipper tubercles (Fish & Battle, 1995).

Table 5.1 Tubercles' amplitudes and wavelength sizes

Configurations	Label	A/W ratio
A=0	Baseline	0
A=30 (0.03C), W=110 (0.11C)	A3W11	0.27
A=60 (0.06C), W=110 (0.11C)	A6W11	0.54
A=60 (0.06C), W= 210 (0.21C)	A6W21	0.28
A=60 (0.06C), W= 430 (0.43C)	A6W43	0.14
A=110 (0.11C), W= 430 (0.43C)	A11W43	0.26

To design the modified airfoils, the chord length of the undulating cases varies according to Eq. (5.1) used in (Skillen et al., 2015). Where in Eq. (5.1), Z is the spanwise orient and \bar{C} is the mean chord length.

In order to reduce the computational cost in this study, only one tubercle is studied as shown in Figure 5.2 rather than using multiple tubercles, such as what is shown in Figure 5.1. This work also helps us to better analyze the effect of streamwise vortices, which will be discussed in next sections. In addition, to understand the effect of streamwise vortices on airfoils with multiple tubercles, it is required to first know the effect and behavior of the streamwise vortices on only one tubercle. After that, the effect of streamwise vortices on airfoils with multiple tubercles could be better understood. All the modified airfoils are designed to have the same mean chord length. Thus, all the airfoils have an average chord length of 1 and a span length equal to their wavelength sizes, as shown in Figure 5.2.

$$C(z) = A \cos\left(\frac{2\pi z}{W}\right) + \bar{C} \quad (5.1)$$

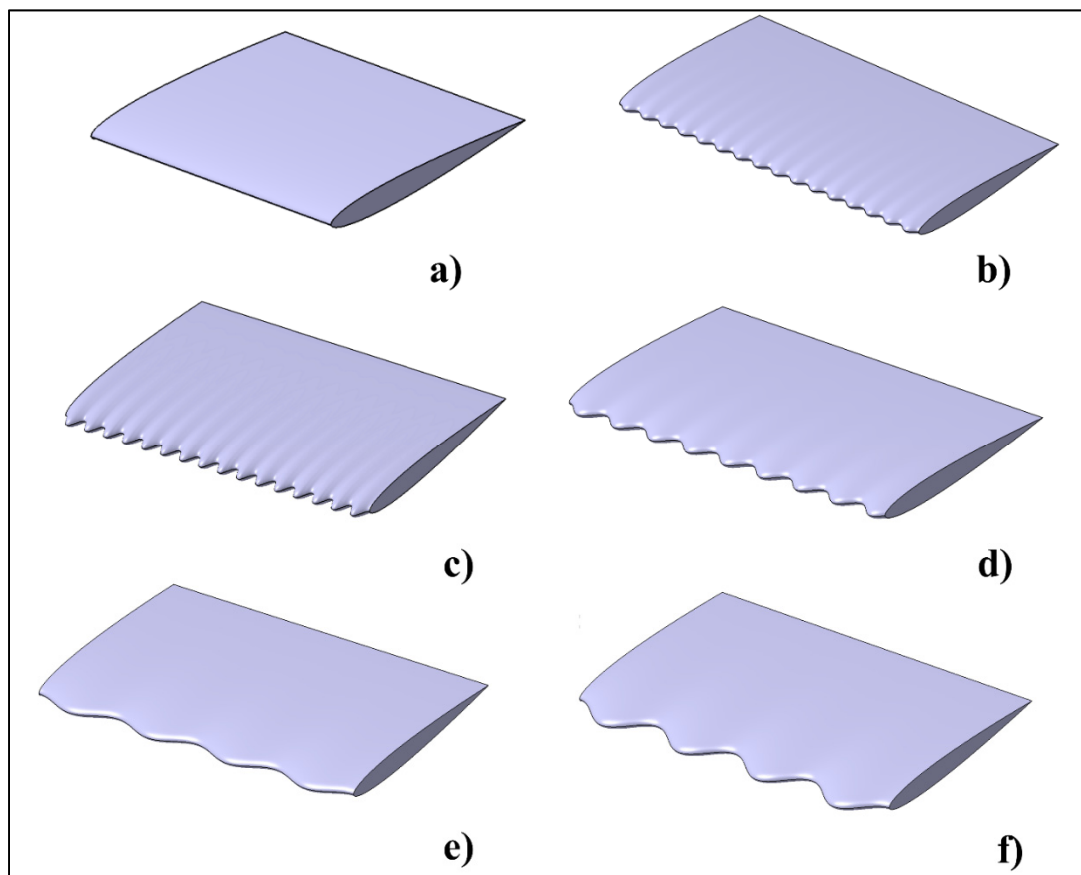


Figure 5.1 Modified airfoil geometries with multiple tubercles a) baseline
b) A3W11 C) A6W11 D) A6W21 E) A6W43 and F) A11W43

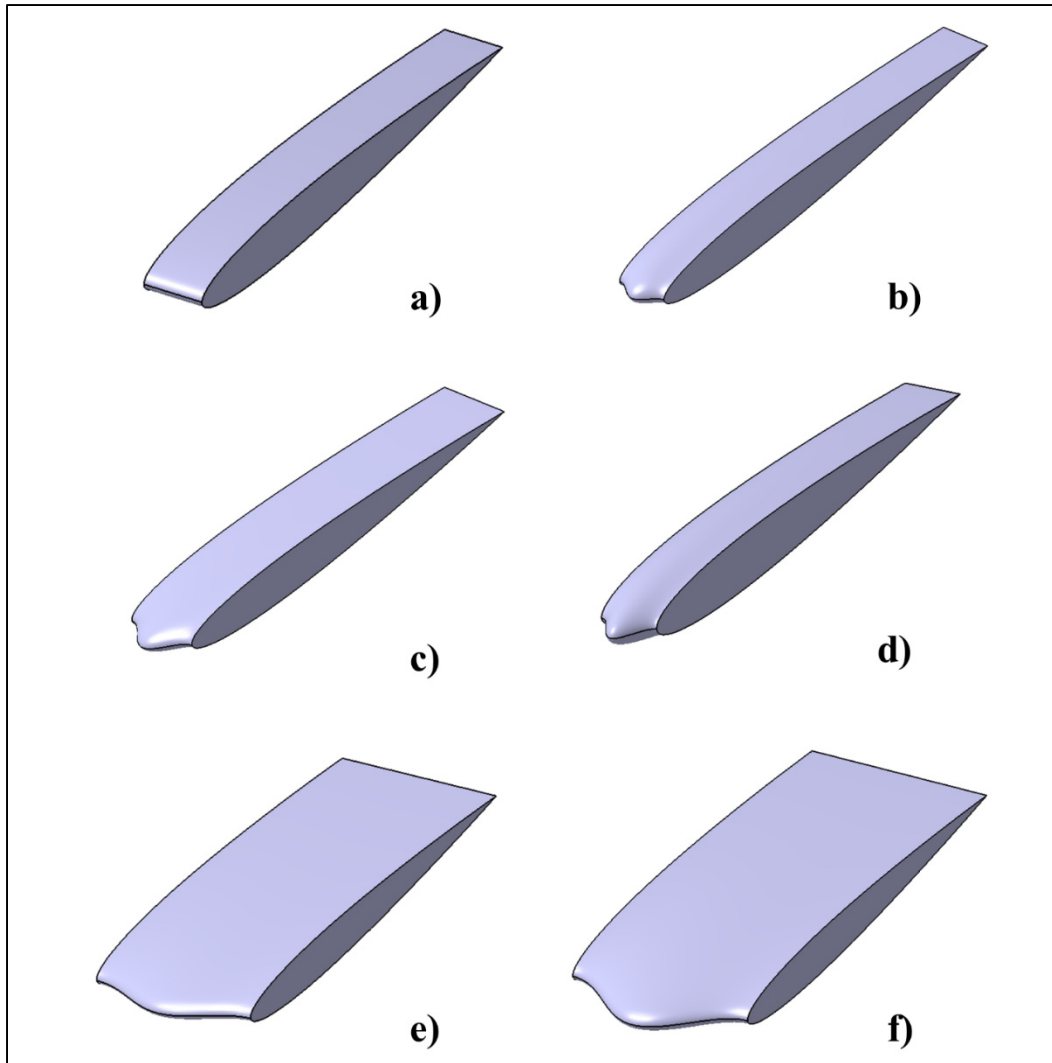


Figure 5.2 Modified airfoil geometries with single tubercles a) baseline b) A3W11 C) A6W11 D) A6W21 E) A6W43 and F) A11W43

5.3.2 Equations and turbulence modeling

In this research, the $k-\varepsilon$ turbulence model (ANSYS, 2016; Spalding, 1974) is used to analyze the baseline and modified airfoils. Working with limited computational resources, the mesh refinement is set to a first node at $y^+ > 30$. The value of $y^+ > 30$ was chosen based on the recommendations mentioned in (Spalding, 1974; Wilcox, 1998). Besides that, in other numerical researches done on the effect of leading-edge tubercle on flipper models such as the

research of Pedro & Kobayashi (2008), the chosen value of $y^+ > 30$ has proved to provide good agreement of the numerical results in comparison with the experimental data.

The numerical results show good agreement with the experimental data available for the validation of the results on the baseline NACA 0010 airfoil, which will be discussed in the next sections. The detailed formulation of the turbulence model used in this research is as follows:

5.3.2.1 k - ε turbulence modeling

The continuity and momentum equations used in the k - ε turbulence modeling (Spalding, 1974; Wilcox, 1998) are shown in Eq. (5.2) and (5.3), respectively:

$$\frac{\partial \rho}{\partial t} + \frac{\partial}{\partial x_j} (\rho U_j) = 0 \quad (5.2)$$

$$\frac{\partial \rho U_i}{\partial t} + \frac{\partial}{\partial x_j} (\rho U_i U_j) = -\frac{\partial p'}{\partial x_i} + \frac{\partial}{\partial x_j} \left[\mu_f \left(\frac{\partial U_i}{\partial x_j} + \frac{\partial U_j}{\partial x_i} \right) \right] \quad (5.3)$$

In the above equations, U_i and U_j are the i and j components of velocity respectively, ρ is the density considered constant (due to incompressible flow simulations), μ_f is the effective viscosity accounting for turbulence shown in Eq. (5.4), P is the pressure, and p' is the modified pressure as shown in Eq. (5.5) .

$$\mu_f = \mu + \mu_t \quad (5.4)$$

$$p' = P + \frac{2}{3} \rho K + \frac{2}{3} \mu_f \frac{\partial U_j}{\partial x_j} \quad (5.5)$$

The k - ε model is based on the eddy viscosity concept shown in Eq. (5.4), and assumes that the turbulence viscosity μ_t is linked to the turbulence kinetic energy and dissipation via Eq. (5.6), where C_μ is a constant and its value is illustrated in Table 5.2.

$$\mu_t = C_\mu \rho \frac{k^2}{\varepsilon} \quad (5.6)$$

In the k - ε turbulence modeling, k is the turbulence kinetic energy and ε is the turbulence dissipation. The values of k and ε will be obtained using their transport equations shown in Eq. (5.7) and (5.8), respectively.

$$\frac{\partial(\rho k)}{\partial t} + \frac{\partial}{\partial x_j} (\rho U_j k) = \frac{\partial}{\partial x_j} \left[\left(\mu + \frac{\mu_t}{\sigma_K} \right) \frac{\partial k}{\partial x_j} \right] + P_k - \rho \varepsilon + P_{kb} \quad (5.7)$$

$$\frac{\partial(\rho \varepsilon)}{\partial t} + \frac{\partial}{\partial x_j} (\rho U_j \varepsilon) = \frac{\partial}{\partial x_j} \left[\left(\mu + \frac{\mu_t}{\sigma_\varepsilon} \right) \frac{\partial \varepsilon}{\partial x_j} \right] + \frac{\varepsilon}{k} (C_{\varepsilon 1} P_k - C_{\varepsilon 2} \rho \varepsilon + C_{\varepsilon 1} P_{\varepsilon b}) \quad (5.8)$$

The $C_{\varepsilon 1}$, $C_{\varepsilon 2}$, σ_K , and σ_ε in Eq. (5.7) and (5.8) are constants and their values are shown in Table 5.2. P_k is the turbulence production due to viscous forces shown in Eq. (5.9), and P_{kb} and $P_{\varepsilon b}$ are the production terms due to buoyancy (Spalding, 1974; Wilcox, 1998).

$$P_k = \mu_t \left(\frac{\partial U_i}{\partial x_j} + \frac{\partial U_j}{\partial x_i} \right) \frac{\partial U_i}{\partial x_j} - \frac{2}{3} \frac{\partial U_j}{\partial x_j} \left(3\mu_t \frac{\partial U_j}{\partial x_j} + \rho k \right) \quad (5.9)$$

Table 5.2 Model coefficients used in the k- ε turbulence modeling formulation

$C_{\varepsilon 1}$	1.44
$C_{\varepsilon 2}$	1.92
σ_K	1
σ_{ε}	1.3
C_{μ}	0.09

5.3.2.2 Scalable wall function

To calculate the wall-shear stresses, the scalable wall function is used (ANSYS, 2016; Menter & Esch, 2001). In a scalable wall function an alternative velocity scale of u^* is used (Eq. (5.10)), which remains finite as U_t goes to zero. Then the y^* can be defined as Eq. (5.11) and u_{τ} can be obtained by Eq. (5.12).

$$u^* = C_{\mu}^{1/4} k^{1/2} \quad (5.10)$$

$$y^* = (\rho u^* y) / \mu \quad (5.11)$$

$$u_{\tau} = \frac{U_t}{\frac{1}{\kappa} \ln(y^*) + L} \quad (5.12)$$

In the above equations, u_{τ} is the friction velocity, y is the distance from the wall, y^* is the dimensionless distance from the wall in scalable wall-function, U_t is the known velocity tangent to the wall at a distance of y from the wall, κ is the von Karman constant and its value is 0.4, and L is a log-layer constant depending on wall roughness. The absolute value of the wall shear stress is then obtained from Eq. (5.13).

$$\tau_w = \rho u^* u_\tau \quad (5.13)$$

The scalable wall function limits the y^* value used in the logarithmic formulation by a lower value of:

$$\tilde{y}^* = \max(y^*, 11.06) \quad (5.14)$$

Where 11.06 is the value of y^* at the intersection between the logarithmic and the linear near wall profile. The computed \tilde{y}^* is therefore not allowed to fall below this limit.

At high angles of attack, on the modified airfoils the U-RANS simulation is performed due to the observed unsteadiness which will be explained in section G, when the unsteady flow behavior is discussed. To perform the U-RANS simulation, first a steady-state analysis is done to understand after how many iterations the steady-state solution for the aerodynamic coefficient become stable. It is observed that the steady-state solution for the aerodynamic coefficient of the modified NACA 0010 airfoils become stable (have uniform sin shape) after 45 iterations. Thus, 45 iterations per time-step is used. A time-step study is also carried out, and it is observed that for shorter time-step sizes below 0.25-time units, the lift and drag coefficient values remain constant. Thus, all the calculations are performed with the time-step size of 0.25-time units. The final solution of the U-RANS simulation for the aerodynamic coefficients of all the modified airfoils become steady-state and as a result the U-RANS analysis is performed until the steady-state solution is achieved.

The governing equations for the $k-\varepsilon$ turbulence model are discretized via the Finite Volume-based Finite Element approach developed by ANSYS/CFX. On both steady-RANS and U-RANS simulations, a high resolution (bounded second-order upwind biased discretization) is chosen for advection scheme and for turbulence numerics, the high-resolution option is selected. The second-order backward Euler scheme is also chosen for transient scheme for U-RANS simulations.

A non-dimensional form is used. Thus, the Chord-length (C) and inlet velocity (U) are chosen as reference scales and the Reynolds number is chosen as 2.5×10^5 . To perform the numerical analysis, a rectangular domain with a width of $X/C = 25$, a height of $Y/C = 20$ and a depth equal to the span length or wavelength of each airfoil is created. For example, the domain's depth for the A6W11 airfoil is 0.11, while the domain's depth for the A6W43 airfoil is 0.43. The airfoils had a horizontal distance of 10 from the wind tunnel inlet, 15 from the outlet and a vertical distance of 10 from the upper and lower wind tunnel's upper and lower walls. The angle of attack is changed by rotating the airfoil around ($-Z$) axis. Free slip wall is chosen for upper and lower wall boundaries. A no-slip boundary condition is chosen for the airfoil wall. The uniform Cartesian velocity of 1 in the X direction is considered for the inlet. The pressure outlet is chosen as zero and the periodic boundary condition is applied in the lateral boundaries. The domain is divided into smaller segments to create smaller elements around the airfoil. The boundary condition and the computational model used in this study are shown in Figure 5.3.

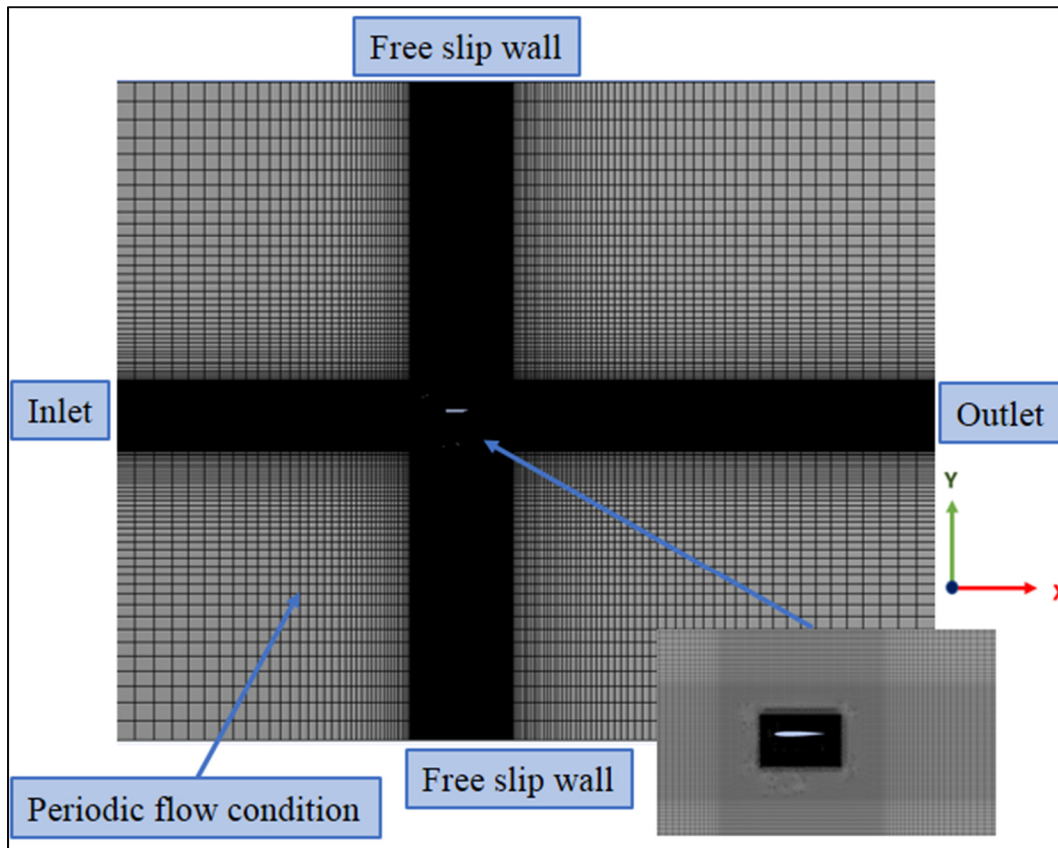


Figure 5.3 Computational domain with segmented mesh and the boundary conditions

5.3.3 Mesh convergence study

The mesh convergence study is carried out by increasing the number of elements in the inner most rectangular segment around the airfoil shown in Figure 5.3 at angle of attack of 6 degrees. The 6-degree angle of attack is chosen based on other literatures (e.g. the research of Dropkin et al. (2012)) and the inner rectangle is chosen to better analyze the effect of mesh resolution around the airfoil.

The results show that increasing the number of elements from 1.4×10^6 to 2.2×10^6 , does not yield significant changes in the generated values of lift and drag the drag coefficient as shown in Table 5.3.

Table 5.3 Mesh convergence study

	Number of elements	C_D	C_L
G₃	886336	0.027477	0.57985
G₂	1377552	0.025242	0.58822
G₁	2217621	0.025915	0.58904

The mesh with 1.4×10^6 elements is therefore considered adequate for this study. The same mesh setting is used for all the modified airfoils and their number of elements are increased based on their shape and wavelength sizes. The number of elements used to analyze the modified airfoils are illustrated in Table 5.4.

Table 5.4 Number of elements used in each airfoil with undulating leading edge

Airfoil	Number of elements
A3W11	1639054
A6W11	2240888
A6W21	3118716
A6W43	5508992
A11W43	5710483

The uncertainty resulting from the discretization in the computations were estimated using the procedure introduced by (Celik et al., 2008) which is based on Richardson extrapolation. The drag coefficient was chosen as the key parameter for this estimation. The grids, G₃, G₂ and G₁ were used for the uncertainty calculation which corresponds to the mesh refinement factor (r) of 1.15 and 1.17 between the mesh pairs respectively. The apparent order P of the method was solved as $P = 8.401012$ using the fixed-point iteration. As a result, the approximated relative error, and fine-grid convergence index were calculated as follows and the relative error

of 2.5% and the fine- grid convergence index of 1.16 % are reported for the computations done in this study.

$$e_a^{21} = \left| \frac{Cd1 - Cd2}{Cd1} \right| = 0.025969516 \quad (5.15)$$

$$GCI_{fine}^{21} = \frac{1.25 * e_a^{21}}{r_{21}^p - 1} = 0.011620102 \quad (5.16)$$

5.3.4 Baseline airfoil validation

As shown in Table 5.5 and Table 5.6, the NACA 0010 and SD8020 airfoils have almost the same geometric characteristics. Since the aerodynamic data for the NACA 0010 airfoil in reference such as (Abbott & Von Doenhoff, 1959) are at higher Reynolds numbers (in the order of 3×10^6 - 6×10^6), consequently, to validate the numerical results for the NACA 0010 airfoil, the numerical results are compared with the experimental data available for the SD8020 airfoil based in the research of Selig *et al.* (1995) that performed at lower Reynolds numbers.

Table 5.5 NACA 0010 airfoil characteristics (% C)

Max thickness	10
Max thickness position	30
Max camber	0
Max camber position	0

Table 5.6 SD 8020 airfoil
characteristics (% C)

Max thickness	10.1
Max thickness position	27.5
Max camber	0
Max camber position	0

The experiment of Selig *et al.* (1995) was carried out at the Reynolds number of 2.0×10^5 . The numerical results are validated using the model with 1.4×10^6 elements at steady state condition and using the same angles of attack and Reynolds numbers used in the research of Selig *et al.* (1995). Different turbulence modeling such as $k-\varepsilon$, Spalart-almaras, $k-\omega$, SST and etc. is tested in Ansys/CFX, and the results using the $k-\varepsilon$ turbulence modeling shows better agreement comparing with the experimental data. As shown in Figure 5.4 and Figure 5.5, good agreement of the results can be seen in both lift and drag coefficient values, respectively. The experimental drag coefficient values were only available up to 8.79 degrees. It should be noted that, the main notion of this research is to perform a parametric study. Thus, the goal was to have a “good enough” quantification of lift/drag coefficients to capture the trend which is sufficient to perform the parametric study. It should be also noted that the differences observed experimental and numerical lift coefficient values at higher angles of attack (around 16, and 18 degrees) are around 20%, which is considered acceptable.

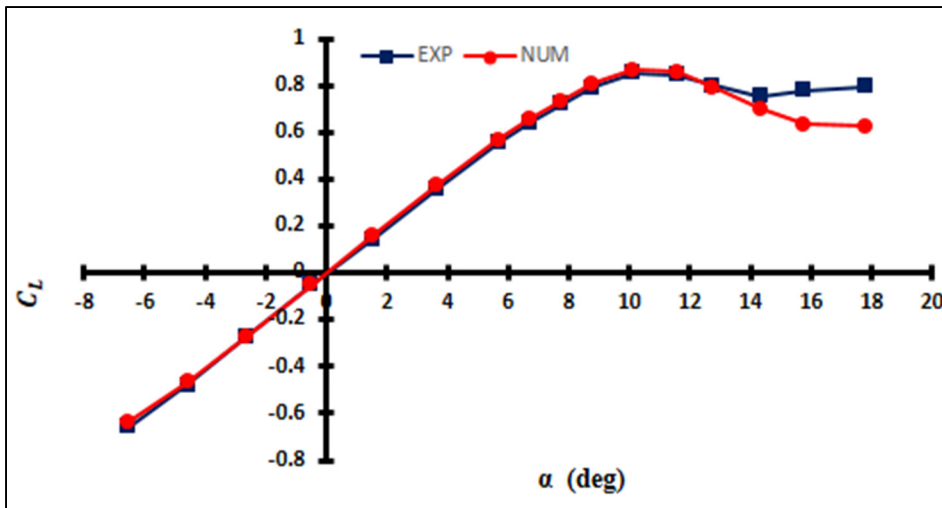


Figure 5.4 Comparison of the lift coefficients in the numerical simulation and experimental research of Selig et al. (1995)

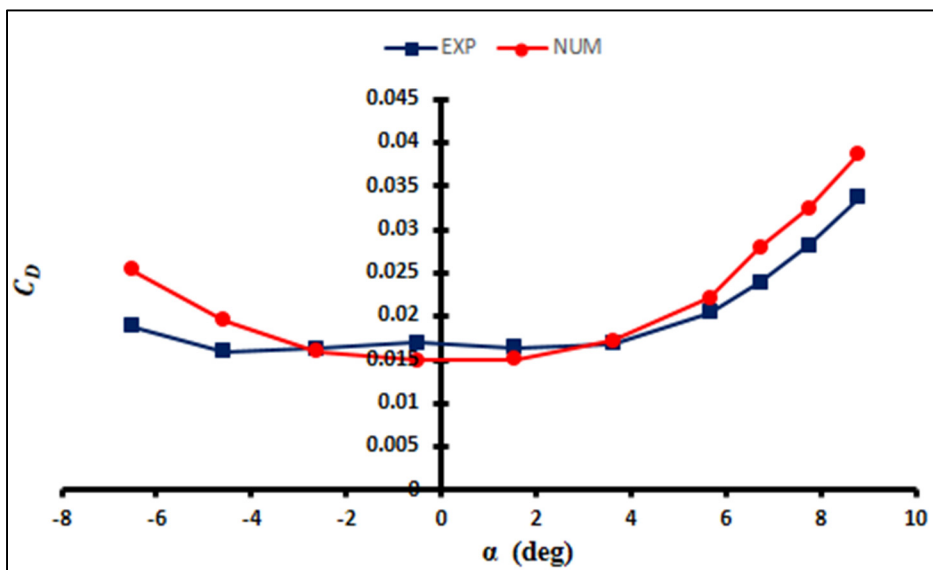


Figure 5.5 Comparison of the drag coefficients in the numerical simulation and experimental research of Selig et al. (1995)

To have a more "localized" validation of the results, the pressure coefficients are compared with the data obtained by the XFLR5 (XFOIL) code (Drela, 2000), and results with an acceptable level of agreement are obtained. For example, as shown in Figure 5.6, at a 0-degree

angle of attack, the XFLR5 (XFOIL) and ANSYS/CFX pressure coefficients on the suction sides of the baseline airfoil at chord-wise locations between $0.1C$ to $0.8C$ with an increment of $0.1C$ are compared and the results demonstrate good agreement.

Table 5.7 Comparison of the lift and drag coefficient obtained by the XFOIL code and ANSYS/CFX at a 0-degree angle of attack

	XFOIL	CFX
C_D	0.011	0.014
C_L	0.	0.0002

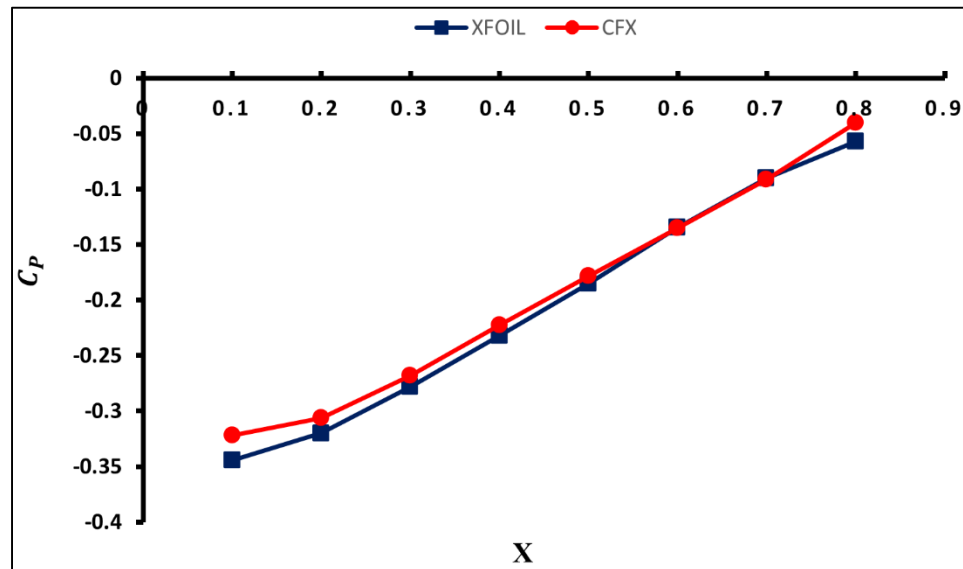


Figure 5.6 Comparison of the pressure coefficients obtained by XFOIL and ANSYS/CFX at a 0-degree angle of attack

Now that the mesh convergence study is done and the results on the baseline airfoil in case of lift, drag, and pressure coefficients are validated, the results can now be discussed.

5.4 Results

In this section, the effect of tubercles' amplitude, wavelength, and amplitude to wavelength ratio sizes on the integral quantities of lift and drag coefficients of the modified airfoils is first discussed. After that, in the subsequent sub-sections, the streamwise vortices and their convergence along the chord are explained. Then, the effect of amplitude and wavelength sizes of the tubercles on the circulation and interaction of the streamwise vortices will be analyzed. Consequently, the differences observed in the lift and drag coefficients results of the modified airfoils will be discussed, at a post-stall angle of attack of 16 degrees. In the end, the reason for the reduction in lift coefficient generation on the modified airfoils compared with the baseline airfoil at pre-stall angles of attack and its relation with the streamwise vortices will be described.

5.4.1 Integral quantities

In this section, the effect of tubercles' geometrical parameters, such as the amplitude, wavelength, and amplitude to wavelength ratio, on the integral quantities of lift and drag coefficients generated by the modified airfoils is discussed.

5.4.1.1 The effect of the amplitude of tubercles on integral quantities

In general, tubercles cause a reduction in the pre-stall lift coefficient while increasing the post-stall lift coefficient of the modified NACA 0010 airfoils. This trend is similar to trend observed in other research done on symmetric airfoils, such as the research of Hansen *et al.* (2011) and Johari *et al.* (2007).

To analyze the effect of amplitudes of the tubercles on lift and drag coefficients, two sets of results are compared, shown in Figure 5.7 and Figure 5.8 respectively. In the first set of results shown in Figure 5.7, the lift coefficient results show that by reducing the amplitude of tubercles, the C_{L_max} and lift coefficient at pre-stall angles of attack increase. It also shows that by increasing the amplitude of the tubercles, the pre-stall lift coefficient is reduced while the

post-stall lift coefficient improves. Increasing the amplitude of the tubercles also results in smoother stall characteristics. In the second set of results shown in Figure 5.8, decreasing the amplitude of the tubercles from A6W11 to A3W11 results in increasing lift coefficients at both pre-stall and post-stall angles of attack. The drag coefficient results on both set of results show that generally smaller amplitude airfoils generate a lower amount of drag coefficient.

5.4.1.2 The effect of the wavelength of tubercles on integral quantities

The effect of the wavelength of tubercles on lift and drag coefficients of the modified airfoils is illustrated in Figure 5.9. It can be seen from Figure 5.9, that by reducing the wavelength of the tubercles, the lift coefficient generally decreases at both pre- and post-stall angles of attack. The drag coefficient results show that the modified airfoils generate a higher amount of drag coefficients in comparison with the baseline airfoil except at 24-degrees. At 24-degrees, the modified airfoils generate lower drag coefficient in comparison with the baseline airfoil. The results show that generally by increasing the wavelength of the tubercles, the drag coefficients increase.

5.4.1.3 The effect of the amplitude to wavelength ratio of tubercles on integral quantities

The modified airfoils with close values of amplitude to wavelength ratio are compared in Figure 5.10. It can be seen from the results illustrated in Figure 5.10, that the $C_{L_{max}}$ is increased by reducing the amplitude and wavelength of the tubercles. For example, on the A11W43 airfoil with the largest amplitude and wavelength of tubercles, $C_{L_{max}}$ is the smallest. Meanwhile, the post-stall lift generation is increased by increasing the amplitude and wavelength of the tubercles. Thus, the A11W43 airfoil, acquires a higher post-stall lift coefficient, as well as the smoother stall characteristics in comparison with the other two airfoils with smaller amplitude and wavelength sizes. Results shown in Figure 5.10 also illustrate that the drag coefficient is increased by increasing the amplitude and wavelength sizes of the tubercles.

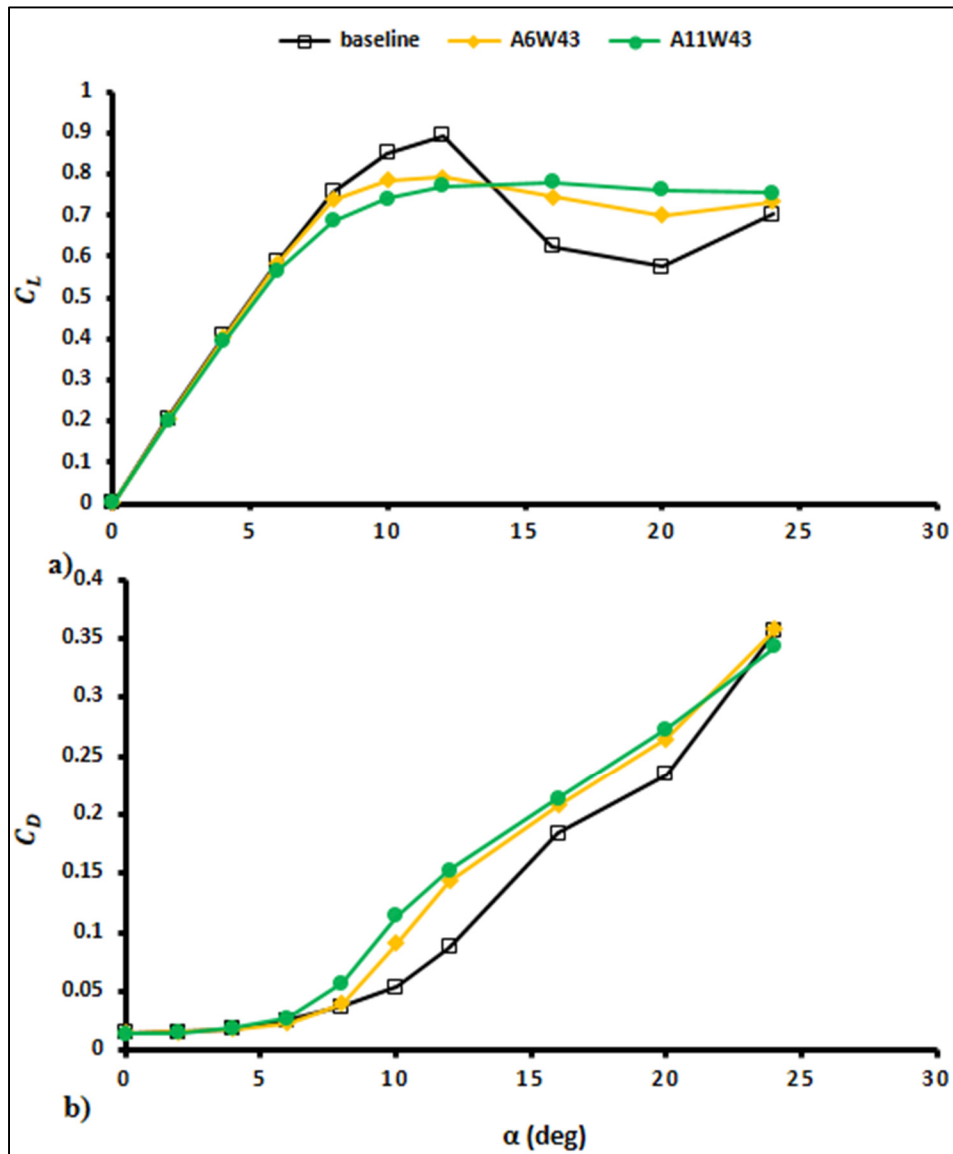


Figure 5.7 Analyzing the effect of the amplitude of tubercles on the lift coefficient (a) and drag coefficient (b) of the modified airfoils

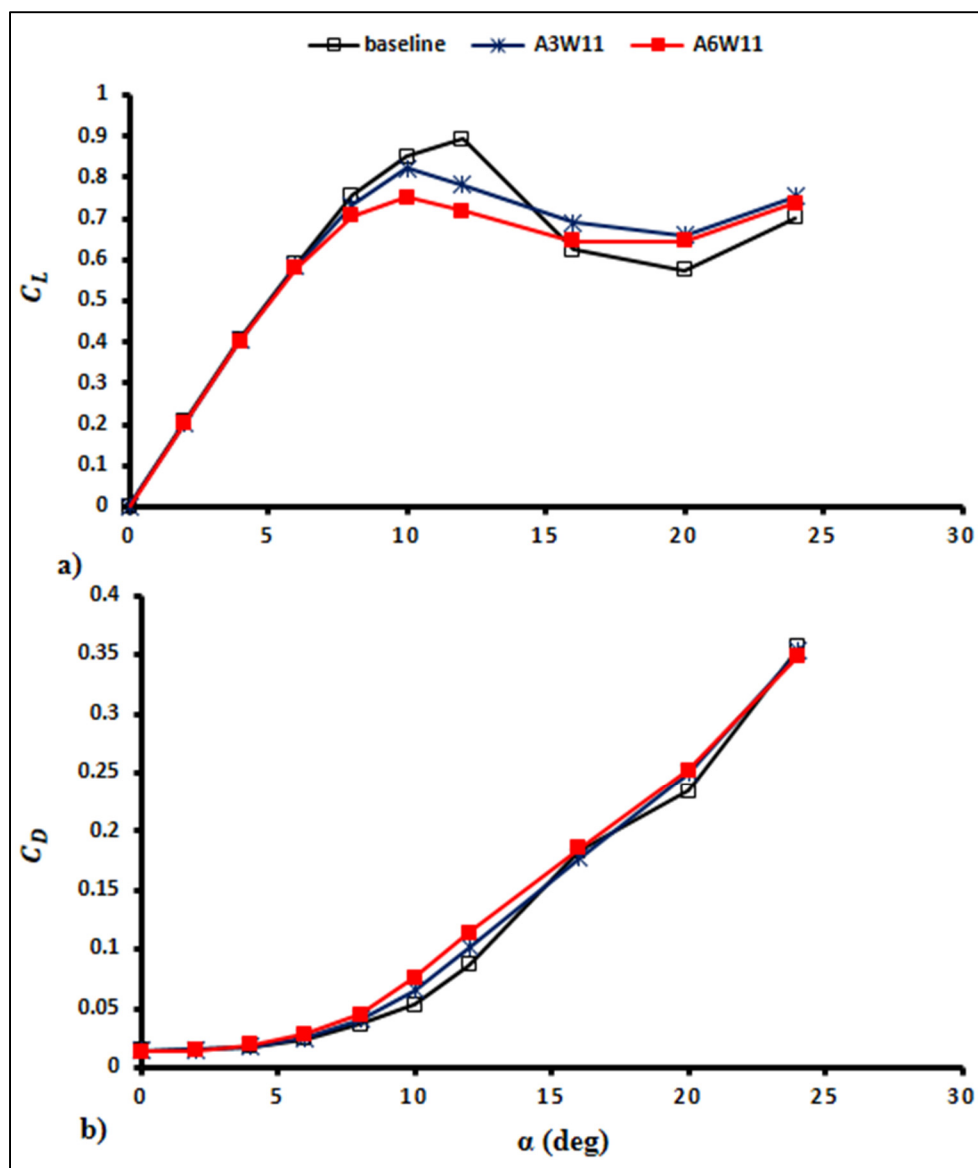


Figure 5.8 Analyzing the effect of the amplitude of tubercles on the lift coefficient (a) and drag coefficient (b) of the modified airfoils

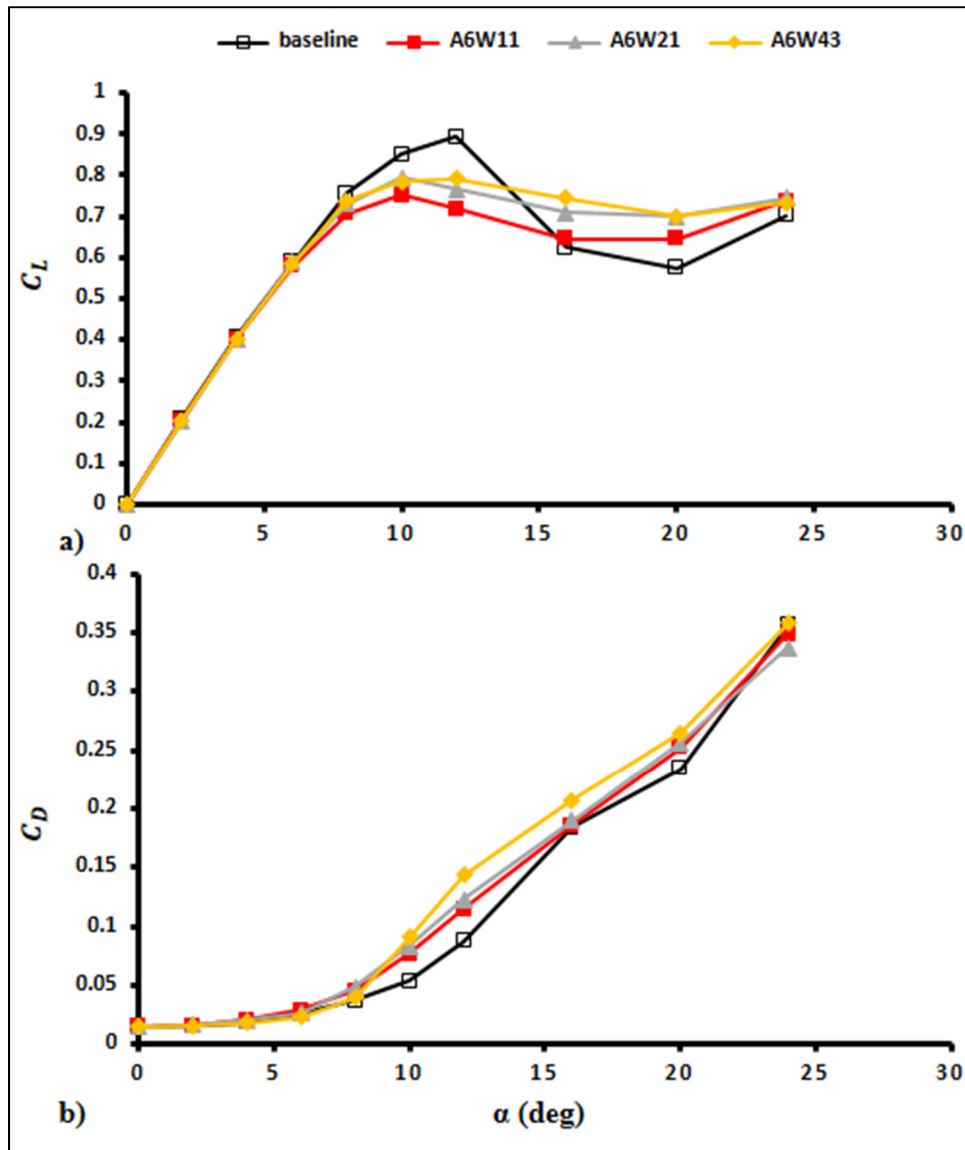


Figure 5.9 Analyzing the effect of the wavelength of tubercles on the lift coefficient (a) and drag coefficient (b) of the NACA 0010 modified airfoils

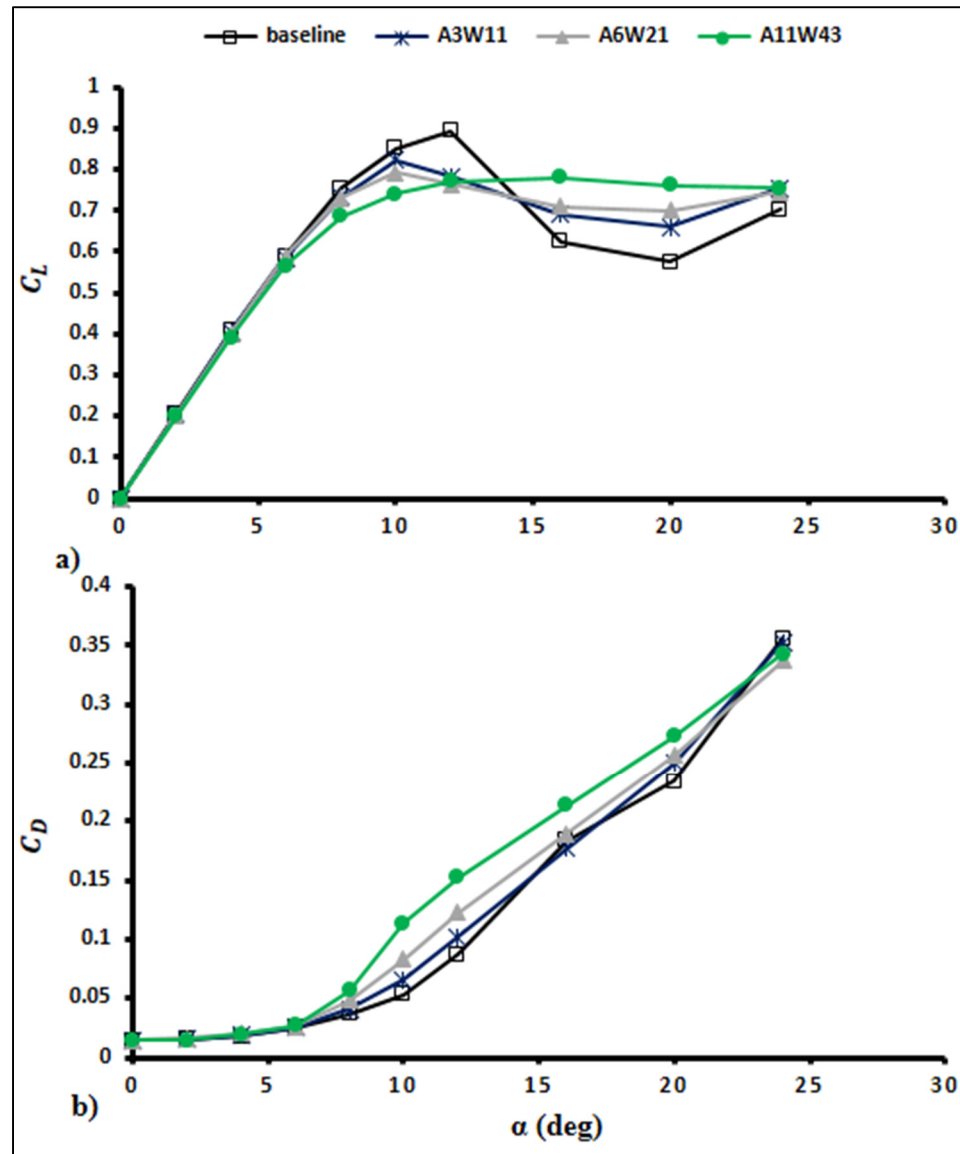


Figure 5.10 Analyzing the effect of the amplitude to wavelength ratio of tubercles on the lift coefficient (a) and drag coefficient (b) of the NACA 0010 modified airfoils

In general, in this section, it is noticed that tubercles reduce the pre-stall lift coefficient while increasing the post-stall lift coefficient, which is the same trend observed in previous research done on symmetric airfoils (Hansen et al., 2011; Johari et al., 2007). The results also show that by reducing the wavelength of the tubercles, the lift coefficient of the modified airfoils is

reduced. Meanwhile, comparing the modified airfoils with close values of amplitude to wavelength ratio has shown that by increasing the amplitude and wavelength of tubercles, the lift coefficient reduces at pre-stall angles of attack, however, at post-stall angles of attack the lift coefficient is increased by increasing the amplitude and wavelength of tubercles. Results also showed that the drag coefficient is increased by increasing the amplitude and wavelength, of tubercles.

5.4.2 The streamwise vortices

In the above section, the effect of amplitude, wavelength, and amplitude to wavelength ratio sizes of the leading-edge tubercles on the integral quantities of the lift and drag coefficient have been analyzed. To understand the effect of amplitude and wavelength sizes of tubercles on the lift and drag coefficient, the behavior and strength of the streamwise vortices on the modified airfoils should be first discussed.

5.4.2.1 Interaction of the streamwise vortices

The streamwise vortices on the A11W43 airfoil at 0, 4, 8, 10, 12, 16, 20 and 24 degrees of angle of attack are illustrated in Figure 5.11. The solid arrow line shows the flow direction relative to the dashed line, which indicates the modified airfoils chord line. It can be seen from Figure 5.11 that the maximum value of the streamwise vortices is generally increased by increasing the angle of attack. Besides that, at each angle of attack the strength of the streamwise vortices decrease in the chordwise direction. This figure also indicates another important general trend of the streamwise vortices. By increasing the angle of attack, the two neighboring, counter-rotating streamwise vortices at each chordwise location is converging towards each other while moving along the chord, until they start to interact and annihilate each other. After the vortex annihilation, the flow completely separates from the surface of the airfoil, which will be discussed more in section 8 of this research. This separation point moves towards the leading-edge by increasing the angle of attack. This trend is observed on all the modified airfoils, such as on A6W11 airfoil, where its relative figures are illustrated in Figure 5.12. It should be noted that to have a better comparison of the streamwise vorticity figures,

the vortices values in some figures of this research work are standardized. This standardization is done, based on the minimum and maximum values of vorticity, found between all the modified airfoils in angles of attack ranges between $0 < \alpha < 16$ degrees. Thus, the streamwise vortices values are standardized based on the minimum and maximum vorticity values of -98 and 98 respectively.

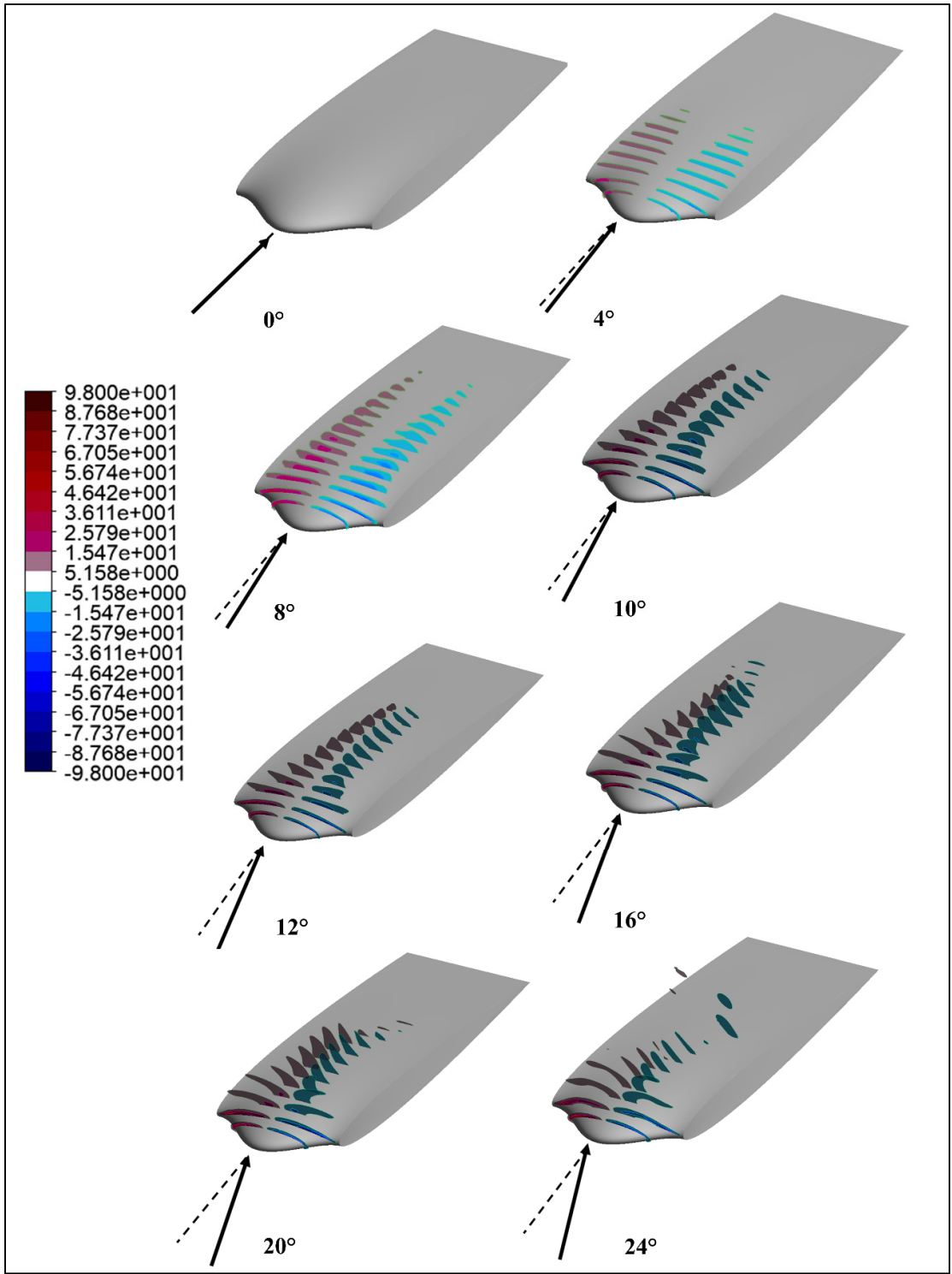


Figure 5.11 Streamwise vortices on A11W43 airfoil at 0, 4, 8, 10, 12, 16, 20, and 24 degrees of angles of attack

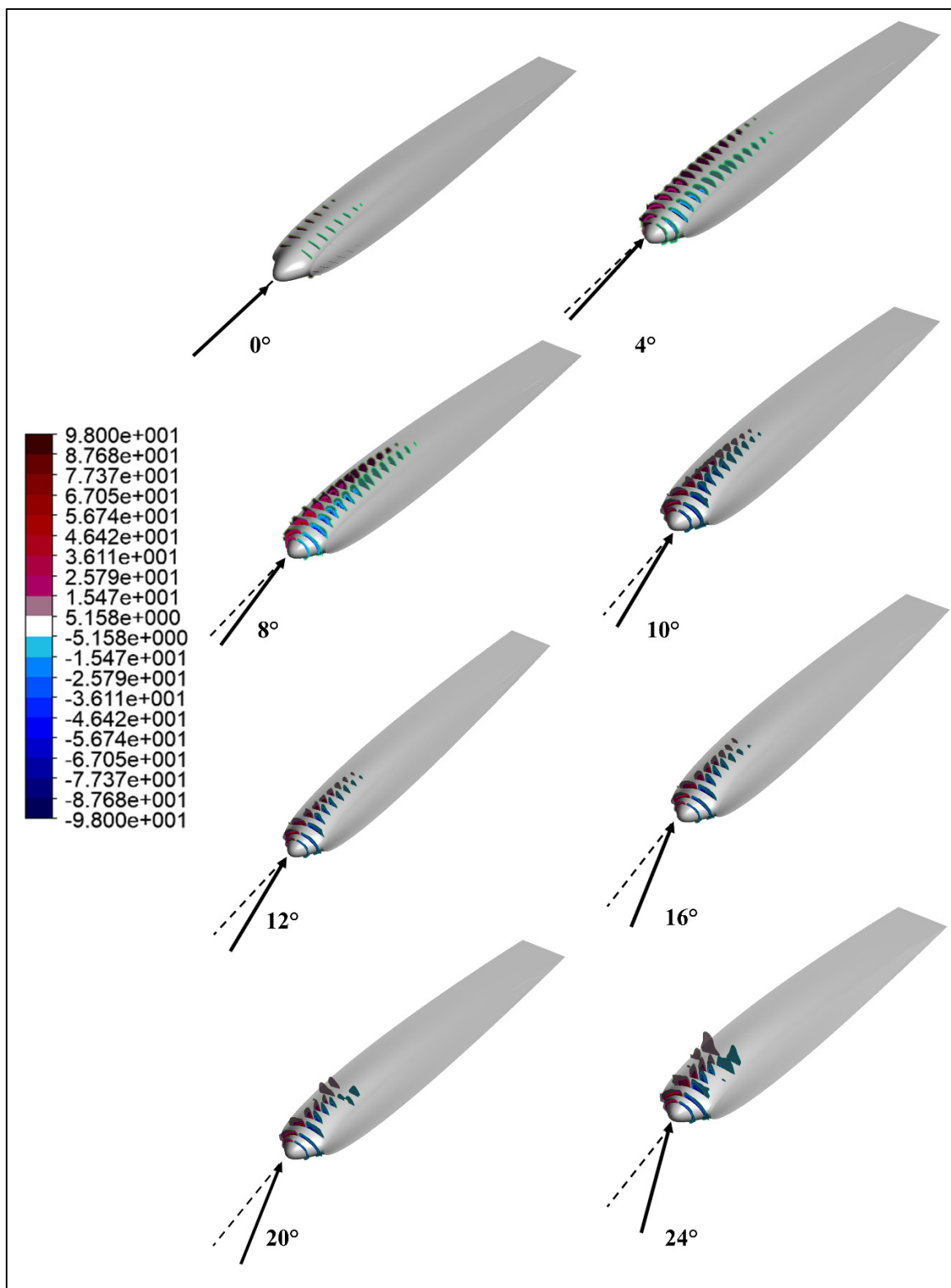


Figure 5.12 Streamwise vortices on A6W11 airfoil at 0, 4, 8, 10, 12, 16, 20, and 24 degrees of angles of attack

In this subsection, the convergence and interaction of the streamwise vortices at high angles of attack are discussed. Now it is time to analyze the circulation/strength of the streamwise vortices.

5.4.2.2 Circulation

In this subsection, the effect of amplitude, wavelength, and the amplitude to wavelength ratio of tubercles on the strength of the streamwise vortices is discussed. The strength of a vortex is quantified by its circulation value. To analyze the strength of streamwise vortices on modified airfoils, the circulation of these vortices is calculated using Eq. (5.17). In Eq. (5.17), $\vec{\omega}$ is the streamwise vorticity vector, \vec{n} is the vector normal to the surface s , ds is the element of surface area and Γ is the circulation. The calculations are done at a slice of $0.05C$ (5% of the mean chord length) at angles of attack of 0, 4, 8, 12, 16, 20 and 24 degrees from the upper surface of the modified airfoils to a distance of 0.5 above it. The calculation were done to a distance of 0.5 to make sure that all the streamwise vortices generated by the tubercles are included in the calculations.

$$\Gamma = \int_s \vec{\omega} \cdot \vec{n} ds \quad (5.17)$$

To be able to compare the circulation of streamwise vortices of modified airfoils, the circulation values are calculated per unit span of the airfoils. Thus, the circulations calculated on each airfoil are divided by its wavelength size. For example, the circulation of the A6W43 airfoil is divided by 0.43, and the circulation of the A3W11 airfoil is divided by 0.11.

The circulation values are all illustrated in Figure 5.13. Meanwhile Figure 5.14_Figure 5.17 illustrate the effect of amplitude, wavelength, and amplitude to wavelength ratio sizes of tubercles on the circulation values. The results of the effect of tubercles' amplitude sizes on the

circulation values illustrated in Figure 5.14 and Figure 5.15 show that by increasing/reducing the amplitude of the tubercles, the circulation of the streamwise vortices is increased/decreased. Meanwhile, the results regarding the effect of tubercles' wavelength sizes illustrated in Figure 5.16, show that by reducing/increasing the wavelength of the tubercles, the circulation values are increased/decreased.

Finally, by comparing the circulations results of the airfoils with close values of tubercles' amplitude to wavelength ratio illustrated in Figure 5.17, it can be seen that by reducing the amplitude and wavelength of tubercles', the circulation of the streamwise vortices decreased. Although, up until the 12-degree angle of attack, the A3W11 and A6W21 airfoils that have close values of tubercles' amplitude to wavelength ratio show almost the same values of circulation, but it can be observed from the results that the airfoils with close values of amplitude to wavelength ratio do not generate exactly the same values of circulation.

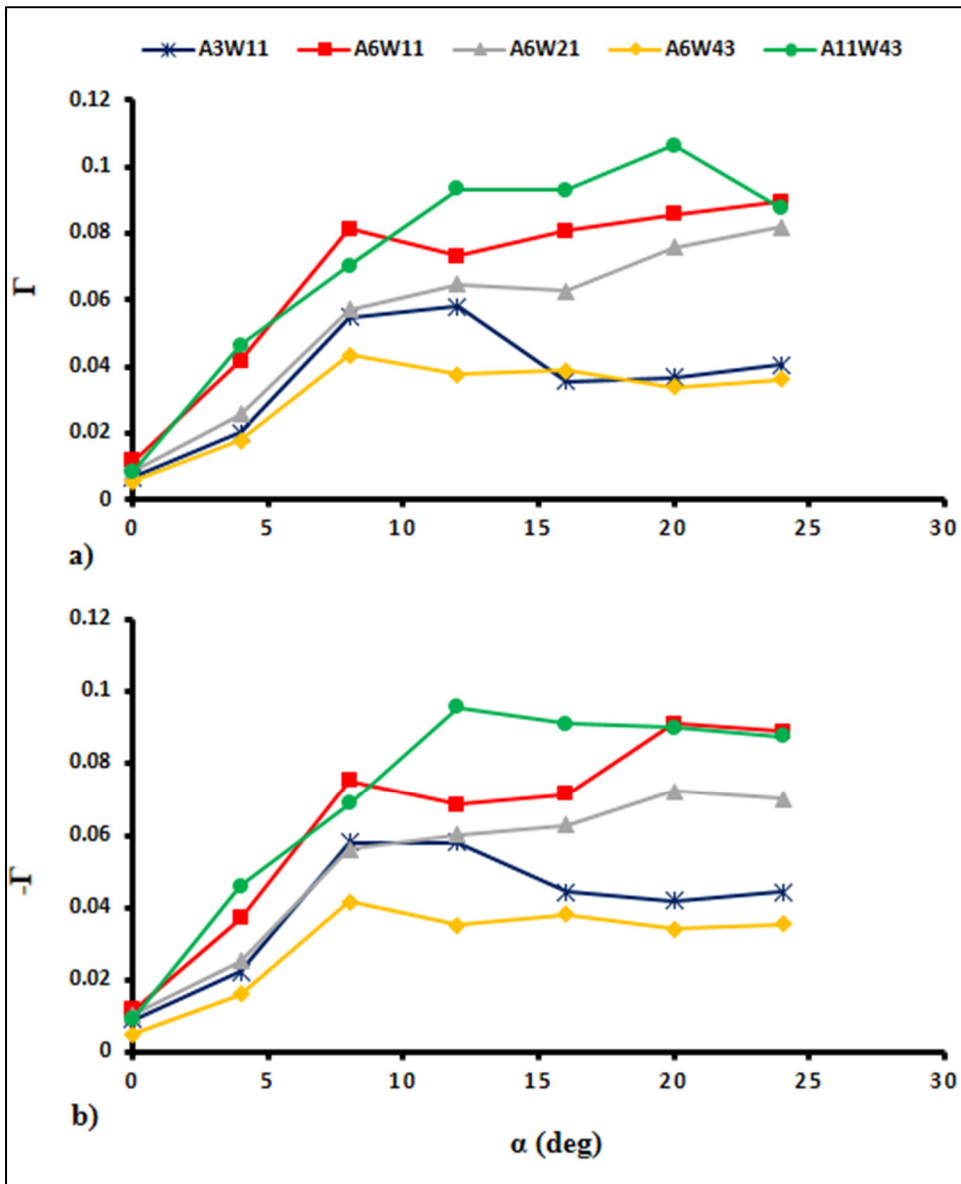


Figure 5.13 Positive (a) and negative (b) circulation values on modified airfoils at 0.05C of the mean-chord length

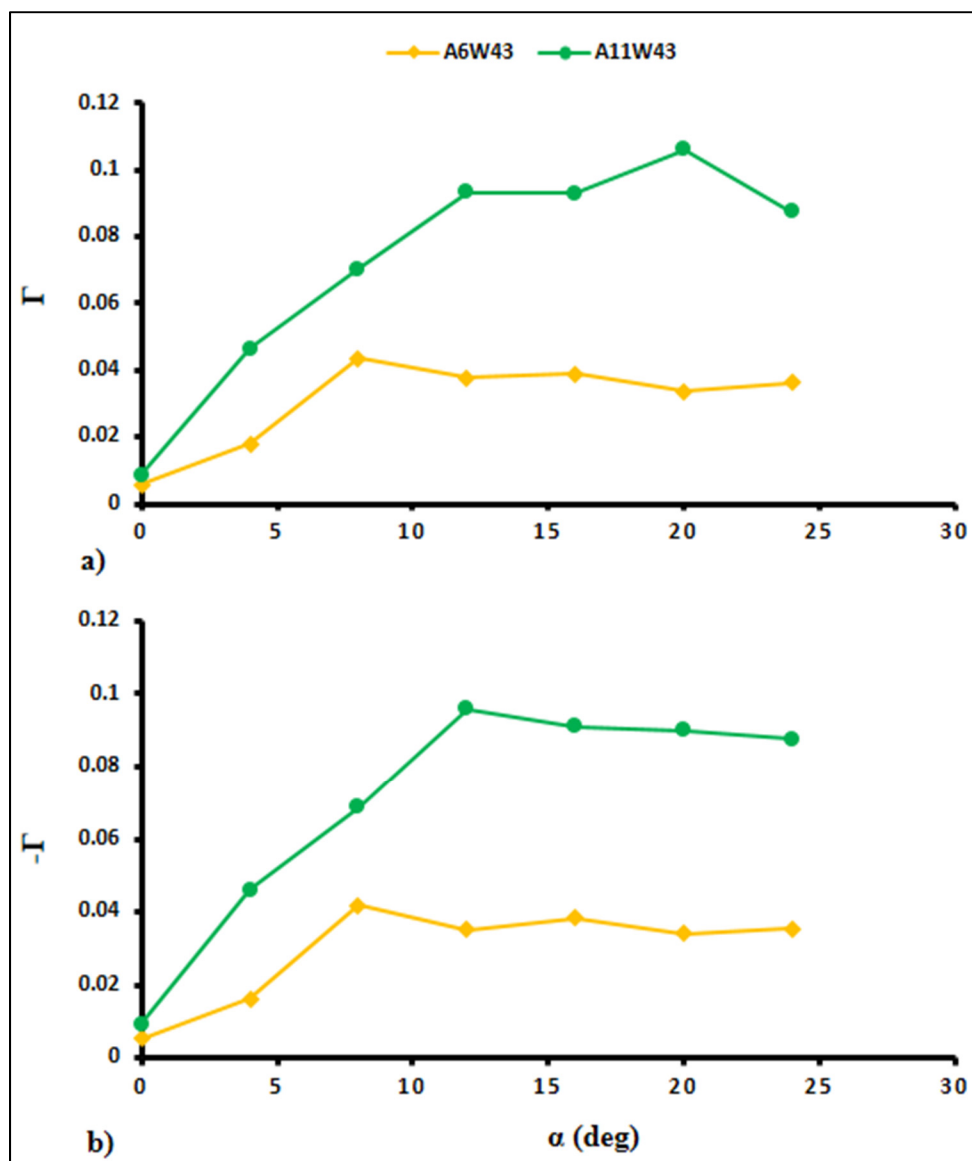


Figure 5.14 Effect of the amplitude of tubercles on positive (a) and negative (b) circulation values

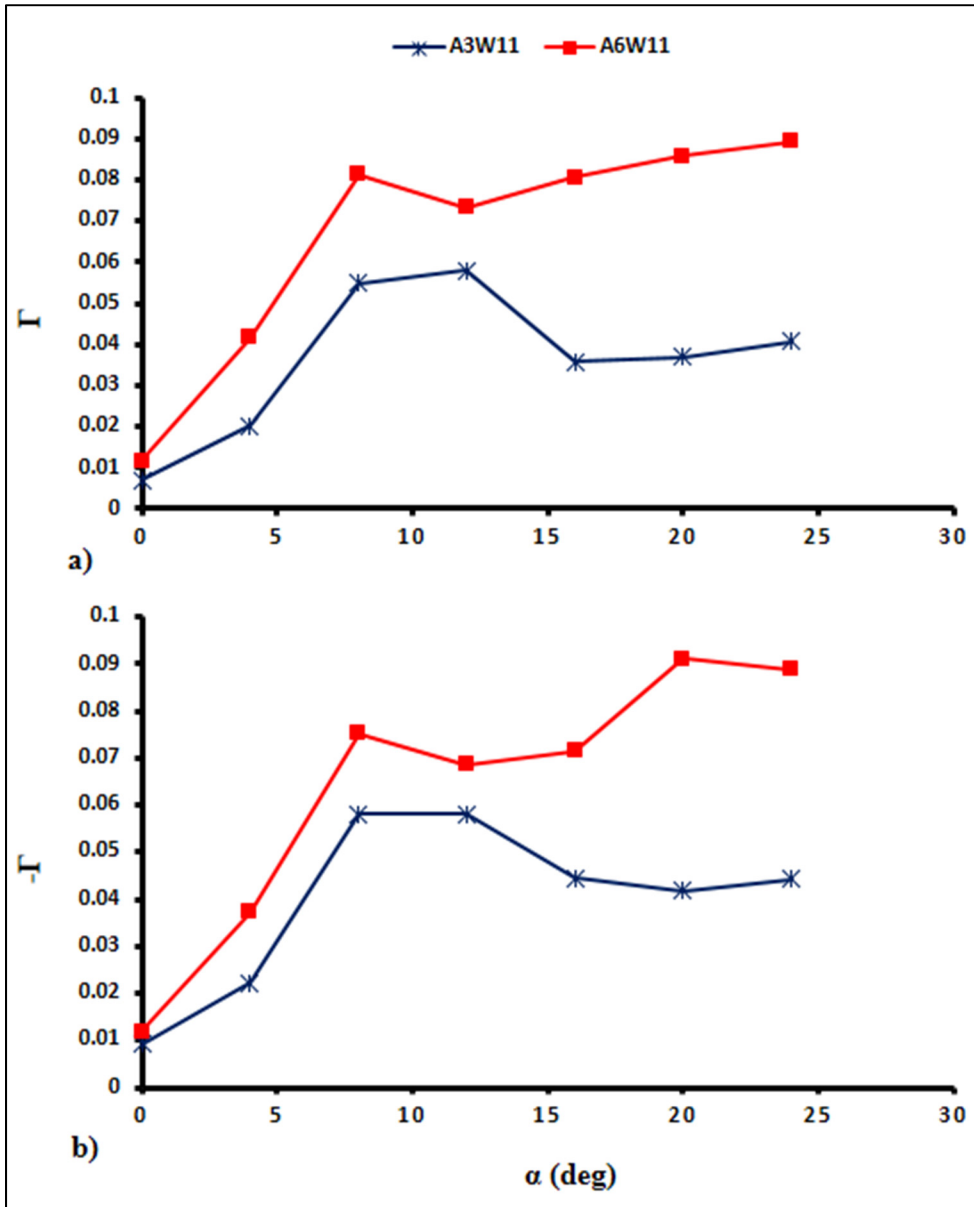


Figure 5.15 Effect of the amplitude of tubercles on positive (a) and negative (b) circulation values

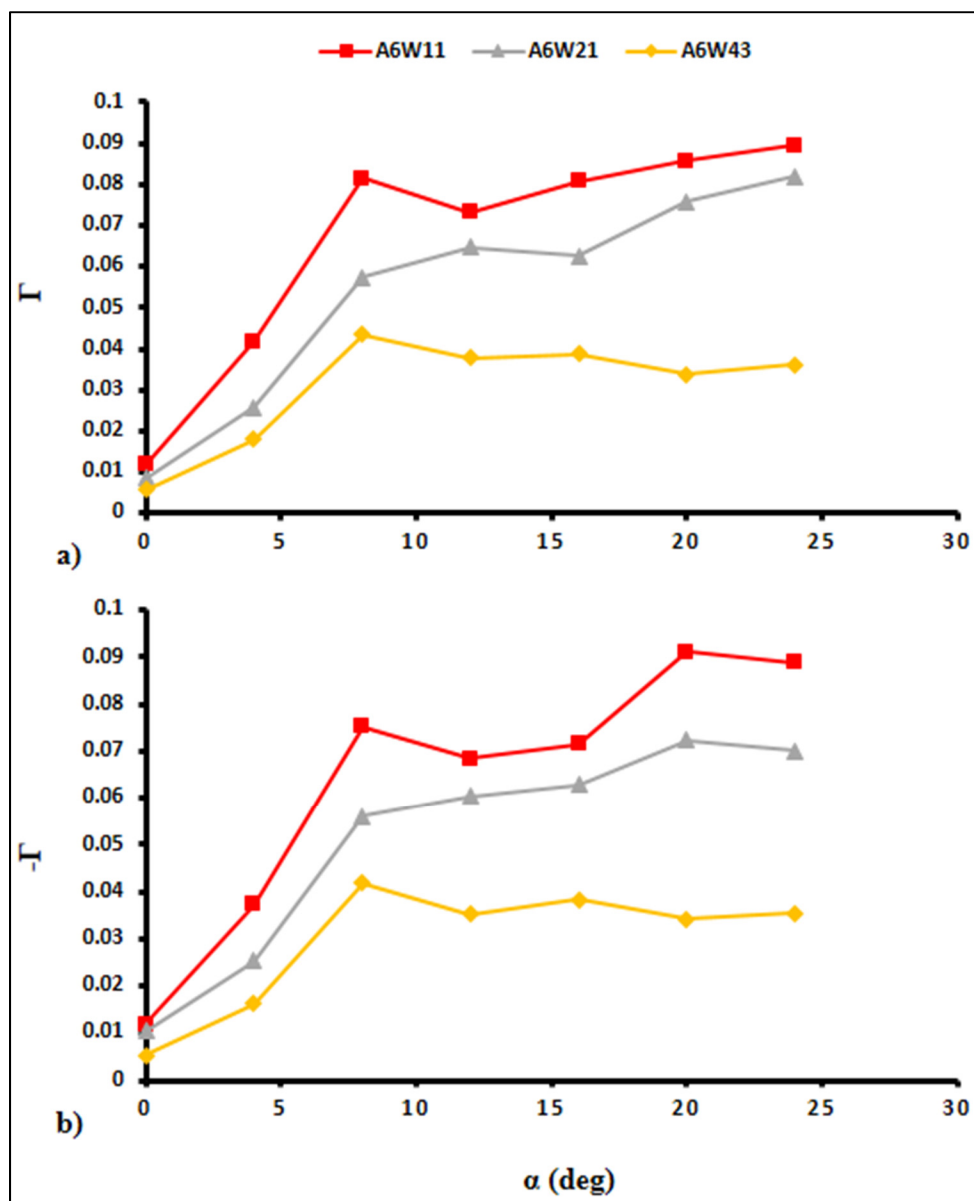


Figure 5.16 Effect of the wavelength of tubercles on positive (a) and negative (b) circulation values

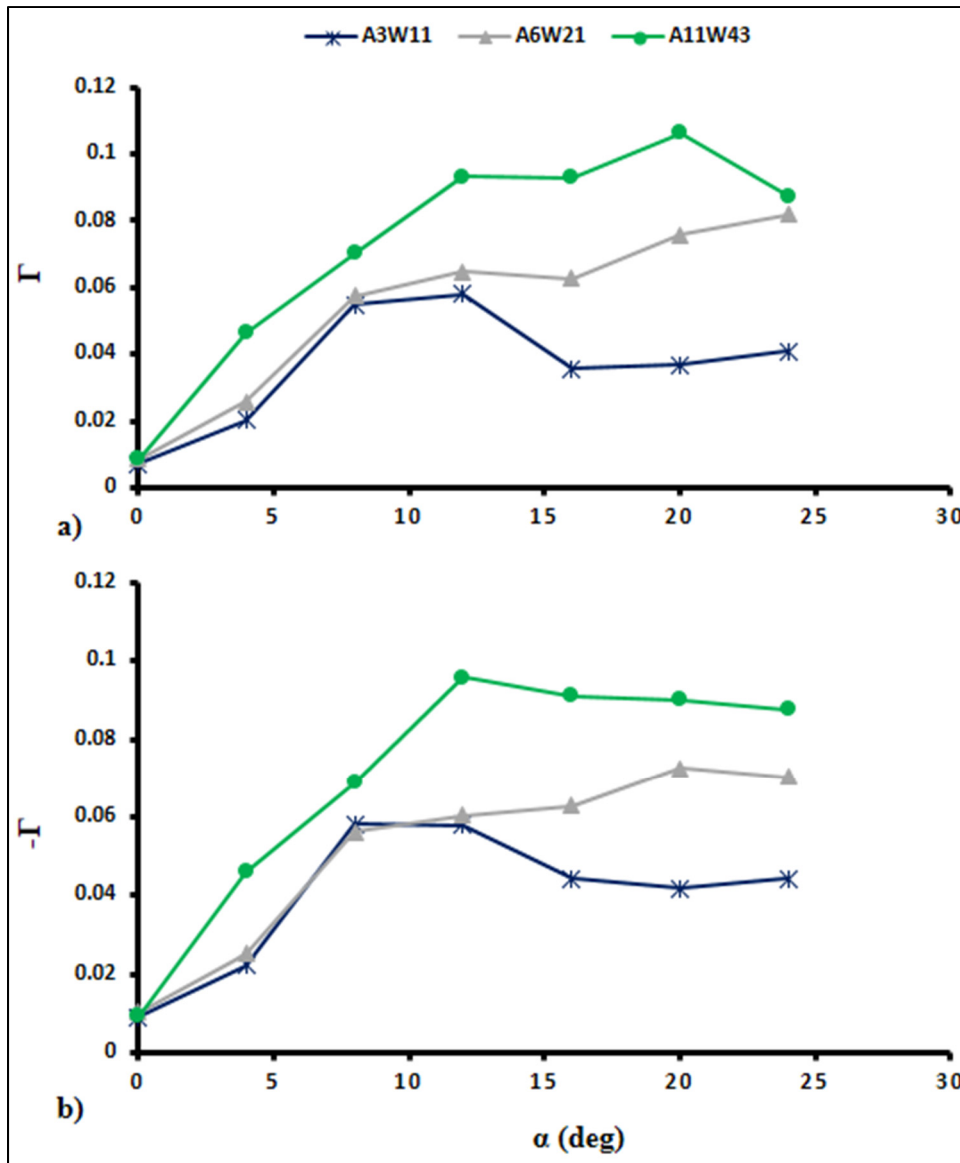


Figure 5.17 Effect of the amplitude to wavelength ratio of tubercles on positive (a) and negative (b) circulation values

In general, a comparison of the results shows that the circulation of the streamwise vortices on the airfoils with leading-edge tubercles is mostly the function of A/C and W/C , and the circulation of the streamwise vortices is increased by reducing the wavelength and increasing the amplitude of the tubercles.

5.4.3 The effect of streamwise vortices on integral quantities

In the previous section, the effect of tubercles' geometrical parameters on the strength of the streamwise vortices was analyzed. Now the relation between the circulation and interaction of the streamwise vortices on the aerodynamic performance of the modified airfoils can be discussed more in detail. All the lift and drag coefficient results obtained in this research on the baseline and modified airfoils are compared in Figure 5.18. Thus, to understand the effect of leading-edge tubercles and the streamwise vortices on the aerodynamic performance of the modified airfoils at both pre-and post-stall angles of attack, two angles of attack of 10 and 16-degrees are chosen to do the comparison of the results, which will be discussed in the following sections.

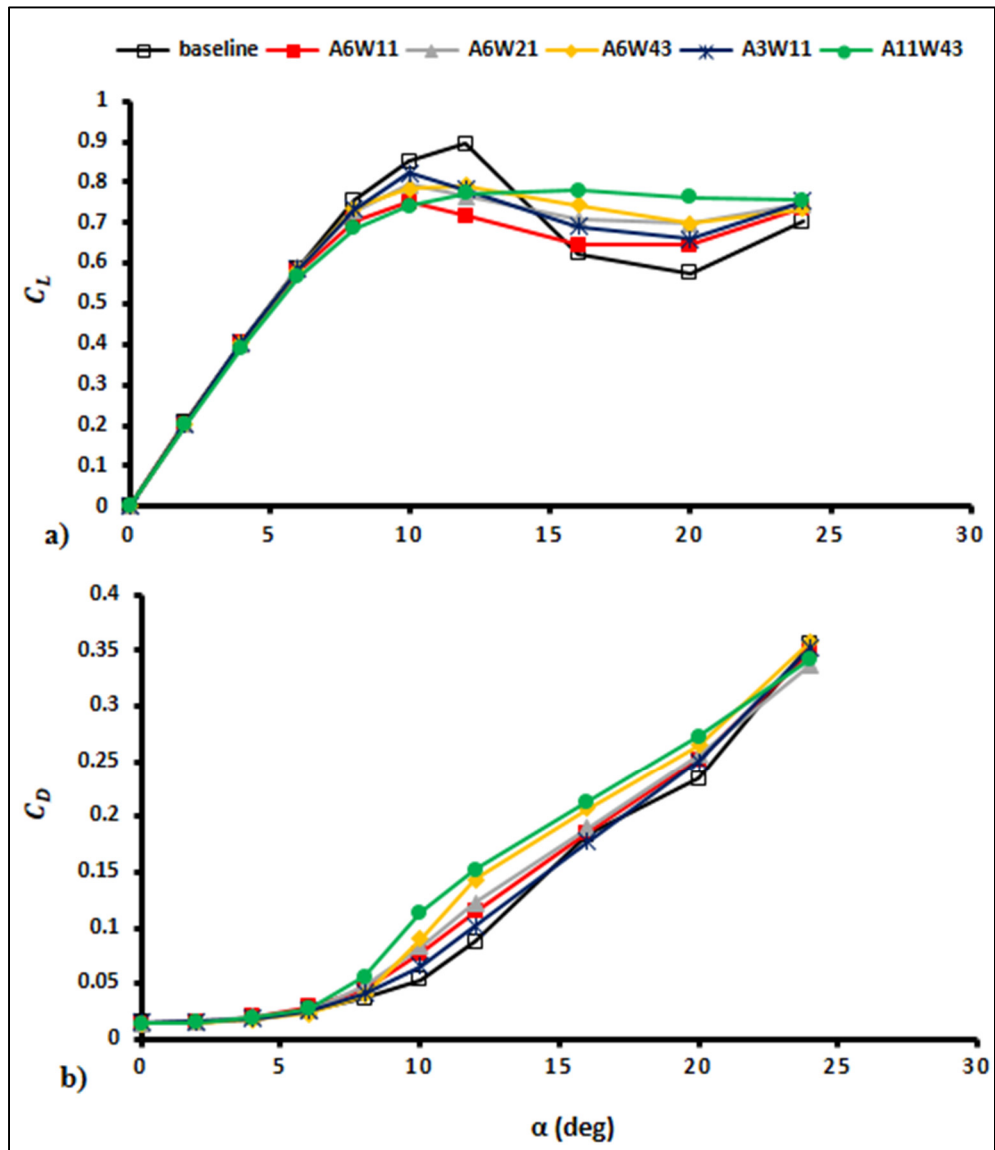


Figure 5.18 Lift (a) and drag (b) coefficient results for all the modified airfoils

5.4.3.1 The effect of the streamwise vortices at post-stall angles of attack

The lift coefficient results depicted in Figure 3.12 show that A11W43, A6W43, A6W21, A3W11, and A6W11 airfoils generate the highest lift coefficients at a 16-degree angle of attack in turn and the baseline airfoil generates the lowest generated lift coefficient.

To understand the effect of the streamwise vortices at post-stall angles of attack, the streamwise wall shear stresses on the modified airfoils at a 16-degree angle of attack are depicted in Figure 5.19. Meanwhile Figure 5.20 shows the streamwise vortices at a 16-degree angle of attack on all the modified airfoils.

As shown in Figure 5.19, most of the flow on the baseline airfoil upper surface is separated, while streamwise vortices prevent the separation of the flow on the modified airfoils. It is advantageous to define two new parameters of "effective length" and "effective mixing" to analyze the effectiveness of the streamwise vortices in energizing the boundary layer on the suction surface of the modified airfoils. The effective length is defined as the chordwise distance that the streamwise vortices can energize the boundary layer. The effective mixing is defined as the intensity or the extent that those vortices energize the boundary layer, which can be noted by higher values of positive streamwise wall-shear stresses.

The effective length of the streamwise vortices on the modified airfoils at a 16-degree angle of attack is measured and illustrated in Table 5.8. The values of effective length were calculated by dividing the mean chord length of the modified airfoils that are energized by the streamwise vortices (has positive values of streamwise wall shear stresses) to the mean chord length of the modified airfoils.

As can be seen in Figure 5.19 and Table 5.8, the effective length of the streamwise vortices is decreased by reducing the wavelength, and amplitude of the tubercles. Meanwhile, the effective mixing of the streamwise vortices is increased by reducing the wavelength and

increasing the amplitude of the tubercles. The degree of effective mixing can be seen by stronger colors, like darker yellow or orange in Figure 5.19.

The effective length of the streamwise vortices is the largest on the A11W43 and A6W43 airfoils, which show the most attached flow regions until 78% and 70% of the mean-chord-length, respectively. To understand the cause for a larger effective length of the streamwise vortices on larger wavelength airfoils, the behavior of the streamwise vortices formed on the modified airfoils must be analyzed. One important point that is observed in the general behavior of the streamwise vortices, is that by increasing the angle of attack, the two neighboring counter-rotating streamwise vortices converge towards each other while moving along the chord (as discussed in Figure 5.11 and Figure 5.12) which causes them to interact and hence begin to annihilate each other. The annihilation of the streamwise vortices, causes to stop the boundary layer energizing process, resulting in the flow separation. This behavior is observed on all the modified airfoils. On larger wavelength airfoils however, the streamwise vortices are more distanced from each other. Thus, the interaction intensity of their streamwise vortices is less in comparison with the shorter wavelength airfoils. This issue causes the increase in the effective length of these streamwise vortices on larger wavelength airfoils of A6W43 and A11W43.

Circulation calculations, in previous sub-section, showed that the circulation of the streamwise vortices is enhanced by increasing the amplitude, and reducing the wavelength of the tubercles. The augmentation in the strength of streamwise vortices by increasing the amplitude of tubercles, is noticeable by comparing the streamwise vortices on A11W43 with A6W43 airfoils, and A6W11 with A3W11 airfoils in Figure 5.20. Besides, the enhancement in the strength of vortices by reducing the wavelength of the tubercles is noticeable by comparing the vortices on A6W43, A6W21, and A6W11 airfoils in the same figure.

As discussed, the circulation of the counter-rotating streamwise vortices on the A11W43 airfoil, is higher than the A6W43 airfoil, due to its larger amplitude size. As a result, the effective mixing of the boundary layer, is also higher on the A11W43 airfoil, compared with

the A6W43 airfoil. Thus, the A11W43 airfoil generates a higher amount of lift coefficient than the A6W43 airfoil.

The other observation in Figure 5.19, is that by decreasing the wavelength of the tubercles, the effective mixing of the boundary layer increase, while the effective length of the streamwise vortices decreases significantly. The increase in the effective mixing of the boundary layer is due to both, an increase in strength as well as, reducing the distancing between the streamwise vortices, by reducing the wavelength of the tubercles. However, reducing the distance between the streamwise vortices increases the intensity of interaction between them. As a result, by reducing the wavelength of tubercles, the streamwise vortices annihilate each other faster, and thus, their effective length is reduced significantly which compensates for the increase in effective mixing by reducing the wavelength of the tubercles. Consequently, by reducing the wavelength of the tubercles, the lift coefficient values of the modified airfoils decrease.

Based on Figure 5.19, the increase in drag coefficient by increasing the amplitude, and wavelength of the tubercles can also be discussed. For example, at 16-degree angle of attack, the A6W11 airfoil generates higher drag coefficients than the A3W11 airfoil. This is because the A6W11 airfoil has stronger and larger separated and reversed flow regions behind its trough sections. Besides that, the drag coefficients are higher on larger wavelength airfoils of A6W43 and A11W43 airfoils, compared with the shorter wavelength airfoils. This is also due to their larger separated and reversed flow regions behind their trough sections. These separated and reverse flows, behind the trough regions of the modified airfoils, are possibly generated because of the effect of the effect of streamwise vortices, which will be discussed in the next subsection.

In conclusion, when analyzing the airfoils with leading-edge tubercles, the circulation, and intensity of interaction of the streamwise vortices appear to be the main parameters governing the flow phenomenon.

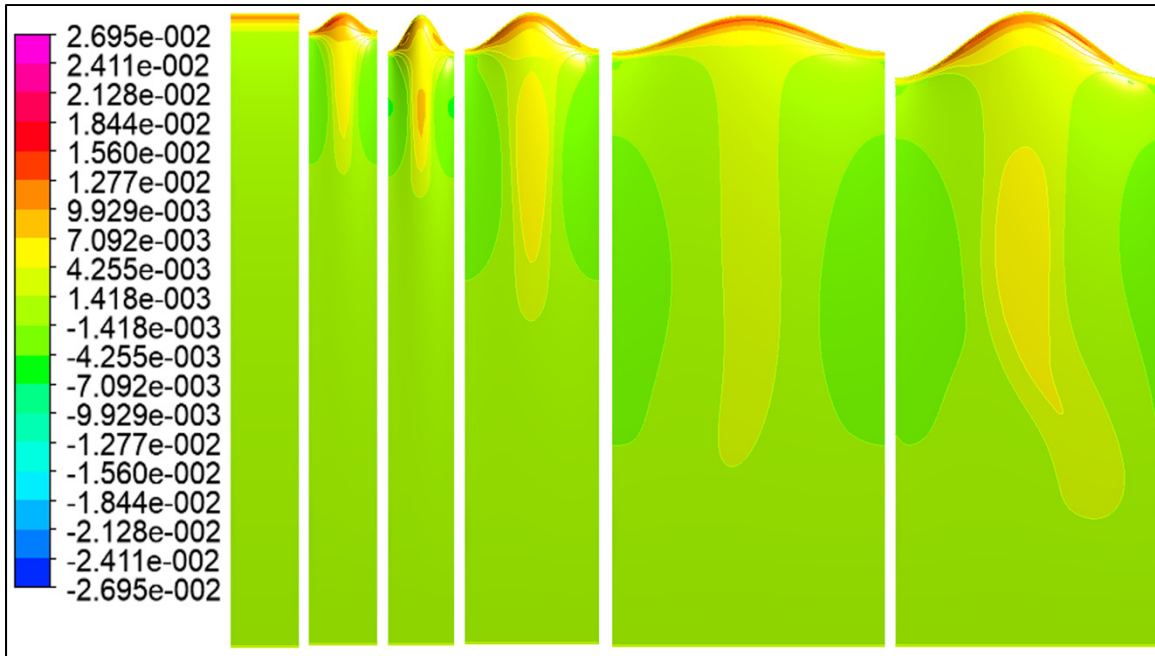


Figure 5.19 Shear stresses from left to right on baseline NACA 0010, A3W11, A6W11, A6W21, A6W43 and A11W43 airfoils at a 16-degree angle of attack

Table 5.8 Effective length of the streamwise vortices on NACA 0010 modified airfoils at a 16-degree AOA

Airfoil Name	A3W11	A6W11	A6W21	A6W43	A11W43
Effective length (% C)	24	27	46	70	78

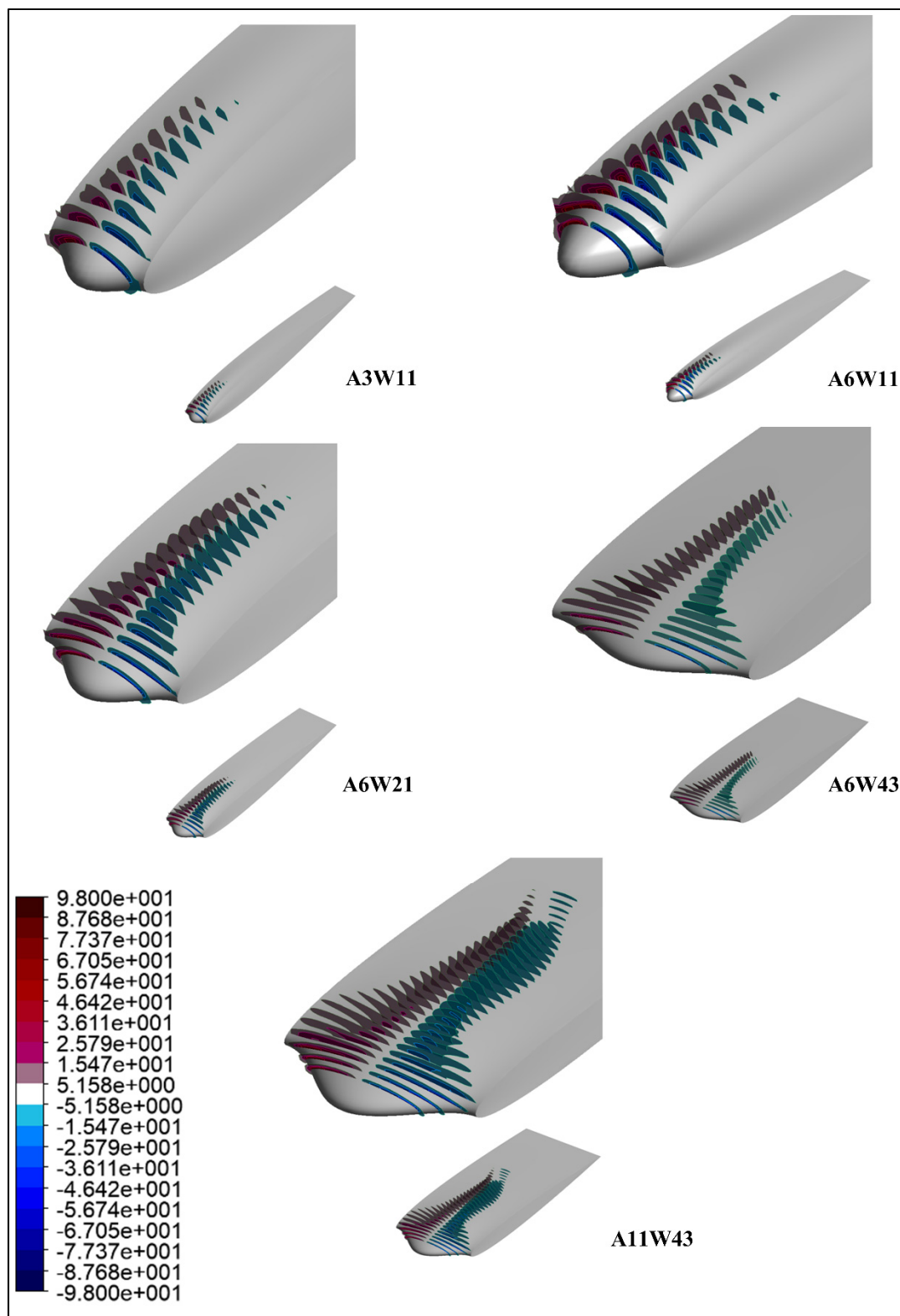


Figure 5.20 Streamwise vortices on the modified airfoils at a 16-degree angle of attack

5.4.3.2 Unsteady flow behavior

As mentioned in the literature review, in the experimental research of Custodio (2012), by increasing the angle of attack, and hence increasing the circulation of the streamwise vortices, the streamwise vortices interaction was occurred which creates a low-frequency unsteadiness.

To assess the possibility of low-frequency unsteadiness at high angles of attack, the U-RANS simulations are carried out. Consequently, the low-frequency unsteadiness is observed at higher angles of attack on the modified airfoils, which occurs due to the interaction of the streamwise vortices. Thus, on the modified airfoils, the steady analysis is performed for the low angles of attack of 0, 2, 4, 6, and 8 degrees and for the angles of attack of 10, 12, 16, 20, and 24 degrees, the U-RANS simulations are performed.

To describe more in-depth the observed unsteadiness, the U-RANS simulation results of the A6W21 airfoil at a 16-degree angle of attack are illustrated in Figure 5.21. This figure shows how the streamwise vortices and streamwise wall-shear stresses are changing over time. As illustrated in Figure 5.21, this unsteadiness causes the counter-rotating streamwise vortices at the regions closer to the trailing edge to have a low-frequency spanwise motion and become small and large at different time steps (time steps of 140 and 145 in this case). This issue causes the low-frequency spanwise motion of the positive streamwise wall-shear stresses (attached flow regions) as a consequence. As can be seen, the attached flow region area is the same at different time-steps, but only the shape of the attached flow region is changing over time with low-frequency motion in the regions closer to the trailing edge. This indicates that the final solution for the aerodynamic coefficients (lift and drag coefficients) in this simulation is steady-state. It should be noted that the streamwise vortices in Figure 5.21 are not standardized to show the effect of the streamwise vortices better.

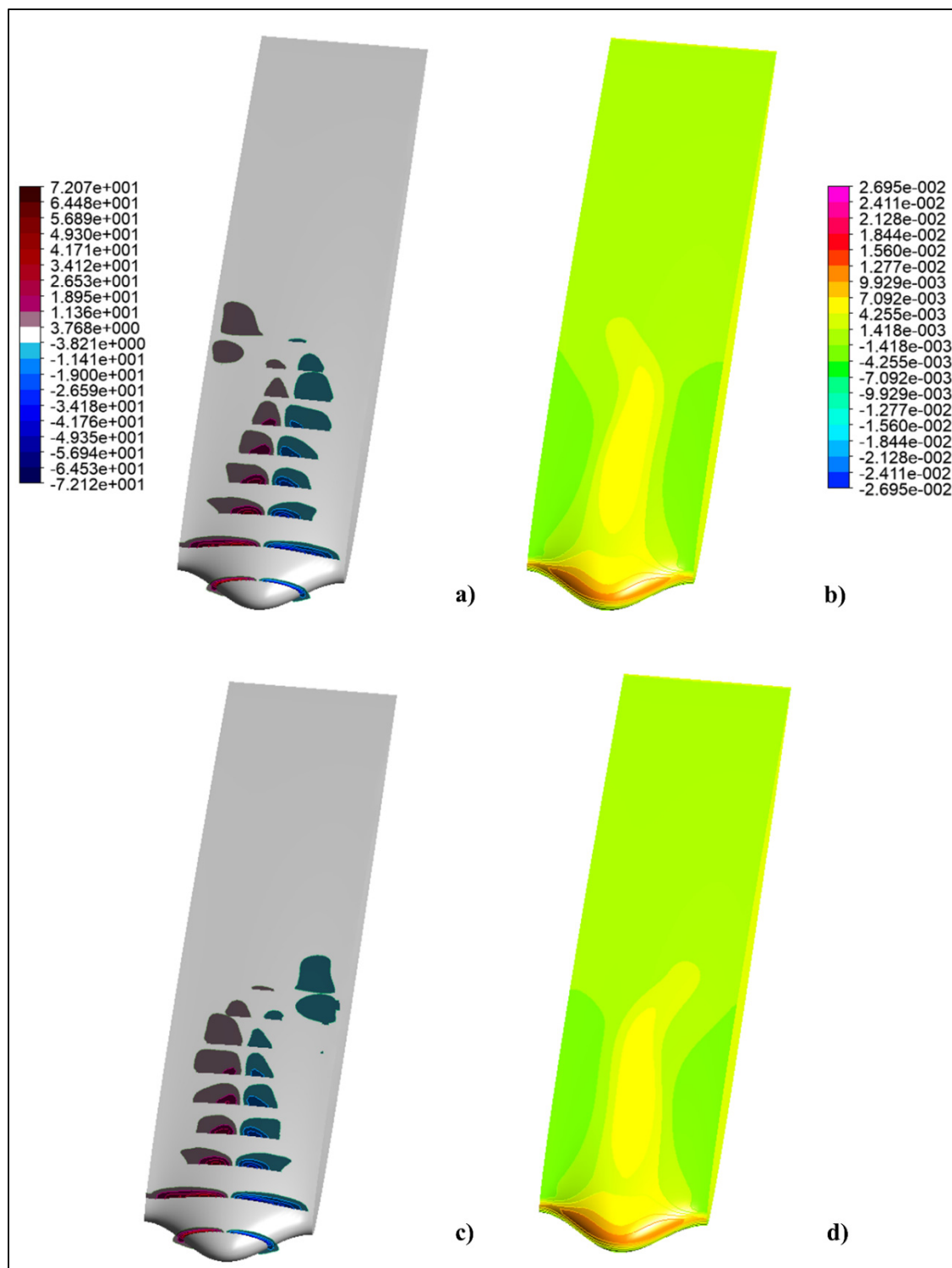


Figure 5.21 Wall shear stresses and streamwise vortices at time-steps of 140 (a and b) and 145 (c and d) on the A6W21 airfoil at a 16-degree AOA

5.4.3.3 The effect of the streamwise vortices at pre-stall angles of attack

At 10-degree angle of attack, the flow behavior is observed to be steady, but the U-RANS mode is still used to confirm these observations. First, the wall shear stresses in the streamwise direction are compared in Figure 5.22, to understand the location of the most attached and separated flow regions. As can be seen in Figure 5.22, at a pre-stall angle of attack of 10-degrees, the flow is mostly attached on the baseline airfoil. This is the reason for a higher amount of lift coefficient on the baseline airfoil in comparison with the other modified airfoils at this angle of attack.

The separated flow regions can be seen behind the trough sections of all the modified airfoils. As discussed in the introduction section, these separated flow regions, originate from the troughs between tubercles (Johari et al., 2007). To understand better the reason for the generation of these separated flow regions, Figure 5.23 illustrates the streamwise vortices versus the tangential projection of the velocity at a slice at $0.2\bar{C}$ of the A11W43 airfoil, where \bar{C} is the mean chord length. As can be seen in Figure 5.23, the streamwise vortices generate upwash and downwash of the flow behind the troughs and peak sections of the modified airfoil, respectively. It should be noted that the streamwise vortices in Figure 5.23 are not standardized and are also illustrated with higher resolution to better illustrate the streamwise vortices. This upwash generates separated flow regions at pre-stall angles of attack, depending on the circulation of the streamwise vortices. For example, as can be seen on the A6W11 and A11W43 airfoils that generate the highest circulation streamwise vortices, the separated flow regions are the strongest (with darker blue color). This means that their streamwise vortices generate a stronger upwash in the regions behind the trough sections. Meanwhile, the separated flow region covers more chordwise positions behind the trough regions of the A11W43 and A6W43 airfoils, in comparison with other modified airfoils with a shorter wavelength. As discussed in the previous sub-section, this is because of less interaction intensity, and hence larger effective length of the streamwise vortices on larger wavelength modified airfoils. Thus, for the same reason that the A11W43 airfoil generates higher lift coefficients at a post-stall angle of attack of 16 degrees, (larger effective length and effective mixing of the streamwise

vortices), this airfoil due to larger strength and effective length streamwise vortices that causes the generation of larger and stronger separated flow regions, generates the lowest value of lift coefficient at a pre-stall angle of attack of 10 degrees.

In addition, the separated flow regions on the A6W11 airfoil cover fewer chordwise locations in comparison with the other larger wavelength-modified airfoils with the same amplitude size. As discussed also in the previous sub-section, this issue is due to the more intense interaction of the streamwise vortices on shorter wavelength airfoils and, hence smaller effective length of streamwise vortices on them.

In a nutshell, it could be said that the same streamwise vortices that cause the creation of attached flow regions at post-stall angles of attack, cause the generation of separated flow regions at the pre-stall angles of attack.

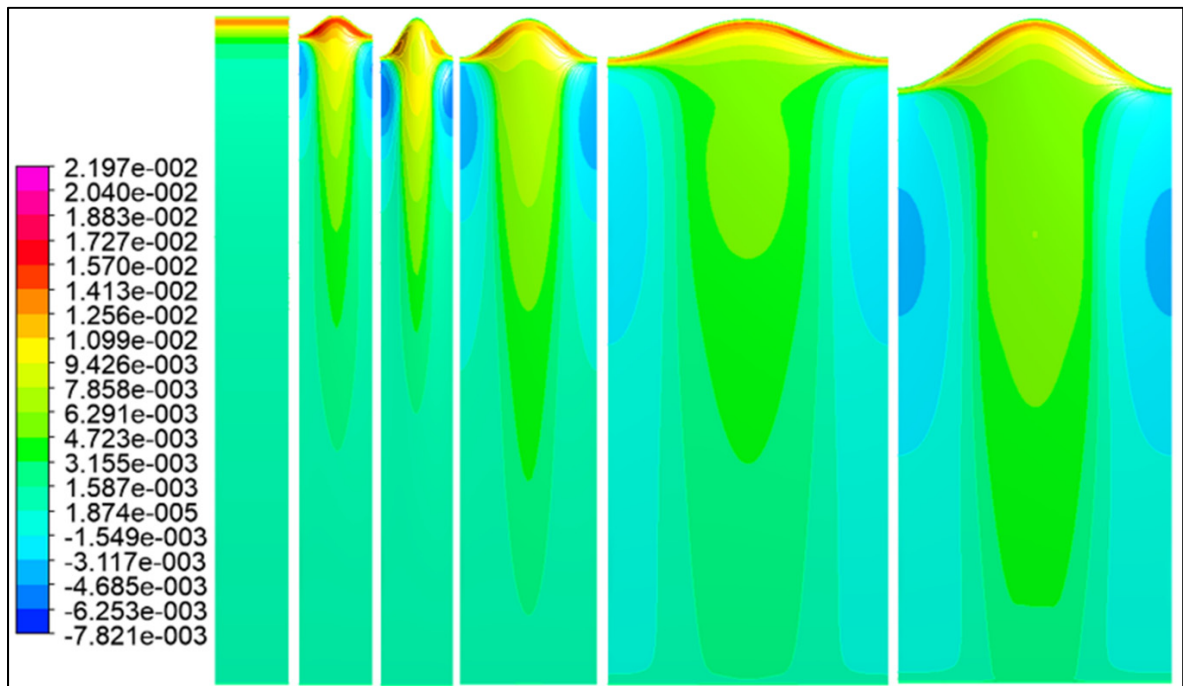


Figure 5.22 Wall Shear stresses from left to right on baseline, A3W11, A6W11, A6W21, A6W43 and A11W43 airfoils at a 10-degree angle of attack

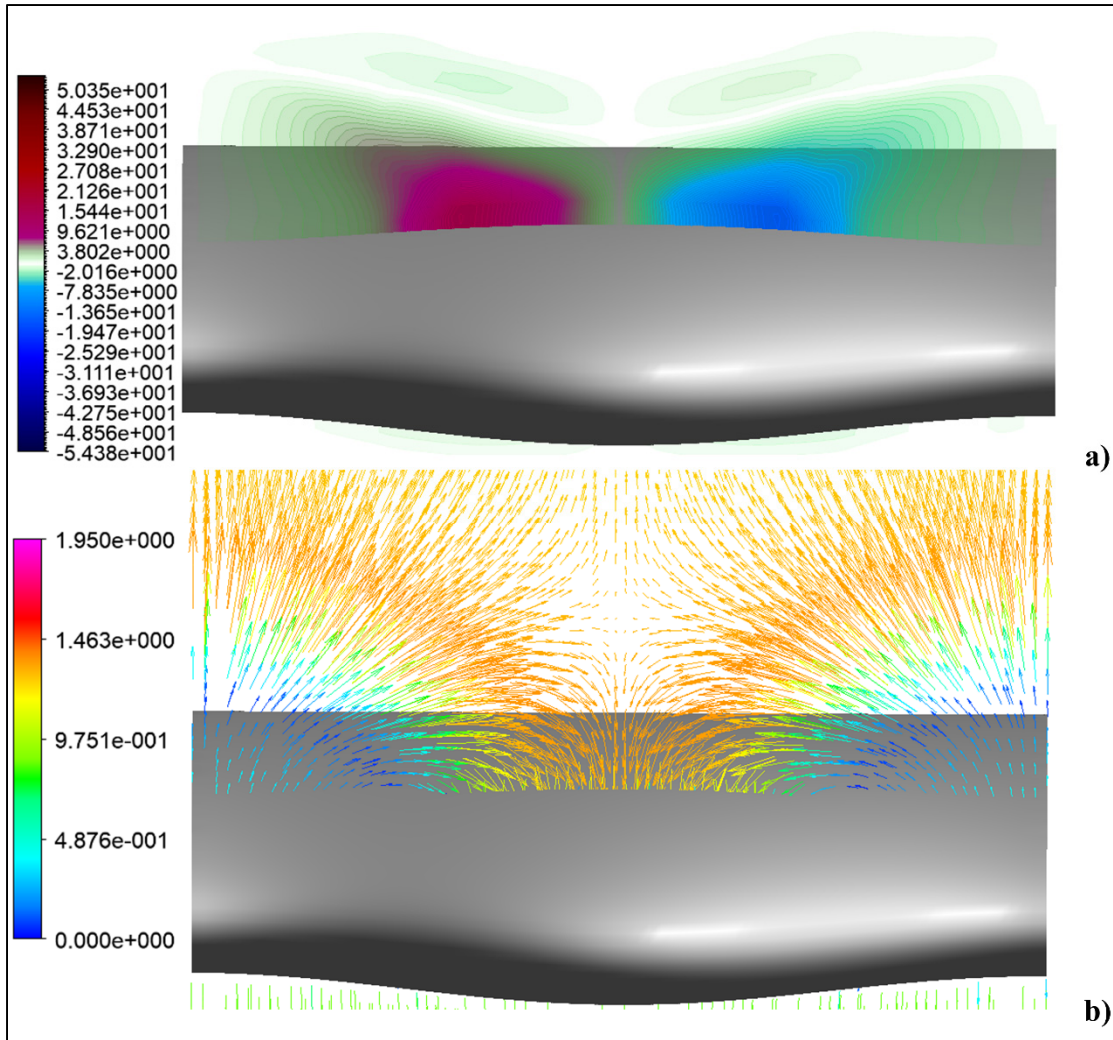


Figure 5.23 Streamwise vorticity (a) vs. tangential projection of the velocity field (b) on A11W43 airfoil at a slice at 0.2 C

5.5 Conclusion

In this research, the effect of leading-edge tubercles on the NACA 0010 airfoil aerodynamic performance is numerically analyzed using the software Ansys/CFX and k- ϵ turbulence modeling. The results on the baseline and five modified airfoils with different amplitude and wavelength sizes are analyzed and compared at the Reynolds number of 2.5×10^5 and at angles of attack ranging between $0 < \alpha < 24$ degrees. The interaction of the streamwise vortices causes some low-frequency unsteadiness, therefore a U-RANS analysis is also carried out for the modified airfoils at higher angles of attack of 10, 12, 16, 20, and 24 degrees.

According to the integral quantities results, in comparison with the baseline airfoil, the leading-edge tubercles increase the post-stall and decrease the pre-stall lift coefficient of the modified airfoils respectively. Besides, by comparing the airfoils with close values of amplitude to wavelength ratio, the post-stall lift coefficient values of the modified airfoils are seen to be increased/decreased, by increasing/decreasing the wavelength, and amplitude of the tubercles.

It is observed that the counter-rotating streamwise vortices are generated due to the effect of leading-edge tubercles on all the modified airfoils. The visualization of the streamwise vortices shows that the maximum value of these vortices is generally enhanced by increasing the angle of attack. Besides that, the calculation of circulation/strength of the streamwise vortices has shown that the strength of these vortices are augmented by reducing the wavelength and increasing the amplitude of the tubercles. Analyzing the streamwise vortices on the modified airfoils show that, by increasing the angle of attack, the counter-rotating streamwise vortices converge toward each other while moving along the chord. Thus, they start to interact and, hence start to annihilate each other. After the annihilation of the streamwise vortices, the energization of the boundary layer stops.

Two new parameters are defined regarding the effectiveness of the streamwise vortices on the energization of the boundary layer on the upper surface of the modified airfoils. They are called the effective length and the effective mixing. The effective length is defined as the chordwise

distance that the streamwise vortices can energize the boundary layer. The effective mixing is defined as the intensity or, the extent that those vortices energize the boundary layer.

By analyzing the streamwise vortices and wall-shear stresses on the modified airfoils, it is observed that by reducing the wavelength of the tubercles the effective mixing of the streamwise vortices increases. This increase in the effective mixing is due to an increase in circulation/strength, as well as the reduction in the distance between the streamwise vortices by reducing the wavelength of tubercles. However, reducing the distance between the streamwise vortices increases the intensity of interaction between them and hence, cause faster annihilation and accordingly, cause the reduction of their effective length significantly. This significant reduction in effective length due to interaction of the streamwise vortices compensates the increase in effective mixing of the streamwise vortices by reducing the wavelength of the tubercles. As a result, the lift coefficient of the modified airfoils is generally decreased by reducing the wavelength of the tubercles.

In addition, it was noted that increasing the amplitude of the tubercles, increases the circulation of the two-neighboring counter-rotating streamwise vortices, and hence increases their effective mixing. Meanwhile, increasing the wavelength of the tubercles increases the distancing between the neighboring counter-rotating streamwise vortices, and consequently reduces the interaction intensity between them. Therefore, it postpones the annihilation of the streamwise vortices and increases their effective length along the chord. Thus, it is concluded in this research that, the amplitude to wavelength ratio of tubercles determines the relation between the circulation and the intensity of interaction of the streamwise vortices. Consequently, by comparing the NACA 0010 modified airfoils with close values of amplitude to wavelength ratio sizes, the airfoils with larger amplitude and wavelength sizes of tubercles generate higher lift coefficient at post-stall angles of attack.

In this research, it is also noted that the separated flow regions are generated behind the trough sections of the modified airfoils, at pre-stall angles of attack. These separated flow regions are responsible for the lift coefficient decrease on the modified airfoils compared with the baseline

airfoil at pre-stall angles of attack. Our results show that these separated flow regions are generated only in the regions where the streamwise vortices exist. Moreover, they are generated due to the upwash of the flow by the streamwise vortices in the regions behind the trough sections. These separated flow regions are also stronger where the higher circulation/strength streamwise vortices exist (e.g., on the (A6W11) and (A11W43) airfoils). Thus, it is concluded in this research that, the separated flow regions behind the trough sections of the modified airfoils are mostly related to the streamwise vortices, their coverage regions, and their circulation/strength.

CHAPTER 6

CONCLUSIONS AND RECOMMENDATIONS

6.1 Conclusions

In this research, the effect of leading-edge tubercles on the symmetric NACA 0010 and high-cambered RAF-19 airfoils' aerodynamic performance is numerically analyzed using the software Ansys/CFX and $k-\varepsilon$ turbulence modeling. On each airfoil, the results on the baseline and five modified airfoils with different amplitude and wavelength sizes are analyzed and compared at the Reynolds number of 2.5×10^5 . The interaction of the streamwise vortices causes some low-frequency unsteadiness, therefore a U-RANS analysis is also carried out for the modified airfoils at higher angles of attack for both airfoil types.

The integral quantities results on the modified NACA0010 airfoils show that the leading-edge undulations decrease the pre-stall lift coefficient while improving the post-stall lift coefficient in comparison with the baseline airfoil. Besides, by comparing the airfoils with close values of amplitude to wavelength ratio, the post-stall lift coefficient values of the modified airfoils are seen to be increased/decreased, by increasing/decreasing the wavelength, and amplitude of tubercles at post-stall angles of attack.

The integral quantities results on the modified high camber RAF-19 airfoils show different trends than that of the symmetric airfoils and the aerodynamic performance improvements in case of lift coefficient on the RAF-19 modified airfoils were only observed in the shortest wavelength and amplitude airfoils of A6W11 and A3W11 respectively. The RAF-19_A3W11 airfoil could increase the C_{Lmax} , as well as the pre-and post-stall lift coefficient (from 10 to 16 degrees of angle of attack), and RAF-19_A6W11 airfoil, only increase the lift coefficient from 10 to 12 degrees of angle of attack. The other modified RAF-19 airfoils did not improve the

lift coefficient for most of the angles of attack studied. Leading-edge tubercles on both airfoil types cause the increase in drag coefficients in comparison with the baseline airfoil. Besides, by increasing the amplitude and wavelength of the tubercles the drag coefficient increased on both high-cambered and symmetric airfoils.

Streamwise vortices and wall shear stresses results show that the counter-rotating streamwise vortices are generated due to the effect of leading-edge tubercles on all the modified airfoils. In this research, the effect of amplitude and wavelength size of tubercles on the strength and interaction of the streamwise vortices and consequently their effect on the lift and drag coefficient of the modified airfoils are discussed. To this author's knowledge, there was no research focused on the effect of the amplitude and wavelength sizes of the leading-edge tubercles on the circulation and interaction of the streamwise vortices. Thus, no research could make a formal quantitative observation, to justify the aerodynamic performance changes observed by changing the wavelength, amplitude, and amplitude to wavelength ratio sizes of the tubercles.

The visualization of the streamwise vortices shows that the maximum value of these vortices is generally enhanced by increasing the angle of attack. Besides that, the calculation of circulation/strength of the streamwise vortices has shown that the strength of these vortices are augmented by reducing the wavelength and increasing the amplitude of the tubercles.

Analyzing the streamwise vortices on all the modified airfoils show that, by increasing the angle of attack, the counter-rotating streamwise vortices converge toward each other while moving along the chord. Thus, they start to interact and annihilate each other. After the annihilation of the streamwise vortices, the energization of the boundary layer stops.

Two new parameters are defined regarding the effectiveness of the streamwise vortices on the energization of the boundary layer on the upper surface of the modified airfoils. They are called the effective length and the effective mixing. Effective length is defined as the chordwise

distance that the streamwise vortices can energize the boundary layer. Effective mixing is defined as the intensity or, the extent that those vortices energize the boundary layer.

By analyzing the streamwise vortices and wall-shear stresses on the modified NACA 0010 airfoils at 16-degree angle of attack, it is concluded that by reducing the wavelength of the tubercles the effective mixing of the streamwise vortices increases. This increase in the effective mixing is due to an increase in circulation/strength, as well as the reduction in the distance between the streamwise vortices by reducing the wavelength of the tubercles. However, reducing the distance between the streamwise vortices increases the intensity of interaction between them and hence, cause the faster annihilation and accordingly, cause the reduction of their effective length significantly. This significant reduction in effective length due to interaction of the streamwise vortices compensates the increase in effective mixing of the streamwise vortices by reducing the wavelength of the tubercles. As a result, the lift coefficient of the NACA 0010 modified airfoils is decreased by reducing the wavelength of the tubercles.

In addition, it was noted that increasing the amplitude of the tubercles, increases the circulation of the two-neighboring counter-rotating streamwise vortices, and hence increases their effective mixing. Meanwhile, increasing the wavelength of the tubercles increases the distancing between the neighboring counter-rotating streamwise vortices, and consequently reduces the interaction intensity between them. This reduction in interaction intensity results in postponing in the annihilation of the streamwise vortices and thus, increasing their effective length along the chord. Thus, it is concluded in this research that, the amplitude to wavelength ratio of tubercles determines the relation between the circulation and the intensity of interaction of the streamwise vortices. Consequently, by comparing the NACA 0010 modified airfoils with close values of amplitude to wavelength ratio sizes, the airfoils with larger amplitude and wavelength sizes generate higher lift coefficient at post-stall angles of attack.

In this research, the reason for the generation of separated flow regions on the airfoils with leading-edge tubercles are discussed. These flow separations, causes the reduction of lift coefficients at pre-stall angles of attack on the modified airfoils compared to the baseline

airfoil. Although many research, discussed the reason for the generation of these separated flow regions, but the reason for their generation are still not completely determined. By analyzing the wall shear stresses on the modified NACA 0010 airfoils at 10-degree angle of attack, it is observed that the separated flow regions are generated only in the regions where the streamwise vortices exist. Additionally, they occur due to the upwash of the flow generated by the streamwise vortices in the regions behind the trough sections. These separated flow regions are also stronger where the larger circulation streamwise vortices exist (e.g., on the smallest wavelength (A6W11) and largest amplitude airfoils (A11W43)). Thus, in this research it is concluded that the separated flow regions behind the trough sections of the modified airfoils are mostly related to the streamwise vortices, their coverage regions and their circulation.

In this study, the effect of spanwise bumps generated due to keeping the thickness to chord ratio constant while designing the airfoils with leading-edge tubercles is also discussed for the first time. In previous literature, it was suggested before to add this parameter as one of the key parameters like the amplitude, wavelength, and amplitude to wavelength ratio sizes as the main characteristics of the airfoils with leading-edge tubercles/undulations. If the thickness to chord ratio is preserved during the design of the modified airfoils, the foil's shape will totally change, and the spanwise ridges and valleys form along the entire chord of the modified airfoils. In this research, all the modified NACA 0010 and Raf-19 airfoils were designed by keeping the thickness to chord ratio constant. However, on the Raf-19 airfoil, due to its higher camber size, these ridges and valleys become more extreme during the design. These more extreme bumps generated on the modified Raf-19 airfoils cause the generated counter-rotating streamwise vortices to rotate more towards the spanwise sides and become more distanced from each other and thus, postpone the interaction of the streamwise vortices. As a result, on the modified RAF-19 airfoils, while reducing the wavelength of the tubercles causes the increase in effective mixing of the boundary layer, the spanwise bump causes the postpone in the interaction and hence annihilation of the streamwise vortices. Therefore, compared to the modified NACA 0010 airfoils, the lift coefficient of the modified RAF-19 airfoils is improved by reducing the wavelength of the tubercles.

6.2 Recommendations

- In this research the effect of tubercles on 2D infinite span wings are studied to better evaluate the effect of amplitude, wavelength, and amplitude to wavelength ratio on the strength and interaction of the streamwise vortices. However, on 3D wings more complicated flow by considering the end effects exists. Thus, the first recommendation for the continuation of this study, is to analyze the effect of these geometrical parameters on 3D finite-span wings.
- In this research, the effect of strength and interaction of the streamwise vortices generated by the leading-edge tubercles on the aerodynamic performance of NACA 0010 and RAF-19 airfoils are discussed. These airfoils have the maximum thickness of $10\%C$. However, the vortices behaviour can be different on different types of airfoils for example on the airfoils with different thickness. Accordingly, the location of the interaction of the streamwise vortices can be fastened or delayed based on the geometric characteristics of the modified airfoils. It is shown in this research that the greater spanwise bump generated by keeping the thickness to chord ratio constant during the design of the modified airfoils is also one of those important geometric parameters. Besides, the interaction of the streamwise vortices might also be fastened or delayed at different Reynolds numbers. Thus, more research can still be done by analyzing the strength and interaction of the streamwise vortices on different types of airfoils, and at different Reynolds numbers.
- Based on the literature (Bolzon et al., 2014; Bolzon, Kelso, & Arjomandi, 2016a; Bolzon, Kelso, & Arjomandi, 2017; Wei, Lian, & Zhong, 2018; Wei, New, & Cui, 2018; Wei, New, Lian, & Zhang, 2019), the studies done on the effect of leading-edge tubercles on swept wings are mostly done on 3D wings with only one amplitude and wavelength size of tubercles. As mentioned by the previous authors (Bolzon et al., 2014; Bolzon et al., 2016a; Bolzon et al., 2017; Wei, Lian, et al., 2018; Wei, New, et al., 2018; Wei et al., 2019), the leading-edge tubercles on swept wings generate an asymmetry in the strength and shape of the two generated counter-rotating streamwise vortices behind each tubercle peak section.

Analyzing the effect of different amplitudes and wavelength sizes of leading-edge tubercles on swept wings can be also an interesting subject of research.

- It was suggested that the favorable behaviors observed in the performance of tubercled lifting bodies are not exclusive to this form of leading-edge configuration (Hansen, 2012; Rostamzadeh, Kelso, Dally, & Hansen, 2013). Hansen (2012) and Rostamzadeh *et al.* (2013) proposed a new modified wing design called "wavy wing" in which the geometric angle of attack changes sinusoidally in the spanwise direction in comparison with the model with tubercles that the chord varies in a sinusoidal manner along the span as shown in Figure 6.1. Wind tunnel force measurements on wavy foils showed similar behavior to the wings with tubercles, such as the gradual stall and increased lift at the post-stall angles of attack. The CFD investigations at the pre-stall angles of attacks also showed the presence of strong counter-rotating streamwise vortices in the wake of the wavy foil, pointing to another notable feature in the flow produced by wings with tubercles. One possible research is to analyze the generation and behavior of the streamwise vortices on wavy wings and analyze their strength and interaction by changing the geometrical parameters (such as their angular amplitude and wavelength sizes). This analysis can be done in the same manner as we analyzed it on 2D wings with leading-edge tubercles in this research.

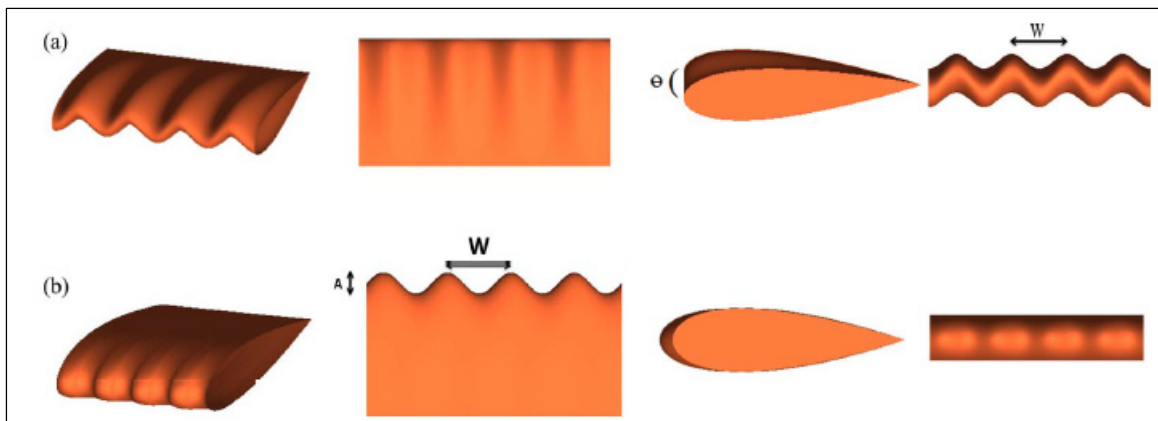


Figure 6.1 Wavy wing section showing peak-to-peak angular amplitude (θ) expressed in degrees and wavelength (w) in millimeters (a), and tubercled wing section showing the amplitude (A) and wavelength (W) expressed in millimeters (b)

Taken from Rostamzade *et al.* (2013)

- One other interesting research can be the analysis of the effect of leading-edge undulations on winglets. For this purpose, leading-edge undulations with different amplitude and wavelength sizes can be designed on a known 3D wing with a winglet and the results of the modified wing can be compared with the baseline counterpart.
- The capability of leading-edge tubercles and leading-edge serrations on noise reduction applications are discussed in many pieces of research (Hersh, Soderman, & Hayden, 1974; Skillen et al., 2015; Teruna, Avallone, Casalino, & Ragni, 2021). Besides, the effect of leading-edge tubercles' amplitude and wavelength sizes on 2-D wings' noise elimination capability are discussed in (Hansen et al., 2010). In that research, the author postulated that the mechanism responsible for the noise reduction might be strongly related to the formation of the streamwise vortices generated by the tubercles. Although they suggested before (Hansen et al., 2011) that the strength of the streamwise vortices is related to the amplitude to wavelength ratio of the tubercles, this time regarding the noise reduction, they noticed that the modified airfoils with the smallest wavelength and largest amplitude sizes perform better in tonal noise elimination. In our research, it was found that the strength of the streamwise vortices is increased by reducing the wavelength and increasing the amplitude of the tubercles. It seems that there are some relations between increasing the strength of the streamwise vortices and the tonal noise elimination capabilities of the airfoils with leading-edge tubercles. One possible research is to analyze the mechanism of the noise reduction on 2D wings with tubercles more thoroughly by considering the strength and also the interaction of the streamwise vortices.

LIST OF REFERENCES

- Abbott, I., & Von Doenhoff, A. (1959). *Theory of Wing Sections*, . New York: Dover.
- Anderson, J. D. (2005). Ludwig Prandtl's boundary layer. *Physics today*, 58(12), 42-48.
- Anderson Jr, J. D. (2017). *Fundamentals of aerodynamics*. Tata McGraw-Hill Education.
- ANSYS, C. (2016). Version 17.0, ANSYS CFX-solver theory guide. Consultée le
- Asghar, A., Perez, R. E., Jansen, P. W., & Allan, W. (2020). Application of leading-edge tubercles to enhance propeller performance. *AIAA Journal*, 58(11), 4659-4671.
- Bolzon, M. (2017). *The effects of tubercles on swept wing performance at pre-stall angles of attack* (The University of Adelaide).
- Bolzon, M., Kelso, R., & Arjomandi, M. (2014, December). *The effects of tubercles on swept wing performance at low angles of attack* présentée à Proceedings of the 19th Australasian fluid mechanics conference.
- Bolzon, M. D., Kelso, R. M., & Arjomandi, M. (2016a). Formation of vortices on a tubercled wing, and their effects on drag. *Aerospace Science and Technology*, 56, 46-55. doi: <http://dx.doi.org/10.1016/j.ast.2016.06.025>
- Bolzon, M. D., Kelso, R. M., & Arjomandi, M. (2016b). Tubercles and their applications. *Journal of aerospace engineering*, 29(1), 04015013. doi: [https://doi.org/10.1061/\(ASCE\)AS.1943-5525.0000491](https://doi.org/10.1061/(ASCE)AS.1943-5525.0000491)
- Bolzon, M. D., Kelso, R. M., & Arjomandi, M. (2017). Performance effects of a single tubercle terminating at a swept wing's tip. *Experimental Thermal and Fluid Science*, 85, 52-68. doi: <http://dx.doi.org/10.1016/j.expthermflusci.2017.02.016>
- Bushnell, D. M., & Moore, K. (1991). Drag reduction in nature. *Annual review of fluid mechanics*, 23(1), 65-79.
- Carreira Pedro, H., & Kobayashi, M. (2008, January). *Numerical study of stall delay on humpback whale flippers* présentée à 46th AIAA aerospace sciences meeting and exhibit.

- Celik, I. B., Ghia, U., Roache, P. J., & Freitas, C. J. (2008). Procedure for estimation and reporting of uncertainty due to discretization in CFD applications. *Journal of fluids Engineering-Transactions of the ASME*, 130(7).
- Custodio, D. (2012). *The effect of humpback whale-like leading edge protuberances on hydrofoil performance* (PhD, WORCESTER POLYTECHNIC INSTITUTE).
- Drela, M., Youngren, D., (2000). XFOIL. Repéré à <http://web.mit.edu/drela/Public/web/xfoil/>
- Dropkin, A., Custodio, D., Henoch, C., & Johari, H. (2012). Computation of flow field around an airfoil with leading-edge protuberances. *Journal of Aircraft*, 49(5), 1345-1355. doi: <https://doi.org/10.2514/1.C031675>
- Fish, F., & Lauder, G. V. (2006). Passive and active flow control by swimming fishes and mammals. *Annu. Rev. Fluid Mech.*, 38, 193-224.
- Fish, F. E. (1999). Performance constraints on the maneuverability of flexible and rigid biological systems. Dans *International symposium on unmanned untethered submersible technology* (pp. 394-406). Citeseer.
- Fish, F. E., & Battle, J. M. (1995). Hydrodynamic design of the humpback whale flipper. *Journal of Morphology*, 225(1), 51-60. doi: <https://doi.org/10.1002/jmor.1052250105>
- Fish, F. E., Howle, L. E., & Murray, M. M. (2008). Hydrodynamic flow control in marine mammals. *Integrative and Comparative Biology*, 48(6), 788-800.
- Forster, K., & White, T. (2014). Numerical investigation into vortex generators on heavily cambered wings. *AIAA journal*, 52(5), 1059-1071. doi: <https://doi.org/10.2514/1.J052529>
- Gerhart, P. M., Gerhart, A. L., & Hochstein, J. I. (2016). *Munson, Young and Okiishi's Fundamentals of Fluid Mechanics* (8th éd.). John Wiley & Sons.
- Guerrero, J. E., Sanguineti, M., & Wittkowski, K. (2020). Variable cant angle winglets for improvement of aircraft flight performance. *Meccanica*, 55(10), 1917-1947.
- Hain, J., Carter, G., Kraus, S., Mayo, C., & Winn, H. (1981). Feeding behavior of the humpback whale, *Megaptera novaeangliae*, in the western North Atlantic [North Eastern States (USA)]. *Fishery bulletin United States, National Marine Fisheries Service*.
- Hansen, K., Kelso, R., & Doolan, C. (2010). Reduction of flow induced tonal noise through leading edge tubercle modifications. Dans *16th AIAA/CEAS Aeroacoustics Conference* (pp. 3700). doi: <https://doi.org/10.2514/6.2010-3700>

- Hansen, K. L. (2012). *Effect of leading edge tubercles on airfoil performance* (PhD, The University of Adelaide).
- Hansen, K. L., Kelso, R. M., & Dally, B. B. (2011). Performance variations of leading-edge tubercles for distinct airfoil profiles. *AIAA journal*, 49(1), 185-194. doi: <https://doi.org/10.2514/1.J050631>
- Hersh, A. S., Soderman, P. T., & Hayden, R. E. (1974). Investigation of acoustic effects of leading-edge serrations on airfoils. *Journal of Aircraft*, 11(4), 197-202. doi: <https://doi.org/10.2514/3.59219>
- Houghton, E. L., & Carpenter, P. W. (2003). *Aerodynamics for engineering students* (5th éd.). Elsevier.
- Johari, H., Henoch, C., Custodio, D., & Levshin, A. (2007). Effects of leading-edge protuberances on airfoil performance. *AIAA journal*, 45(11), 2634-2642. doi: <https://doi.org/10.2514/1.28497>
- Kabir, A., Chowdhury, M. S., Islam, M. J., & Islam, M. (2019). Numerical Assessment of the Backward Facing Step for NACA 0015 Airfoil using Computational Fluid Dynamics. Dans *2019 1st International Conference on Advances in Science, Engineering and Robotics Technology (ICASERT)* (pp. 1-6). IEEE.
- Kurvers, R. H., Krause, S., Viblanc, P. E., Herbert-Read, J. E., Zaslansky, P., Domenici, P., . . . Wilson, A. D. (2017). The evolution of lateralization in group hunting sailfish. *Current Biology*, 27(4), 521-526.
- Lamar, J. E., & Herbert, H. E. (1982). *Production version of the extended NASA-Langley Vortex Lattice FORTRAN computer program. Volume 1: User's guide.*
- Liu, Y., Li, Y., & Shang, D. (2019). The hydrodynamic noise suppression of a scaled submarine model by leading-edge serrations. *Journal of Marine Science and Engineering*, 7(3), 68.
- Malipeddi, A. K., Mahmoudnejad, N., & Hoffmann, K. A. (2012). Numerical analysis of effects of leading-edge protuberances on aircraft wing performance. *Journal of Aircraft*, 49(5), 1336-1344. doi: <https://doi.org/10.2514/1.C031670>
- Menter, F., & Esch, T. (2001). Elements of industrial heat transfer predictions. Dans *16th Brazilian Congress of Mechanical Engineering (COBEM)* (Vol. 109, pp. 650).
- Miklosovic, D., Murray, M., Howle, L., & Fish, F. (2004). Leading-edge tubercles delay stall on humpback whale (*Megaptera novaeangliae*) flippers. *Physics of fluids*, 16(5), L39-L42. doi: <https://doi.org/10.1063/1.1688341>

- Miklosovic, D. S., Murray, M. M., & Howle, L. E. (2007). Experimental evaluation of sinusoidal leading edges. *Journal of Aircraft*, 44(4), 1404-1408. doi: <https://doi.org/10.2514/1.30303>
- National Park & preserve, N. P. s., U.S. Departement of the interior. Humpback Whale Facts. Repéré à https://www.cilc.org/getmedia/1df963e3-0bec-4ee3-93ac-3484ecc5777d/Teacher_Whale-Facts-Sheet.aspx
- Rostamzadeh, N., Kelso, R., Dally, B., & Hansen, K. (2013). The effect of undulating leading-edge modifications on NACA 0021 airfoil characteristics. *Physics of fluids*, 25(11), 117101. doi: <https://doi.org/10.1063/1.4828703>
- Rostamzadeh Torghabeh, N. (2016). *The impact of undulating leading-edge modifications on the flow characteristics of NACA 0021 foils* (The University of Adelaide, Austrailia).
- Skillen, A., Revell, A., Pinelli, A., Piomelli, U., & Favier, J. (2015). Flow over a wing with leading-edge undulations. *Aiaa Journal*, 53(2), 464-472. doi: <https://doi.org/10.2514/1.J053142>
- Spalding, B. E. L. a. D. B. (1974). THE NUMERICAL COMPUTATION OF TURBULENT FLOWS. *COMPUTER METHODS IN APPLIED MECHANICS ANR ENGINEERING (NORTH-HOLLAND PUBLISHING COMPANY)*. doi: [https://doi.org/10.1016/0045-7825\(74\)90029-2](https://doi.org/10.1016/0045-7825(74)90029-2)
- Stein, B., & Murray, M. (2005). Stall mechanism analysis of humpback whale flipper models. *Proceedings of Unmanned Untethered Submersible Technology (UUST), UUST05*, 5.
- Sudhakar, S., Venkatakrishnan, L., & Ramesh, O. (2020). The influence of leading-edge tubercles on airfoil performance at low reynolds numbers. *AIAA Scitech 2020 Forum*, 1(PartF). doi: <https://doi.org/10.2514/6.2020-2219>
- Taheri, A. (2018). On the hydrodynamic effects of humpback whale's ventral pleats. *American Journal of Fluid Dynamics*, 8(2), 47-62. doi: <https://doi.org/10.5923/j.ajfd.20180802.02>
- Teruna, C., Avallone, F., Casalino, D., & Ragni, D. (2021). Numerical investigation of leading edge noise reduction on a rod-airfoil configuration using porous materials and serrations. *Journal of Sound and Vibration*, 494, 115880. doi: <https://doi.org/10.1016/j.jsv.2020.115880>
- Van Nierop, E. A., Alben, S., & Brenner, M. P. (2008). How bumps on whale flippers delay stall: an aerodynamic model. *Physical Review Letters*, 100(5), 054502. doi: <https://doi.org/10.1103/PhysRevLett.100.054502>

- Watts, P., & Fish, F. E. (2001a). The influence of passive, leading edge tubercles on wing performance. Dans *Proc 12th Internat Symp Unmanned Untethered Submersible Tech. Durham, NH: Autonomous Undersea Systems Institute.*
- Watts, P., & Fish, F. E. (2001b). The influence of passive, leading edge tubercles on wing performance. Dans *Proc. Twelfth Intl. Symp. Unmanned Untethered Submers. Technol. Auton. Undersea Syst. Inst. Durham New Hampshire.*
- Weber, P. W., Howle, L. E., & Murray, M. M. (January, 2010). Lift, drag, and cavitation onset on rudders with leading-edge tubercles. *Marine Technology and Sname News*, 47(01), 27-36.
- Wei, Z., Lian, L., & Zhong, Y. (2018). Enhancing the hydrodynamic performance of a tapered swept-back wing through leading-edge tubercles. *Experiments in Fluids*, 59(6), 103. doi: <https://doi.org/10.1007/s00348-018-2557-5>
- Wei, Z., New, T. H., & Cui, Y. (2018). Aerodynamic performance and surface flow structures of leading-edge tubercled tapered swept-back wings. *AIAA Journal*, 56(1), 423-431. doi: 10.2514/1.J055663
- Wei, Z., New, T. H., Lian, L., & Zhang, Y. (2019). Leading-edge tubercles delay flow separation for a tapered swept-back wing at very low Reynolds number. *Ocean Engineering*, 181, 173-184. doi: <https://doi.org/10.1016/j.oceaneng.2019.04.018>
- Wilcox, D. C. (1998). *Turbulence modeling for CFD* (Vol. 2). DCW industries La Canada, CA.
- Woodward, B. L., Winn, J. P., & Fish, F. E. (2006). Morphological specializations of baleen whales associated with hydrodynamic performance and ecological niche. *Journal of Morphology*, 267(11), 1284-1294. doi: 10.1002/jmor.10474
- Yoon, H., Hung, P., Jung, J., & Kim, M. (2011). Effect of the wavy leading edge on hydrodynamic characteristics for flow around low aspect ratio wing. *Computers & Fluids*, 49(1), 276-289. doi: <https://doi.org/10.1016/j.compfluid.2011.06.010>
- Zhang, M., Wang, G., & Xu, J. (2013). Aerodynamic control of low-Reynolds-number airfoil with leading-edge protuberances. *AIAA journal*, 51(8), 1960-1971. doi: <https://doi.org/10.2514/1.J052319>